

# Multi-contrast Magnetic Resonance Imaging of Myelin and Iron in the Brain

DISSERTATION

for the award of the degree

*"Doctor rerum naturalium"*

of the Georg-August-Universität Göttingen

within the doctoral program Systems Neuroscience  
of the Georg-August University School of Science (GAUSS)

submitted by

Rakshit Dadarwal

from Gulabbari, Rajasthan, India

Göttingen, 2021

## **Thesis Committee**

Prof. Dr. Susann Boretius

*Functional Imaging Laboratory, German Primate Center (DPZ), Göttingen*

Prof. Dr. Wolfgang Brück

*Institute for Neuropathology, University Medical Center Göttingen (UMG)*

Prof. Dr. Klaus-Armin Nave

*Dept. of Neurogenetics, Max Planck Institute for Experimental Medicine, Göttingen*

## **Members of the Examination Board**

**Referee:** Prof. Dr. Susann Boretius

*Functional Imaging Laboratory, German Primate Center (DPZ), Göttingen*

**2<sup>nd</sup> Referee:** Prof. Dr. Wolfgang Brück

*Institute for Neuropathology, University Medical Center Göttingen (UMG)*

## **Further members of the Examination Board**

Prof. Dr. Klaus-Armin Nave

*Dept. of Neurogenetics, Max Planck Institute for Experimental Medicine, Göttingen*

Prof. Dr. Dr. Hannelore Ehrenreich

*Clinical Neuroscience, Max Planck Institute for Experimental Medicine, Göttingen*

PD. Dr. Peter Dechent

*Institute for Cognitive Neurology, University Medical Center Göttingen (UMG)*

Prof. Dr. med. Christine Stadelmann-Nessler

*Institute for Neuropathology, University Medical Center Göttingen (UMG)*

Date of oral examination: December 14, 2021



## ABSTRACT

The non-invasive characterization of brain myelin has essential applications in basic neuroscience and the clinical management of white matter brain diseases and other inflammatory and neurodegenerative diseases. Magnetic resonance imaging (MRI) provides a variety of image contrasts that change in relation to myelin alterations. However, it is not clear how these potential MRI biomarkers of myelin reflect the underlying tissue structure at the meso- and microscale. Due to physical and technical limitations, the spatial resolution of MRI is poor in comparison to the size of tissue constituents. Thus, the observed effects in each image voxel are the sum of a set of tissue substructures. As a result, numerous biophysical mechanisms contribute to the MRI signal in an image voxel.

This thesis evaluates currently used MRI contrast mechanisms regarding their ability to serve as *in vivo* biomarkers for myelin- and age-related changes in the brain. To this end, mouse mutants of myelin genes and non-human primates at different ages have been examined using these MRI techniques, including diffusion-based MRI (dMRI), Quantitative Susceptibility Mapping (QSM), and MR techniques utilizing the transfer of magnetization.

dMRI has the ability to link the MRI measurements at a millimeter scale to tissue microstructures on a scale much smaller than the nominal image resolution. The reason for this is that the measured MR signal originates from the random motion of water molecules in the brain tissue at the cellular level. The difficulty lies in the disentanglement of the contributors to this MR signal, as the signal is eventually averaged over an image voxel of several micrometers. A variety of mathematical models has been proposed to decipher the tissue properties from the obtained dMRI signal. However, it is not clear how effectively these methods capture myelin and axon alterations. In my first study ([Chapter 1](#)), I explored four different approaches of signal modeling to fit the dMRI signal obtained from mouse mutants with varying levels of myelin and axonal abnormalities. I discovered that most quantitative estimates of dMRI are sensitive to myelin and axon alterations but with poor specificity when compared to the tissue characteristics revealed by electron microscopy.

A still relatively new MRI technique that is sensitive to myelin and iron in the brain tissue is QSM. QSM has been applied in patients with demyelinating and neurodegenerative diseases as well as in human studies on healthy aging. Non-human primates (NHP), our closest relatives in the animal kingdom, are of particular value for studying age-related alterations in the brain as we share many similarities in neuroanatomy and cognitive abilities. In NHP, QSM has, however, not yet been established. In my second study ([Chapter 2](#)), I established QSM and the mapping of its counterpart, the effective transverse relaxation rate

( $R_2^*$ ) in the macaque monkey brain. I then compared the results of QSM and the values of  $R_2^*$  to those in the human brain. I observed comparable QSM and  $R_2^*$  results in subcortical regions of the human and monkey brains, except for the red nucleus, where humans showed higher magnetic susceptibility compared to macaques. Significant differences in QSM were also observed in white matter structures, such as in the body of the corpus callosum and the anterior commissure. Here, monkeys showed a lower susceptibility than humans. In addition, I discovered that the reference brain region chosen to normalize the QSM values could significantly affect comparative QSM studies in humans and NHPs. Another intriguing observation was that the human cerebrospinal fluid had a paramagnetic QSM contrast, whereas the monkey cerebrospinal fluid was diamagnetic, best explained by the significantly higher iron content in humans.

Quantitative MRI and, in particular, region-of-interest analyses using techniques such as the one mentioned above significantly benefit (or even require) species-specific anatomical MRI atlases. The macaque brain atlases that are currently publicly available are from rhesus macaques, which have a different brain morphology than cynomolgus macaques, the NHP species most used in biomedical research and preclinical studies. Moreover, the majority of rhesus macaque atlases rely on  $T_1$ -weighted images only. These atlases provide an excellent gray-to-white matter contrast but lack, for instance, contrast from subcortical structures. In my third study ([Chapter 3](#)), I developed the Deutsches Primatenzentrum cynomolgus macaque (DPZCYNO) template. This dedicated high-resolution (0.25 mm) atlas was designed with a stereotaxic orientation for single-subject MR image standardization and anatomical structural localization. This stereotaxic orientation is particularly necessary for invasive studies, which, for instance, require a precise targeting of brain regions by the inserted electrodes. In addition, to overcome the limitations of a single MRI contrast, I created MRI templates from multiple anatomical ( $T_1$ -weighted,  $T_2$ -weighted, Magnetization Transfer weighted, and Multi-echo gradient-recalled echo) and parametric (QSM,  $R_2^*$ , magnetization transfer saturation, and apparent  $T_1$  relaxation time) contrasts. These multi-contrast MRI templates will aid in anatomical structure delineation and parcellation by improving contrast from all tissue types.

Acquiring data from many MRI sequences is not always feasible in non-human primates. Constraints imposed by anesthesia and animal health limit the available measurement time. Similar limitations exist for data acquisition in human patients. As shown in this thesis, a single MRI contrast is, however, insufficient to generate satisfactory contrasts from all types of brain tissue. In my fourth study ([Chapter 4](#)), I developed a strategy for obtaining a good cortical, subcortical, and white matter contrast by using only two ( $T_1$ -weighted and QSM) MRI contrasts. The developed weighted linear fusion of QSM and  $T_1$ -weighted images (TQ-SILiCON) significantly improved the visualization and segmentation of gray-to-white matter in the macaque brain. I also demonstrated that the TQ-SILiCON approach

works equally well for humans and improves human brain tissue segmentation. Furthermore, TQ-SILiCON required data sets could be obtained using clinically available MRI systems and in a reasonably short measurement time.

In my fifth and final study ([Chapter 5](#)), I employed the developed methods and pipelines to explore healthy brain aging in two NHP species, the cynomolgus macaque and the marmoset monkey. These species are increasingly utilized in preclinical studies to test novel treatment approaches to slow down aging and age-related decline of cognitive abilities. However, there is still insufficient knowledge about how well non-human primate models resemble the process of aging in humans. Utilizing the multi-contrast approach, I discovered an age-related increase of QSM and  $R_2^*$  in subcortical structures in both macaque and marmoset. This is most likely due to an accumulation of iron, as preliminary histological analyses of the species studied by us suggested this, and it is very much in line with previous reports on humans. Future studies involving advanced histological analyses will be performed to validate the proposed multi-contrast approach.

# Contents

ABSTRACT	iii
o INTRODUCTION	i
o.1 MRI methods to image myelin and iron . . . . .	2
o.2 Combination of MRI contrasts . . . . .	9
o.3 Aim of the thesis . . . . .	11
1 COMPARISON OF CURRENT DIFFUSION MRI METHODS IN MYELIN MOUSE MUTANTS	12
1.1 Introduction . . . . .	13
1.2 Materials and Methods . . . . .	16
1.3 Results . . . . .	17
1.4 Discussion . . . . .	23
2 QSM AND $R_2^*$ MAPPING IN HUMAN AND NON-HUMAN PRIMATE BRAINS	25
2.1 Introduction . . . . .	26
2.2 Materials and Methods . . . . .	28
2.3 Results . . . . .	32
2.4 Discussion . . . . .	40
3 A MULTI-CONTRAST MRI TEMPLATE OF THE CYNOMOLGUS MACAQUE BRAIN	43
3.1 Introduction . . . . .	44
3.2 Materials and Methods . . . . .	45
3.3 Results . . . . .	52
3.4 Discussion . . . . .	62
4 FUSION OF QUANTITATIVE SUSCEPTIBILITY MAPS AND $T_1$ -WEIGHTED IMAGES IMPROVE BRAIN TISSUE CONTRAST IN PRIMATES	65
4.1 Introduction . . . . .	66

4.2	Materials and Methods . . . . .	68
4.3	Results . . . . .	71
4.4	Discussion . . . . .	82
5	MULTI-CONTRAST MRI OF THE AGING BRAIN - A COMPARATIVE STUDY OF CYNOMOLGUS MACAQUES AND COMMON MARMOSETS	86
5.1	Introduction . . . . .	87
5.2	Materials and Methods . . . . .	88
5.3	Results . . . . .	94
5.4	Discussion . . . . .	103
6	GENERAL DISCUSSION AND CONCLUSIONS	107
	APPENDIX A SUPPLEMENTARY MATERIAL	110
	APPENDIX B RESEARCH OUTPUTS	121
	REFERENCES	124
	DECLARATION	158

# Listing of figures

1	Myelin imaging using MRI . . . . .	3
1.1	Diffusion MRI models of white matter . . . . .	15
1.2	Regions-of-interest for diffusion data analysis . . . . .	17
1.3	Diffusion MRI maps of wild-type and knockout mice . . . . .	18
1.4	DTI analysis plots . . . . .	19
1.5	DKI analysis plots . . . . .	20
1.6	WMTI analysis plots . . . . .	21
1.7	NODDI analysis plots . . . . .	22
1.8	Electron microscopy images of wild-type and knockout mice . . . . .	23
2.1	QSM and $R_2^*$ data analysis pipelines . . . . .	30
2.2	Human and monkey brain regions-of-interest . . . . .	31
2.3	Averaged human and monkey brain QSM and $R_2^*$ maps . . . . .	33
2.4	QSM and $R_2^*$ maps of human and monkey brain basal ganglia . . . . .	34
2.5	QSM and $R_2^*$ analyses in subcortical areas . . . . .	35
2.6	QSM and $R_2^*$ analyses in white matter areas . . . . .	36
2.7	QSM TE dependence in the human and monkey brain . . . . .	37
2.8	QSM TE dependence in cerebrospinal fluid . . . . .	38
2.9	QSM, $R_2^*$ and color-coded FA maps for the corpus callosum . . . . .	39
2.10	DTI results for the corpus callosum . . . . .	39
2.11	NODDI results for the corpus callosum . . . . .	40
3.1	Preprocessing of multi-contrast MRI images . . . . .	48
3.2	The stereotaxic orientation of the DPZCYNO templates . . . . .	52
3.3	Multi-contrast MRI templates of the cynomolgus macaque monkey . . . . .	53
3.4	Comparison of $T_1w$ and QSM templates . . . . .	54
3.5	Mean displacement map . . . . .	55
3.6	Tissue segmentation using $T_1w$ and SILiCON images . . . . .	56

3.7	T <sub>1</sub> w tissue segmentation misclassifications . . . . .	57
3.8	The DPZCYNO cortical surfaces . . . . .	58
3.9	Cortical thickness map . . . . .	58
3.10	Cortical myelin maps . . . . .	60
3.11	The DPZCYNO template parcellations . . . . .	61
4.1	The macaque brain in T <sub>1</sub> w and QSM images . . . . .	72
4.2	QSM image and subcortical structures on a 3D rendering . . . . .	73
4.3	The TQ-SILiCON data analysis workflow . . . . .	74
4.4	Macaque brain T <sub>1</sub> w, QSM, and TQ-SILiCON images . . . . .	75
4.5	The dentate nucleus in T <sub>1</sub> w, QSM, and TQ-SILiCON images . . . . .	76
4.6	White matter surface with subcortical structures . . . . .	77
4.7	Tissue segmentation using macaque brain T <sub>1</sub> w and TQ-SILiCON images . . . . .	78
4.8	T <sub>1</sub> w tissue segmentation misclassifications in the macaque brain . . . . .	79
4.9	Human brain T <sub>1</sub> w, QSM, and TQ-SILiCON images . . . . .	80
4.10	Tissue segmentation using human brain T <sub>1</sub> w and TQ-SILiCON images . . . . .	81
4.11	T <sub>1</sub> w tissue segmentation misclassifications in the human brain . . . . .	82
5.1	Macaques and marmosets: number and age . . . . .	89
5.2	Brain regions-of-interest in macaques and marmosets . . . . .	94
5.3	The average brain templates of macaques of various ages . . . . .	95
5.4	The average brain templates of marmosets of various ages . . . . .	95
5.5	QSM and R <sub>2</sub> <sup>*</sup> analyses . . . . .	97
5.6	MTsat, and T <sub>1</sub> app analyses . . . . .	98
5.7	Diffusion MRI analyses . . . . .	99
5.8	Gray-white matter volume ratio in macaques and marmosets vs. age . . . . .	100
5.9	Corpus callosum morphometric and microstructural characteristics . . . . .	101
5.10	QSM TE dependence in the macaque and marmoset brain . . . . .	102
A.1	QSM and R <sub>2</sub> <sup>*</sup> maps of human and monkey brain superior colliculus . . . . .	110
A.2	Unreferenced and CSF normalized magnetic susceptibility values . . . . .	111
A.3	QSM vs. R <sub>2</sub> <sup>*</sup> scatterplot . . . . .	112
A.4	QSM TE dependence in the human and monkey brain . . . . .	112
A.5	QSM and R <sub>2</sub> <sup>*</sup> orientation dependence . . . . .	113
A.6	Regions-of-interest used for the contrast-to-noise ratio estimation . . . . .	113
A.7	Multi-contrast DPZCYNO templates . . . . .	114
A.8	Morphological analysis of cynomolgus and rhesus macaque brains. . . . .	116
A.9	Hippocampus morphometric and microstructural characteristics . . . . .	117
A.10	QSM and R <sub>2</sub> <sup>*</sup> maps in the young and old marmoset brains . . . . .	118

A.11	QSM, $R_2^*$ , MTsat, and $T_{1app}$ in young and old marmosets . . . . .	119
A.12	The marmoset brain's subcortical regions-of-interest . . . . .	120



# List of Tables

1.1	Wild-type and knockout mouse strains . . . . .	16
2.1	MRI parameters for the monkey and human brain QSM and dMRI scans . . . . .	29
2.2	Cerebrospinal fluid and whole-brain magnetic susceptibility values . . . . .	35
3.1	MRI parameters for the macaque brain $T_1w$ , $T_2w$ , and ME-GRE scans . . . . .	46
3.2	MRI parameters for the macaque brain MTw, PDw, and $T_1w$ scans . . . . .	47
4.1	MRI parameters for the macaque and human brain $T_1w$ and QSM scans . . . . .	69
5.1	MRI parameters for the marmoset brain ME-GRE and dMRI scans . . . . .	90
5.2	MRI parameters for the marmoset brain MTw, PDw, and $T_1w$ scans . . . . .	91
5.3	MRI parameters for postmortem marmoset brains . . . . .	105
A.1	The contrast-to-noise ratio in the symmetric DPZCYNO templates . . . . .	115
A.2	The contrast-to-noise ratio in the asymmetric DPZCYNO templates . . . . .	115

LOOK TO THIS DAY,  
FOR IT IS LIFE, THE VERY BREATH OF LIFE.  
IN ITS BRIEF COURSE LIE  
ALL THE REALITIES OF YOUR EXISTENCE;  
THE BLISS OF GROWTH,  
THE GLORY OF ACTION,  
THE SPLENDOR OF BEAUTY.  
FOR YESTERDAY IS ONLY A DREAM,  
AND TOMORROW IS BUT A VISION.  
BUT TODAY, WELL LIVED,  
MAKES EVERY YESTERDAY A DREAM OF HAPPINESS,  
AND EVERY TOMORROW  
A VISION OF HOPE.  
LOOK WELL, THEREFORE, TO THIS DAY.  
(ANCIENT SANSKRIT)

# Acknowledgments

First and foremost, I want to express my gratitude to Professor Susann Boretius, my Ph.D. supervisor. She believed in me and supported me with all of her resources. She has served as a guardian for me for the past five years. My soul will be eternally grateful for her supervision, guidance, and kindness.

I would like to thank Professor Wolfgang Brück and Professor Klaus-Armin Nave, my Thesis Advisory Committee members, for their unwavering support and encouragement. I appreciate their time and the assistance provided by their laboratories.

The members of Functional Imaging Lab have been my family for the past five years. They have all been so gracious to me. Amir Moussavi, Shereen Petersen, and Kristin Kötz were always there for me, no matter what. Thank you for taking care of all of my appointments, translating so many documents for me, and assisting me in infinite ways. Since the day I arrived in Göttingen, Amir Moussavi was always there for me whether I needed help with an MRI scanner or MRI data analysis. His generosity and support mean a lot to me. Nikoloz Sirmopilatze has been my long-term office mate and friend with whom I have shared innumerable moments. I appreciate his kindness; my chats with him have taught me a lot. Tor Rasmus Memhave joined us late, but he has been a wonderful and supportive office mate ever since. Michael Ortiz-Rios has been a pleasure to talk to and learn from over the last two years. I am grateful for his friendly and welcoming demeanor. Judith Mylius has been extremely helpful and supportive. I appreciate her assistance in obtaining marmoset aging data. My gratitude also extends to my colleagues Jürgen Baudewig, Renate Schweizer, Melanie Bückner, Marco Deckers, Yasemin Betül Gültekin, Vladislav Kozyrev, Daniel Hillier, Majid Ramedani, Ina Barnekow, Ellen Wiese, Simon Weber, Davood Bakhtiari, and Aref Kalantari Sarcheshmeh for their support and kindness. Kristin Kötz, Kerstin Fuhrmann, Jessica König, and Sina Bode provided invaluable support with data collection and phantom preparation. Thank you for always being kind to me and always being willing to help me.

I am grateful to everyone who, via various means, assisted me in managing my health. Spe-

cial thanks go out to all of my doctors in Göttingen and the staff at the Universitätsmedizin Göttingen.

I would like to thank my collaborator, Dr. Wiebke Möbius, and her group for their unwavering support and assistance.

I am thankful to Professor Hannelore Ehrenreich for her personal support.

I would like to express my gratitude to everyone at the Systems Neuroscience office and the GGNB office for their constant support and assistance.

Thanks to the master's and bachelor's students who worked with me - Luzia Hintz, Adrián Palacios Muñoz, Claudia Serrano Ferrel, Jiaxin Xiao, and Niklas Binder.

I am thankful to everyone who has helped me create good memories, especially all of my friends. I appreciate all of the time and effort that you have put into me.

For all of these years, the University Sports Center has been my second home. Thank you to all of my teammates and partners in cricket, badminton, jogging, and yoga.

I am grateful for my family's unconditional love, acceptance and emotional support. Their values have shaped me into the person I am today.

Thank you, Mother Nature, for giving me a beautiful life and for looking after me.

*NOW is the only reality. All else is either memory or imagination.*

Osho



## Introduction

Myelin is an essential part of the nervous system. In vertebrates, myelin provides insulation to the axons to set the structural basis for saltatory action potential propagation. In saltatory conduction, the action potential only travels between the unmyelinated axonal segments (the nodes of Ranvier). Myelin in the Central Nervous System (CNS) is synthesized and metabolically supported by oligodendrocytes, a type of neuroglial cell. In addition, oligodendrocytes play a significant role in supporting axonal integrity [Lappe-Siefke et al., 2003, Nave & Werner, 2021] and activity-dependent myelination [Moore et al., 2020]. Multilayered and spirally wrapped cell membrane sheath of myelin comprises very high lipid (~70-80% of dry weight) membrane structure and low protein constituents (~20-30%) [Morell & Quarles, 1999, Nave & Werner, 2014]. Myelin incorporates approximately 40% water.

Myelin and iron are crucial for normal healthy brain function and several neurological diseases. Myelin establishes the foundation for typical motor, sensory, and cognitive activities by promoting fast impulse propagation. Furthermore, the dynamics of myelin change with time in the human brain, which is important for plasticity and healthy aging studies [Faizy et al., 2020, Fields, 2015]. Damaged myelin causes disruptions in neuronal communication and the transmission of fast impulse propagation. Myelin loss (dys- and demyelination) is a prevalent symptom of several nervous system diseases, including multiple sclerosis [Stadelmann et al., 2011]. Furthermore, iron aids in the transport of oxygen, the synthesis of neurotransmitters, and the production of myelin in the brain. The accumulation of iron has been linked to several neurodegenerative diseases and healthy brain aging [Schneider, 2020].

The assessment of myelin using *in vivo* methods is essential for a deeper understanding of the myelin-associated pathophysiology. In addition, *in vivo* myelin assessment aids in the identification of myelin-related diseases by detecting the underlying pattern of myelin degradation and its influence on surrounding tissues. Monitoring myelin is also vital for developing a therapeutic cure or evaluating pharmacological therapies for myelin repair or remyelination. Invasive measures of myelin include immunohistochemical staining that provides greater detail of the microstructural tissue environment. However, the intrusive nature of histology restrains its use in everyday clinical practice. On the other hand, Magnetic Resonance Imaging (MRI) is a tool for measuring myelin *in vivo* non-invasively. Non-invasive *in vivo* approaches to measuring myelin are essential due to their clinical relevance.

MRI has the ability to visualize tissue microstructure at the sub-millimeter level non-invasively and offers excellent soft-tissue contrast *in vivo*. Myelin and iron are a source of many MRI contrasts with varying sensitivity and specificity [Barkovich, 2005, Lazari & Lipp, 2021]. In many autoimmune chronic diseases of the CNS, the non-invasive nature of MRI allows *in vivo* longitudinal assessment of myelin production, disruption of its sheath formation, and myelin sheath destruction. The use of MRI for disease diagnosis and long-term monitoring of the treatment and disease progression is essential. MRI works equally well for human and non-human primates, as well as for rodents.

Myelin structure and function in healthy and pathological conditions can be better understood using animal models with myelin-specific mutations or myelin-associated gene manipulations (transgenic animals). A lot has been known and available in rodent research to link human physiology and function to the underlying structure. Mouse models have aided our understanding of disease genes and the proteins encoded by them. All of this contributes to understanding several key issues, such as what kind of cellular processes can trigger different types of neurological disorders. However, not all findings in rodents translate well to humans. Non-human primates (NHPs), on the other hand, are phylogenetically closely related to humans and have similar physiology and neuroanatomy. NHPs have made a significant contribution to the development of basic knowledge of human brain architecture, circuitry, and functions. NHPs have a distinct advantage over rodents as animal models. NHP research has resulted in the development of clinical treatments and has significant promise for biomedical translational research. NHP may also help us better understand the underlying changes in gray-white matter integrity, myelin, and iron, as well as the underlying mechanisms that underpin many demyelinating and neurodegenerative diseases.

## 0.1 MRI METHODS TO IMAGE MYELIN AND IRON

MRI provides a range of brain tissue imaging contrasts with varying sensitivity and specificity to the myelin and iron. Most of the MRI-measured brain tissue contrasts are sensitive to the

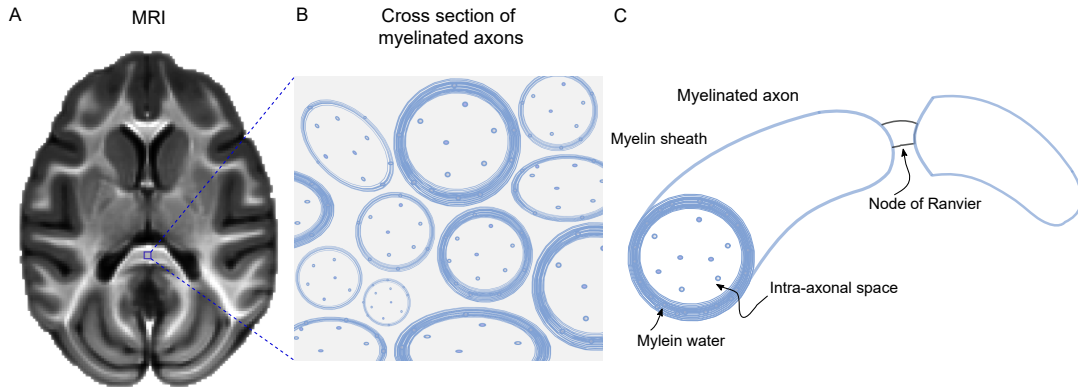
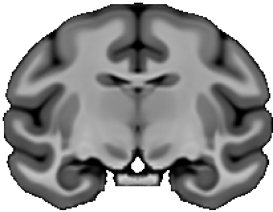


**Figure 1:** A. An MR image of a macaque monkey's brain. B. The microstructure of the corpus callosum tissue is depicted. The axons are myelinated to variable degrees, and their diameter varies from axon to axon. C. In a single myelinated axon, water protons are trapped inside the axon and in the myelin bilayers.

spatial distribution of myelin. But this distribution overlap with the distribution of other substrates such as iron. Here we present an overview of qualitative and quantitative MRI contrasts that are sensitive to myelin and iron in the brain.

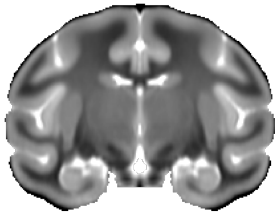
## QUALITATIVE CONTRASTS

### 0.1.1 $T_1$ -WEIGHTED MRI ( $T_1w$ )



The  $T_1$ -weighted ( $T_1w$ ) MRI sequence is mostly used for the imaging of brain anatomy. The  $T_1w$  image contrast is determined by  $T_1$  properties (i.e.,  $T_1$ -relaxation time (cerebrospinal fluid > gray matter > white matter)) of the underlying tissue. Because of the presence of myelin and other macromolecules, the white matter has a shorter  $T_1$  than gray matter. In case of inflammation, edema, and hemorrhage, an increase in water content in the tissue prolongs the  $T_1$  relaxation time, and the tissue appears hypo-intense on  $T_1w$  images. The similar appearance of all pathologies on the  $T_1w$  image compromises the specificity to underlying tissue changes. Moreover,  $T_1w$  images are qualitative in nature, and quantitative  $T_1$  relaxation time calculation necessitates precise dedicated measurements.

### 0.1.2 T<sub>2</sub>-WEIGHTED MRI (T<sub>2</sub>w)

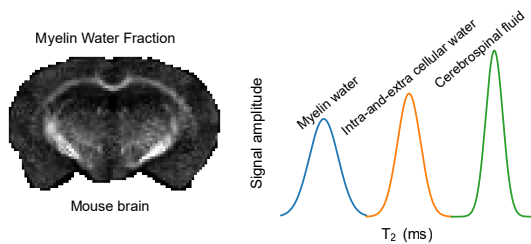


The T<sub>2</sub>-weighted (T<sub>2</sub>w) MRI sequence is perhaps the most widely used MRI sequence in clinical routines to image brain pathologies. The T<sub>2</sub>w image contrast is determined by the measured tissue's T<sub>2</sub> relaxation times (cerebrospinal fluid > gray matter > white matter). T<sub>2</sub> relaxation is affected by tissue's local water content and its interactions with the surrounding tissue components such as lipids and proteins. White matter in the brain has a shorter T<sub>2</sub> than gray matter and cerebrospinal fluid due to the presence of myelin and other macromolecules. Increased water content in pathological conditions such as inflammation, edema, and acute hemorrhage appears hyper-intense on the T<sub>2</sub>w image due to an increase in T<sub>2</sub>. These hyper-intense areas have a similar appearance in all pathological states and are difficult to discern on conventional T<sub>2</sub>w images.

### QUANTITATIVE CONTRASTS

Several biophysical mechanisms influence MRI contrasts in general in a complex tissue environment. To determine the particular contribution of various tissue components such as myelin, advanced quantitative approaches are required. To quantify myelin in the CNS, several quantitative measures have been proposed. The most commonly used quantitative methodologies are myelin water imaging, diffusion MRI, magnetization transfer, magnetic susceptibility, and effective transverse relaxation rate, which are summarized in this section.

### 0.1.3 MYELIN WATER IMAGING



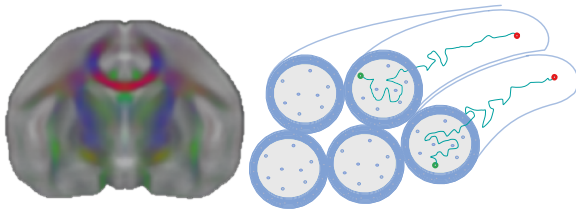
In CNS tissues, water molecules can be identified in three primary tissue environments, including freely available water pool (primarily cerebrospinal fluid), restricted water pool (intra and extra-cellular water), and bound pool (myelin or macromolecular pool). All these three compartments have a unique range of T<sub>2</sub>



relaxation times at 3T, cerebrospinal fluid ( $T_2 > 120$  ms), intra and extra-cellular ( $T_2 \sim 100$  ms), and myelin water ( $T_2 < 40$  ms), enabling separation of their relative contribution to the overall voxel signal. Myelin Water Imaging (MWI) measures water molecules trapped between lipid bilayers of the CNS myelin sheath, contributing to 10 to 15 % of the overall signal from a white matter voxel [MacKay et al., 1994]. The ratio of the myelin water component to the total water signal is called the myelin water fraction (MWF). The traditional approach to estimate MWF relies on the Carr-Purcell-Meiboom-Gill (CPMG) method for multi-component  $T_2$  mapping (MacKay and Laule, 2016). In this approach, multiple echo times are measured to fit the exponential signal decay.

MWI has been extensively used to study myelin development [Bouhrara et al., 2020], healthy aging [Faizy et al., 2020], and myelin related alterations in several neurological diseases, including multiple sclerosis [Abel et al., 2020, Vargas et al., 2015], neuromyelitis optica spectrum disorder [Manogaran et al., 2016], stroke [Borich et al., 2013], traumatic brain injury [Wright et al., 2016], cervical spondylotic myelopathy [Liu et al., 2017]. Even though some histological results have validated the sensitivity of MWI to underlying myelin alterations, there are some confounding factors such as inter-compartmental water exchange, the mcDESPOT approach for compartmental fitting is not always applicable, and myelin debris, to name a few [Dula et al., 2010, Lee et al., 2021, MacKay & Laule, 2016, McCreary et al., 2009]. All of these confounding factors limit MWI's usefulness and complicate the interpretation of obtained results.

#### 0.1.4 DIFFUSION MRI



The water molecules in biological tissues are displaced in a Brownian motion. This movement of water molecules can be used to probe the tissue microstructures at a millimeter voxel scale [Bihan, 1995, Le Bihan et al., 1992]. The quantitative estimation of a water molecule's diffusion can be done via apparent diffusion coefficient (ADC). The straightforward method for fitting the observed diffusion MRI (dMRI) signal is Diffusion Tensor Imaging (DTI) [Basser et al., 1994]. The DTI model measures diffusivity (mean, axial, and radial) and the degree of anisotropy of diffusion (fractional anisotropy) in brain tissues. The movement of water molecules along the axon creates a highly anisotropic environment, which makes fractional anisotropy a marker of white matter tissue integrity. In addition, axial and radial diffusivities are sensitive to axonal and myelin integrities. To date, DTI is the most widely used non-invasive approach for studying tissue

microstructure *in vivo* [Le Bihan et al., 2001, Alexander et al., 2007]. However, DTI modeling is focused on the oversimplification that diffusion in biological tissue is isotropic and follows a Gaussian distribution. This assertion ignores the fact that Brownian motion, or random walk of water molecules in biological tissues, is hampered and restricted by cellular boundaries and other tissue constituents.

Diffusion Kurtosis Imaging (DKI) is a DTI extension that determines how much diffusion deviates from Gaussianity or is non-gaussian [Jensen et al., 2005]. Mean kurtosis, radial kurtosis, and axial kurtosis are three new scalar parameters added to the DTI estimated parameters by this expansion. DKI is clinically viable and commonly used in applications including stroke [Hui et al., 2012], traumatic brain injury [Stokum et al., 2015], aging [Gong et al., 2014], and other CNS diseases [Steven et al., 2014]. DKI parameters, like DTI parameters, are sensitive to underlying microstructural changes, but their limited precision makes biophysical interpretation difficult [Fieremans et al., 2011].

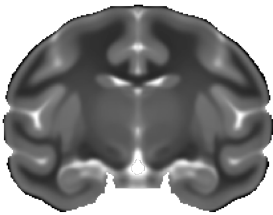
Several advanced biophysical multi-compartment models have been developed to estimate tissue compartment volume fraction by observing the behavior of the diffusion signal. DKI parameters are biophysically interpreted using the white matter tract integrity (WMTI) model [Fieremans et al., 2011]. The WMTI model estimates the axonal water fraction, intra-axonal and extra-axonal diffusivities, and the tortuosity of the extra-axonal space using a two-tensor compartment model for well-aligned white matter fiber configuration. The Neurite orientation dispersion and density imaging (NODDI) and multi-compartment spherical mean technique (mcSMT) models estimate intra-neurite (axon + dendrite) volume fraction from a clinically viable data acquisition scheme [Kaden et al., 2016, Zhang et al., 2012]. NODDI divides each voxel's diffusion signal into three compartments: intra-neurite, extra-neurite, and cerebrospinal fluid. The intra-neurite signal is modeled as a stick (zero-radius cylinder), the extra-neurite signal as a cylindrically symmetric tensor, and cerebrospinal fluid as free isotropic diffusion.

Along with regular models (DTI and DKI), these advanced biophysical models have been used to improve specificity to the underlying tissue microstructural changes in aging [Cox et al., 2016], multiple sclerosis [Luo et al., 2019a], Alzheimer's disease [Fu et al., 2020], Parkinson's disease [Mitchell et al., 2019], amyotrophic lateral sclerosis [Swash et al., 2020], brain tumors [Lampinen et al., 2017], epilepsy [Winston et al., 2020], ischemia [Hara et al., 2019], Huntington's disease [Zhang et al., 2018], traumatic brain injury [Churchill et al., 2017], schizophrenia [Kraguljac et al., 2019], and cervical spondylotic myelopathy [Iwama et al., 2020]. However, their sensitivity to alterations in myelin and axons is still restricted, and more research is needed to eliminate simplistic assumptions and fixed parameters in model fitting [Jelescu et al., 2020].

dMRI based fiber tractography is a non-invasive method of identifying fiber bundles and fiber pathways within the brain. In the field of connectomics, fiber tractography plays an im-

portant role in determining the anatomical connections between different parts of the brain. Fiber tracking is a potent approach for visualizing white matter fiber bundles that has a wide range of applications in neurosurgical plannings [Golby et al., 2011] and investigation of stroke [Mukherjee, 2005], multiple sclerosis [Shu et al., 2011], epilepsy [Engel et al., 2013], and neurodegenerative diseases [Müller & Kassubek, 2013, Ciccarelli et al., 2008]. However, technical constraints restrict the technique’s biological accuracy and demand a careful interpretation of results [Jeurissen et al., 2019].

#### 0.1.5 MAGNETIZATION TRANSFER



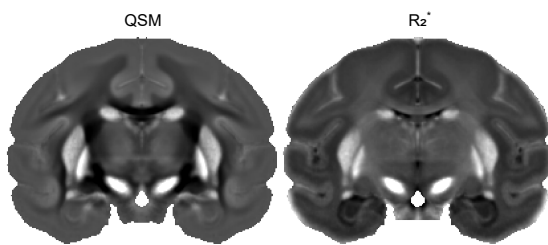
MT refers to the contrast that originated from the exchange of magnetization between the bound pool and free water pool in the brain tissue [Edzes & Samulski, 1978, Wolff & Balaban, 1989]. In biological tissues, hydrogen nuclei can be a part of two existing pools, the free water pool, and the bound pool. Free water pool consists of mobile protons in free, abundant water, and it is a primary and dominant source of MRI observed signal in standard MRI. The bound pool consists of immobile and restricted hydrogen nuclei that are bound to macromolecular tissue constituents like lipids, protein, and other large cellular components. These bound pool hydrogen nuclei or protons are not directly MR visible due to their very short  $T_2$  relaxation times ( $< 0.1$  ms) [Boer, 1995a]. In Magnetization Transfer (MT) imaging, the application of off-resonance RF pulse (or MT pulse) saturates the protons in the bound or macromolecular pool. The macromolecular pool has a broad range of resonance frequencies. This property can be exploited to excite the macromolecular pool using a pulse with an offset from the resonance frequency of water or Larmor frequency. The saturation of macromolecular protons influences the spin state of protons in the free water pool through exchange processes, which results in magnetization transfer between the macromolecular and free water pools. This transfer of magnetization is observed as the MT effect in which the MR signal attenuates. This signal attenuation caused by the MT effect can be exploited to assess the macromolecular/myelin content indirectly. MT measured quantitative parameter maps show sensitivity to the white matter tissue structures and macromolecules [Boer, 1995b].

Magnetization transfer ratio (MTR) can be computed voxel-wise by taking the percentage difference between signals acquired with and without off-resonance MT saturation pulse [Dousset et al., 1992]. Measured MTR is sensitive to the density of macromolecules and  $T_1$  relaxation [Henkelman et al., 2001]. To improve MTR by correcting it for  $B_1$  inhomogene-

ity and  $T_1$  relaxation, MT saturation (MTsat) imaging was developed [Helms et al., 2008]. MTsat index has been shown to be more sensitive to white matter tissue and myelin alterations than MTR [Lema et al., 2017].

However, in MT imaging, the amount of observed MT effect depends on the choice of off-resonance RF power and frequency offset to the resonance frequency of water [Henkelman et al., 2001]. This reduces the reproducibility of MT studies across laboratories and introduces bias into meta-analytic studies [Lazari & Lipp, 2021, Mancini et al., 2020].

#### 0.1.6 QUANTITATIVE SUSCEPTIBILITY MAPPING AND EFFECTIVE TRANSVERSE RELAXATION RATE



Magnetic susceptibility is the ability of a material to get magnetized when exposed to an intense uniform magnetic field. The induced magnetization in a substance or biological tissue component alters the magnetic field around it. MRI measured phase and magnitude images are sensitive to this local susceptibility change between tissues and contain a wealth of information. The gradient echo (GRE) sequence is used to acquire magnitude and phase data to generate susceptibility-weighting imaging (SWI) contrast. SWI is beneficial in determining the amount of iron and myelin in the brain and other tissue components that change the local magnetic field [Haacke et al., 2004, Robinson & Bhuta, 2011, Shmueli et al., 2009]. SWI does this by observing changes in susceptibility across various tissue components, such as deoxygenated blood, blood products, ferritin, and calcium. Measuring and monitoring iron and myelin *in vivo* dramatically benefits in several neurologic disorders, including aging, multiple sclerosis, Parkinson’s disease, stroke, traumatic brain injuries, vascular malformations, and brain tumors [Chai et al., 2017, Eskreis-Winkler et al., 2017, Guan et al., 2017, Haacke et al., 2009b, Li et al., 2014, Park et al., 2009, Schweser et al., 2010, Wu et al., 2010].

A three-dimensional GRE sequence allows data acquisition with long echo times by maintaining good image quality. Multi-echo GRE (ME-GRE) data can provide distinct quantitative measures of iron and myelin biomarkers in the form of effective transverse relaxation rate ( $R_2^*$ ) and quantitative susceptibility mapping (QSM) as an extension to SWI. This ME-GRE measured magnitude and phase images are processed to create an  $R_2^*$  and magnetic susceptibility (QSM) map. ME-GRE measured magnitude images can be used to calculate the effective transverse relaxation rate ( $R_2^*$ ) by fitting the magnitude (exponential) signal decay

across all echo times. QSM reconstruction requires phase images and entails three primary steps. (1) Phase unwrapping: MRI measured phase is wrapped in the interval  $[\pi, -\pi]$ . However, the actual phase is uncertain and might be any value. So removal of these phase wraps is needed by the addition or subtraction of integer multiplication of  $2\pi$  [Robinson et al., 2017]. (2) Background field removal: magnetic field perturbations observed in phase contain both local and background fields. Background field variations are induced by main magnetic field inhomogeneity and must be eliminated [Li & Leigh, 2001]. (3) Susceptibility maps can be calculated by solving the ill-conditioned phase to susceptibility inverse problem [Liu et al., 2009]. QSM measured magnetic susceptibility values are linearly proportional to the concentration of the substance that induces a susceptibility effect. The terms paramagnetic and diamagnetic susceptibilities are used relative to the susceptibility of a reference brain tissue. Iron is paramagnetic (positive susceptibility) and myelin and calcium are diamagnetic (negative susceptibility) relative to surrounding tissue. The magnetic susceptibility values are measured in parts per million (ppm) in reference to brain tissue.

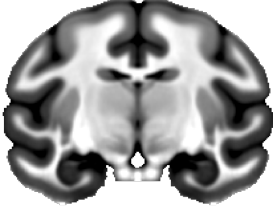
QSM and  $R_2^*$  maps have been used to evaluate iron load and myelin alterations in several neurological diseases, including aging [Betts et al., 2016], multiple sclerosis [Langkammer et al., 2013, Zhang et al., 2016a], Parkinson's disease [Acosta-Cabronero et al., 2017], Huntington's disease [D et al., 2016], cerebral microbleeds [Liu et al., 2012] and hemorrhage [Chen et al., 2013].

## 0.2 COMBINATION OF MRI CONTRASTS

Single MRI contrasts are sensitive to different aspects of the same thing; merging two or more MRI contrast can be helpful to compensate one's limitations with another. In recent years several approaches have been explored by combining multiple MRI contrasts to enhance the sensitivity of MRI markers to the underlying tissue.

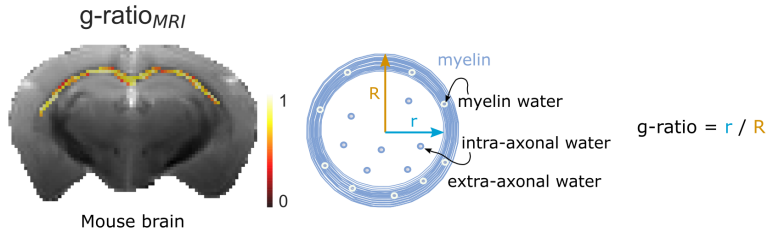
Cortical areas are responsible for higher-order cognitive functions and play a crucial role in human development. However, the dynamics of cortical myelin development and its contribution to the brain's lifelong plasticity remain unclear [Timmmler & Simons, 2019]. The role of cortical myelination in neuronal plasticity, how it's controlled, and why cortical gray matter myelin is necessary are all unanswered questions. MRI can play a significant role in understanding how myelin is regulated in the cortex and how abnormal myelin is linked to several neurological disorders.

### 0.2.1 $T_1w / T_2w$ RATIO



$T_1w$  and  $T_2w$  images are sensitive to myelin. Taking a ratio of raw  $T_1w$  and  $T_2w$  images provides a qualitative parameter called the  $T_1w/T_2w$  ratio, which has been shown to be sensitive to the cortical myelin [Glasser & Essen, 2011]. The  $T_1w/T_2w$  ratio has been used to detect demyelinated cortex in multiple sclerosis and Alzheimer's [Luo et al., 2019b, Nakamura et al., 2017], as well as cortical microstructure maturation [Norbom et al., 2020]. The intensity of  $T_1w$  and  $T_2w$  images varies depending on the magnetic field strength and measurement sequence, making it difficult to compare across studies and a reliable marker for cortical myelin assessment.

### 0.2.2 MYELIN G-RATIO



The myelin g-ratio is a ratio of the inner and outer diameter of the myelin sheath. The g-ratio is used to determine the extent of axonal myelination, which varies from axon to axon and changes in many neurological diseases. Since axons' inner and outer diameters must be estimated to calculate the myelin g-ratio, a single MRI contrast is insufficient to capture both, and more than one MRI contrast is needed. Diffusion MRI is the best technique for assessing the inner diameter of myelin since advanced diffusion MRI biophysical models can estimate the intracellular volume fraction metric. The outer diameter of the myelin sheath can be quantified using myelin water imaging or magnetization transfer saturation imaging, which detects water protons trapped in the myelin sheath (i.e., myelin volume fraction). This estimated myelin volume fraction is further used to scale diffusion MRI measured intracellular volume fraction into the axonal volume fraction. The myelin volume fraction and axonal volume fraction can then be used to calculate the g-ratio [Stikov et al., 2015]. The measured g-ratio in the white matter of human and macaque brains was found to be close to 0.7 [Stikov et al., 2015]. Moreover, the MRI-measured g-ratio in the splenium of the macaque corpus callosum was in accordance with ex-

vivo histological findings [Stikov et al., 2015]. However, it has been shown that estimation of the axonal volume fraction and myelin volume fraction is method-dependent [Ellerbrock & Mohammadi, 2018]. In addition, a calibration procedure is required to achieve high repeatability, comparability, and similar values compared to histological values [Ellerbrock & Mohammadi, 2018]. The g-ratio calculations in MRI are done voxel-by-voxel, which means that a single g-ratio value is calculated from hundreds or thousands of axons with varying degrees of myelination [Campbell et al., 2018].

### 0.3 AIM OF THE THESIS

Imaging myelin and iron is essential for monitoring the pathological evolution of demyelinating and neurodegenerative diseases, as well as to predict and evaluate treatment response. However, there is no gold standard for *in vivo* myelin MR imaging. Despite a large number of studies over the last two decades, no unique myelin-specific MR biomarker has been discovered. There is a lot of discussion in the quantitative MRI field regarding which sequence and contrast to use and how many MRI modalities to include in the data collection in order to get an appropriate level of sensitivity and specificity to myelin. Furthermore, the inconsistencies in the choice of MRI contrast type and data collection make meta-analytic studies more prone to biases. *In vivo* myelin MR imaging lacks a gold standard, necessitating the use of animal models to validate existing methods and the comparison of MRI measurements to histology.

Therefore, the main goal of this work was to evaluate the sensitivity and specificity of several potential MRI measured biomarkers of myelin and iron. In particular, I addressed the following questions:

- How sensitive and specific are available diffusion MRI techniques to myelin and axon-related changes?
- How comparable are human and NHP brains in terms of iron and myelin content?
- How well do NHPs reflect the human aging process?

In order to answer these questions, I also developed a multi-contrast MRI template for the cynomolgus macaque brain and a method to efficiently fuse  $T_1w$  and quantitative susceptibility maps. The fused image enhances the visualization and segmentation of brain tissues in primates by providing a unique brain tissue contrast.

*Sadness is silent, it is yours. It is coming because you are alone. It is giving you a chance to go deeper into your aloneness. Rather than jumping from one shallow happiness to another shallow happiness and wasting your life, it is better to use sadness as a means for meditation. Witness it. It is a friend! It opens the door of your eternal aloneness.*

Osho

# 1

## Comparison of current diffusion MRI methods in myelin mouse mutants

### PEOPLE INVOLVED IN THE STUDY

**Rakshit Dadarwal**<sup>1,2</sup>, Amir Moussavi<sup>1</sup>, Wiebke Möbius<sup>3</sup>, Klaus-Armin Nave<sup>3</sup>, and Susann Boretius<sup>1,2</sup>

1. Functional Imaging Laboratory, German Primate Center – Leibniz Institute for Primate Research, Göttingen, Germany
2. Georg-August University of Göttingen, Göttingen, Germany
3. Department of Neurogenetics, Max Planck Institute for Experimental Medicine, Göttingen

### ABSTRACT

Diffusion MRI (dMRI) plays a significant role in the noninvasive characterization of brain tissue microstructure. dMRI is sensitive to myelin and axon-related alterations because the measured signal is influenced by various tissue constituents, such as axonal density, fiber orientation, and myelination. Several mathematical models have been developed to fit the dMRI



signal. However, the interpretation of model findings has proven to be difficult. In this study, we used four mouse models with altered myelin and axonal damage to assess the sensitivity and specificity of available dMRI models. The dMRI models used in this study ranged from traditional Diffusion Tensor Imaging (DTI) to more advanced models, including Diffusion Kurtosis Imaging (DKI), White Matter Tract Integrity (WMTI), and Neurite Orientation Dispersion and Density imaging (NODDI). Furthermore, MRI results were compared to those of electron microscopy. All of the dMRI models were sensitive to myelin and axon-related alterations to different degrees of specificity. We believe this study could help us better understand the robustness of available dMRI models in determining underlying myelin and axon-related changes.

The following is the outcome of the work outlined in this chapter:

**Rakshit Dadarwal**, Amir Moussavi, and Susann Boretius. *"The effects of b-shell selection on estimation of multi-compartment microscopic diffusion parameters"*, In: Proceedings of the 34th Annual Meeting of the European Society for Magnetic Resonance in Medicine and Biology (ESMRMB), Barcelona, Spain 2017; Abstract 206.

**Rakshit Dadarwal**, Amir Moussavi, Wiebke Möbius and Susann Boretius. *"How do current diffusion-based MR methods reflect hypomyelination – comparison of diffusion tensor, neurite orientation dispersion and density, and diffusion kurtosis imaging"*, In Proceedings of the Joint Annual Meeting of the International Society for Magnetic Resonance in Medicine (ISMRM) – European Society for Magnetic Resonance in Medicine and Biology (ESMRMB), Paris, France 2018; Abstract 3219.

**Rakshit Dadarwal**, Amir Moussavi, Wiebke Möbius, and Susann Boretius. *"Quantification of white matter tract integrity in hypomyelination"*, In Proceedings of the 11th Federation of European Neuroscience Societies (FENS), Berlin, Germany 2018.

## 1.1 INTRODUCTION

dMRI plays a significant role in the noninvasive characterization of brain tissue microstructure by measuring signal attenuation produced by diffusing water molecules [Le Bihan et al., 2001]. The MRI measured diffusion signal is influenced by various tissue constituents, such as axonal density, fiber orientation, and myelination. A variety of diffusion signal representations and microstructure models have been proposed to decipher the underlying tissue mechanisms [Alexander et al., 2019]. The sensitivity and specificity of available dMRI models to measured tissue microstructure vary. Some methods, such as DTI, are currently the gold

standard for *in vivo* disease diagnosis in day-to-day clinical routines [Le Bihan et al., 2001]. However, the interpretation of dMRI findings has proven to be difficult, particularly under pathological conditions, where demyelination, axonal injury, and cellular infiltration can all influence the diffusion-weighted signal in distinct and even opposing ways [Jelescu et al., 2020]. A histological validation is required before considering quantitative values measured by dMRI as a useful diagnostic for underlying microstructural alterations. Clinical translation of advanced biophysical models demands an understanding of the associated challenges and a clear interpretation of the results.

In this study, we aimed to figure out how variations in myelin composition and axonal density modify the dMRI signal and how well currently available mathematical models reflect these changes. We evaluated DTI, DKI, WMTI, and NODDI on postmortem mouse brains.

DTI estimates the fractional anisotropy (FA), in addition to the mean (MD), axial (AD), and radial (RD) diffusivities [Basser et al., 1994]. It has been shown that FA and MD show signs of disturbed tissue microstructure differentiated and specified by the AD and RD. An increase in RD specifically reflects myelin loss and demyelination, while a decrease in AD indicates axonal injury or damage [Aung et al., 2013]. MD or the apparent diffusion coefficient (ADC) is sensitive to the total amount of water in the tissue (e.g., inflammation, edema, gliomas). DKI provides parameters such as the mean (MK), axial (AK), and radial (RK) kurtosis [Jensen et al., 2005, Fieremans et al., 2011]. Hypomyelination has been associated with decreased MK and RK, with very little change in AK [Kelm et al., 2016]. WMTI results in axonal water fraction (AWF), representing the fraction of water in the intra-axonal space. In addition to AWF, WMTI provides diffusivities for the intra-axonal and extra-axonal compartments, called intra-axonal diffusivity ( $D_{axon}$ ), and extra-axonal axial ( $D_{e,\parallel}$ ) and radial ( $D_{e,\perp}$ ) diffusivities. The AWF is sensitive to axonal loss or demyelination, and  $D_{e,\perp}$  is sensitive to demyelination, whereas  $D_{axon}$  and  $D_{e,\parallel}$  are unaffected by myelin alterations [Falangola et al., 2014, Jelescu et al., 2016, Kelm et al., 2016]. The  $D_{axon}$  and  $D_{e,\parallel}$  are sensitive to structural changes in the intra-axonal space (e.g., due to axonal bending) and in the extra-axonal space (e.g., due to gliosis, loss of oligodendrocytes, extracellular inflammation), respectively [Benitez et al., 2014]. NODDI provided intra-cellular volume fraction (ICVF) is sensitive to myelinated neurite density [Jespersen et al., 2010] and axonal loss [Gong et al., 2020, Wang et al., 2019].

The use of both *in vivo* and *ex vivo* animal models is required for the validation of MRI methods. On the one hand, *in vivo* MRI allows for imaging of an animal while it is still alive, without any tissue dehydration and fixation produced tissue integrity upset, but it has scan time limitations. Postmortem MRI, on the other hand, can examine brain microstructure with high resolution, less motion, and a higher signal-to-noise ratio (SNR). To obtain a resolu-

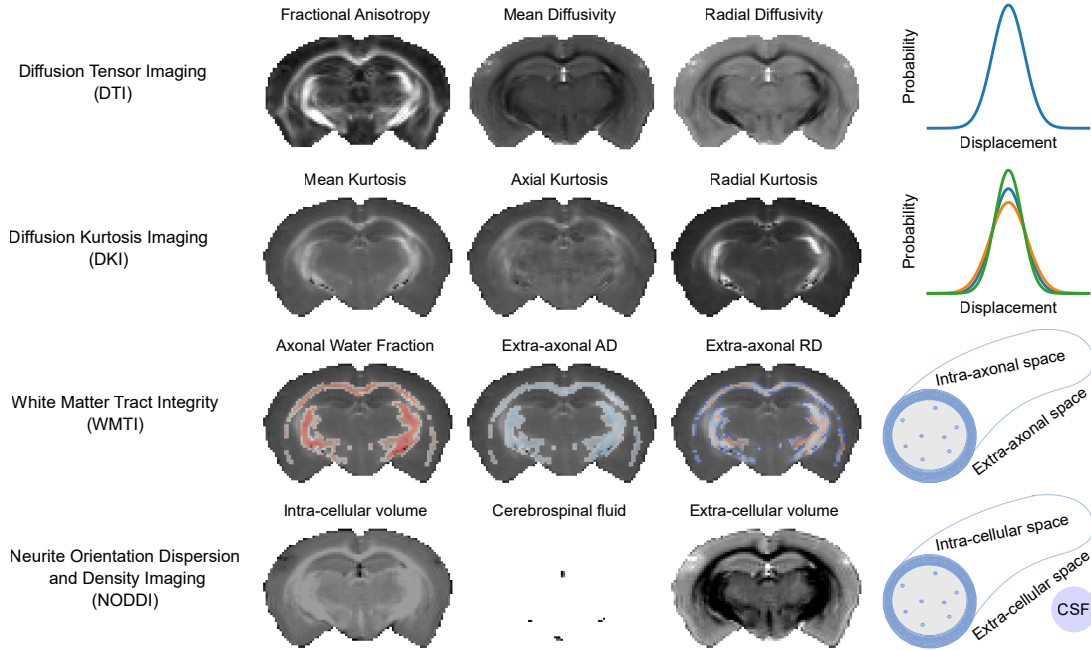


**Figure 1.1:** dMRI models of white matter. The fitting of DTI models is based on the assumption that water molecule diffusion in the brain follows a Gaussian distribution. The DKI model addresses non-Gaussian (deviation from Gaussian) diffusion effects, which are a drawback of the DTI model. The WMTI model extends the DKI model into a biophysical model for white matter regions by dividing white matter tissue water into two non-exchanging compartments, an intra-axonal space, and an extra-axonal space. The NODDI model fits a three compartmental model to the whole brain to predict the fractions of intra-cellular, extra-cellular, and isotropic (cerebrospinal fluid) compartments.

tion many times lower than histological imaging, postmortem imaging often requires MRI scanners equipped with strong magnetic field and gradient strengths. The majority of high-resolution imaging is carried out at the expense of longer data acquisition times. However, postmortem brain samples can be used for sectioning, histological staining, and proteomic analysis, all of which investigate and evaluate the underlying tissue microstructure and provide ground truth for MRI validation.

In this study, we tested current state-of-the-art dMRI methods on mouse models with various myelin and axon-related pathologies. The MRI results are compared to those from high-pressure freezing electron microscopy. Three of the four knockouts had alterations in the myelin basic protein (MBP), resulting in partial or complete myelin loss. MBP is a protein found in myelin-forming glia and a structural component of compressed myelin. MBP is essential for the development of myelin's major dense line [Raasakka et al., 2017]. When the MBP gene is knocked out, the myelin becomes less compacted and lacks the primary dense

lines, as seen in shiverer knockouts [Martin et al., 2006, Readhead & Hood, 1990]. In the fourth knockout model, a 2', 3' -cyclic nucleotide 3'-phosphodiesterase (CNP) deficit was induced. CNP is a protein that support and maintains axons and is produced by myelin-forming glia. Although there is no or very little evidence of altered myelin in CNP knockout mice, there is a significant axonal loss and swelling throughout the white matter, resulting in severe neurodegenerative diseases and premature mortality [Lappe-Siefke et al., 2003].

The following are the four adult wild-type and knockout mouse strains studied:

Genetic name	Abbreviation	Knockout type	Age (weeks)	Number of animals	Sex
$Mbp^{sh/sh}$ ( <i>shiverer</i> )	SHIV	Dysmyelination	-	12 (6 WT, 6 MT)	-
$Mbp^{neo/neo}$	MBP-LacZ	Hypomyelination	15	10 (5 WT, 5 MT)	6 M and 4 F
$Mbp^{fl/fl*Emx1^{cre}}$	MBPFLX-EXEC	Regional specific knockout targeting	26	9 (4 WT, 5 MT)	9 M
$Cnp^{null/null}$	CNCE	CNP deficiency	16	8 (4 WT, 4 MT)	6 M and 2 F

**Table 1.1:** The four adult wild-type (WT) and knockout (MT) mouse strains.

## 1.2 MATERIALS AND METHODS

Adult wild-type (WT) and knockout (Shiverer, *Mbp*-neo, *Mbp*-iKO, and *Cnp1*-null) mice were sacrificed and transcardially perfused with phosphate-buffered saline and paraformaldehyde (PFA). Subsequently, the brain was prepared and stored in 4% PFA.

MR measurements of the isolated brains were performed at a 9.4 T Bruker BioSpec MR system using a four-channel surface coil for signal detection. Diffusion-weighted images were acquired using a diffusion-weighted spin-echo sequence (b-values = 3000 and 6000 s/mm<sup>2</sup>, diffusion gradient directions = 30 each b-value, gradient duration and separation = 4 ms and 15 ms, Echo time/ repetition time = 23/2000 ms, spatial resolution = 125 × 125 × 500 μm<sup>3</sup>, field-of-view = 16 × 16 mm<sup>2</sup>, number of averages = 6, and total scan time = 27 hours).

Diffusion-weighted images were denoised and corrected for eddy current and motion distortions [Andersson et al., 2003, Garyfallidis et al., 2014, Veraart et al., 2016]. All diffusion-weighted images were registered to mean b0 images using ANTs affine registration [Avants

et al., 2008]. These preprocessed DWI images were used to fit the DTI, DKI, WMTI, and NODDI models [Basser et al., 1994, Fieremans et al., 2011, Zhang et al., 2012, Daducci et al., 2015, Garyfallidis et al., 2014]. Only DWI images with b-values of 3000 s/mm<sup>2</sup> were used to fit the DTI model.

Regions-of-interest: The corpus callosum, cortex, and fimbria were manually segmented using the ITK-SNAP segmentation tool [Yushkevich et al., 2006] on the FA map of each mouse brain.

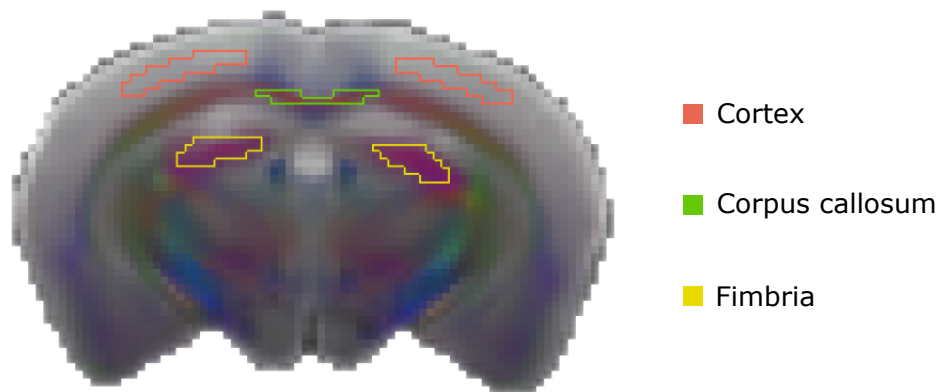


**Figure 1.2:** Segmented regions-of-interest (ROIs) in the mouse brain. Gray and white matter ROIs were segmented manually using the ITK-SNAP tool. The cortex, corpus callosum, and fimbria ROIs are depicted in coronal view of an average color-coded FA map. The color coding of the white matter fiber tract bundles indicates their orientation. Red: Left-Right; Green: Anterior-Posterior; and Blue: Superior-Inferior.

The diffusion metrics in the wild-type and knockout groups were compared using the student's t-test.

### 1.3 RESULTS

The DTI, NODDI, DKI, and WMTI parameter maps from wild-type (WT) and MBPFLX-EXEC (MT) group are shown in Figure 1.3. In compared to the WT group, the MT group showed lower contrast in FA, ICVF, MK, AK, RK, and AWF maps and increased contrast in MD and RD maps, particularly in the white matter. The MD contrast in the white matter of the MT group was essentially identical to the gray matter contrast.

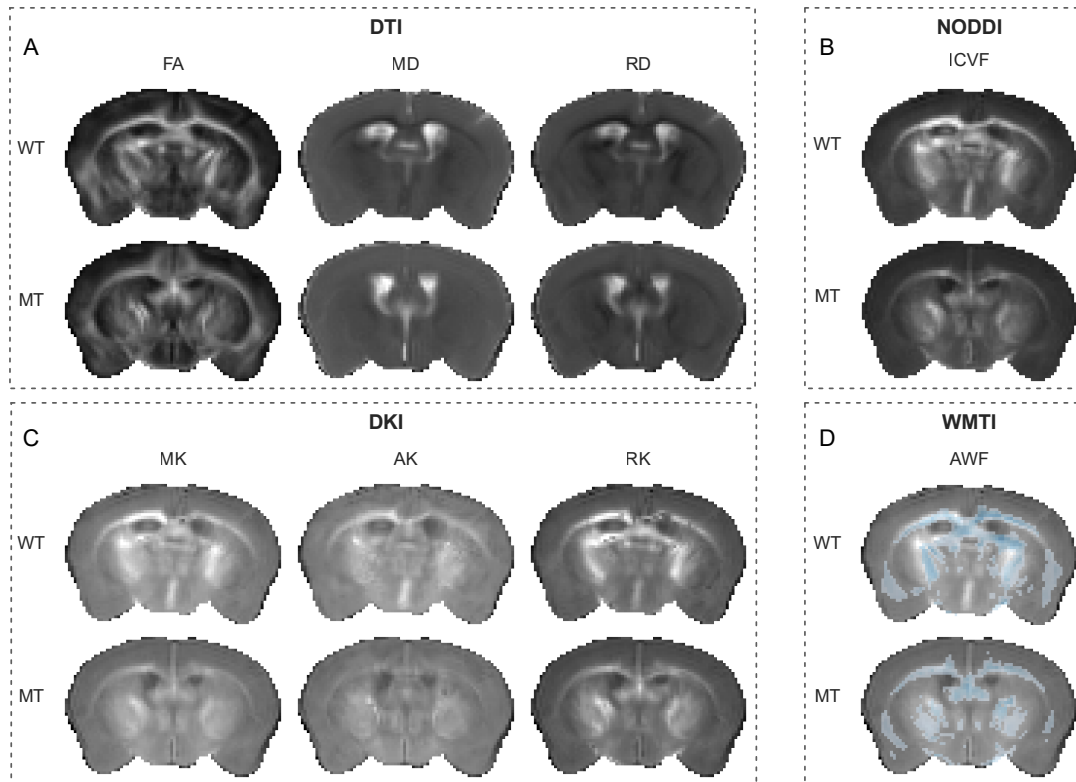


**Figure 1.3:** Representative coronal DTI, NODDI, DKI, and WMTI computed parameter maps of wild-type (WT) and mutant mice with an expression of the MBPFLX-EXEC (MT). In the white matter areas, there was a decrease in DTI estimated FA and an increase in MD and RD. In addition, the MBPFLX-EXEC mice demonstrated a reduction in the NODDI calculated ICVF, DKI calculated MK, AK, and RK, and WMTI calculated AWF, in the white matter areas. The AWF maps are overlaid on the DKI MK maps (D).

### 1.3.1 DTI

The DTI ROI analysis results for the cortex, corpus callosum, and fimbria are shown in Figure 1.4. The quantitative values obtained from MBPFLX-EXEC, CNCE, MBP-LacZ, and SHIV knockouts were normalized to their respective wild-type group values. The cortex remained unchanged between the wild-type and knockouts. However, the MBPFLX-EXEC, MBP-LacZ, and SHIV knockouts showed obvious signs of hypomyelination and dysmyelination in the corpus callosum, with reduced FA and increased MD and RD. The hypomyelination and dysmyelination effects were more pronounced in the white matter corpus callosum than in the fimbria. In the fimbria, only the MBPFLX-EXEC knockout showed reduced FA

and increased MD and RD. The CNCE knockout revealed no changes in any of the DTI metrics, except for an increase in AD in the fimbria.

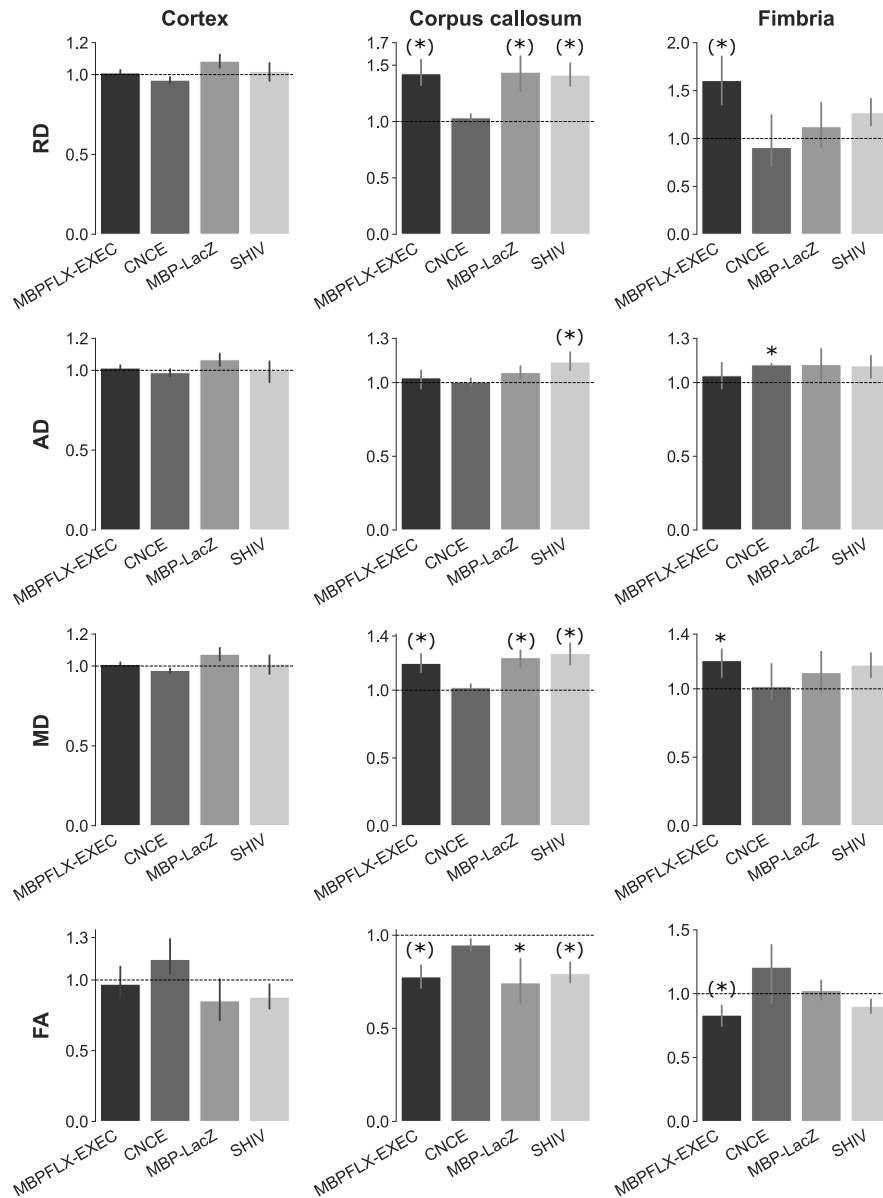


**Figure 1.4:** Bar plots showing DTI ROI analysis results for all knockouts. Bar height represents the WT normalized ROI means for each knockout group. The error bars show a 95% of a confidence interval. (\*)  $P < 0.01$  and \*  $P < 0.05$ .

### 1.3.2 DKI

The DKI ROI analysis results for the cortex, corpus callosum, and fimbria are shown in Figure 1.5. The cortex remained unchanged between the wild-type and knockouts, except for the reduced AK in the SHIV knockout. However, the MBPFLX-EXEC, MBP-LacZ, and SHIV knockouts showed obvious signs of hypomyelination and dysmyelination in the corpus callosum, with reduced RK, AK, and MK in the corpus callosum. The hypomyelination and dysmyelination effects were more pronounced in the white matter corpus callosum than in the fimbria. In the fimbria, only MBPFLX-EXEC and SHIV knockouts showed reduced RK, AK, and MK. The CNCE knockout revealed a reduced RK in the corpus callosum, while AK and MK were unaffected.

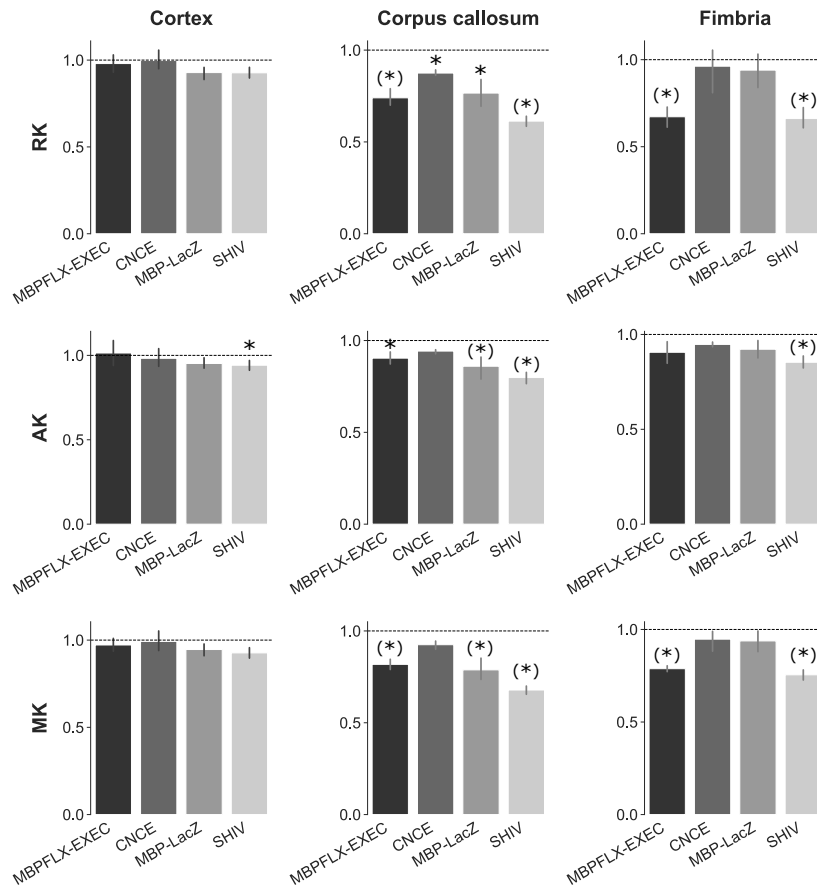


**Figure 1.5:** Bar plots showing DKI ROI analysis results for all four knockouts. For each knockout, the height of the bars denotes the WT normalized ROI mean. The error bars show a 95% of a confidence interval. (\*)  $P < 0.01$  and \*  $P < 0.05$ .



### 1.3.3 WMTI

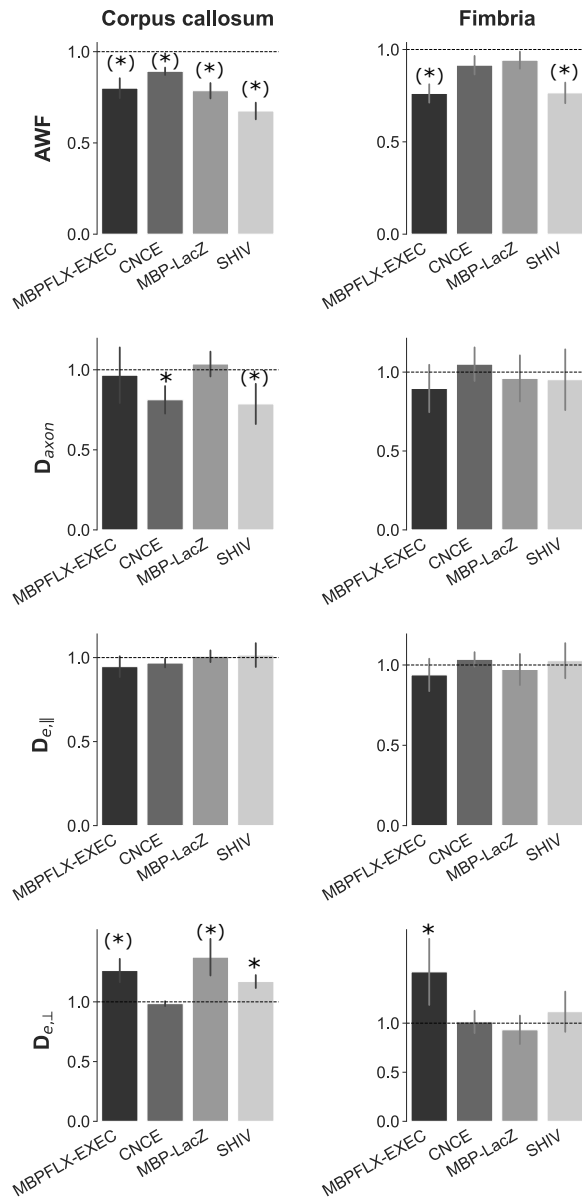


**Figure 1.6:** The findings of the WMTI ROI analysis for each of the four knockout groups are represented as bar graphs. The error bars show a 95% of a confidence interval. (\*) P < 0.01 and \* P < 0.05.

The WMTI analysis results for the corpus callosum, and fimbria are shown in Figure 1.6. The

MBPFLX-EXEC, MBP-LacZ, and SHIV knockouts showed obvious signs of hypomyelination and dysmyelination in the corpus callosum, with reduced AWF, and increased  $D_{e,\perp}$ . The hypomyelination and dysmyelination effects were more pronounced in the white matter corpus callosum than in the fimbria. In the fimbria, only MBPFLX-EXEC knockout showed reduced AWF, and increased  $D_{e,\perp}$ . The CNCE knockout also revealed obvious signs of axonal loss in the corpus callosum, with reduced AWF and  $D_{axon}$ , while  $D_{e,\perp}$  was unaffected.

### 1.3.4 NODDI

The NODDI analysis results for the cortex, corpus callosum, and fimbria are shown in Figure 1.6. The cortex remained unchanged between the wild-type and knockouts. However, the MBPFLX-EXEC, MBP-LacZ, and SHIV knockouts showed significantly reduced ICVF in the corpus callosum and fimbria. We found a decrease in ICVF in hypomyelination and dysmyelination, which is surprising given that ICVF is a measure of axonal or neurite density. The CNCE knockout had no effect on ICVF in the corpus callosum and fimbria.

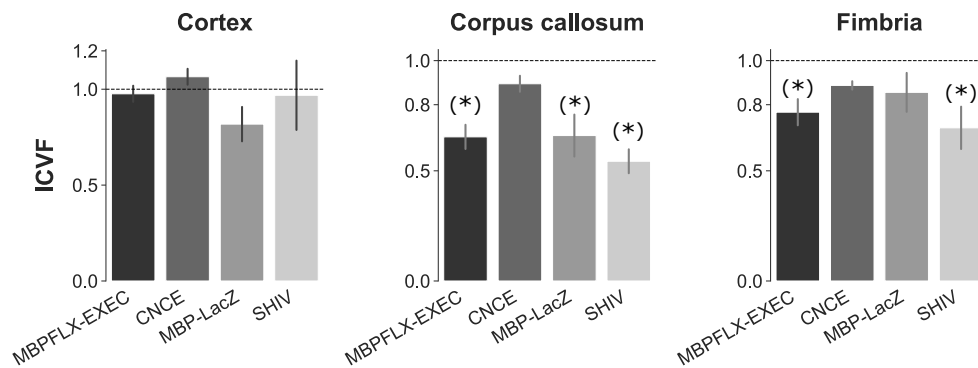


**Figure 1.7:** Bar plots showing NODDI ROI analysis results for all four knockouts. The error bars show a 95 % of a confidence interval. (\*)  $P < 0.01$  and \*  $P < 0.05$ .

### 1.3.5 ELECTRON MICROSCOPY

The optic tract of CNCE and SHIV knockouts, and the corpus callosum of MBP-LacZ knockouts, were studied using electron microscopy (Figure 1.8). In compared to WT, myelin in the CNCE knockout optic tract is nearly intact, albeit there were evidence of axonal injury and inflammation, including enlarged inner tongues (arrows) and axonal swelling (Figure 1.8A). In the MBP-LacZ knockout corpus callosum, MBP deficiency and significantly thinner myelin were found (Figure 1.8B). The SHIV knockout optic tract showed a lack of MBP, myelin deficiency, and naked axons (arrows) throughout the brain (Figure 1.8C).

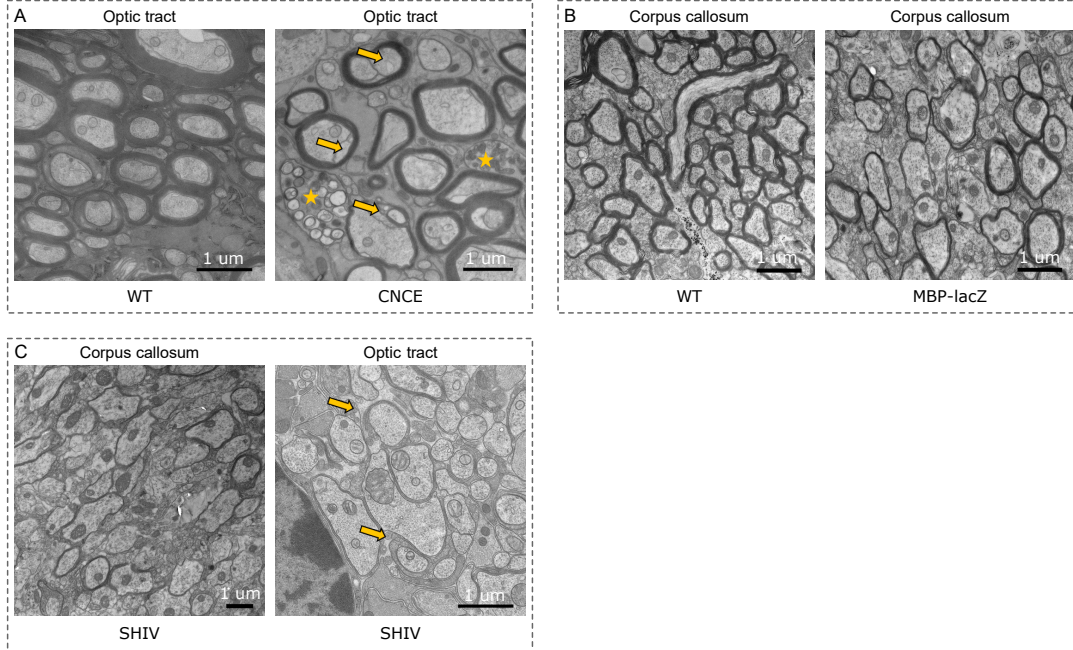


**Figure 1.8:** **A.** Images of the optic tract electron microscopy in WT and CNCE mice. Myelin is almost intact in CNCE knockout, but there is evidence of axonal injury and inflammation, such as larger inner tongues (arrows) and axonal edema. **B.** When compared to WT, the MBP-LacZ group has an MBP deficiency and much thinner myelin. **C** The SHIV knockout showed a lack of MBP, lack of myelin and naked axons throughout the brain.

#### 1.4 DISCUSSION

In this study, we utilized conventional and advanced diffusion methods (DTI, DKI, WMTI, and NODDI) to probe myelin and axonal abnormalities in the four different mouse lines. Three of the four mouse lines had MBP-related changes, while the fourth exhibited deficit in the CNP. The MBP altered lines MBPFLX-EXEC and MBP-LacZ exhibited hypomyelination, whereas SHIV showed dysmyelination.

DTI showed sensitivity to hypomyelination and dysmyelination in the MBPFLX-EXEC, MBP-LacZ, and SHIV knockouts. However, DTI metrics failed to detect any changes in the CNCE knockout, implying that DTI is unable to differentiate minor axonal density changes. DTI results are in line with the previous research stating that DTI is sensitive to detect a decrease in myelination but insensitive to differentiate minor changes in axonal density [Kelm et al., 2016]. However, several studies have also reported the sensitivity of DTI to axonal injury and axonal loss [Fox et al., 2011, Song et al., 2003]. As per the DKI findings, hypomyelination and dysmyelination in the corpus callosum caused reductions in MK, AK, and RK.

Earlier studies using DKI's sensitivity to identify myelin and axonal alterations had similar outcomes [Kelm et al., 2016, Guglielmetti et al., 2016].

The WMTI results demonstrate that AWF is influenced by both myelin and axonal loss. The reduced AWF in hypomyelination, dysmyelination, and axonal loss reflected its sensitivity to changes in both axons and myelin. However,  $D_{e,\perp}$  is only sensitive to hypomyelination and dysmyelination, but not to the axonal loss. These results agree with previous research showing that AWF decreases and  $D_{e,\perp}$  increases with myelin loss, and  $D_{axon}$  and  $D_{e,\parallel}$  are primarily unaffected by subtle changes in myelination [Guglielmetti et al., 2016, Jelescu et al., 2016, Zhou et al., 2020]. Interestingly, the decrease in  $D_{axon}$  was only observed in the CNCE and SHIV knockouts, indicating its sensitivity to changes in axonal density. In the CNCE knockout, the significantly reduced AWF and  $D_{axon}$  in the corpus callosum accurately represent the underlying tissue alterations only specific to axons. Considering that AWF is a measure of axonal integrity, it is worth noting that in the MBPFLX-EXEC, MBP-LacZ and SHIV knockouts, the AWF was likewise sensitive to hypomyelination and dysmyelination, though axons were unaffected.

The NODDI results showed that hypomyelination and dysmyelination caused a decrease in ICVF in the corpus callosum. These findings corroborate prior studies that showed ICVF is sensitive to changes in myelination and axonal density [Wang et al., 2019].

In conclusion, all dMRI models were sensitive to hypomyelination, dysmyelination, and axonal loss to varying degrees.

There were four main limitations in this study. The first was that each group had a smaller number of animals to study. The second issue is that long dMRI data acquisition increases the temperature of the scanned brain, which might cause changes in measured and intrinsic tissue diffusivities. Third, the influence of the fixation method and MR-sensitive PFA solution can be detrimental for some tissue microstructures and the native water diffusion within the brain. Fourth, just a few selected brain structures were used as regions-of-interest for quantitative analysis. It has been demonstrated in earlier studies that fixation decreases diffusivity [Schmierer et al., 2008]. It is also worth noting that the electron microscopy images for the CNCE group come from the optic tract, which was not used as a region-of-interest.

In future studies stabilizing the temperature of the scanned brains might lead to more consistent results. In addition, by optimizing available acquisition sequences or employing improved sequences like 3D diffusion-weighted Fast Spin-echo, the overall scan time can be reduced while keeping high signal-to-noise ratio. The source of artifacts can be reduced by keeping the brain stable inside the PFA-filled vessel. Including more white and gray matter regions in the ROI analysis would provide a more comprehensive view of the underlying pathology. The inclusion of multiple MRI contrasts, such as MWI and MT, will strengthen the findings.

*Look at the trees, look at the birds, look at the clouds, look at the stars... and if you have eyes you will be able to see that the whole existence is joyful. Everything is simply happy. Trees are happy for no reason; they are not going to become prime ministers or presidents and they are not going to become rich and they will never have any bank balance. Look at the flowers - for no reason. It is simply unbelievable how happy flowers are.*

Osho

2

## QSM and $R_2^*$ mapping in human and non-human primate brains

### AUTHORS

**Rakshit Dadarwal**<sup>1,2</sup>, Amir Moussavi<sup>1</sup> and Susann Boretius<sup>1,2</sup>

1. Functional Imaging Laboratory, German Primate Center – Leibniz Institute for Primate Research, Göttingen, Germany
2. Georg-August University of Göttingen, Göttingen, Germany

### ABSTRACT

Quantitative Susceptibility Mapping (QSM) and effective transverse relaxation rate ( $R_2^*$ ) are sensitive to tissue iron and myelin content in neural tissue. The iron-rich subcortical nuclei produce excellent contrast in QSM and  $R_2^*$  maps, which is not available with conventional  $T_1$ - and  $T_2$ -weighted structural MRI sequences. Even though QSM and  $R_2^*$  are widely utilized to examine human brain tissue alteration in both healthy and diseased conditions, they are not often used in non-human primates (NHPs). NHPs are an essential model organism to improve our understanding of human neuroanatomy, brain circuitry, and functions in both healthy and pathological states. Several attempts have been made in the past to comprehend

and compare the physiology and neuroanatomy of NHPs to that of humans using a number of available MRI contrasts. However, little is known about *in vivo* similarities and differences in iron and myelin content in the human and monkey brain subcortical and white matter regions.

In this study, we evaluated and compared the QSM and  $R_2^*$  maps for the human and monkey brain. We imaged human and monkey brains with the same magnetic field strength (3 Tesla) and similar MRI data acquisition parameters, which allowed us to achieve an outstanding human-monkey brain comparison. Moreover, we quantified QSM and  $R_2^*$  values in gray and white matter tissue and show that QSM and  $R_2^*$  values in the human and monkey brains are almost identical, with the exception of a few areas such as the red nucleus. Furthermore, we also investigated the sensitivity of QSM to echo times. Finally, we used diffusion MRI (dMRI) data to compare structural features of the underlying tissue microstructure to explore the relationship between white matter QSM and  $R_2^*$  values to myelin and axonal content.

The work described in this chapter resulted in the following output:

**Rakshit Dadarwal**, Luzia Hintz, Amir Moussavi, and Susann Boretius. "*Quantitative Susceptibility Mapping of the Brain – A Comparative in vivo Study of Humans and Nonhuman Primates*", In Proceedings of the 27th Annual Meeting of the International Society for Magnetic Resonance in Medicine (ISMRM), Montreal, QC, Canada 2019; Abstract 4921.

**Rakshit Dadarwal**, Amir Moussavi, and Susann Boretius. "*Quantitative Susceptibility Mapping (QSM): Echo time dependence in the human and non-human primate brain*", In Proceedings of the 36th Annual Scientific Meeting of the European Society for Magnetic Resonance in Medicine and Biology (ESMRMB), Rotterdam, Netherlands 2019; Abstract S20.05.

**Rakshit Dadarwal**, Amir Moussavi, and Susann Boretius. "*QSM and  $R_2^*$  mapping in human and non-human primate brains*" (manuscript in preparation).

## 2.1 INTRODUCTION

Non-human primates (NHPs) are phylogenetically closely related to humans and have similar physiology and neuroanatomy. The understanding of the human brain neuroanatomy, circuitry, and functions have relied heavily on NHP models. NHP models have also aided

in developing treatments for human diseases, such as the development of deep brain stimulation for Parkinson’s disease treatment [Vitek & Johnson, 2019, Utter & Basso, 2008]. Although, it is not always clear how well monkeys could reflect the human brain organization in health and disease. The comparison of human and monkey brains *in vivo* benefits from non-invasive imaging techniques such as MRI, which can be applied similarly to image the human and monkey brain.

A variety of MRI imaging techniques, including structural MRI (e.g.,  $T_1$ -weighted and  $T_2$ -weighted) [Rilling, 2006], dMRI [Caspers et al., 2011, Hofer et al., 2008, Li et al., 2013], and functional MRI [Logothetis et al., 1999, Logothetis, 2003, Wey et al., 2014], have been used to compare human and monkey brain physiology and neuroanatomy. However, the *in vivo* evaluation of brain iron has not yet caught the focus of many comparative primate neuroimaging studies. Therefore, determining the amount of iron in the human and monkey brain subcortical nuclei is crucial for understanding neural substrates and molecular physiological mechanisms in the NHP brain.

The most appropriate methods for detecting iron concentration in the brain are QSM and  $R_2^*$ . QSM and  $R_2^*$  are sensitive to changes in brain tissue chemical composition and tissue microstructure [Acosta-Cabronero et al., 2013, Haacke et al., 2004, Shmueli et al., 2009, Wang & Liu, 2015]. Iron and myelin are the predominant sources of QSM contrast [Duyn & Schenck, 2017, Hametner et al., 2018, Langkammer et al., 2012]. Moreover, iron and myelin are required for vital cerebral functions, and non-invasive characterization of both has a wide range of applications, ranging from improving clinical investigations to gaining a better understanding of healthy aging and neurological diseases such as Multiple Sclerosis [Bian et al., 2016, Chawla et al., 2018], demyelinating diseases [Zhang et al., 2016b], Huntington’s disease [Bergen et al., 2016], Parkinson’s disease [Langkammer et al., 2016], traumatic brain disease [Chai et al., 2017], and Alzheimer’s disease [Acosta-Cabronero et al., 2013, Moon et al., 2016].

Importantly, several studies have shown that QSM is highly sensitive to MRI acquisition parameters such as magnetic field strength, echo time (TE), and brain orientation relative to the static magnetic field [Deistung et al., 2013, Wharton & Bowtell, 2012, Sood et al., 2017]. Recent studies have shown the sensitivity of QSM to the TE, which suggests that a slight change in TE can lead to a dramatic change in the reconstructed magnetic susceptibility values [Cronin et al., 2017, Sood et al., 2017, Biondetti et al., 2020]. However, the intrinsic nature of susceptibility TE dependence is not very clear and requires further investigations. Multi-contrast MRI techniques may aid in demonstrating and interpreting the relationship between susceptibility TE dependency and underlying tissue microstructure. Our study included dMRI as a measure of tissue microstructure for better interpretation of QSM and its TE dependence in human and monkey brains.

In this work, we compared QSM and  $R_2^*$  in human and monkey brains using data ac-

quired with nearly identical MRI parameters. We combined QSM and  $R_2^*$  provided information with dMRI measured tissue microstructure information to comprehend better the subtle anatomical and physiological similarities and differences between human and monkey brains. Furthermore, comparing magnetic susceptibility and  $R_2^*$  in human and monkey brains is essential for improving the clinical translation of NHP models of neurological and psychiatric diseases.

## 2.2 MATERIALS AND METHODS

### 2.2.1 ANIMALS AND HUMAN VOLUNTEERS

The MRI data were obtained from five healthy adult female cynomolgus macaque monkeys (*Macaca fascicularis*) and six healthy female human volunteers. Five adult macaques were between the ages of 7 - 9 years old (weighing between 3.9 and 6 kg), and six human adults were between 23 and 29 years old. Measurements on human volunteers were performed after written informed consent. The protocol was reviewed by the ethics committee of the Georg-August-University of Göttingen.

### 2.2.2 ANIMAL EXPERIMENTS

All monkeys were purpose-bred, raised, and housed according to the standards for macaques of the German Primate Center (Göttingen, Germany). All aspects of the study were conducted in accordance with national and international guidelines of the German Animal Protection Law and the European Union Directive 2010/63/EU for the Protection of Animals used for Scientific Purposes. The study was approved by the local authorities, the Animal Welfare Service, Lower Saxony State Office for Consumer Protection and Food Safety (license number 33.19-42502-04-16/2278).

In preparation for anesthesia, the macaques were deprived of food overnight. Anesthesia was induced by a mixture of ketamine ( $8.05 \pm 2.65$  mg per kg body weight) and medetomidine ( $0.02 \pm 0.01$  mg per kg) and maintained by isoflurane (0.8 - 1.7 % in oxygen and ambient air) via endotracheal tube and pressure-controlled active ventilation. The monkeys were placed in a prone position, and their heads were fixed in an MR-compatible stereotactic apparatus (Kopf 1430 M, [kopfinstruments.com](http://kopfinstruments.com)).

### 2.2.3 MRI DATA ACQUISITION

We acquired all brain images with a 3 T MR system (MAGNETOM Prisma, Siemens Healthineers, Erlangen) equipped with a 7 cm single loop coil for macaque monkeys and a 20-channel head coil for human brain imaging. The imaging protocol included multi-echo



gradient-recalled echo (ME-GRE) and diffusion-weighted acquisitions. MRI scans from human volunteers were performed supine, while monkey scans were performed in prone positions. MR parameters for both humans and monkeys are listed in Table 2.1.

Parameters	Monkey		Human	
	QSM	dMRI	QSM	dMRI
Pulse sequence	3D ME-GRE	2D PGSE	3D ME-GRE	2D PGSE
Native resolution (mm <sup>3</sup> )	0.31 × 0.31 × 0.31	0.9 × 0.9 × 0.9	0.75 × 0.75 × 0.75	1.5 × 1.5 × 1.5
Field of view (mm <sup>2</sup> )	97 × 120	396 × 639	195 × 240	210 × 207
Acquisition matrix	312 × 384	88 × 142	260 × 320	140 × 138
b-value (s/mm <sup>2</sup> )	–	0, 1000, 2000	–	0, 1000, 2000
Diffusion gradient directions	–	30	–	64
Total acquisition time (min)	24	27	17.5	19
TR/TE (ms)	57/[3.7/50.4]	6500/54.4	57/[3.7/50.4]	8800/54.4
Number of echo times	10	–	10	–
Pixel bandwidth (Hz/Px)	250	1174	250	1116

**Table 2.1:** Monkey and human QSM and dMRI data acquisition parameters. Abbreviations: ME-GRE - Multi-echo gradient-recalled echo; PGSE - Pulsed gradient spin-echo, TR - repetition time; TE - echo time.

We also obtained non-diffusion-weighted images of the human and monkey brains in the opposite phase-encode direction (anterior-to-posterior and posterior-to-anterior) to correct dMRI data for susceptibility-induced distortions.

#### 2.2.4 DATA ANALYSES

##### QSM AND $R_2^*$

QSM and  $R_2^*$  data analyses pipelines likewise for humans and monkeys are schematically illustrated in Figure 2.1. We corrected the measured multi-echo gradient-recalled echo (ME-GRE) magnitude images for bias fields using *N4BiasFieldCorrection* [Tustison et al., 2010]. We pixel-wise averaged the sum of squared ME-GRE magnitude images across echo times. We used the magnitude sum images to create brain masks using ITK-SNAP [Yushkevich

et al., 2006]. Moreover, we created average human and monkey brain templates by aligning all subjects' brain images into a common space utilizing ANTs template creation pipeline [Avants et al., 2011].

Human and monkey  $R_2^*$  maps were calculated by fitting the ME-GRE magnitude signal decay across all echo times with a mono-exponential model [Pei et al., 2015]. The ventricular cerebrospinal fluid (CSF) segmentation (Figure 2.2B) was carried out on each subject's  $R_2^*$  map using ITK-SNAP [Yushkevich et al., 2006].

QSM maps of humans and monkeys were reconstructed using coil combined ME-GRE phase data. This QSM reconstruction included phase unwrapping using the best-path algorithm, background field removal using Laplacian boundary value and variable spherical mean value filtering algorithms, and solving the inversion problem using the multiscale dipole inversion approach [Abdul-Rahman et al., 2007, Acosta-Cabronero et al., 2018, Zhou et al., 2014]. Finally, a QSM and  $R_2^*$  atlases were created using the previously calculated warps from subject GRE magnitude image to common template space (Figure 2.3).

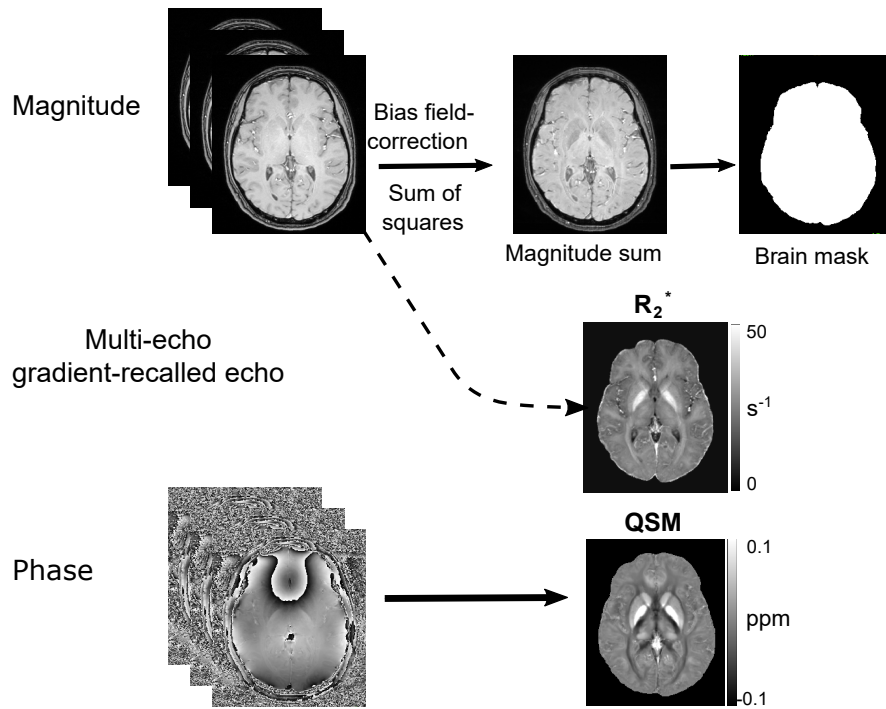


**Figure 2.1:** Schematic illustration of the QSM and  $R_2^*$  data analysis pipelines for human and monkey brains multi-echo gradient-recalled echo data.

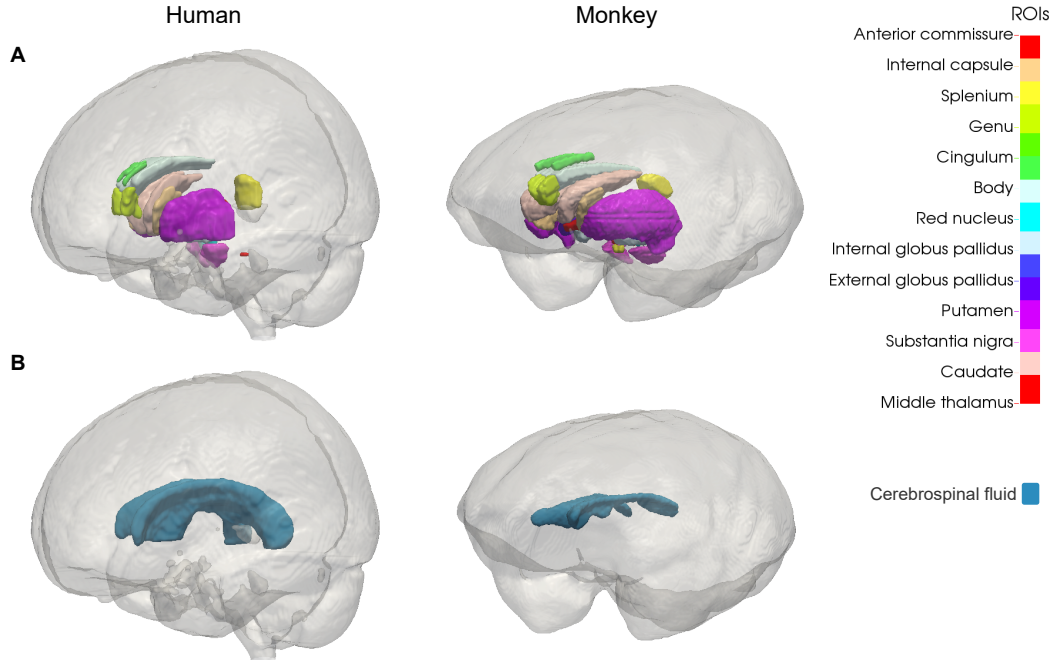


**Figure 2.2:** **A.** Summary of the location and volume of thirteen different bilaterally segmented brain regions: the middle thalamus, caudate, substantia nigra, putamen, external and internal globus pallidus, red nucleus, corpus callosum genu, body, and splenium, cingulum, internal capsule, and anterior commissure. **B.** The ventricular cerebrospinal fluid region's segmented volume in human and monkey brains.

The analyzed regions-of-interest (ROIs) were segmented manually on human and monkey brain QSM atlases using ITK-SNAP [Yushkevich et al., 2006]. All the ROIs were defined in both hemispheres, as shown in Figure 2.2A. The segmented brain regions included structures from the subcortex and white matter, namely, the middle thalamus, caudate, putamen, substantia nigra, internal and external parts of the globus pallidus, red nucleus, corpus callosum genu, body, and splenium, cingulum, internal capsule, and anterior commissure. Some brain regions, e.g., thalamus and corpus callosum, include profound heterogeneity within the area. The thalamus consists of several gray matter nuclei, showing varying iron and myelin content, considering that We included only the middle thalamus. Similarly, the corpus callosum was also divided into three sub-regions based on anatomical locations: genu, corpus callosum body, and splenium. The Corpus callosum body is the remaining part of the corpus callosum between the genu and splenium area. The segmented ROI volumes were inversely warped into subjects' native space.

QSM maps were produced for all ten individual echoes from ME-GRE phase data to determine QSM echo time dependence. The temporal responses of magnetic susceptibility

for all ROIs in gray and white matter are plotted in Figure 2.8.

## dMRI

The pipelines provided at [github.com/RDadarwal/Diffusion-MRI](https://github.com/RDadarwal/Diffusion-MRI) were used to analyze monkey and human brain dMRI data. Diffusion-weighted images were denoised [Veraart et al., 2016], and corrected for susceptibility distortions, eddy current distortions, and subject movement artifacts [Andersson et al., 2003, Andersson & Sotiropoulos, 2016].

We fitted a diffusion tensor model to the corrected dMRI data [Basser et al., 1994] to calculate axial diffusivity (AD), radial diffusivity (RD), mean diffusivity (MD), and fractional anisotropy (FA). The three-compartment Neurite Orientation Dispersion and Density Imaging (NODDI) [Zhang et al., 2012] model was fitted using the Accelerated Microstructure Imaging via Convex Optimization (AMICO) [Daducci et al., 2015] to assess Intra-cellular Volume Fraction (ICVF), and orientation dispersion (OD) index. Diffusion data from one human subject was not included in the final analysis due to its poor data quality. Human and monkey brain atlases were created by aligning non-diffusion-weighted images into a common space utilizing ANTs rigid, affine, and nonlinear registrations [Avants et al., 2008].

The ROIs were segmented manually on the average color-coded FA atlases, based on the clarity of structures using ITK-SNAP [Yushkevich et al., 2006]. The segmented white matter ROIs were the corpus callosum genu, body, and splenium.

## STATISTICS

Human-monkey brain differences in QSM,  $R_2^*$ , and quantitative dMRI parameters were probed using paired t-test statistics. To account for the effect of multiple comparisons, a statistical threshold of  $p < 0.003$  (i.e., Bonferroni-corrected  $p < 0.05$  for 13 tests) was used for QSM and  $R_2^*$  analyses, and  $p < 0.016$  (i.e., Bonferroni-corrected  $p < 0.05$  for 3 tests) for dMRI ROI analysis.

## 2.3 RESULTS

In the QSM and  $R_2^*$  average templates, the subcortical structures of the human and monkey brains showed increased contrast than the rest of the brains (Figure 2.3). The gray matter of the human and monkey brain QSM templates showed paramagnetic susceptibility contrast, while the white matter tissue exhibited diamagnetic susceptibility contrast.

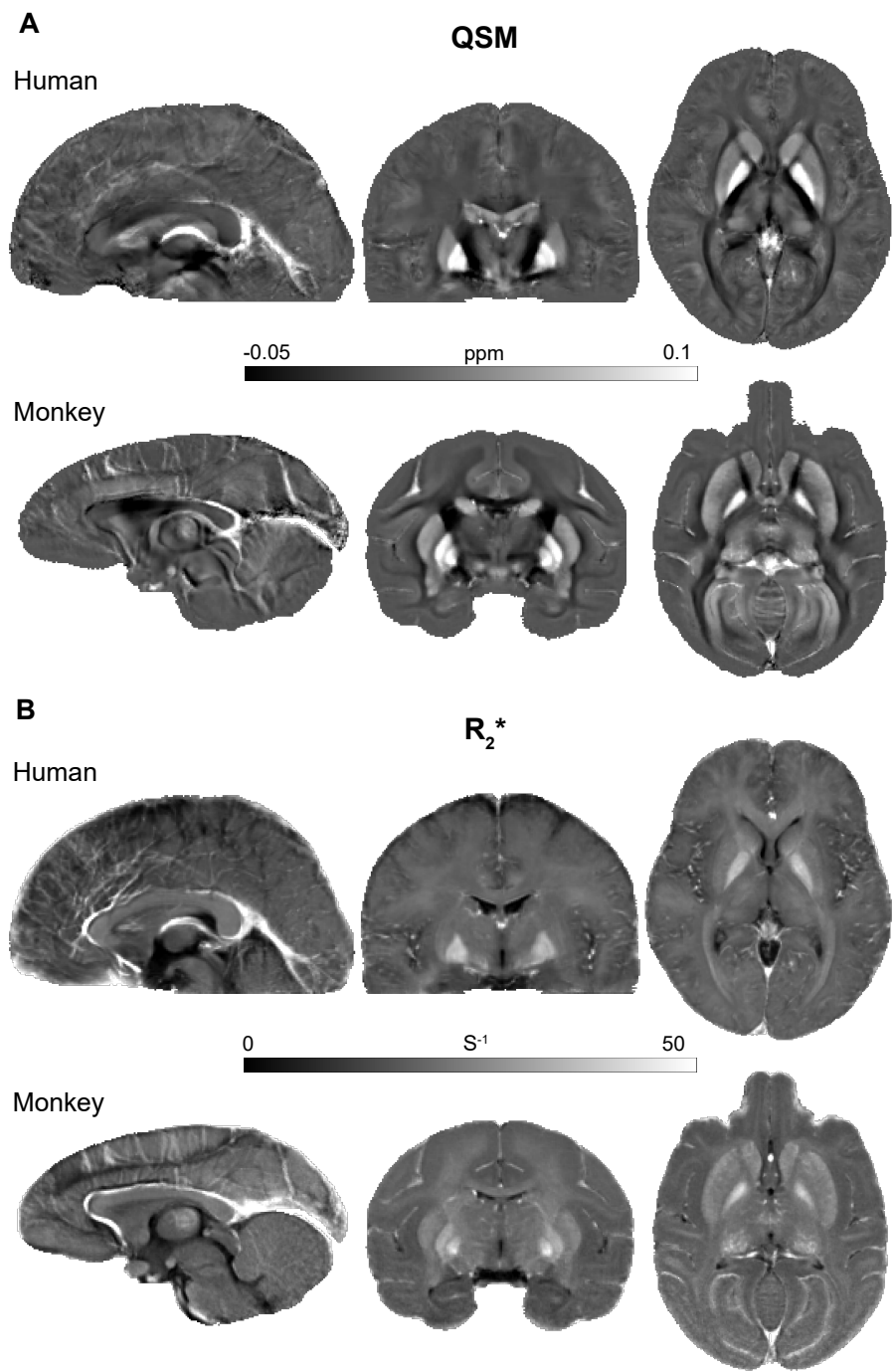
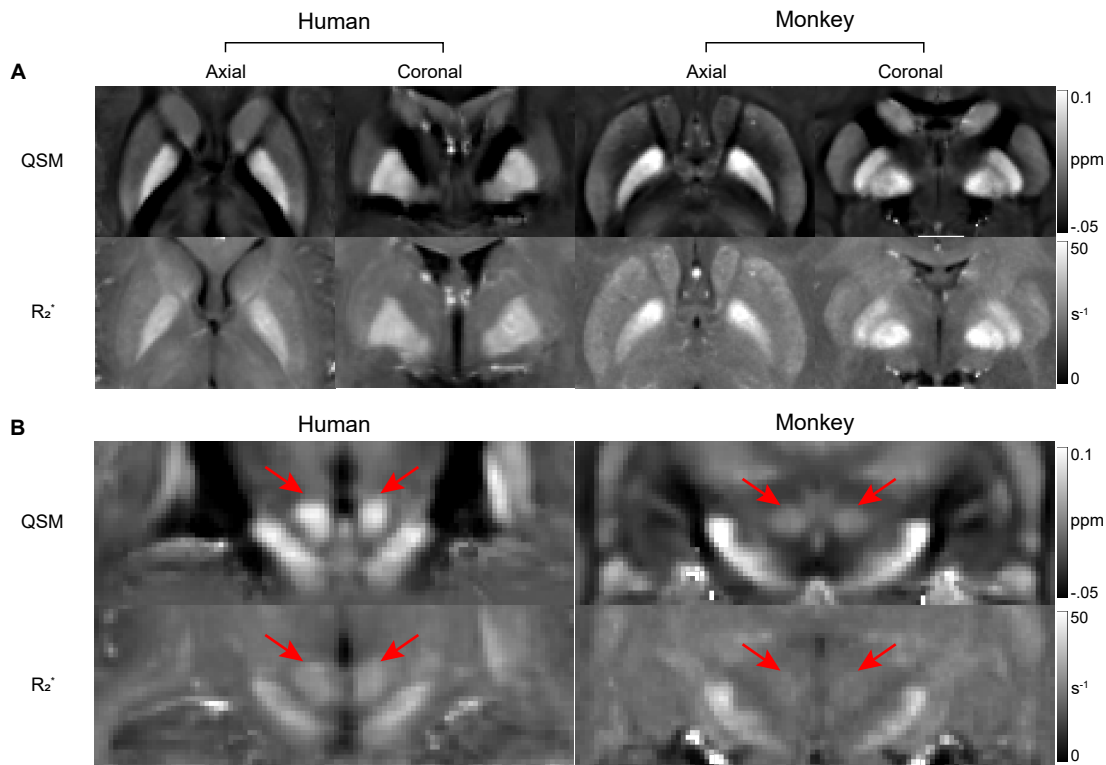


Figure 2.3: Population-averaged human and monkey brain QSM and R<sub>2</sub><sup>\*</sup> maps in sagittal, coronal, and axial planes.



**Figure 2.4:** A. QSM and  $R_2^*$  templates highlight the basal ganglia in the human and monkey brain. The basal ganglia nuclei, such as caudate, putamen, and globus pallidus (both internal and external), showed a similar contrast in human and monkey brains. B. In the coronal section of human and monkey brain templates, the red nucleus QSM and  $R_2^*$  contrasts. Humans had higher QSM and  $R_2^*$  values in the red nucleus than monkeys.

### 2.3.1 QSM – A COMPARISON BETWEEN HUMAN AND MONKEY BRAINS

The analysis of the QSM requires normalization of reconstructed raw magnetic susceptibility values to any brain tissue (e.g., whole-brain, CSF) susceptibility. Our study found the whole-brain normalized magnetic susceptibility results approximately similar to the unreferenced magnetic susceptibility results (Figures 2.5A, 2.6A, and Supplementary Figure A.2). The whole-brain magnetic susceptibility values in humans and monkeys were very small in magnitude and were chosen as a reference to normalize the raw QSM values. Another commonly used reference is CSF, which showed substantial susceptibility differences in the human and monkey brains (Supplementary Figure A.2). The CSF and whole-brain magnetic susceptibility values in humans and monkeys are in Table 2.2.

The gray matter QSM analysis revealed similar magnetic susceptibility values in human

	Monkey	Human
CSF [ppm]	$-10 \pm 8 \times 10^{-3}$	$15 \pm 5 \times 10^{-3}$
Whole-brain [ppm]	$7 \pm 2 \times 10^{-4}$	$-87.6 \pm 1 \times 10^{-4}$

**Table 2.2:** CSF and whole-brain magnetic susceptibility values in the monkey and human brains.

and monkey brains, with the exception of the red nucleus, where the human brain exhibited much higher magnetic susceptibility values ( $0.07 \pm 0.01$  ppm) than the monkey brain ( $0.03 \pm 0.01$  ppm) (Figure 2.5A). The human and monkey brains showed identical magnetic susceptibility values in the middle thalamus and other subcortical structures such as the putamen, caudate, substantia nigra, internal and external segments of globus pallidus. The external globus pallidus (GPe) revealed the highest magnetic susceptibility values in both human and monkey brains.

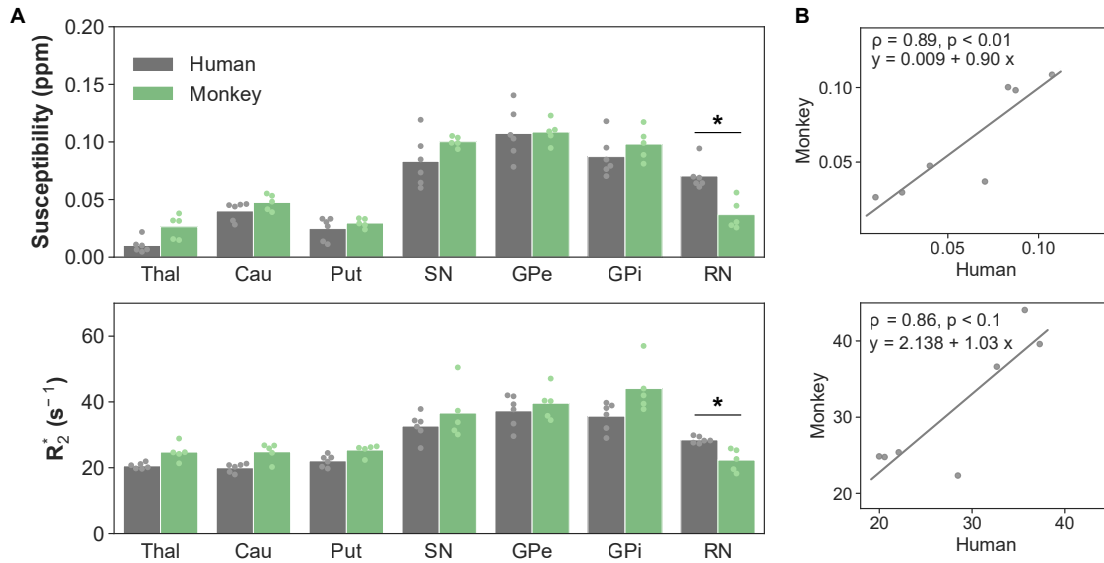


**Figure 2.5:** Human and monkey brain QSM (whole-brain referenced) and  $R_2^*$  regional summary statistics for subcortical gray matter ROIs. Bar plots show the mean and the distribution of individual observations for human and monkey brains. **A.** Mean whole-brain referenced magnetic susceptibility and  $R_2^*$  with the scattered plotted distribution of observations for individual subject values. **B.** Regression analysis between human and monkey brain QSM and  $R_2^*$  including Pearson's correlation coefficient ( $\rho$ ) and two-sided p-value ( $p$ ). Abbreviations: Thal - middle thalamus, Cau - caudate, Put - putamen, SN - substantia nigra, GPe - external globus pallidus, GPi - internal globus pallidus, and RN - red nucleus.

QSM analysis for white matter ROIs exhibited significant differences in the corpus callosum body and anterior commissure, where monkeys had relatively higher diamagnetic susceptibility values than humans (Figure 2.6A). Moreover, there were no significant variations

in magnetic susceptibility values in the genu, splenium, cingulum, and internal capsule. The human and monkey brain's cingulum had the highest diamagnetic susceptibility values. Magnetic susceptibility values exhibited higher inter-ROI variability than  $R_2^*$  values in both human and monkey brains.

Linear regression analysis of QSM and  $R_2^*$  between the human and monkey brain are illustrated in Figure 2.6B include Pearson's regression coefficient, regression slope and intercept, and p-value.

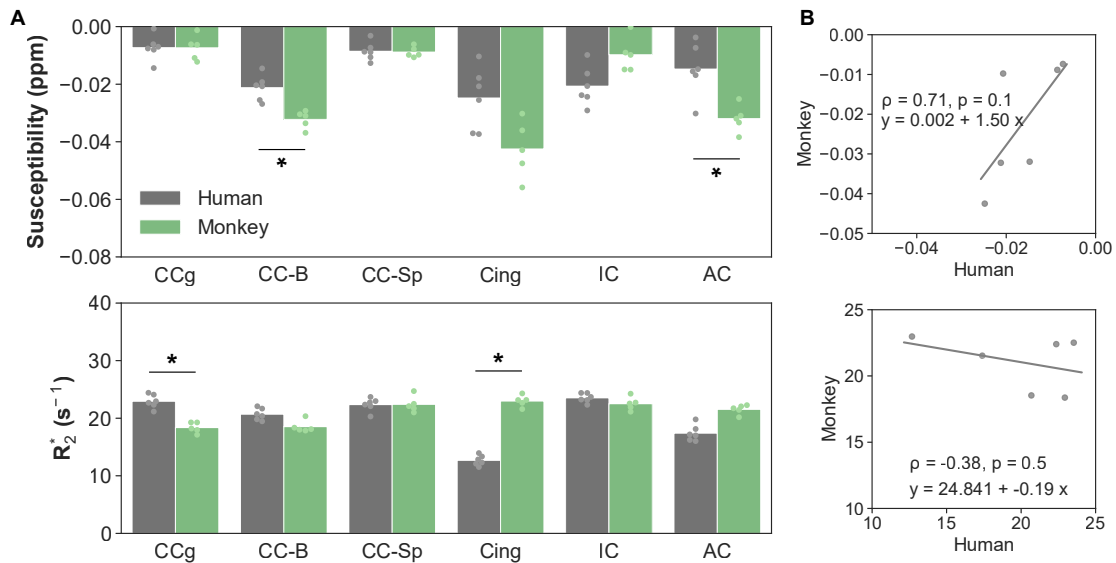


**Figure 2.6:** Human and monkey brain QSM (whole-brain referenced) and  $R_2^*$  regional summary statistics for white matter ROIs. Bar plots showing the mean and the distribution of individual observations for human and monkey brains. **A.** Mean whole-brain referenced magnetic susceptibility and  $R_2^*$  with the scattered plotted distribution of observations for individual subject values. **B.** Regression analysis between human and monkey brain QSM and  $R_2^*$  including Pearson's correlation coefficient ( $\rho$ ) and two-sided p-value ( $p$ ). Abbreviations: Thal - middle thalamus, Cau - caudate, Put - putamen, SN - substantia nigra, GPe - external globus pallidus, GPI - internal globus pallidus, and RN - red nucleus.

### 2.3.2 $R_2^*$ – A COMPARISON BETWEEN HUMAN AND MONKEY BRAINS

The  $R_2^*$  results in human and monkey gray matter ROIs were identical to the QSM results. Only the red nucleus showed substantial  $R_2^*$  differences (human =  $28 \pm 1.0 s^{-1}$ ; monkey =  $22 \pm 3.4 s^{-1}$ ).  $R_2^*$  values in the basal ganglia of human and monkey brains were found to be similar in both species (Figure 2.5A).

The human brain corpus callosum genu had significantly higher  $R_2^*$  values than the monkey brain (Figure 2.6A). The human brain cingulum, on the other hand, had substantially



lower  $R_2^*$  values than the monkey brain cingulum. Furthermore, no significant  $R_2^*$  changes were found between the human and monkey brain ROIs such as the body, splenium, internal capsule, and anterior commissure.

### 2.3.3 QSM TE DEPENDENCE

QSM TE dependence was observed in most analyzed gray and white matter ROIs in humans and monkeys but to varying degrees. Figure 2.7 provides QSM temporal (tQSM) profiles for four gray (middle thalamus, caudate, substantia nigra, and red nucleus) and four white matter (genu, body, cingulum, and anterior commissure) regions. The rest of the ROIs' tQSM profiles are shown in the supplementary Figure A.4. All of these tQSM profiles were consistent between measurements and only differed by brain regions. Larger structures, such as the corpus callosum, demonstrated considerable heterogeneity within the structure and varied temporal profiles for distinct substructures, such as the corpus callosum genu and body (Figure 2.7).

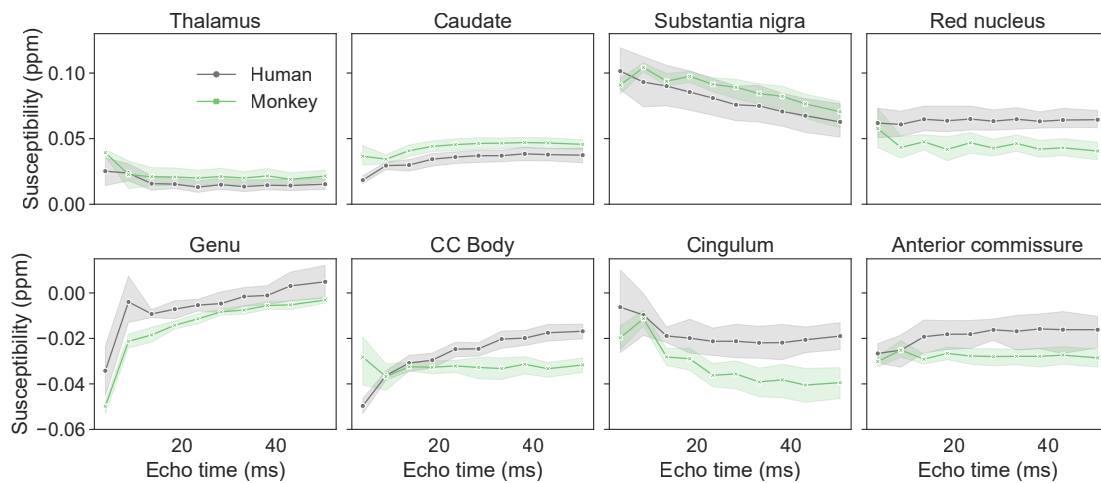


**Figure 2.7:** QSM values as a function of TE for gray matter (top row) and white matter (bottom row) areas. QSM temporal (tQSM) profile results are shown for the middle thalamus, caudate, substantia nigra, red nucleus, genu, CC body, cingulum, and anterior commissure. The individual plot shows the temporal susceptibility response for the group mean (thin dotted line) and confidence interval (Shaded area). The human and monkey brain showed a similar pattern in susceptibility values with echo time. The human brain showed a positive shift toward higher susceptibility values than the monkey brain in some brain regions.

Gray matter regions such as the middle thalamus and substantia nigra displayed similar tQSM curve profiles in the human and monkey brains. Compared to the human brain, the tQSM curve profile in the caudate shifted towards higher susceptibility values in the monkey brain. Moreover, in humans, the red nucleus tQSM profile showed a positive shift and

enhanced nonlinear dependency compared to the monkey brain. These findings were in line with the QSM comparative analysis, which demonstrated that the red nucleus of the human brain had higher QSM than that of the monkey brain.

White matter TE dependence analyses revealed similar trends in tQSM profiles for genu and anterior commissure in human and monkey brains. At the same time, tQSM profiles in the corpus callosum body of the monkey brain indicated stronger nonlinearity and an increasing trend with an increase in TE than in the human brain. In contrast to the monkeys, the human tQSM profile in the corpus callosum body demonstrated less TE dependence. The cingulum of monkeys showed a positive shift toward higher magnetic susceptibility values when compared to the human brain (Figure 2.7).

We discovered that CSF magnetic susceptibility levels were essentially independent of TEs in both human and monkey brains (Figure 2.8). However, these observed values were paramagnetic in the human brain and diamagnetic in the monkey brain.

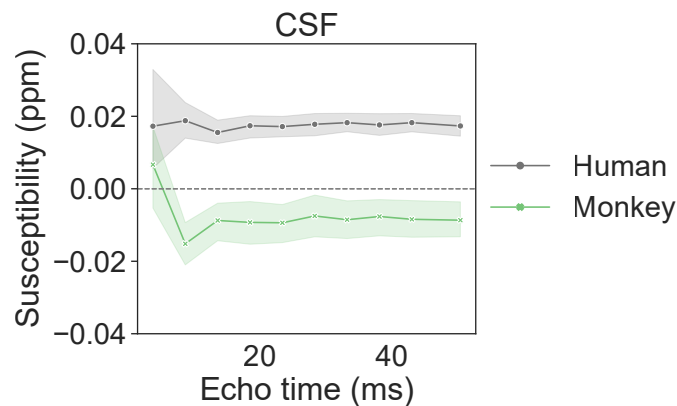


**Figure 2.8:** QSM temporal (tQSM) profiles for the CSF in human and monkey brains. The TE does not affect the tQSM profile in the human and monkey brain. The observed tQSM shows positive susceptibility values in the human brain and negative susceptibility values in monkeys.

#### 2.3.4 dMRI

The DTI analysis showed similar FA values in the human and monkey brain corpus callosum ROIs (genu, body, and splenium). The observed MD values were higher in the monkey brain than the human brain, as shown in Figure 2.10. No significant variations in FA were observed between human and monkey brains. Moreover, the observed differences in MD were due to increased AD in the genu and splenium and higher RD in the monkey brain’s body compared to the human brain.

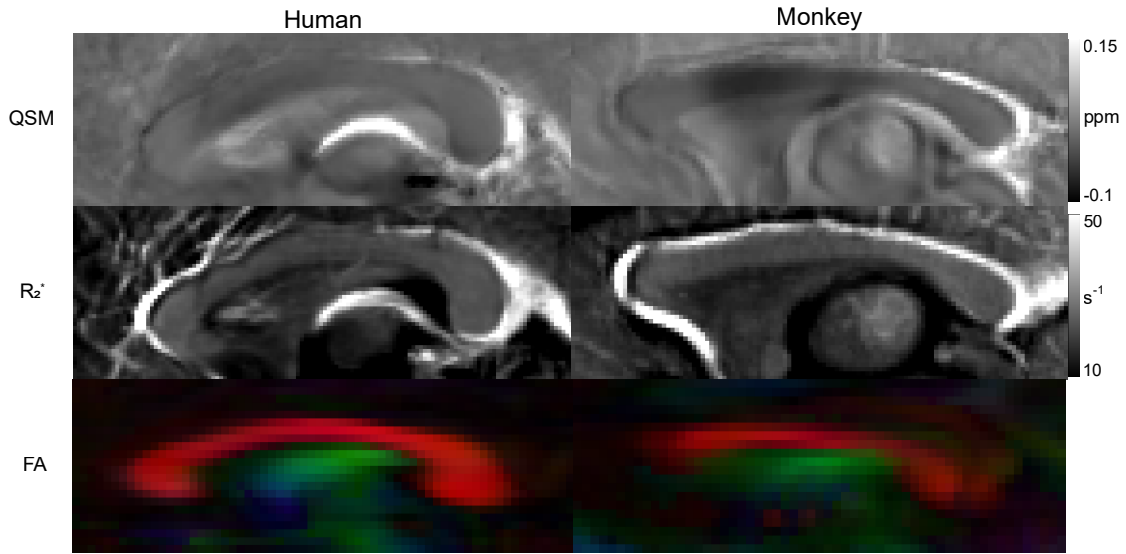


**Figure 2.9:** The corpus callosum QSM,  $R_2^*$  and color-coded FA contrasts in the axial and sagittal sections of the human and monkey brain templates. When comparing the QSM map to the  $R_2^*$  and FA maps, contrast differences in distinct parts of the corpus callosum are readily visible.

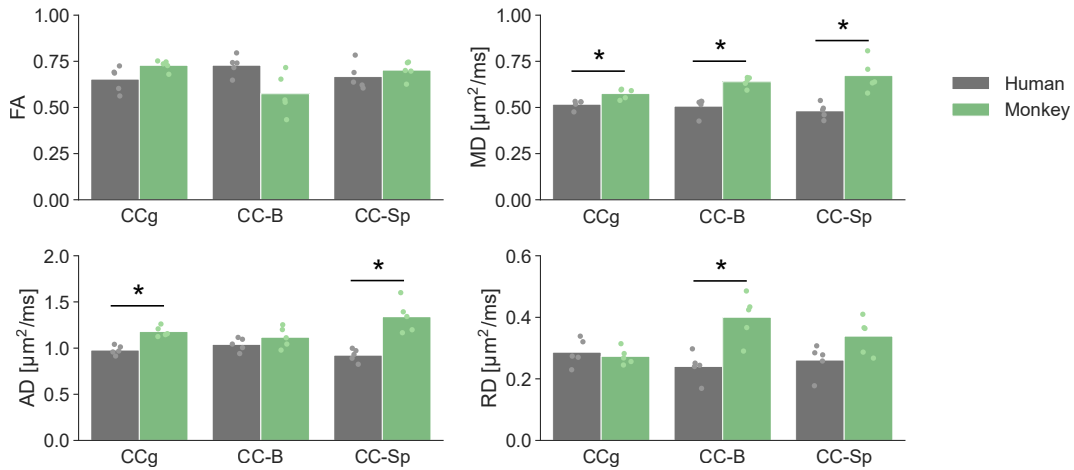


**Figure 2.10:** DTI results in summary statistics for three different corpus callosum structures in the human and monkey brains. There were no substantial differences in FA between the human and monkey brains. On the other hand, the MD demonstrates the considerable disparities in all three analyzed corpus callosum areas between humans and monkeys.

The NODDI analysis revealed higher ICVF values in the human brain corpus callosum genu, body, and splenium than the monkey brain (Figure 2.11). However, there were no significant differences in OD index values between human and monkey brains.

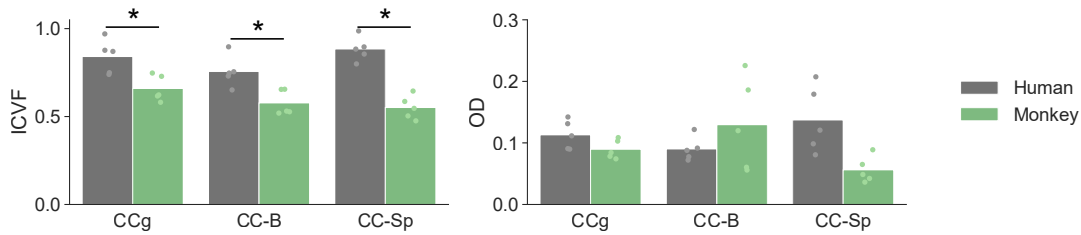


**Figure 2.11:** NODDI results in summary statistics for three different corpus callosum structures in human and monkey brains.

## 2.4 DISCUSSION

This *in vivo* study compares QSM and  $R_2^*$  in the human and monkey brains. To our knowledge, this is the first study that directly compares human and monkey brain QSM and  $R_2^*$  using identical MRI acquisition parameters. The analyzed QSM, and  $R_2^*$  values in the human and monkey brain gray and white matter regions-of-interest were almost identical except for a few regions. In addition, we investigated the QSM echo time dependence in the subcortical and white matter areas of the human and monkey brains. Furthermore, we used quantitative dMRI results to learn more about the identified similarities and differences in QSM and  $R_2^*$  between human and monkey brains.

QSM provides relative estimates of magnetic susceptibility rather than providing absolute values. These estimates of relative magnetic susceptibility must be referenced to the susceptibility values of a specific brain region. The problem of selecting an appropriate reference region is yet unsolved. Previous research has compared and demonstrated QSM's reference region reliance [Feng et al., 2018, Straub et al., 2017]. The CSF susceptibility values found in the human brain in this study were consistent with those reported in the literature [Straub et al., 2017]. However, as compared to human CSF values, monkey CSF had diamagnetic susceptibility values. These magnetic susceptibility discrepancies using CSF as a reference region could lead to erroneous disparities in susceptibilities between human and monkey brains. In an existing study, iron levels in the CSF of a rhesus monkey brain ( $35.9 \pm 15.1 \mu\text{g}/\text{dl}$ ) were found to be higher than in the human brain ( $1.5 \mu\text{g}/\text{dl}$ ), contrary to what we have observed [Altman & Dittmer, 1974, Hambleton et al., 1981].

The whole-brain referenced magnetic susceptibility and  $R_2^*$  values in the investigated subcortical ROIs were identical in human and monkey brains, except for the red nucleus. The red nucleus of the human brain had higher magnetic susceptibility and  $R_2^*$  values than that of the monkey brain. The observed variances could be due to differences in red nucleus organization between bipedal and quadrupedal species. The parvicellular red nucleus development in the human and monkey brain red nuclei are known to differ [Onodera & Hicks,

2009, Hicks & Onodera, 2012]. Because of the importance of the red nucleus in complex task performance, further research is needed to understand the organizational differences between bipedal and quadrupedal species' red nuclei [Basile et al., 2021].

There were substantial changes in QSM and  $R_2^*$  values between human and monkey brains in some white matter ROIs. In comparison to the human brain, the monkey brain corpus callosum body and cingulum have higher diamagnetic susceptibility values, indicating more myelin content. However, combining two distinct effects in white matter structures, the orientation of fibers in relation to the magnetic field and variations in the tissue microstructure, could explain these discrepancies overall. In this study, human volunteers had a supine position, and monkeys had a prone position inside the scanner. The orientation of fiber tracts in reference to the magnetic field direction changes when you go from supine to prone. However, the fiber bundles that connect the two hemispheres (callosal fibers) run in a similar direction. We conducted a pilot study to evaluate the effects of fiber bundle orientation relative to the magnetic field on QSM and  $R_2^*$ . In this pilot study, postmortem monkey brain measurements were carried out in supine and prone positions inside the MRI scanner. The postmortem monkey brain measurements yielded QSM and  $R_2^*$  values that were not substantially different between the two head positions (Supplementary Figure A.5). The observed percent (%) change in QSM and  $R_2^*$  values from supine to prone positions does not account for all *in vivo* variations in human and monkey brain magnetic susceptibility and  $R_2^*$  values.

Previous research has reported that the corpus callosum in the human and monkey brains has a similar topographic organization [Hofer et al., 2008]. In addition, as compared to the monkey brain, the parietal and temporal sectors of the human corpus callosum have higher FA values [Caminiti et al., 2013]. Our DTI results showed no significant differences in FA between human and monkey brains. Monkeys have higher MD values and lower ICVF values compared to humans, indicating less tissue integrity and axonal density. However, higher AD values in corpus callosum genu and splenium could not be explained based on available data.

QSM relies on the assumption that the measured phase in a voxel is linearly related to the TE and local field perturbations. Moreover, recent work has shown that GRE measured frequency and phase evolution do not hold this presumption, and phase and frequency in a voxel evolve nonlinearly with TE [Biondetti et al., 2020, Tandler & Bowtell, 2019]. This nonlinear phase evolution occurs in the presence of tissue microstructure or due to phase unwrapping errors [Cronin et al., 2017, Biondetti et al., 2020]. The results of our QSM TE dependence in the human brain were comparable to those of a previous study [Sood et al., 2017]. A previous study also demonstrated that the acquisition parameter and TE choice can impact the observed QSM TE dependence [Lancione et al., 2019]. However, in this study,

we provide an excellent human and monkey brain comparison by maintaining all acquisition parameters and TEs the same. More investigation into the temporal dependence of magnetic susceptibility could shed light on its relationship with tissue microstructure.

In conclusion, QSM and  $R_2^*$  analyses in human and monkey brains will help us better understand tissue substrate similarities and differences. Importantly, acquiring MRI data in the same way in humans and monkeys aids in the development of a comprehensive understanding of QSM and  $R_2^*$  measured iron and myelin levels in the subcortical and white matter areas. In order to further investigate the source of differences in human and monkey brain CSF magnetic susceptibilities, we obtained human and monkey CSF samples from healthy human volunteers and monkeys. A brain phantom with human and monkey CSF will be built in the future, and both samples will be measured simultaneously using the same equipment at a 3 T MRI scanner. In addition, to examine magnetic susceptibility and  $R_2^*$  discrepancies in the human and monkey brain red nucleus and white matter regions, high-resolution quantitative MRI and histology comparisons are required.

*Faith is the act of seeing beyond the region of the possibility  
of the senses, the mind, and intelligence.*

Radhanath Swami

# 3

## A multi-contrast MRI template of the cynomolgus macaque brain

### AUTHORS

**Rakshit Dadarwal** and Susann Boretius

Functional Imaging Laboratory, German Primate Center – Leibniz Institute for Primate Research, Göttingen, Germany

Georg-August University of Göttingen, Göttingen, Germany

### ABSTRACT

Neuroimaging studies in non-human primates benefit from the use of standardized species-specific brain templates for reporting research findings. The availability of species-specific brain templates enables the comparison of neuroimaging data across multiple sources and sites via a common standardized anatomical space. However, the available rhesus macaque brain templates do not generalize well to other macaque species. The rhesus macaque templates do not capture morphometric features of the cynomolgus macaque. Moreover, while T<sub>1</sub>-based brain templates are excellent in gray-white matter contrast, T<sub>1</sub> alone does not differentiate across all brain tissue types (e.g., cortical, subcortical, and white matter). Notably,

many iron-rich structures in subcortical nuclei show better differential contrast with  $T_2^*$ -weighted sequences. In this work, we constructed high-quality standardized symmetric and asymmetric multi-contrast MRI brain templates using cynomolgus macaque monkey scans. The multi-contrast templates improved single volume registration to a standardized anatomical space and provided accurate delineations of cortical and subcortical brain structures.

The work described in this chapter resulted in the following output:

**Rakshit Dadarwal**, and Susann Boretius. "*Multi-contrast MRI Atlas of the cynomolgus Macaque Brain*" In: Proceedings of the 29th Annual Meeting of the International Society for Magnetic Resonance in Medicine (ISMRM), (Virtual) (2021).

**Rakshit Dadarwal**, and Susann Boretius. "*A multi-contrast MRI template of the cynomolgus macaque monkey*" (manuscript in preparation).

### 3.1 INTRODUCTION

Like human neuroimaging studies, non-human primate (NHP) neuroimaging studies require a standard anatomical template to facilitate reproducible research (data analysis and comparison) across studies and laboratories. Standardization of single-subject image data to the anatomical template must be to the species-specific template to overcome inter-species variability. Anatomical templates make identifying the right structural area in MRI studies easier and guide the accurate placement of electrodes or needles in NHPs. Precision targeting in tracer injection experiments [Majka et al., 2016, Murayama et al., 2006] and creating a lesion in a particular part of the brain [Kunimatsu et al., 2015, Vaidya et al., 2019], needs an excellent contrast from the area of interest.

Cynomolgus monkeys (*Macaque fascicularis*), also known as crab-eating or long-tailed macaques, are extensively used in neuroscience and biomedical research and have played an essential role in pharmaceutical drug trials and vaccine development [Bonfanti et al., 2009, Brennan et al., 2017, Weber et al., 2020].

Our study addresses two significant issues that limit the use of currently openly available macaque templates: First, most available macaque templates do not sufficiently represent the cynomolgus macaque. The majority of available macaque brain templates and atlases are from rhesus macaques [Calabrese et al., 2015, Essen & Dierker, 2007, Frey et al., 2011, Liu et al., 2009, McLaren et al., 2009, Reveley et al., 2017, Rohlfing et al., 2012, Rushmore et al., 2020, Saleem & Logothetis, 2012, Seidlitz et al., 2018, Shi et al., 2017, Weiss et al., 2020] and do not adequately capture the cynomolgus macaque's anatomy [Frey et al., 2011, Gucht et al., 2006, Kirk, 2006, McLaren et al., 2009]. The openly available cynomolgus macaque template, MNI [Frey et al., 2011], and others [Ballanger et al., 2013, Collantes et al., 2009]



were constructed using data obtained at low field strength (1.5 Tesla) and with low spatial resolution, which overall led to a reduced signal-to-noise ratio (SNR) and contrast-to-noise ratio (CNR). Furthermore, existing atlases only provide labels for a few regions-of-interest (ROI) and do not cover all brain structures. Therefore, a dedicated cynomolgus template accompanied by tissue parcellation is required for single cynomolgus macaque data standardization and anatomical structural localization.

The second issue with available cynomolgus macaque brain templates is the lack of multiple imaging contrasts, as most of the available templates only provide structural  $T_1$ -weighted images [Lv et al., 2021]. Different MRI contrasts offer complementary information and are sensitive to varying properties of the biological tissues [Cercignani & Bouyagoub, 2018, Dadarwal & Boretius, 2021a]. The inclusion of numerous MRI contrasts allows us to better visualize cortical, subcortical, and white matter structures and facilitates fine anatomical tissue segmentation and classification [Xiao et al., 2015]. The multi-contrast approach can also enhance the translation capacity of non-human primate studies to human studies. As quantitative parametric maps account for inter-regional variations better than qualitative parametric maps. The availability of numerous MRI contrasts also offers the opportunity to create synthetic MRI contrasts with enhanced tissue information.

This study provides high-quality multi-contrast symmetric and asymmetric MRI templates of the cynomolgus macaque brain, as well as comprehensive anatomical parcellations. We created the templates from high-resolution structural ( $T_1$ -weighted,  $T_2$ -weighted, Magnetization Transfer weighted, and Multi-echo gradient-recalled echo) and parametric (magnetic susceptibility, effective transverse relaxation rate, magnetization transfer saturation index, and apparent  $T_1$  relaxation time) MRI contrasts from a cohort of 14 female cynomolgus macaques. The multi-contrast-based symmetric and asymmetric cynomolgus templates with 0.25 mm and 0.5 mm isotropic resolution can serve as a final standard stereotaxic space for the neuroscience and biomedical research community. All the MRI templates with their tissue probability masks, anatomical parcellations (including cortical, subcortical, and white matter ROIs), and brain surfaces will be made available to the scientific community on Zenodo ([zenodo.org](https://zenodo.org)).

## 3.2 MATERIALS AND METHODS

### 3.2.1 SUBJECTS

Our subject cohort included 14 female long-tailed macaques (*Macaca fascicularis*). Five macaques were between the ages of 7 - 9 years old, and nine macaques were between the ages of 16 - 18 years old.

### 3.2.2 ANIMAL EXPERIMENTS

All monkeys were purpose-bred, raised, and housed according to the standards for macaques of the German Primate Center (Göttingen, Germany). All aspects of the study were conducted in accordance with national and international guidelines of the German Animal Protection Law and the European Union Directive 2010/63/EU for the Protection of Animals used for Scientific Purposes. The study was approved by the local authorities, the Animal Welfare Service, Lower Saxony State Office for Consumer Protection and Food Safety (license number 33.19-42502-04-16/2278). In preparation for anesthesia, the macaques were deprived of food overnight. Anesthesia was induced by a mixture of ketamine ( $8.05 \pm 2.65$  mg per kg body weight) and medetomidine ( $0.02 \pm 0.01$  mg per kg) and maintained by isoflurane (0.8 - 1.7% in oxygen and ambient air) via endotracheal tube and pressure-controlled active ventilation. The monkeys were placed in a prone position, and their heads were fixed in an MR-compatible stereotactic apparatus (Kopf 1430 M, [kopfinstruments.com](http://kopfinstruments.com)).

### 3.2.3 MRI DATA ACQUISITION

All brain images were acquired at a 3T scanner (MAGNETOM Prisma, Siemens Healthineers, Erlangen) using a 7 cm single loop circular coil. The imaging protocol included structural T<sub>1</sub>-weighted (T<sub>1</sub>w), T<sub>2</sub>-weighted (T<sub>2</sub>w), multi-echo gradient-recalled echo (ME-GRE), magnetization transfer-weighted (MTw), proton density-weighted (PDw), and T<sub>1</sub>w acquisitions, as detailed in Table 3.1 and Table 3.2.

Parameters	T <sub>1</sub> w	T <sub>2</sub> w	ME-GRE
Pulse sequence	3D MPRAGE	Spin echo	3D Gradient echo
Native resolution (mm <sup>3</sup> )	0.5 × 0.5 × 0.5	0.4 × 0.4 × 0.9	0.31 × 0.31 × 0.31
Field of view (mm <sup>2</sup> )	107 × 127	108 × 128	97 × 120
Acquisition matrix	216 × 256	270 × 320	312 × 384
Number of slices	180	50	144
Total acquisition time (min)	14.3	5.2	24
TR/TE (ms)	2700/2.7	8000/17	57/[3.7/4.9/48]
Flip angle (degree)	8	180	20
Pixel bandwidth (Hz/Px)	250	250	250

**Table 3.1:** MRI acquisition parameters for T<sub>1</sub>w, T<sub>2</sub>w, and ME-GRE scans.

Parameters	MTw	PDw	T <sub>1</sub> w
Pulse sequence	3D FLASH	3D FLASH	3D FLASH
Native resolution (mm <sup>3</sup> )	0.5 × 0.5 × 0.5	0.5 × 0.5 × 0.5	0.5 × 0.5 × 0.5
Field of view (mm <sup>2</sup> )	107 × 127	107 × 127	107 × 127
Acquisition matrix	216 × 256	216 × 256	216 × 256
Number of slices	128	128	128
Total acquisition time (min)	15.3	6.3	5.1
TR/TE (ms)	30/3.2	25/3.2	10/3.2
Flip angle (degree)	5	5	15
Pixel bandwidth (Hz/Px)	300	300	300
Number of averages	2	1	2

**Table 3.2:** MRI acquisition to quantify MTsat and T<sub>1</sub>app required MTw, PDw, and T<sub>1</sub>w scans. MRI acquisition parameters for MTw, PDw, and T<sub>1</sub>w scans.

### 3.2.4 DATA ANALYSES

#### PREPROCESSING

Preprocessing of T<sub>1</sub>w, T<sub>2</sub>w, MTw, and mean ME-GRE (mGRE) (mean across echo times) images was performed using interfaces from the Nipype [Gorgolewski et al., 2011] library, as depicted in Figure 3.1A. Each subject’s T<sub>1</sub>w, T<sub>2</sub>w, MTw, and ME-GRE DICOM images were first converted into Nifti format using *Dcm2nii* [Li et al., 2016]. The T<sub>1</sub>w, T<sub>2</sub>w, MTw, and mGRE Nifti images were denoised using ANTs *DenoiseImage* [Manjón et al., 2010]. The segmentation of the brain mask for each MRI contrast was carried out manually using the ITK-SNAP segmentation tool [Yushkevich et al., 2006] due to the lack of automatic skull-stripping tools for the monkey brain. The constructed brain masks were then used as an input for bias removal using ANTs *N4BiasFieldCorrection* [Tustison et al., 2010] and subsequently in skull-stripping. The skull-stripped T<sub>2</sub>w, MTw, and mGRE images were then registered linearly (affine) to the T<sub>1</sub>w brain image from the same subject using ANTs Registration [Avants et al., 2008].

#### T<sub>1</sub>W TEMPLATE CREATION

The T<sub>1</sub>w template was generated using a python pipeline ([github.com/CoBrALab/twolevel\\_ants\\_dbm](https://github.com/CoBrALab/twolevel_ants_dbm)) based on ANTs template creation script (*antsMultivariateTemplateConstruction2.sh*). This pipeline uses symmetric normalization (SyN) [Avants et al., 2008] algorithmic approach to nonlinearly register all the T<sub>1</sub>w brain scans to create an unbiased group average template image. The final template was termed the Deutsches Primatenzentrum cynomolgus macaque (DPZCYNO) template. The NMT v2 [Jung et al.,

2021] template was used as a target template for the stereotaxic orientation of the DPZCYNO template Figure 3.4. The asymmetric DPZCYNO was created using the 14 anatomical scans. These anatomical scans were first duplicated and mirrored about the plane between the hemispheres to generate the symmetric DPZCYNO templates. We then used the resulting 28 volumes to generate the symmetric template.

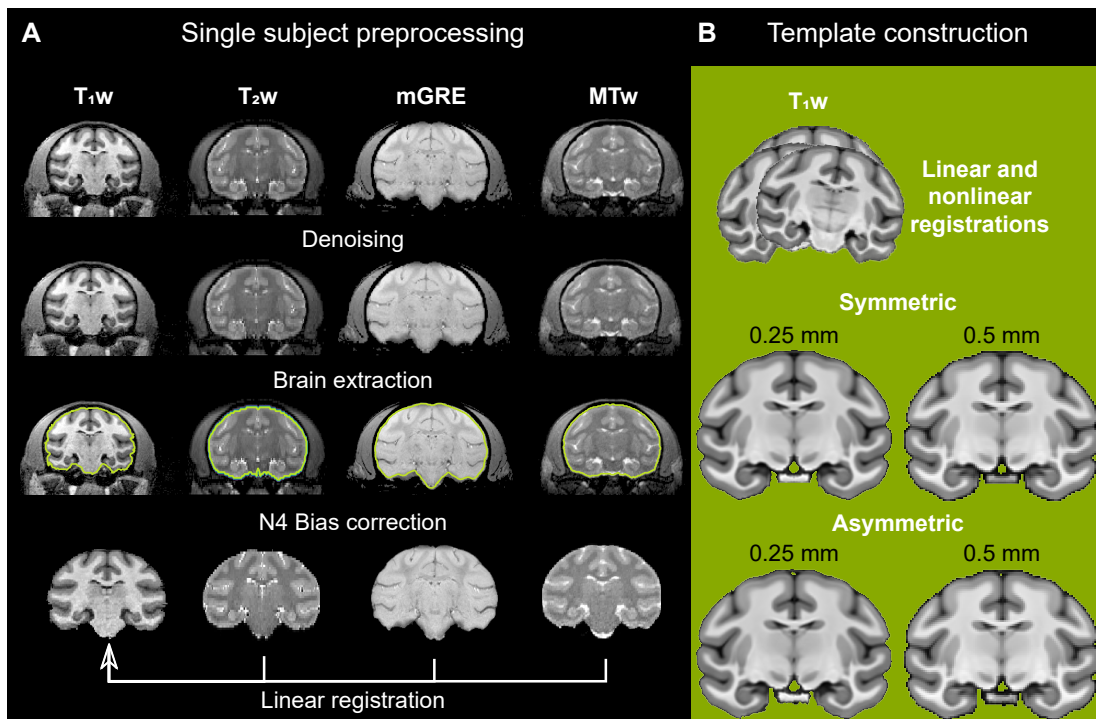


**Figure 3.1:** A. Preprocessing of Multi-contrast ( $T_1w$ ,  $T_2w$ , mGRE, and MTw) MRI images for a single subject. B. The construction of unbiased asymmetric and symmetric brain templates using cohorts of 14 and 28 scans (14 original and 14 mirrored), respectively. The preprocessing steps included image denoising, brain extraction, bias field correction for the  $T_1w$ ,  $T_2w$ , mGRE, MTw contrasts, and linear registration of  $T_2w$ , MTw, and mGRE images to the  $T_1w$  image.

## MEAN DISPLACEMENT MAP

To assess the morphometric differences across the 14 anatomical scans, we calculated the displacement map by taking the average of the diffeomorphic warp fields from 14 subject spaces to the asymmetric template space. The mean displacement map shows the amount of the average displacement at each voxel in each spatial dimension (i.e.,  $x,y,z$ ) between the subjects and template, as shown in Figure 3.5.

## CONTRAST-TO-NOISE RATIO (CNR)

On each structural and parametric template, we calculated the contrast-to-noise ratio (CNR) to quantify how distinguishable two tissue classes are from one another. Here, the CNR was evaluated by using the following formula:

$$CNR = \frac{\text{mean}(X_i) - \text{mean}(X_j)}{\text{standard deviation (CSF)}} \quad (3.1)$$

Class  $X_i$  refers to cortical gray matter and subcortical gray matter, while class  $X_j$  refers to white matter and subcortical gray matter tissue. These two classes were combined to make three possible pairs.

The CNRs were estimated using the full brain cerebrospinal fluid (CSF), cortical gray matter, white matter, and subcortical gray matter ROI labels, excluding the cerebellum, and pons regions, as shown in Supplementary Figure A.6.

## SEGMENTATION

The  $T_1w$  template was used to create the DPZCYNO brain mask using the ITK-SNAP tool [Yushkevich et al., 2006]. Furthermore, ANTs Atropos (*antsAtroposN4.sh*) was used to classify DPZCYNO  $T_1w$  template brain tissues into three classes (CSF, gray matter, and white matter). The resultant output comprised CSF, gray matter, and white matter segmentation masks with their associated probabilistic maps. We manually edited the binary gray matter segmentation mask to produce a cortical mask. Other binary masks for the left and right hemispheres, subcortical and non-cortical regions, were created to be used in the surface generation pipeline for surface filling.

## CORTICAL THICKNESS, SURFACE CURVATURE, AND SURFACE AREA

We derived the cortical thickness of the symmetric and asymmetric DPZCYNO templates using a volumetric-based approach, which requires segmented cortical gray matter and white matter masks as input. The cortical thickness was estimated using ANTs *KellyKapowski*, which is based on the DiReCT method [Das et al., 2009]. The mean and Gaussian curvatures and surface area for the symmetric and asymmetric DPZCYNO templates were calculated using ANTs *SurfaceCurvature*.

## SURFACE GENERATION

The DPZCYNO template surface maps were derived using a semi-automatic approach based on *precon\_all* ([github.com/neurabenn/precon\\_all](https://github.com/neurabenn/precon_all)). *Precon\_all*, which is an animal surface generation pipeline that also works for non-human primates. To run this cortical surface generation pipeline, the DPZCYNO structural  $T_1w$  template with a whole-brain mask was used for brain extraction, and masks of the left and right cerebral hemispheres, brainstem, cerebellum, and subcortical nuclei were supplied as an input for white matter filling. The output surface maps are shown in Figure 3.7.

## QUANTITATIVE SUSCEPTIBILITY MAPPING (QSM) AND EFFECTIVE TRANSVERSE RELAXATION RATE ( $R_2^*$ )

ME-GRE magnitude and phase data were used to calculate  $R_2^*$  and QSM maps.  $R_2^*$  maps were calculated by fitting the ME-GRE magnitude signal decay across all echo times with a mono-exponential model [Pei et al., 2015]. QSM maps were reconstructed using coil combined ME-GRE phase data. This QSM reconstruction included phase unwrapping using the best-path algorithm, background field removal using Laplacian boundary value and variable spherical mean value filtering algorithms, and solving the inversion problem using the multiscale dipole inversion approach [Abdul-Rahman et al., 2007, Acosta-Cabronero et al., 2018, Zhou et al., 2014].

## MAGNETIZATION TRANSFER

Magnetization Transfer saturation index (MTsat) and apparent longitudinal relaxation time ( $T_{1app}$ ) maps were estimated using the method described by [Helms et al., 2008]. The method's steps were implemented in MATLAB R2018a (The Mathworks Inc., Natick, MA) and are available at [github.com/RDadarwal/MTsat-MRI](https://github.com/RDadarwal/MTsat-MRI).

## $T_2w$ , MTw, QSM, AND $R_2^*$ TEMPLATES

ANTs *ApplyTransforms* was used to concatenate the linear deformation fields from single subject structural contrasts ( $T_2w$ , MTw, and mGRE) to the same subject's  $T_1w$  image and nonlinear deformation field from the subject's  $T_1w$  image to the final DPZCYNO  $T_1w$  template. Furthermore, these concatenated deformation fields were used to transform all structural ( $T_2w$ , MTw, and mGRE) and parametric (QSM,  $R_2^*$ , MTsat, and  $T_{1app}$ ) images from the native subject space into the DPZCYNO  $T_1w$  template space. Finally, the population-averaged symmetric and asymmetric  $T_2w$ , MTw, mGRE, QSM,  $R_2^*$ , MTsat, and  $T_{1app}$  templates were created by computing a pixel-wise mean across subjects.

## SYNTHETIC IMAGES VIA A LINEARLY-WEIGHTED COMBINATION OF CONTRASTS (SILICON)

We have used a weighted linear combination to fuse multiple symmetric DPZCYNO templates. Multiple variable structural and parametric contrasts including  $T_1w$ ,  $T_2w$ ,  $MTw$ ,  $QSM$ ,  $R_2^*$ , and  $MTsat$  were chosen to maximize contrast in the synthetic image. Fifty weights ( $W$ ) for  $T_1w$  were generated at random between 0 and 1, while for  $T_2w$ ,  $MTw$ ,  $QSM$ ,  $R_2^*$ , and  $MTsat$ , between -1 and 1.  $T_1w$ ,  $T_2w$ , and  $MTw$  signal intensities and  $QSM$ ,  $R_2^*$ , and  $MTsat$  values ( $X$ ) were normalized to a range of 0 to 1 before entering into the fusion equation,

$$Y_i = \sum_{c=1}^6 W_c \cdot X_{ci} \quad (3.2)$$

In order to automatically select the most promising image fusion (i.e., weights), CNRs and Linear Discriminant Analysis (LDA) accuracy score were used as follow: The minimum threshold set for the CNR between gray matter and white matter was 3, while the threshold for the CNR between subcortical gray matter and white matter was 2. Moreover, to maintain the low contrast differences between the gray matter and subcortical gray matter, the maximum CNR threshold was set to 0.5. The threshold for the LDA accuracy score was set to 0.90. The selected fusion image obtained the highest LDA accuracy score out of fifty iterations and met all of the CNR requirements.

## CORTICAL MYELIN MAPPING

The  $T_1w/T_2w$  ratio is commonly used as a surrogate for myelin content.  $T_1w/T_2w$  maps were generated using each subject's  $T_1w$  and  $T_2w$  scans. The resulting output  $T_1w/T_2w$  maps were then nonlinearly warped into the DPZCYNO template space. Finally, we mapped the  $T_1w/T_2w$  template volume map onto the DPZCYNO template surfaces using Connectome Workbench [Marcus et al., 2011].

## REGISTRATION TO OTHER MACAQUE TEMPLATES

The DPZCYNO template brain parcellations were extracted from the already available rhesus macaque atlases. To obtain ROI labels in the DPZCYNO space, we nonlinearly registered the DPZCYNO  $T_1w$  template to the NMT v2 symmetric [Jung et al., 2021], D99 [Reveley et al., 2017, Saleem & Logothetis, 2012], and INIA19 [Rohlfing et al., 2012] templates using ANTs Registration [Avants et al., 2011]. We used the resultant NMT v2 to DPZCYNO warp files to transform the Cortical Hierarchy Atlas of the Rhesus Macaque (CHARM) [Jung et al., 2021] and Subcortical Atlas of the Rhesus Macaque (SARM) [Hartig et al., 2021] par-

cellations from the NMT v2 space to the DPZCYNO space. We used the D99 template to DPZCYNO warp files to transform the D99 atlas parcellation into the DPZCYNO space. Finally, we used the INIA19 template to DPZCYNO warp files to transform the INIA19-NeuroMaps white matter parcellation into the DPZCYNO space.

### 3.3 RESULTS

#### 3.3.1 MULTI-CONTRAST DPZCYNO TEMPLATES

We have constructed symmetric and asymmetric multi-contrast MRI templates in the stereotaxic orientation (Figure 3.2) for the cynomolgus macaque brain. The multiple MRI contrasts consisted of both structural ( $T_1w$ ,  $T_2w$ , ME-GRE, and MTw), as well as parametric (QSM,  $R_2^*$ , MTsat, and  $T_{1app}$ ) templates (Figure 3.3). The symmetric and asymmetric DPZCYNO templates provided a clear visualization of cortical, subcortical, and white matter structures. The CNR results for all the symmetric and asymmetric templates are listed in Supplementary Table A.1 and Supplementary Table A.2, respectively. The symmetric  $T_1w$  template provided an excellent cortical gray-to-white matter contrast (CNR = 3.1). In contrast, mGRE, QSM, and  $R_2^*$  templates provided an excellent contrast from subcortical gray matter structures. In comparison to the symmetric  $T_1w$  template, the symmetric QSM template substantially enhanced visibility of subcortical structures such as the superior colliculus, thalamus, substantia nigra, caudate, putamen, external and internal segments of the globus pallidus, optic tract, internal capsule, and the dentate nucleus (Figure 3.4). However, the  $T_1w$  template had the highest cortical gray matter and white matter contrast, while the mGRE, QSM, and  $R_2^*$  templates had the lowest. The MTw,  $T_2w$ , MTsat, and  $T_{1app}$  templates provided an outstanding gray-white matter tissue contrast in the brain.

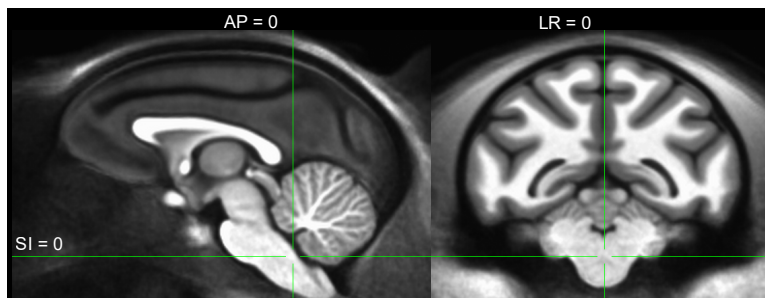


**Figure 3.2:** The stereotaxic orientation and coordinate space of the symmetric and asymmetric DPZCYNO templates. Stereotaxic orientation was determined by the unbiased template construction with a rigid alignment of scans to the symmetric NMT v2 rhesus macaque template. The DPZCYNO template orientation is similar to the Horsley-Clarke stereotaxic apparatus, which will provide a useful guide for neurosurgical planning in the cynomolgus macaque. Abbreviations: AP = Anterior-Posterior axis, SI = Superior-Inferior axis, LR = Left-Right axis.



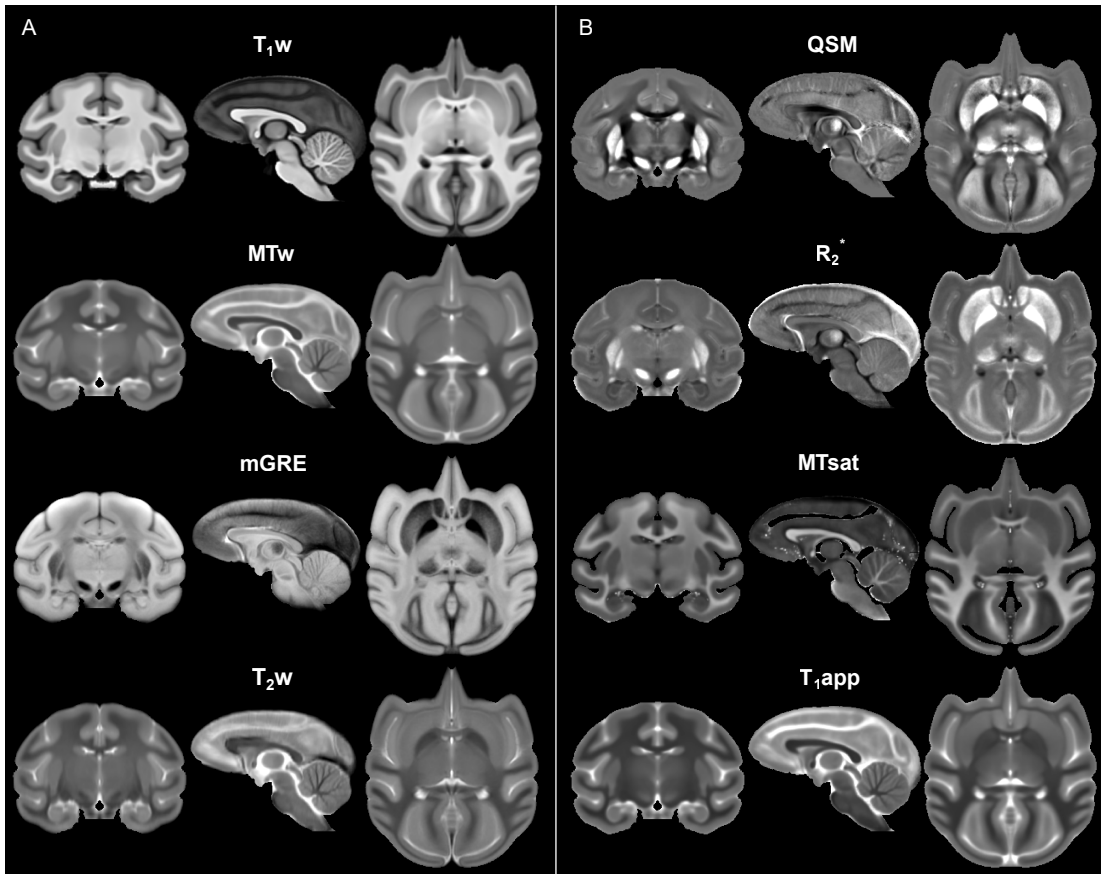


**Figure 3.3:** The symmetric multi-contrast MRI templates for cynomolgus macaque monkey brain. A) Native MRI contrast templates include  $T_{1w}$ , MTw, mean GRE (mGRE), and  $T_{2w}$  templates. B) Quantitative contrast templates include QSM,  $R_2^*$ , MTsat, and  $T_{1app}$ . The  $T_{1w}$  template gives great cortical gray-to-white matter contrast, whereas the mGRE, QSM, and  $R_2^*$  contrasts are rich in contrast from the deep subcortical structures.

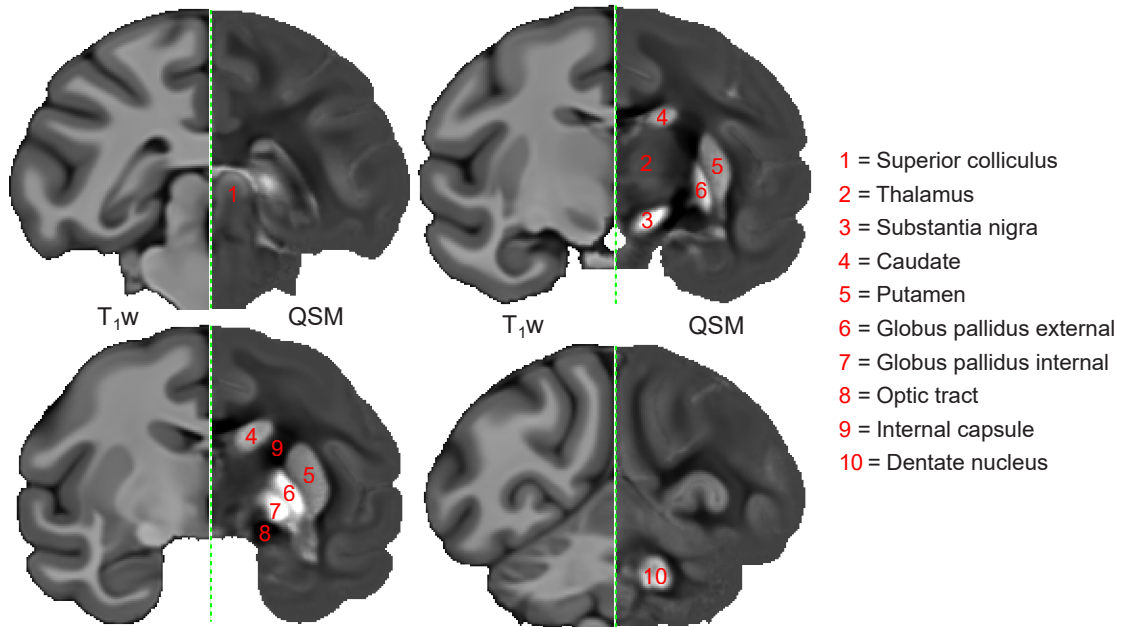


**Figure 3.4:** The symmetric  $T_1w$  template (left) coronal images are compared to the symmetric QSM template (right).  $T_1w$  template shows an excellent gray-white matter contrast, whereas the QSM contrast shows a unique and rich contrast from subcortical structures. The highlighted areas on the QSM template include the superior colliculus, thalamus, substantia nigra, caudate, putamen, external and internal segments of the globus pallidus, optic tract, internal capsule, and the dentate nucleus.

### 3.3.2 MEAN DISPLACEMENT MAP

The average deformations between a single subject  $T_1w$  image and the asymmetric  $T_1w$  template are shown in the mean displacement map. Significant deformations were seen in the frontal and occipital portions of the brain, as shown by the representation of the mean displacement map on the asymmetric DPZCYNO template surfaces (Figure 3.5). The frontal and occipital areas are well-known for their extreme variability. The mean displacement map's mean was 0.31 mm, which was smaller than the structural voxel dimension (0.5 mm).

### 3.3.3 SILiCON

The LDA accuracy score for the chosen SILiCON image was 0.93. The SILiCON image had weight combinations of 0.69, 0.52, -0.46, -0.46, -0.11, and 0.36 for the  $T_1w$ ,  $T_2w$ , MTw, QSM,  $R_2^*$ , and MTsat templates, respectively. The CNR value for gray matter and white

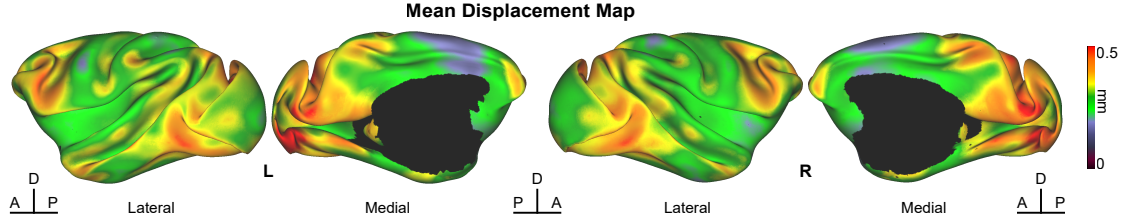


**Figure 3.5:** Mean displacement map (average deformation between each subject and the asymmetric DPZCYNO template). The average deformation at each voxel is the mean absolute value of all subject's average diffeomorphic warp fields from the subject's native space to the asymmetric DPZCYNO template space. Lateral and medial views of the mean displacement map on the mid-cortical surface are shown for the 14 scans used for the asymmetric template construction. Deformation was most significant in some parts of the frontal and occipital areas. We observed the mean displacement map's average (mean MDM = 0.31 mm) to be less than the dimension of a structural voxel (0.5 mm). Abbreviations: L - left, R - right, A - anterior, P - posterior, and D - dorsal.

matter in the SILiCON image was 3.3, 2.9 for subcortical gray matter and white matter, and 0.4 for gray matter and subcortical gray matter.

As demonstrated in Figure 3.6, the SILiCON image displayed outstanding contrast in both cortical and subcortical areas.

### 3.3.4 TISSUE SEGMENTATION

A three-tissue segmentation algorithm resulted in CSF, gray matter, and white matter segmentation masks with their probabilistic maps. Segmentation masks were created with a 50 % probability. The symmetric  $T_1w$  segmentation resulted in a clear separation of CSF from gray-to-white matter tissue (Figure 3.6). However, of the subcortical structures, only the caudate and putamen were included in the derived gray matter mask. The remaining subcortical areas were incorrectly classified in the white matter segmentation mask (Figure 3.6).

When compared to the symmetric  $T_1w$  segmentation, the symmetric SILiCON based gray-white matter segmentation resulted in improved gray-white matter segmentation (Figure 3.6). The majority of subcortical structures were part of the SILiCON derived gray matter segmentation mask.

### 3.3.5 MORPHOMETRY

The anterior-posterior dimension of the symmetric DPZCYNO  $T_1w$  template brain is 62.75 mm, the medial-lateral dimension is 50.25 mm (both left and right hemispheres combined), and the dorsal-ventral dimension is 38.50 mm. The brain mask's total intracranial volume is 64.70 cc, including the cerebellum and pons.

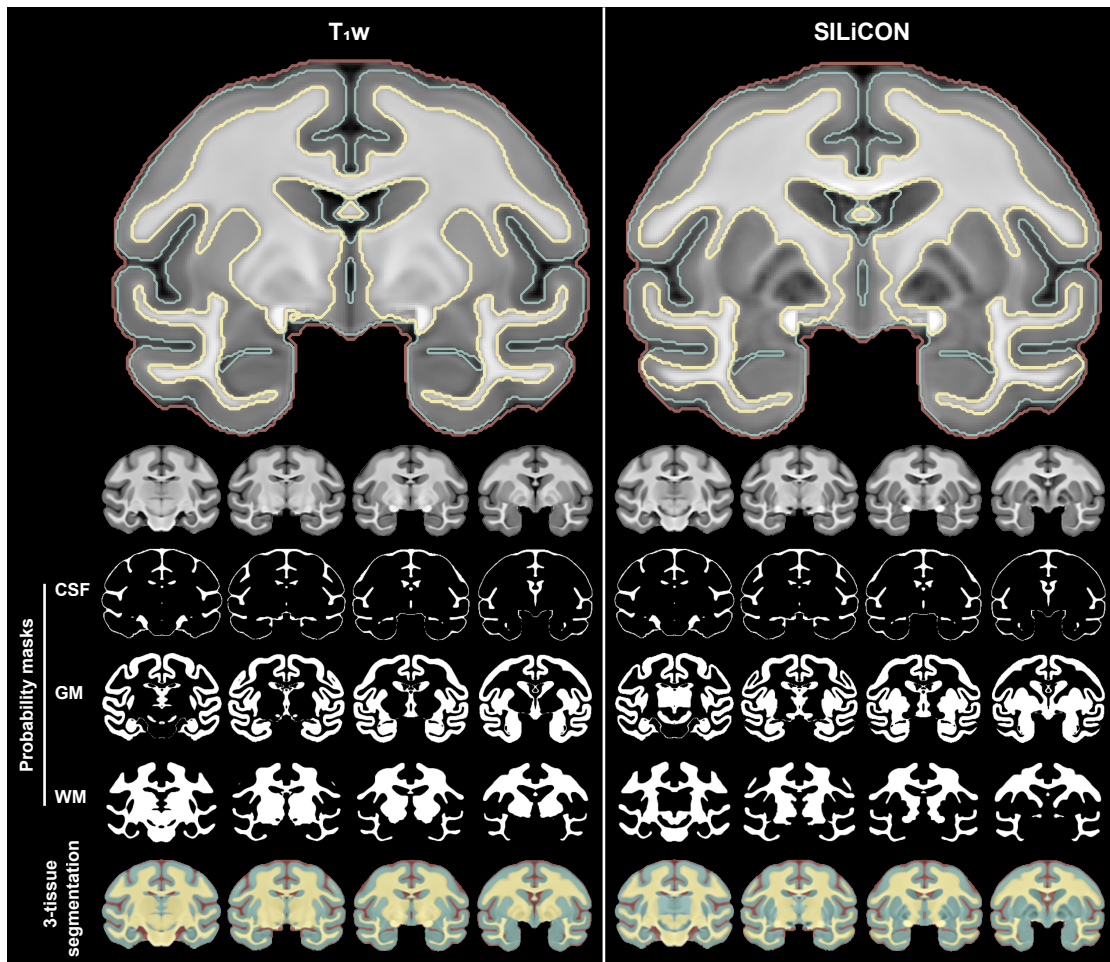


**Figure 3.6:** The symmetric  $T_1w$  template and symmetric SILiCON image brain tissue segmentation results. The automatic three-class tissue segmentation results in CSF, gray matter, white matter probability masks, and a three-tissue segmentation image. The symmetric  $T_1w$  segmentation misclassifies most of the subcortical structures as a part of the white matter. In contrast, symmetric SILiCON segmentation showed an improved delineation of gray matter and white matter. As a result, the majority of subcortical structures were classified as gray matter rather than white matter. Abbreviations: CSF - cerebrospinal fluid, GM - gray matter, and WM - white matter.

The symmetric  $T_1w$  template-based 3-tissue segmentation classified the total intracranial volume into a CSF volume of 11.5 cc, a gray matter volume of 31.5 cc, and a white matter volume of 21.7 cc. The segmented white matter and gray matter volumes were over- and under-estimated. The use of symmetric SILiCON image for gray-white matter segmentation improved these over- and under-estimated volumes, as shown in Figures 3.6 and 3.7. The symmetric SILiCON image-based segmentation categorized the total gray-white matter volume

into a gray matter volume of 31.8 cc, and a white matter volume of 21.4 cc. The cortical gray matter mask was 27 cc in volume.

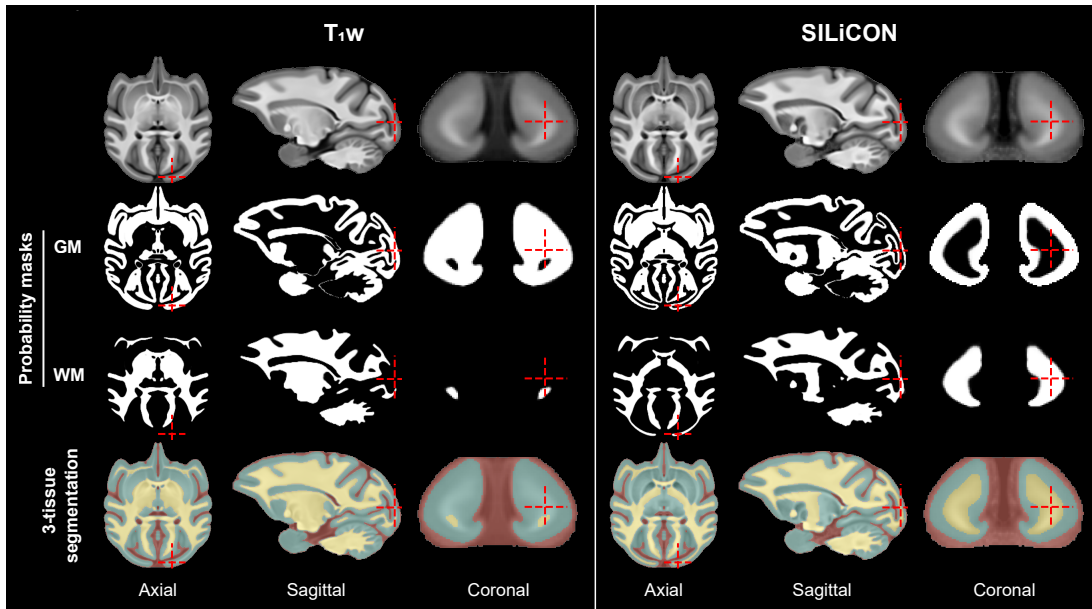


**Figure 3.7:** The symmetric  $T_1w$  template and symmetric SILiCON image segmentation results. The symmetric  $T_1w$  segmentation misclassifies some gray-to-white matter structures (highlighted structure in the visual cortex). Symmetric SILiCON segmentation, on the other hand, improved the delineation of cortical gray/white matter. Abbreviations: GM - gray matter, and WM - white matter.

### 3.3.6 SURFACES

We provide white matter, mid-cortical, and gray matter surfaces of the symmetric and asymmetric DPZCYNO templates (Figure 3.8). The white matter surface represents the interface between gray-to-white matter. The gray matter surface or pial surface represents the interface between gray matter and CSF. And the final mid-cortical surface represents the mid-distance between the white matter and pial surface boundary. The mid-cortical surface is the most commonly used surface to visualize statistical parametric maps.

We provide essential tissue masks to generate surfaces for a single cynomolgus macaque  $T_1w$  scan using *precon\_all*. All the generated symmetric and asymmetric DPZCYNO template surfaces are saved in the GIFTI format. They are compatible with the FreeSurfer volume viewer (*freeview*) and the Connectome Workbench viewer (*wb\_view*) [Marcus et al., 2011, Fischl, 2012].

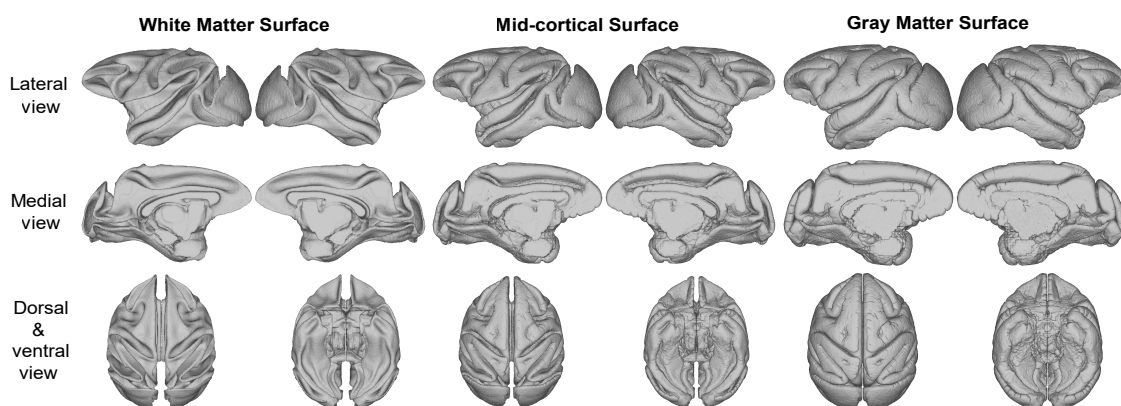


**Figure 3.8:** The symmetric DPZCYNO cortical surfaces. The symmetric DPZCYNO surfaces of white matter, mid-cortical, and gray matter in lateral, medial, dorsal, and ventral views. The white matter surface is based on the boundary between gray matter and white matter, and the gray matter surface or pial surface is based on the border between gray matter and CSF. The mid-cortical surface represents the surface that is mid-distance between white matter and pial.

### 3.3.7 CORTICAL THICKNESS AND CORTICAL MYELIN MAPPING

The cortical thickness was estimated using the symmetric DPZCYNO  $T_1w$  template, as shown in Figure 3.9. In both hemispheres, the average cortical thickness was the same (1.944 mm). The thickest ( $\sim 3-4$  mm) portions of the cortex were found to be the medial prefrontal cortex (area 9), anterior cingulate cortex (area 24), and motor cortex.

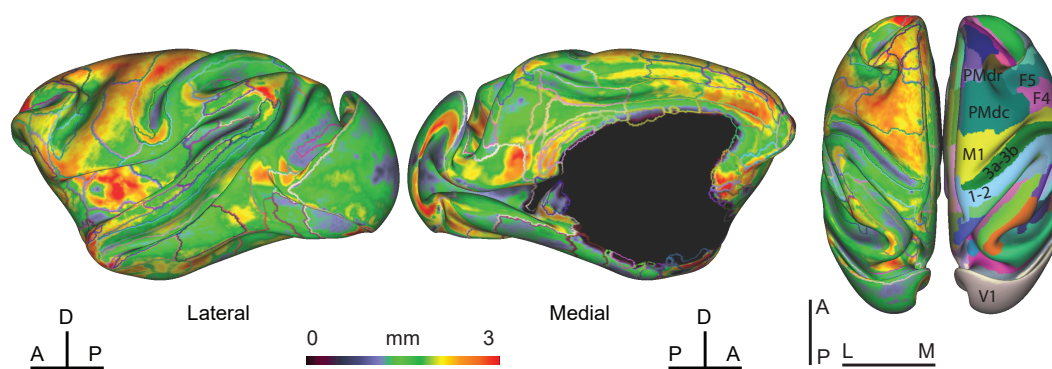


**Figure 3.9:** The symmetric DPZCYNO cortical thickness map on the very inflated mid-cortical surfaces in lateral, medial, and dorsal views. The highest cortical thickness values were observed in the prefrontal cortex compared to the caudal areas. The cortical thickness values in the sulci were lower than in the gyri. Abbreviations: PMdr - rostral dorsal premotor cortex, PMdc - caudal dorsal premotor cortex, M1 - primary motor cortex, F5 - area F5 of the ventral premotor cortex, and F4 - area F4 of the ventral premotor cortex. Abbreviations: A - anterior, P - posterior, D - dorsal, L - lateral, and M - medial.

The cortex's somatosensory, visual, and auditory areas were among the thinnest ( $\sim 1-2$  mm). The sulci had a thinner cortical thickness than the gyri. The DPZCYNO's cortical thickness characteristics matched those of rhesus macaques in previous studies [Lepage et al., 2021, Seidlitz et al., 2018, Wagstyl et al., 2015].

We used four myelin mapping methods, including the  $T_{1w}/T_{2w}$  ratio, MTsat, apparent longitudinal relaxation rate ( $R_{1app}$ , the inverse of the  $T_{1app}$ ), and  $R_2^*$ . To varying degrees, all of these parametric contrasts are sensitive to various biophysical properties of myelin. The  $T_{1w}/T_{2w}$  ratio (Figure 3.10) showed higher values in the primary visual cortex, motor cortex, and somatosensory cortex compared to the other areas of the brain. Similarly, MTsat maps also showed higher values in the motor and sensory cortex and the areas of the posterior parietal cortex.  $R_{1app}$  maps showed higher values in the motor and sensory cortex, primary visual cortex, and intraparietal area.  $R_2^*$  only showed higher values in the primary visual cortex compared to the rest of the brain.



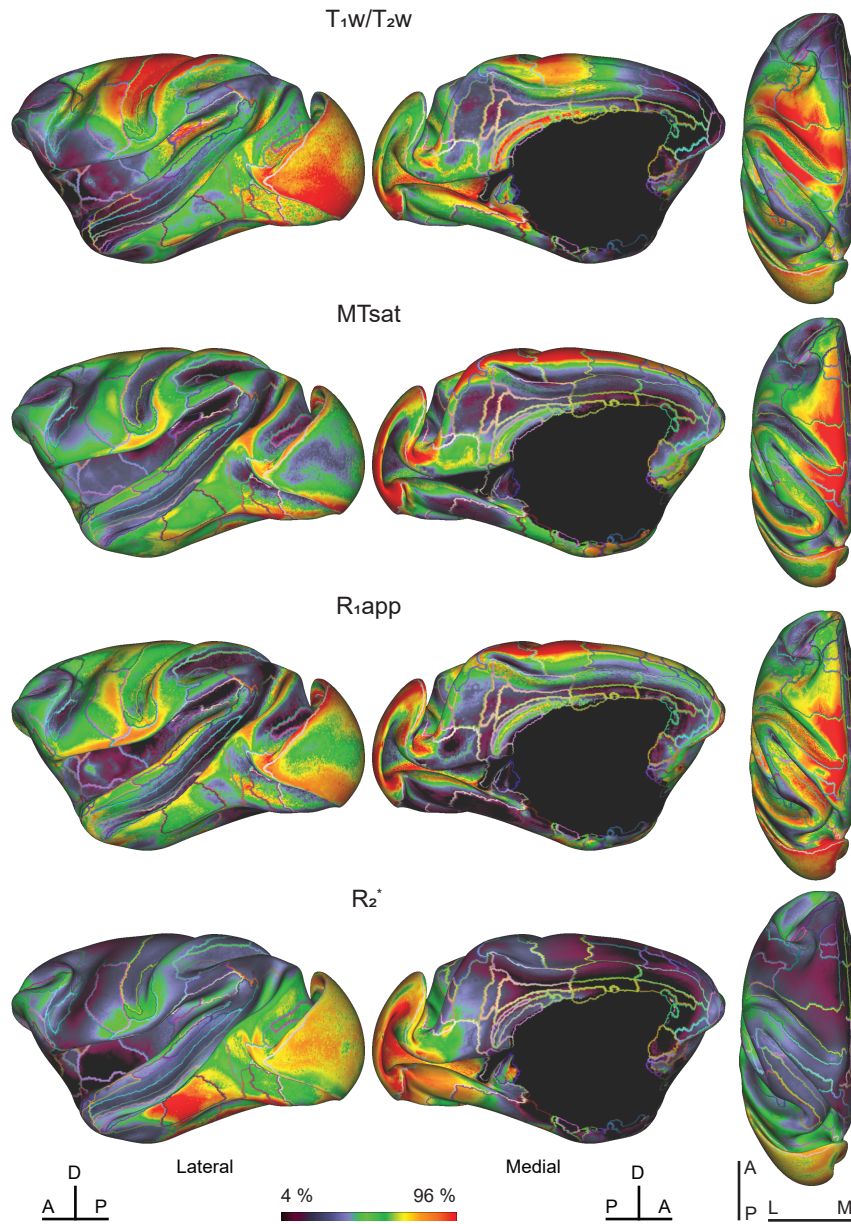


**Figure 3.10:** Surface maps illustrating several approaches that show sensitivity to cortical myelination. Cortical myelin maps are shown on the very inflated mid-cortical surfaces to reveal underlying myelin patterns.  $T_1w/T_2w$ ,  $MT_{sat}$ , and  $R_{1app}$  maps displayed highly myelinated motor and sensory cortical areas. The myelination in the primary visual cortex was captured more by  $T_1w/T_2w$  ratio and  $R_2^*$  maps than  $MT_{sat}$  and  $R_{1app}$  maps. Abbreviations: A - anterior, P - posterior, D - dorsal, L - lateral, and M - medial.



### 3.3.8 REGIONAL PARCELLATION OF THE DPZCYNO

The NMT v2 template was used to propagate CHARM and SARM hierarchical parcellations into the DPZCYNO template space. D99 and NeuroMaps labels were also propagated into the DPZCYNO template space from the D99 and INIA19 templates, respectively. After manually fixing some of the imperfections, the CHARM, SARM, D99, and NeuroMaps labels accurately represented the respective anatomical structure, as shown in Figure 3.11. We provide volumetric transformations to and from the NMT v2, D99, and INIA19 templates with the DPZCYNO template package to facilitate seamless integration with the rhesus macaque atlas work.

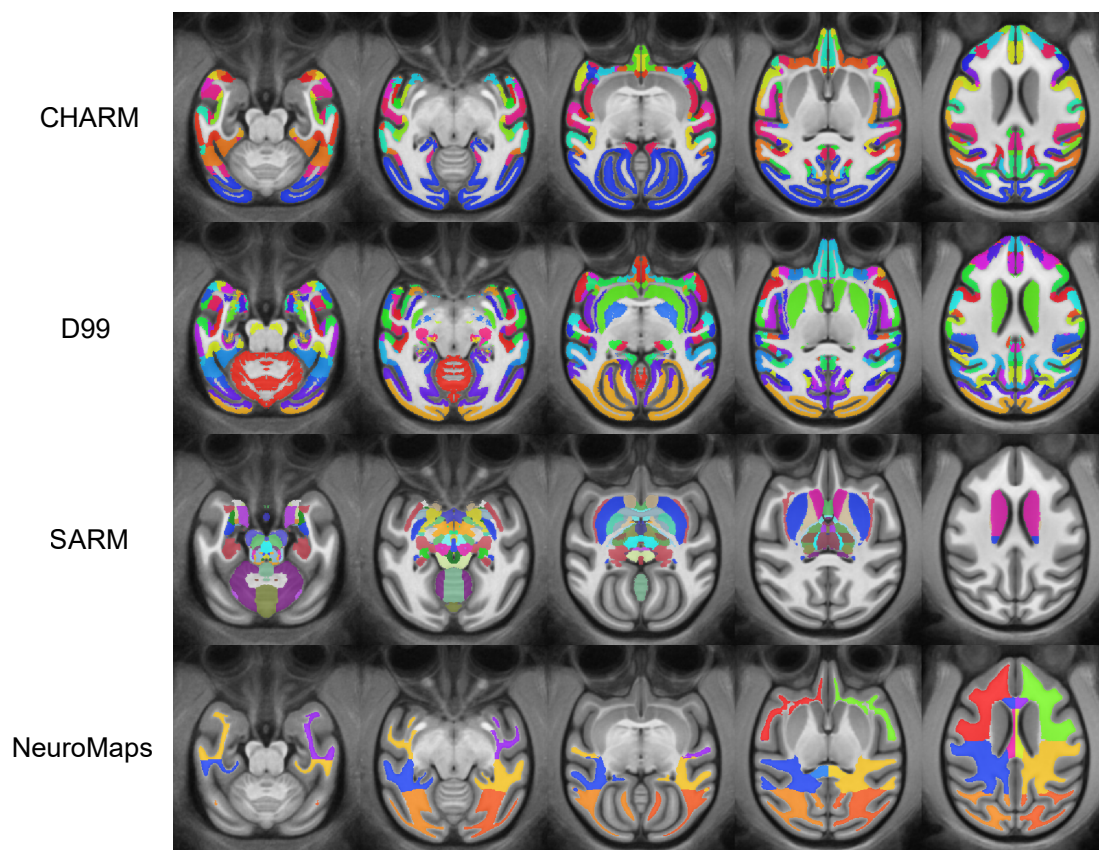


**Figure 3.11:** The Cortical Hierarchy Atlas of the Rhesus Macaque (CHARM), D99, Subcortical Atlas of the Rhesus Macaque (SARM), and NeuroMaps white matter ROI labels. The CHARM and SARM parcellations were produced using the CHARM and SARM level 6 ROI labels.

### 3.4 DISCUSSION

The DPZCYNO is a high-resolution multi-contrast MRI template space for cynomolgus macaque neuroimaging studies, complete with templates, masks, segmentation, and surfaces. The DPZCYNO templates provide high-resolution symmetric and asymmetric targets for the alignment of cynomolgus macaque MRI scans to a standardized stereotaxic space. Moreover, the DPZCYNO T<sub>1</sub>w template, as well as binary hemispheric and tissue masks, will serve as a standard template for surface generation. Finally, we provide cortical, subcortical, and white matter parcellations, enabling ROI-based structural and functional connectivity analyses.

In this study, we present multi-contrast MRI templates for the macaque monkey brain. The presented templates included both the structural (T<sub>1</sub>w, T<sub>2</sub>w, MTw, and ME-GRE) and parametric contrasts (QSM, R<sub>2</sub><sup>\*</sup>, MTsat, and T<sub>1</sub>app). The availability of high-resolution structural and parametric contrasts at 0.25 mm spatial resolution made it feasible to resolve cortical gray/white matter, as well as many hidden deep subcortical structures with fine details (Figure 3.3 and 3.4).

The DPZCYNO T<sub>1</sub>w template’s anatomical details are comparable to the available high-resolution rhesus macaque template [Jung et al., 2021]. However, the global intracranial brain volume of rhesus and cynomolgus macaques differs significantly. The intracranial brain volume measured in the cynomolgus macaque (64.70 cc) is smaller than the rhesus macaque (91.76 cc) [Jung et al., 2021]. It was previously demonstrated that cynomolgus and rhesus macaques have different endocranial volumes, inferior frontal cortex shapes, and sulcal patterns [Frey et al., 2011, Gucht et al., 2006, Kirk, 2006, McLaren et al., 2009]. Similar to prior findings, our current work on determining the log Jacobian determinant values between cynomolgus and rhesus macaque T<sub>1</sub>w brain templates also discovered morphometric discrepancies between both macaque species (Supplementary Figure A.8). Hence, a specialized high-resolution template for the brain of the cynomolgus macaque will allow for more reproducible scientific outcomes in a variety of disciplines, from electrophysiology to structural and functional MRI.

Most available macaque templates are based on a single MRI contrast, often/typically one of T<sub>1</sub>w, T<sub>2</sub>w, and diffusion-weighted [Calabrese et al., 2015, Essen & Dierker, 2007, Frey et al., 2011, Liu et al., 2020b, McLaren et al., 2009, Reveley et al., 2017, Rohlfing et al., 2012, Rushmore et al., 2020, Saleem & Logothetis, 2012, Seidlitz et al., 2018, Shi et al., 2017, Weiss et al., 2020]. Because of their high gray-white matter contrast, T<sub>1</sub>w and T<sub>2</sub>w images are commonly utilized as templates. However, their utility in anatomical structural delineation and tissue parcellation is limited because of the weak contrast from subcortical regions. Additional MRI contrasts, such as T<sub>2</sub><sup>\*</sup> and QSM, have been found to be helpful in human neuroimaging studies for generating subcortical contrast [Bazin et al., 2020, Alke-

made et al., 2017, Xiao et al., 2015]. QSM measures the spatial distribution of magnetic susceptibility in tissue [Haacke et al., 2004, Haacke et al., 2005, Langkammer et al., 2012]. The presence of iron in the brain’s subcortical regions contributes to the enhanced QSM contrast, similar to  $R_2^*$ . This effect helps delineate subcortical brain regions such as the internal and external globus pallidus, substantia nigra, red nucleus, and thalamus. Quantitative contrasts such as MT saturation index (MTsat) and apparent  $T_1$  ( $T_{1app}$ ) are sensitive to the concentration of myelin in the white matter tissue. The MTsat and  $T_{1app}$  contrasts provide excellent gray-white matter contrast originating from sources such as myelin, which dominates MT exchange [Helms et al., 2008].

Consistent with previous research,  $T_{1w}/T_{2w}$  ratio was highest in extensively myelinated areas of the brain, such as the sensory-motor, visual, and auditory cortex [Burt et al., 2018, Glasser & Essen, 2011, Shams et al., 2019]. MTsat and  $R_{1app}$  maps, which are also known to be sensitive to cortical myelination [Hagiwara et al., 2018, McColgan et al., 2021, Shams et al., 2019], exhibited similar patterns to  $T_{1w}/T_{2w}$  ratio.  $R_2^*$  maps exhibited increased values specifically in the visual cortex. The amount of iron and myelin in the visual cortex has been demonstrated to affect  $R_2^*$  [Edwards et al., 2018, McColgan et al., 2021].  $T_{1w}/T_{2w}$  ratio, MTsat,  $R_{1app}$ , and  $R_2^*$  all showed different levels of sensitivity to cortical myelination. These techniques indirectly evaluate myelin and are sensitive to a variety of biophysical and microstructural tissue properties [Lazari & Lipp, 2021, Möller et al., 2019, Does, 2018].

Multiple MRI structural and parametric contrast templates in the same orientation space provide numerous opportunities for improving tissue segmentation and anatomical structural parcellation. The DPZCYNO multi-contrast templates might help in the creation of more precise parcellations as well as the improvement of existing parcellations. Another use of the DPZCYNO multi-contrast templates is to generate a unique image capturing information from all forms of tissue contrast. The linearly-weighted fusion of multi-contrast DPZCYNO templates yields a synthetic contrast that is rich in every tissue contrast, ranging from cortical gray matter to white matter, as well as subcortical structures. The SILiCON image enhanced the subcortical contrast while preserving the  $T_{1w}$ -like gray-white matter contrast. The SILiCON segmentation results substantially enhanced the gray-white matter segmentation results as compared to  $T_{1w}$  (Figure 3.6). We believe improved segmentation and tissue probability masks in the standard template space will be essential for single macaque scan segmentation and parcellation. We may also use the multi-contrast fusion approach for other forms of MRI contrast. The idea of combining multiple MRI contrasts with random weighting may be further developed by putting more informed constraints on the generated weights.

A limitation of our study was that it only included a relatively small number of subjects. All of them were females. Gender differences may lead to an underestimation of brain tissue volumes, as studies in rhesus macaques have shown that females have a smaller brain volume compared to males [Franklin et al., 2000]. In this study, a single loop circular coil was used to

acquire the MRI data, which has some inherent issues such as full brain coverage and a low signal-to-noise ratio. A multi-channel receive coil could have been a great asset to enhance SNR and contrast between tissue classes. Another drawback is the age gap between the subject cohorts, with five individuals being young and nine being old.

In conclusion, we believe the multi-contrast DPZCYNO templates, accompanying segmentation masks, and surface maps can be used in various neuroimaging applications in non-human primates. The DPZCYNO templates will allow neuroscientists across labs to better reproduce findings from electrophysiological and MRI studies in cynomolgus macaques. Finally, the availability of MRI templates from different MRI contrasts such as  $T_{1w}$ ,  $T_{2w}$ , GRE, QSM,  $R_2^*$ , MTsat, and  $T_{1app}$  would benefit the macaque neuroimaging community by providing complementary information about all brain tissues.

*You make different colors by combining those colors that already exist.*

Herbie Hancock

# 4

## Fusion of quantitative susceptibility maps and $T_1$ -weighted images improve brain tissue contrast in primates

### AUTHORS

**Rakshit Dadarwal**<sup>1,2</sup>, Michael Ortiz-Rios<sup>1</sup> and Susann Boretius<sup>1,2</sup>

1. Functional Imaging Laboratory, German Primate Center – Leibniz Institute for Primate Research, Göttingen, Germany
2. Georg-August University of Göttingen, Göttingen, Germany

### ABSTRACT

Recent progress in quantitative susceptibility mapping (QSM) has enabled the accurate delineation of submillimeter scale subcortical brain structures in humans. QSM reflects the magnetic susceptibility arising from the spatial distribution of iron, myelin, and calcium in the brain. However, the simultaneous visualization of cortical, subcortical, and white matter structure remains challenging, utilizing QSM data solely. Here we present TQ-SILiCON, a fusion method that enhances the contrast of cortical and subcortical structures and provides

an excellent white matter delineation by combining QSM and conventional  $T_1$ -weighted ( $T_1w$ ) images. In this study, we first established QSM in the macaque monkey to map iron-rich subcortical structures. Implementing the same QSM acquisition and analyses methods allowed a similar accurate delineation of subcortical structures in humans. Moreover, applying automatic brain tissue segmentation to TQ-SILiCON images of the macaque improved the classification of the brain tissue types as compared to the single  $T_1w$  contrast. Furthermore, we validate our dual-contrast fusion approach in humans and similarly demonstrate improvements in automated segmentation of cortical and subcortical structures. We believe the proposed contrast will facilitate translational studies in non-human primates to investigate the pathophysiology of neurodegenerative diseases that affect the subcortical structures of the basal ganglia in humans.

The work described in this chapter resulted in the following output:

**Rakshit Dadarwal** and Susann Boretius. *"Merging  $T_1$ -weighted images with QSM provides a unique contrast for brain tissue segmentation in humans and non human primates"*, In: Proceedings of the 29th Annual Meeting of the International Society for Magnetic Resonance in Medicine (ISMRM), (Virtual) (2021).

**Dadarwal, R.**, Ortiz-Rios, M., Boretius, S., 2021. *"Fusion of quantitative susceptibility maps and  $T_1$ -weighted images improve brain tissue contrast in primates"*. <https://doi.org/10.1101/2021.10.05.462876> ([link to the article](#)).

#### 4.1 INTRODUCTION

Precise delineation of brain structures plays a crucial role in neuroscience and medical imaging. Segmentation of brain structures is crucial for surgical planning and image-guided intervention and for the follow-up monitoring of brain changes in health and disease. In particular, quantitative analyses of tissue morphology and clinical diagnosis strongly rely on the precise segmentation of cortical and subcortical structures. For example, during interventional applications in primates, precise targeting of subcortical structures is critical for the delivery of pharmacological and optogenetic agents into deep brain nuclei and is aided by cortical brain tissue segmentation during MRI-guided interventions.

In both humans and non-human primates (NHPs),  $T_1$ -weighted images ( $T_1w$ ) are widely used for the anatomical visualization of brain tissue structures.  $T_1w$  provides excellent contrast for the segmentation of brain tissue classes such as gray matter, white matter, and cerebrospinal fluid. To better segment brain tissue, it is common to apply automatic volumetric

and surface-based algorithms to the anatomical  $T_1w$  datasets [Postelnicu et al., 2009]. However, automated segmentation algorithms underperform in NHPs on  $T_1w$  images, mainly due to inhomogeneities arising from the use of surface coils. Furthermore, on  $T_1w$ , subcortical structures appear very similar to white matter, hampering a correct segmentation. As a result, when using  $T_1w$ , automatic tissue segmentation algorithms may misclassify subcortical deep gray matter nuclei as part of white matter tissue in humans and NHPs.

In contrast to  $T_1w$ , Quantitative Susceptibility Mapping (QSM) provides vibrant contrast in subcortical deep gray matter nuclei, particularly within basal ganglia due to the high iron abundance within these structures [Langkammer et al., 2012, Ramos et al., 2014]. QSM is a rapidly evolving technique that uses gradient-recalled echo phase images to quantify the spatial distribution of magnetic susceptibility [Haacke et al., 2004, Haacke et al., 2005]. QSM contrast arises from the magnetic components in the tissue, such as iron, myelin, and calcium. The presence of myelin in the white matter results in diamagnetic susceptibility [Langkammer et al., 2012]. In contrast, the presence of tissue iron in the form of ferritin macromolecules is the predominant contributor to the paramagnetic susceptibility of gray matter, including the cortex and subcortical structures. Significant progress in the post-processing of QSM data has enabled the accurate identification of small subcortical structures in humans [Guan et al., 2019, Schenck & Zimmerman, 2004]. In particular, changes in the QSM maps in the basal ganglia have emerged as a potential biomarker for Parkinson’s disease and other neurodegenerative diseases [Guan et al., 2019, Schenck & Zimmerman, 2004, Shahmaei et al., 2019]. However, our current understanding of the underlying sources that might give rise to contrast changes within basal ganglia and cortex remains elusive.

In this context, comparative neuroimaging in NHPs may be of particular value. NHPs offer similar brain organization as that of humans, and established knowledge exists about the anatomical and functional organization of the cortico-striatal-thalamic circuitry, much of which had been gained from immunohistochemistry [Hadaczek et al., 2016], pharmacological [Baron et al., 2002], neurophysiological and microsimulation [Nambu et al., 2015] techniques. Despite the gain in knowledge, the translation gap between non-invasive NHP research and human neuroimaging remains large. As an example, while QSM has been widely utilized in several human neuroimaging studies [Blezer et al., 2007, Haacke et al., 2009a, Langkammer et al., 2016, Ravanfar et al., 2021, Shmueli et al., 2009], QSM has not been adopted as rapidly in the NHPs neuroimaging community [Dadarwal et al., 2019, Dadarwal et al., 2021, Dadarwal & Boretius, 2021b, Yoshida et al., 2021].

Given the rich contrast in subcortical structures arising from high-resolution QSM and the gray-white contrasts available in  $T_1w$  images, we aimed to develop a method for improving the visualization and segmentation of cortical and subcortical gray matter structures using the information provided by both  $T_1w$  and QSM contrast. Toward this end, we derive a fusion image by merging  $T_1w$  and QSM images using a linearly-weighted fusion algorithm which

we term  $T_1w$ -QSM Synthetic Images via a Linearly-weighted combination of CONtrasts (TQ-SILiCON).

Our method has the potential to improve the MRI-guided estimation of deep brain stimulation sites in NHPs. Additionally, we tested our approach in healthy humans, demonstrating the potential of our dual-contrast acquisition and segmentation algorithm for applications across both primate species.

## 4.2 MATERIALS AND METHODS

### 4.2.1 ANIMALS AND HUMAN VOLUNTEERS

In the present study, four healthy long-tailed female cynomolgus macaques (*Macaca fascicularis*) and three male human adults were used to obtain all neuroimaging data. The four adult macaques were between the ages of 7.7 - 8.7 years old (weighing between 3.9 and 6 kg). The three human adults were between the ages of 25 and 30 years. Measurements on human volunteers were performed after written informed consent. The protocol was reviewed by the ethics committee of the Georg-August-University of Göttingen.

### 4.2.2 ANIMAL EXPERIMENTS

All monkeys were purpose-bred, raised, and housed according to the standards for macaques of the German Primate Center (Göttingen, Germany). All aspects of the study were conducted in accordance with national and international guidelines of the German Animal Protection Law and the European Union Directive 2010/63/EU for the Protection of Animals used for Scientific Purposes. The study was approved by the local authorities, the Animal Welfare Service, Lower Saxony State Office for Consumer Protection and Food Safety (license number 33.19-42502-04-16/2278).

In preparation for anesthesia, the macaques were deprived of food overnight. Anesthesia was induced by a mixture of ketamine ( $8.05 \pm 2.65$  mg per kg body weight) and medetomidine ( $0.02 \pm 0.01$  mg per kg) and maintained by isoflurane (0.8 - 1.7 % in oxygen and ambient air) via endotracheal tube and pressure-controlled active ventilation. The monkeys were placed in a prone position, and their heads were fixed in an MR-compatible stereotactic apparatus (Kopf 1430 M, [kopfinstruments.com](http://kopfinstruments.com)).

### 4.2.3 MRI DATA ACQUISITION

All data were acquired with a 3 T MR system (MAGNETOM Prisma, Siemens Healthineers, Erlangen) equipped with a 7 cm single loop coil for macaque and a 20-channel head coil for human brain imaging. The imaging protocol included anatomical  $T_1w$  and multi-echo



gradient-recalled echo (ME-GRE) acquisitions. MR parameters for both macaques and humans are shown in Table 4.1.

Parameters	Macaque		Human	
	T <sub>1w</sub>	QSM	T <sub>1w</sub>	QSM
Pulse sequence	3D MPRAGE	3D ME-GRE	3D MPRAGE	3D ME-GRE
Native resolution (mm <sup>3</sup> )	0.5 × 0.5 × 0.5	0.31 × 0.31 × 0.31	0.8 × 0.8 × 0.8	0.75 × 0.75 × 0.75
Field of view (mm <sup>2</sup> )	108 × 128	97 × 120	300 × 320	195 × 240
Acquisition matrix	216 × 256	312 × 384	240 × 256	260 × 320
Number of averages	2	1	1	1
Total acquisition time (min)	14.3	24	6.3	7
TR/TE (ms)	2.7/2700	57/[3.7/4.9/48]	2.2/2400	41/[4.5/4.5/36]
Inversion time (ms)	850	–	1000	–
Flip angle (degree)	8	20	8	20
Pixel bandwidth (Hz/Px)	250	250	220	260

**Table 4.1:** Macaque and human T<sub>1w</sub> and QSM data acquisition parameters. Abbreviations: TR - repetition time; TE - echo time.

#### 4.2.4 DATA ANALYSES

T<sub>1w</sub> and ME-GRE images of both macaque and humans were converted from dicom to nifti format using the function *Dcm2nift* [Li et al., 2016]. ME-GRE magnitude images were pixel-wise averaged across echo times. T<sub>1w</sub> and mean ME-GRE magnitude images were denoised using ANTs *DenoiseImage* [Manjón et al., 2010]. The denoised volumes were then used to manually create brain masks using the ITK-SNAP segmentation tool [Yushkevich et al., 2006]. We followed a manual segmentation process due to the unavailability of sufficient automatic brain segmentation tools for the cynomolgus macaque brain. These brain masks were then used to correct T<sub>1w</sub> images from the bias fields using ANTs *N4BiasFieldCorrection* [Tustison et al., 2010]. The skull-stripped mean ME-GRE magnitude images were affinely registered to the subject T<sub>1w</sub> brain volume using the ANTs registration algorithm [Avants et al., 2008].

QSM maps of monkeys and humans were reconstructed using coil combined ME-GRE phase data. This QSM reconstruction included phase unwrapping using the best-path algorithm, background field removal using Laplacian boundary value and variable spherical mean

value filtering algorithms, and solving the inversion problem using the multiscale dipole inversion approach [Abdul-Rahman et al., 2007, Acosta-Cabrero et al., 2018, Zhou et al., 2014].

To create symmetric brain atlases for better comparison,  $T_1w$  and QSM images were duplicated and mirrored to the hemispheric plane. Using ANTs nonlinear registration [Avants et al., 2008], we constructed symmetric population-averaged  $T_1w$  atlases of macaque and humans by aligning all of the native and mirrored scans. The output deformation maps from subject mean ME-GRE magnitude to symmetric population-averaged  $T_1w$  atlas were then used to create symmetric population-averaged QSM atlases for both macaques and humans. A weighted linear combination was used to fuse symmetric population-averaged  $T_1w$  and QSM atlases. The weights ( $W$ ) for  $T_1w$  were generated at random between 0 and 1, while for QSM, between -1 and 0.  $T_1w$  signal intensities and QSM values ( $X$ ) were normalized to a range of 0 to 1 before entering it into the fusion equation,

$$Y_i = \sum_{c=1}^c W_c \cdot X_{ci} \quad (4.1)$$

The generated synthetic images ( $Y_i$ ) were evaluated for only unique contrasts by discarding images with poor contrast-to-noise ratio (CNR) between all tissue classes (e.g., CSF, cortical and subcortical gray matter, and white matter) and based on a linear discriminant analysis (LDA) accuracy score. The LDA model was trained with Scikit-learn [Pedregosa et al., 2011] to identify tissue classes that were manually selected on  $T_1w$  and QSM atlases by drawing respective regions-of-interest (ROIs) using the ITK-SNAP tool [Yushkevich et al., 2006]. These ROIs were also used to calculate the CNR between gray matter and white matter, subcortical gray matter and white matter, and gray matter and subcortical gray matter. The CNRs were estimated using the following formula:

$$CNR = \frac{\text{mean}(X_i) - \text{mean}(X_j)}{\text{standard deviation (CSF)}} \quad (4.2)$$

Class  $X_i$  refers to cortical gray matter and subcortical gray matter, while class  $X_j$  refers to white matter and subcortical gray matter tissue. These two classes were combined to make three possible pairs.

In order to automatically select the most promising image fusion (i.e., weights), CNRs and LDA accuracy score were used as follow: For the average macaque brain, the minimum threshold set for the CNR between gray matter and white matter was 3, while the threshold for the CNR between subcortical gray matter and white matter was 2. Moreover, to maintain the low contrast differences between the gray matter and subcortical gray matter, the

maximum CNR threshold was set to 0.5. The threshold for the LDA accuracy score was set to 0.90. The selected fusion image obtained the highest LDA accuracy score out of fifty iterations and met all of the CNR requirements.

To evaluate the potential of the created fusion image for automatic tissue segmentation, ANTs Atropos was applied on both single-subject  $T_1w$  images and TQ-SILiCON of macaques and humans. In the case of TQ-SILiCON, CSF was extracted beforehand, and a two-class segmentation (gray and white matter) was performed.

### 4.3 RESULTS

This work aimed to establish multi-contrast imaging based on  $T_1w$  and high-resolution QSM in NHPs. Below we describe our  $T_1w$  and QSM results for identifying specific tissue structures in the cortex and subcortical gray matter nuclei. From the  $T_1w$  and QSM images, we developed a fusion technique called TQ-SILiCON, enabling the improved automatic segmentation of white matter and cortical and subcortical gray matter. Importantly, we also evaluated our fusion strategy in humans and showed the potential of our approach for translational studies.

#### 4.3.1 ESTABLISHING QSM IN NHPs

$T_1w$  images of the macaque brain provided excellent gray-to-white matter contrast along the cortical surface. However, major subcortical deep gray matter nuclei remained challenging to delineate on  $T_1w$ . In subcortical structures,  $T_1w$  contrast largely delineated the caudate and putamen from the adjacent white matter, while the remaining deep gray matter nuclei – contrast-wise – were identical to the neighboring white matter (Figure 4.1A and B). In contrast, QSM substantially enhanced the visibility of subcortical deep gray matter nuclei from other parts of the macaque brain (Figure 4.1A). Enhanced contrast on the QSM map clearly delineated subcortical structures such as caudate, putamen, external and internal segments of globus pallidus, thalamus, substantia nigra, and red nucleus. Due to their paramagnetic contrast, all of these deep gray matter nuclei appeared bright on the QSM map compared to the surrounding dark appearing white matter areas with diamagnetic susceptibility contrast (Figure 4.1).

Interestingly, QSM contrast of the macaque thalamus highlighted different subnuclei such as pulvinar based on their varying susceptibility patterns (Figure 4.1B). Among all subcortical deep gray matter nuclei in the macaque brain, the globus pallidus had the highest QSM contrast, followed by the substantia nigra, caudate, putamen, red nucleus, and thalamus, reflecting a distinct amount of iron concentration. An important feature to highlight from the QSM contrast was the clear distinction of the internal and external segments of the

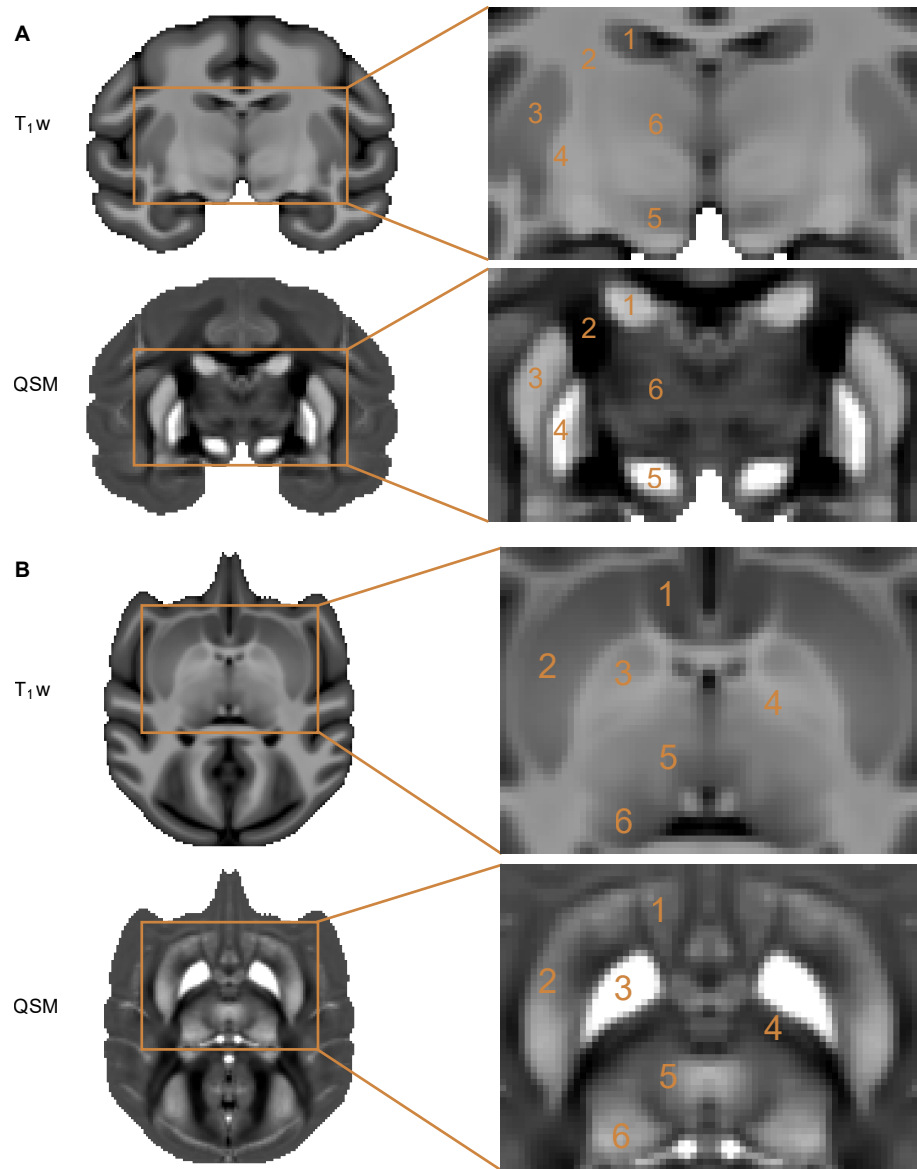


**Figure 4.1:** A. T<sub>1</sub>w and QSM coronal images of the macaque brain. T<sub>1</sub>w images provide excellent contrast between white and gray matter. However, a magnified visualization of subcortical structures reveals relatively low contrast. On the other hand, QSM coronal images provide a unique contrast in the subcortical structures but low contrast in the white and gray matter. The locations of iron-rich subcortical structures are indicated on the magnified visualization of T<sub>1</sub>w and QSM images: 1 - caudate, 2 - internal capsule, 3 - putamen, 4 - globus pallidus, 5 - substantia nigra, and 6 - thalamus. B. T<sub>1</sub>w and QSM axial images of the macaque brain. The marked areas on the magnified visualization of T<sub>1</sub>w and QSM images are 1 - accumbens, 2 - putamen, 3 - globus pallidus, 4 - internal capsule, 5 - thalamus, and 6 - pulvinar.

globus pallidus. Furthermore, QSM contrast allowed precise delineation of subcortical deep gray matter structures (Figure 4.2).

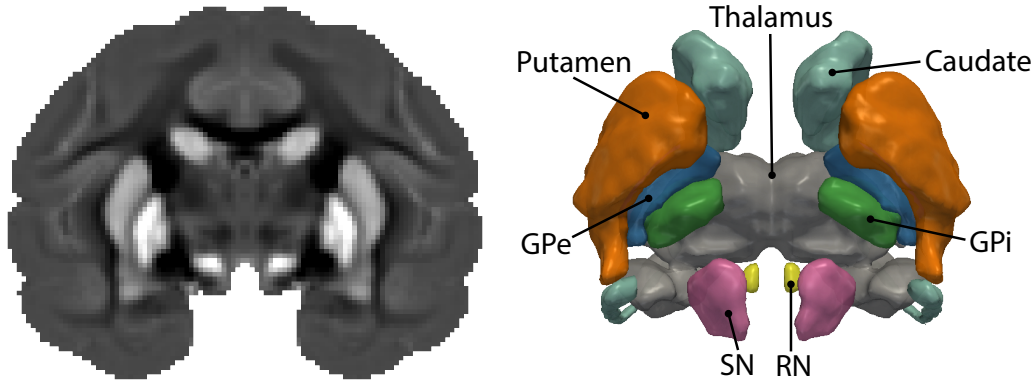


**Figure 4.2:** QSM coronal image of the macaque brain showing the iron-rich subcortical structures on a 3D rendering: putamen, caudate, globus pallidus external (GPe), globus pallidus internal (GPi), thalamus, substantia nigra (SN), and red nucleus (RN).

While the QSM map provided improved visualization of the iron-rich subcortical deep gray matter from the rest of the brain (Figure 4.2), QSM contrast lacked the high gray-white matter contrast as compared to  $T_1w$  along the cortical surface and in the deep brain areas such as those of the hippocampus. To circumvent the constraint of a single contrast, we pursued an analytical strategy that combines two MRI contrasts that are sensitive to different tissue substrates. Next, we demonstrate the linearly-weighted combination of  $T_1w$  and QSM images which provides some promising results applied to both NHPs and human neuroimaging data.

4.3.2 MERGING  $T_1w$  AND QSM PROVIDES A 3D DATA SET WITH ENOUGH OF CONTRAST FOR SEGMENTING SUBCORTICAL AND CORTICAL TISSUE IN NHPs

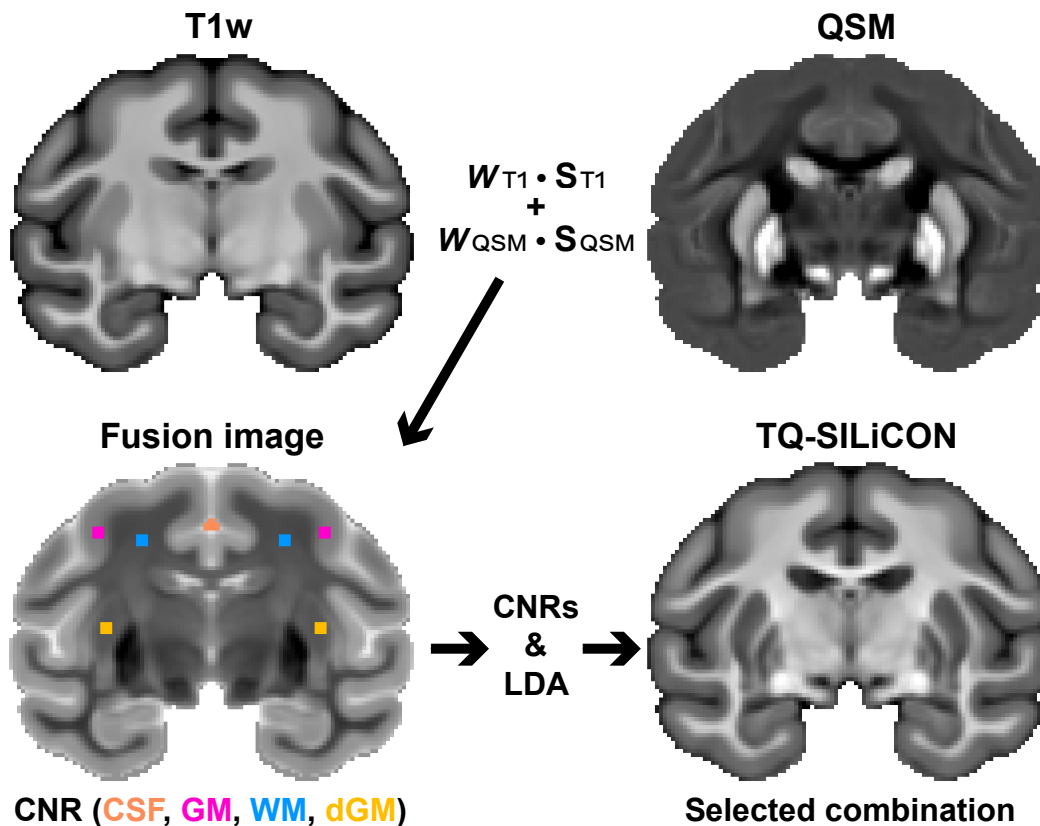


**Figure 4.3:** The TQ-SILiCON data analysis workflow.  $T_1w$  and QSM images were fused using a linearly-weighted combination.  $W_{T1}$  and  $W_{QSM}$  are randomly generated weights for the  $T_1w$  and QSM images, while  $S_{T1}$  and  $S_{QSM}$  are the normalized signal intensities of the  $T_1w$  and QSM images. The generated fused images were evaluated based on their contrast-to-noise ratio (CNR) and linear discriminant analysis (LDA) accuracy score between different tissue classes (CSF, GM, WM, and dGM). Abbreviations: CSF - cerebrospinal fluid, GM - gray matter, WM - white matter, and dGM - subcortical deep gray matter.

We devised a workflow for fusing  $T_1w$  and QSM images (Figure 4.3), which uses a linearly-weighted combination of the two image contrasts. The data-driven approach selected a fusion image with weight combinations of 0.83 and -0.87 for the  $T_1w$  and QSM images, respectively. The output TQ-SILiCON image had a CNR value of 3.3 between gray matter and white matter, 2.8 between subcortical gray matter and white matter, and 0.4 between gray matter and subcortical gray matter. In addition, for the average macaque brain, TQ-

SILiCON had the highest LDA accuracy score of 0.93.

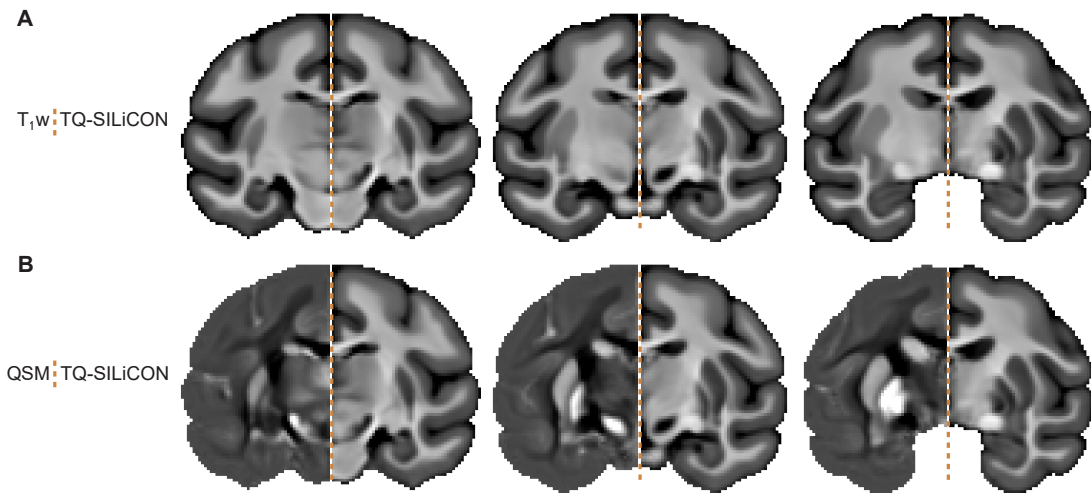


**Figure 4.4:** **A.** The TQ-SILiCON (right) coronal images of an average macaque template are compared to the average T<sub>1w</sub> (left). **B.** Similarly, the TQ-SILiCON (right) is compared to QSM images (left). In comparison to the T<sub>1w</sub> scan, the TQ-SILiCON has enhanced subcortical contrast while maintaining high gray and white matter contrast, which the QSM map lacks.

In macaques, the average TQ-SILiCON showed both excellent gray-to-white matter and deep gray matter contrast. It amplified the contrast in subcortical structures and maintained white matter landmarks in delineating subcortical structures from adjacent white matter tissue. In comparison to the average T<sub>1w</sub> image, TQ-SILiCON is superior in the delineation of subcortical structures (Figure 4.4). Anatomically, we were able to identify the following nuclei (Figures 4.4, 4.5, and 4.6): Caudate, putamen, external and internal globus pallidus, thalamus, substantia nigra, red nucleus, and dentate nucleus. When comparing the average TQ-SILiCON image to the average QSM map, the TQ-SILiCON image showed exceptional gray-white contrast evidently not present in the QSM map (Figures 4.4, 4.5, and 4.6).

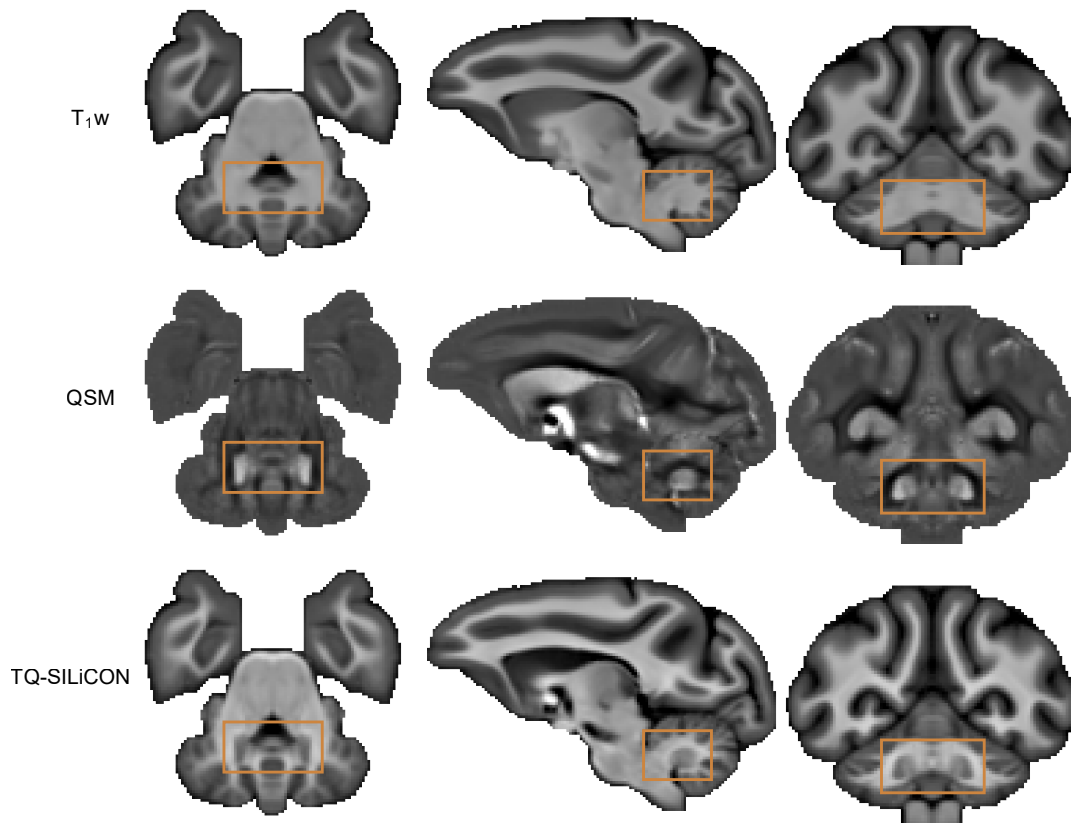


**Figure 4.5:** T<sub>1</sub>w, QSM, and TQ-SILiCON in the axial, sagittal, and coronal planes highlighting the dentate nucleus in the cerebellum of the macaque monkey. Notice the enhanced contrast (shaded orange square) of the dentate in both the QSM and the TQ-SILiCON images.



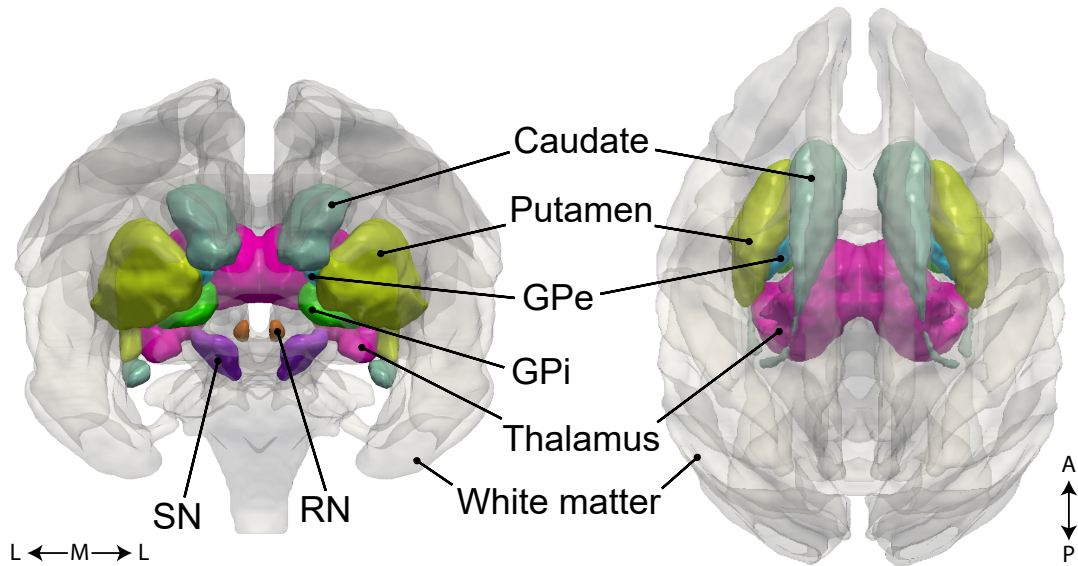


**Figure 4.6:** TQ-SILiCON allows whole-brain cortical and subcortical segmentation of the brain tissue. The white matter surface (transparent) of the macaque brain allows visualization of the color segmented subcortical deep gray matter nuclei. The highlighted subcortical nuclei include the caudate, putamen, globus pallidus external (GPe), globus pallidus internal (GPi), thalamus, substantia nigra (SN), and red nucleus (RN). Lateral (L) - Medial (M) - Lateral (L) and Anterior (A) - Posterior (P).

To further demonstrate the applicability of our fusion technique to single-subject macaque datasets, we performed tissue segmentation of gray matter and white matter on both the original  $T_1w$  volume and the TQ-SILiCON volume (Figure 4.7). The segmentation showed an improved gray-white matter delineation as compared to the output segmentation from the  $T_1w$  volume.  $T_1w$  image-based segmentation misclassified both some subcortical structures as white matter (Figure 4.7) and some white matter regions as gray matter, including the extreme capsule, external capsule, and lateral medullary lamina, which were correctly classified as white matter by TQ-SILiCON-based segmentation (Figure 4.8).

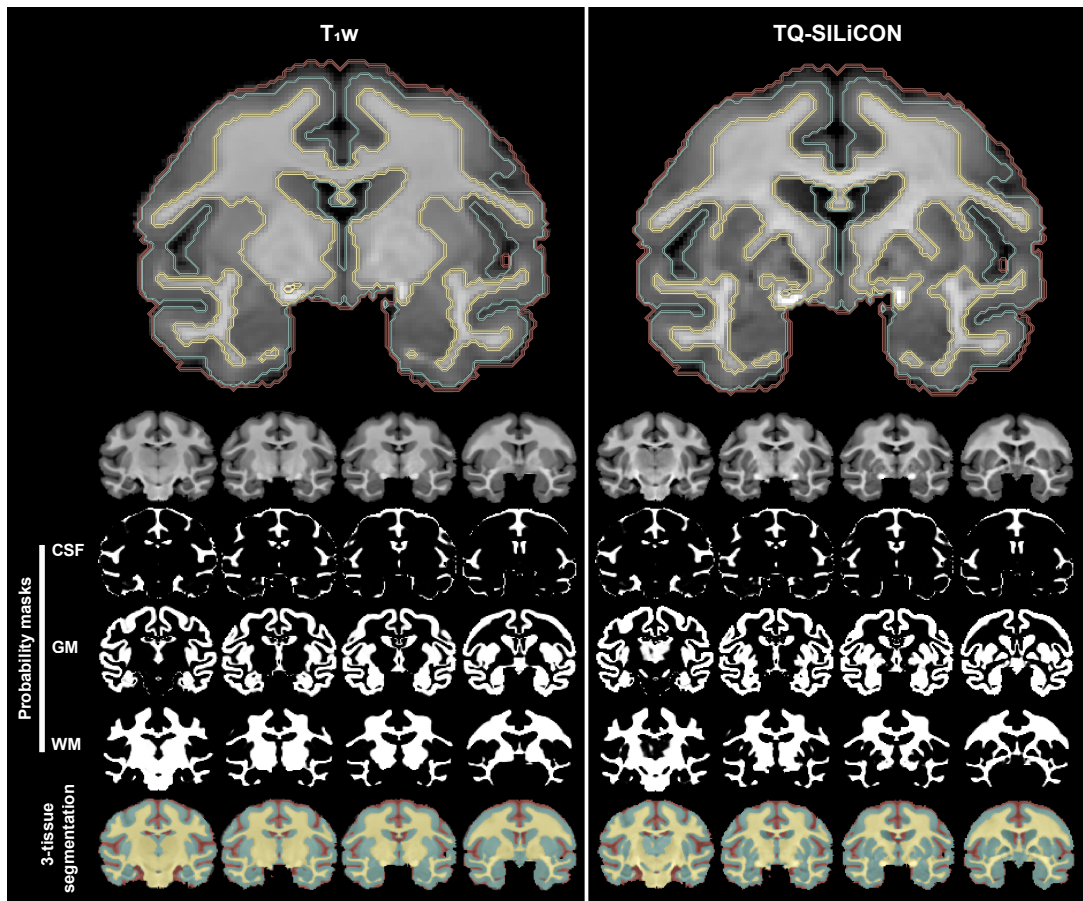


**Figure 4.7:** Coronal view of single macaque brain tissue segmentation using  $T_1w$  (left) and TQ-SILiCON images (right). TQ-SILiCON enables better tissue classification of gray matter and white matter. The bottom shows the semi-transparent color-coded tissue classification of the CSF, GM, and WM. Abbreviations: CSF - cerebrospinal fluid, GM - gray matter, and WM - white matter.

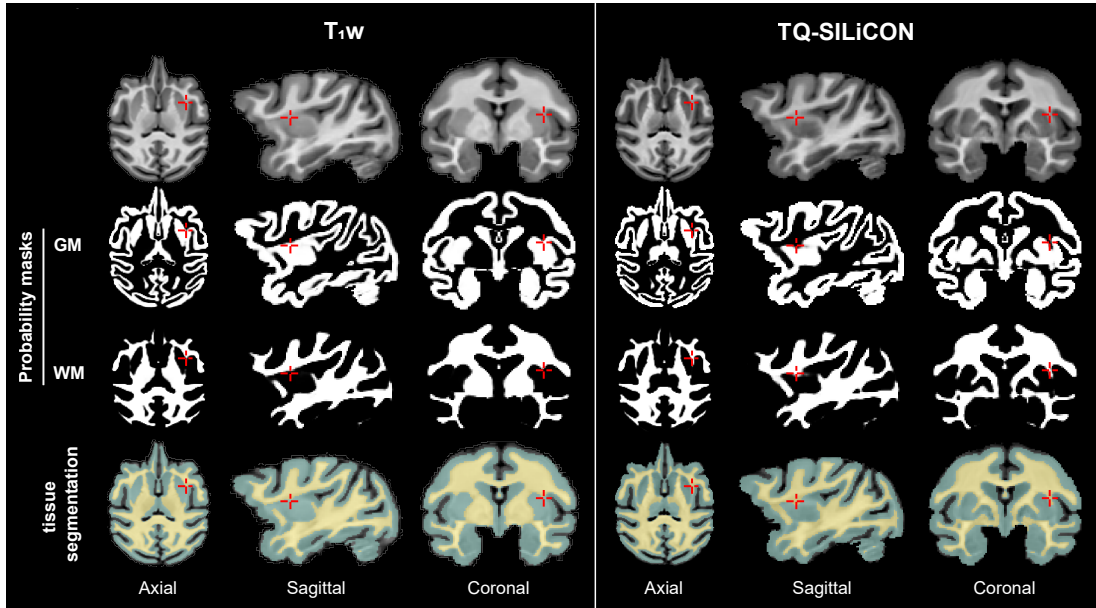


**Figure 4.8:**  $T_1w$  and TQ-SILiCON image segmentation results for a single macaque brain.  $T_1w$  segmentation misclassifies some white matter areas as gray matter (highlighted area in the external capsule). TQ-SILiCON image segmentation, on the other hand, improved cortical gray/white matter delineation. Abbreviations: GM - gray matter, and WM - white matter.

In summary, our fusion technique based on  $T_1w$  and QSM resulted in a contrast-enhanced  $T_1w$ -like 3D dataset that improved the automated segmentation algorithm and resulted in a more precise segmentation of gray and white matter in NHPs.

#### 4.3.3 TQ-SILiCON ENABLES THE PRECISE SEGMENTATION OF HUMAN CORTICAL AND SUBCORTICAL BRAIN TISSUE

The TQ-SILiCON method also enabled an improved tissue segmentation of the human brain. By using the same weights as in macaques (e.g., 0.83 and -0.87), TQ-SILiCON of the human brain contained both excellent gray-white and deep gray matter contrast, as illustrated in Figure 4.9. In comparison to the average  $T_1w$  image, the average TQ-SILiCON revealed enhanced visibility and better delineation of subcortical structures. When comparing the average TQ-SILiCON to the average QSM map, the TQ-SILiCON image showed exceptional  $T_1w$ -like gray-white contrast that the QSM image lacked (Figure 4.9).

The single-subject human segmentation results and the derived tissue probability masks are illustrated in Figure 4.10. The TQ-SILiCON image-based segmentation correctly categorized the extreme capsule and external capsule as white matter and subcortical nuclei as gray matter, while the  $T_1w$  image-based segmentation did not. In addition,  $T_1w$  image-based

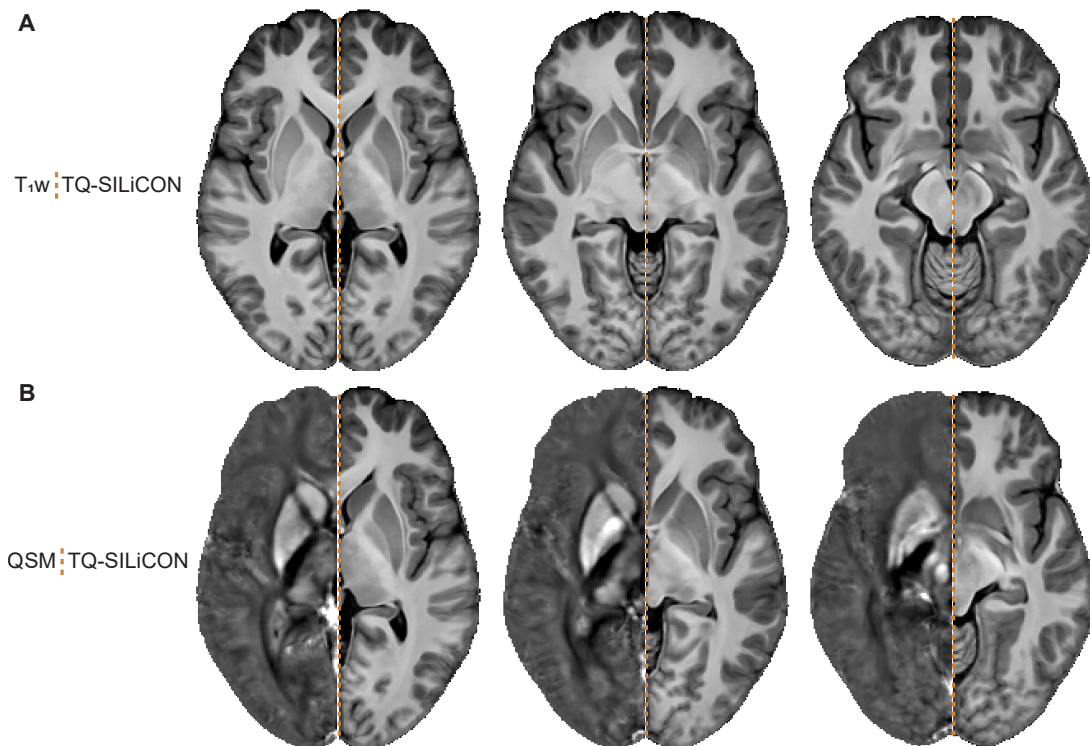


**Figure 4.9:** **A.** The TQ-SILiCON (right) axial images of an average human template are compared side-to-side to the average  $T_1w$  (left). **B.** Similarly, the TQ-SILiCON (right) is compared to QSM images (left). In comparison to the  $T_1w$  scan, the TQ-SILiCON has enhanced subcortical contrast while maintaining high gray and white matter contrast, which the QSM map lacks.

segmentation misclassified white matter areas around the pre-and postcentral gyrus as gray matter in some human subjects, whereas TQ-SILiCON-based segmentation accurately classified gray matter structures from neighboring white matter areas (Figure 4.11).

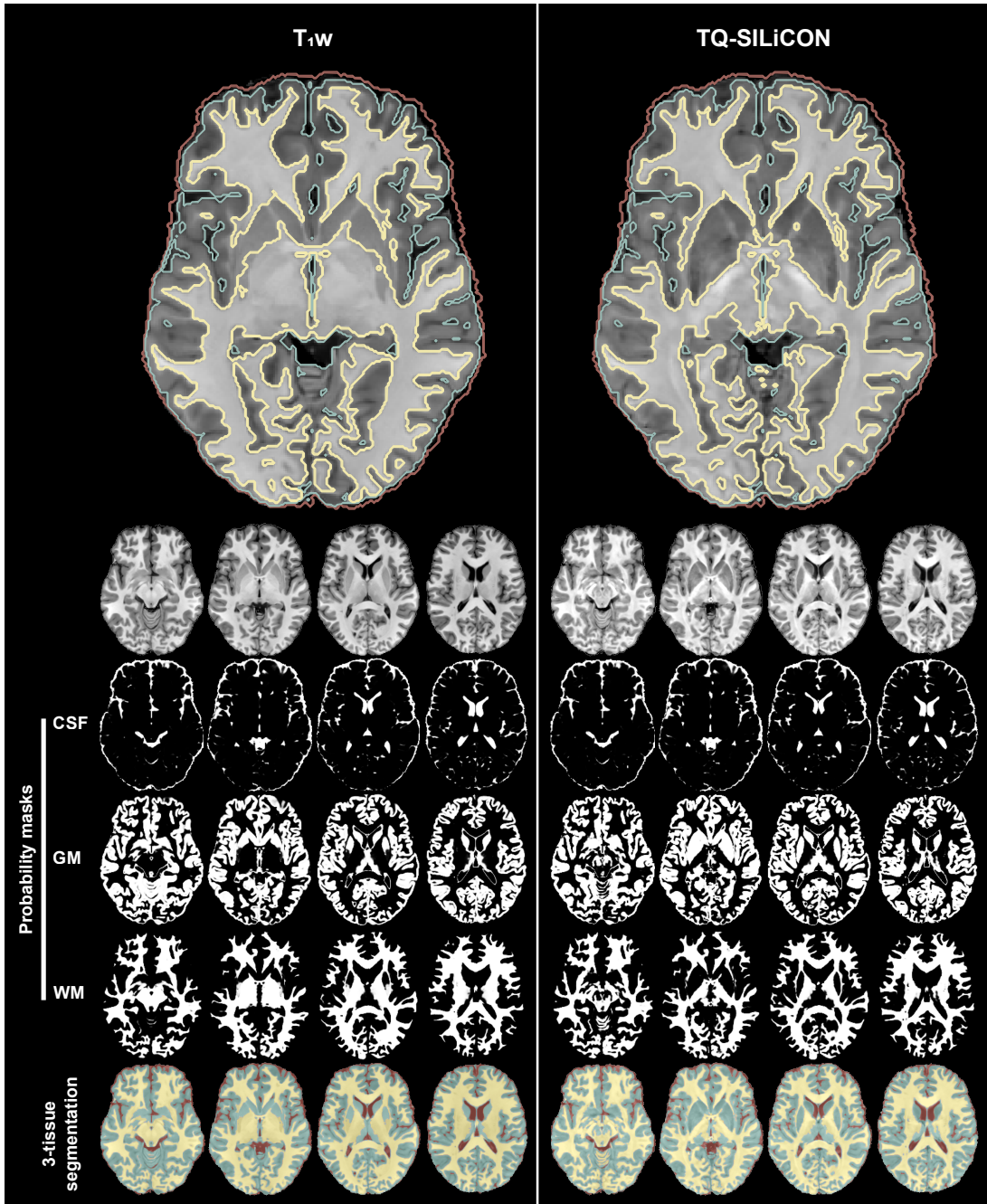
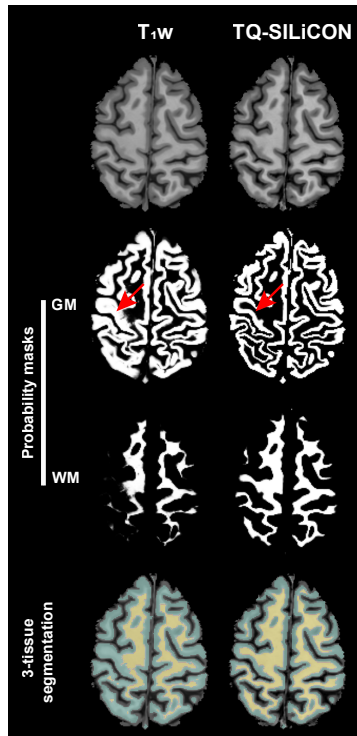


Figure 4.10: Axial view of single human brain tissue segmentation using  $T_1w$  (left) and TQ-SILiCON images (right). TQ-SILiCON enables better tissue classification of gray matter and white matter. The bottom shows the semi-transparent color-coded tissue classification of the CSF, WM, and GM. Abbreviations: CSF - cerebrospinal fluid, GM - gray matter, and WM - white matter.





**Figure 4.11:** The axial view of  $T_1w$  and TQ-SiLiCON image segmentation results for a single human brain.  $T_1w$  segmentation misclassifies some white matter areas as gray matter (highlighted area). TQ-SiLiCON image segmentation, on the other hand, improved cortical gray/white matter delineation. Abbreviations: GM - gray matter, and WM - white matter.

#### 4.4 DISCUSSION

In this study, we established an image contrast based on  $T_1w$  and high-resolution QSM. This method, termed TQ-SiLiCON, allowed us to automatically segment cortical and subcortical gray matter structures in NHPs and in humans. With the image quality achieved in a reasonable measurement time, this contrast may facilitate translational studies in NHPs for investigating the pathophysiology of subcortical structures in humans. In the following, we will first discuss the advantages of QSM, including its potential in the study of basal-ganglia circuits of primates. We will then discuss the advantages and limitations of combining QSM and  $T_1w$  and how TQ-SiLiCON could be used for neuroimaging applications in humans.

QSM is still a relatively new MRI technique that uses phase images to map the spatial distribution of paramagnetic and diamagnetic susceptibility [Haacke et al., 2004, Haacke et al., 2005]. The enhanced contrast of brain tissue largely arises from different concentrations of iron, myelin, and calcium [Haacke et al., 2005].

The absolute values derived from QSM could vary between MR systems and measurements as they could depend on the carrier frequency of the radio pulse, the  $B_0$  field, and the frequency drift [Liu et al., 2015]. However, relative magnetic susceptibilities (e.g., relative to cerebrospinal fluid or the overall brain) have been shown to be reproducible and to be a common feature, particularly of the basal ganglia in humans [Li et al., 2011, Wharton & Bowtell, 2015]. As described in healthy humans and during human development, QSM values have been reproducibly linked to iron concentration [Bilgic et al., 2012]. With increasing age, particularly subcortical deep gray matter structures show an increase in magnetic susceptibility in both humans [Bilgic et al., 2012, Keuken et al., 2017] and NHPs [Dadarwal et al., 2021]. Moreover, increased susceptibility has been observed in neurodegenerative diseases such as amyotrophic lateral sclerosis, Alzheimer's, Parkinson's, and Huntington's disease [Haacke et al., 2005].

In contrast to humans, only a few studies have applied QSM in NHPs [Wen et al., 2020, Yoshida et al., 2021, Dadarwal et al., 2019, Dadarwal et al., 2021]. The study by Yoshida et al. 2021 [Yoshida et al., 2021] reported an increased magnetic susceptibility in basal ganglia structures of the rhesus macaque, in close accordance with our findings in the cynomolgus macaque. Similarly, in our QSM maps, we observed high susceptibility in the caudate, putamen, globus pallidus (internal and external segments), thalamus, substantia nigra, red nucleus, and dentate gyrus of the cerebellum (Figures 4.2 and 4.5). Importantly, while many of the enhanced subcortical structures are known to harbor iron, it is not well understood which substances and structures are most relevant for the bulk susceptibility. For instance, the degree of contribution from myelin, especially along the white matter projections zones of the basal-ganglia cerebellar circuit, is not well understood. Identifying the sources that give rise to the increased susceptibility *in vivo* has significant clinical implications for neurodegenerative diseases and aging [Ravanfar et al., 2021]. Further immunohistochemistry studies in NHPs might provide a better understanding of the neural substrates and molecular physiological mechanisms of the iron content and could enable means for quantifying the degree of iron contribution to the QSM map of the brain. Moreover, exploring cortical and subcortical structures by neuroimaging and interventional studies in NHPs [Klink et al., 2021] may improve our understanding of the cortico-striatal-thalamic circuits and may guide therapeutic interventions. For example, the subthalamic nucleus (STN) is a typical target for deep brain stimulation (DBS) studies; its accurate delineation might aid in the physiological characterization of neuronal responses and microstimulation parameters, as has been shown in human patients undergoing DBS treatment [Liu et al., 2015]. In addition, the delineation of the internal and external globus pallidus can aid in the MRI-guided targeting of the inhibitory and excitatory output of the cortico-striatal-thalamic circuit during micro-stimulation. The identification and visualization of small subcortical structures are likewise beneficial for neuroscientists implementing optogenetic [Galvan et al., 2017, Inoue et al., 2015] or chemoge-

netic interventions [Mimura et al., 2021]. Hence, the correct delineation of the subcortical deep gray matter nuclei, while maintaining adequate anatomical information of the whole brain, is crucial for precise interventional studies and clinical applications.

While QSM provides an outstanding contrast of deep gray nuclei, white matter structures are much better delineated on  $T_1w$ . So, by linearly combining these two contrasts, we used the best of both worlds (Figure 4.6). As shown in the TQ-SILiCON image, our dual-fusion approach facilitated the delineation of the macaque brain’s cerebral cortex, white matter, and deep gray matter nuclei resulting in an overall  $T_1w$ -like appearance. We believe TQ-SILiCON can aid stereotactic interventions of small subcortical structures such as the subthalamic nucleus, and it may be generally helpful for interventional studies combining neuroimaging and perturbation methods in NHPs.

Another useful application for the TQ-SILiCON is for the development of brain atlases in humans and NHPs.  $T_1w$  is typically used in human and NHP brain atlases due to its excellent white and gray matter contrast. However, given that  $T_1w$  alone is insufficient, neuroimaging studies in humans explored the use of additional MRI contrasts such as  $T_2$ -weighted,  $T_2^*$ -weighted, and QSM to generate contrast from subcortical deep gray matter nuclei [Alkemade et al., 2017, Bazin et al., 2020, Xiao et al., 2015]. The available macaque atlases such as the D99 [Saleem & Logothetis, 2012] and the NMT [Hartig et al., 2021, Jung et al., 2021, Seidlitz et al., 2018] incorporate parcellations based on  $T_1w$  only, in combination with the prior knowledge from post-mortem histology. In the future, we believe that adding multi-contrast acquisitions might aid in the development of more precise atlas parcellations and clearer delineation of regional boundaries, although with the limitation of an increase in acquisition time. However, our proposed TQ-SILiCON approach might be a more viable option for obtaining a shorter in-session acquisition.

The accurate segmentation of gray and white matter tissue is not only essential for basic neuroscience applications but also for clinical diagnostics. For example, during brain development, aging, and neurological diseases specific volumetric changes might occur that might require precise segmentation and delineation of the overall structure [Liu et al., 2015]. Importantly, algorithms for automatic brain tissue segmentation typically utilize template-derived tissue probability masks (CSF, gray matter, and white matter) to initiate the segmentation process of a single subject volume. TQ-SILiCON atlases may aid in the generation of more accurate probability masks. As demonstrated by our automated tissue segmentation analyses, TQ-SILiCON outperformed  $T_1w$  based tissue segmentation in both macaques (Figure 4.7) and humans (Figure 4.10). Interestingly, TQ-SILiCON not only provided a better delineation of subcortical gray matter structures, but it also improved the assignment of white matter structures such as the extreme and external capsule and white matter areas around the pre-and postcentral gyrus (Figures 4.8 and 4.11), even in single subjects. However, one limitation of our TQ-SILiCON approach relates to the segmentation of the CSF



areas, which occasionally exhibited a comparable contrast to the basal ganglia. In our analyses, we bypassed this limitation by segmenting the CSF based on  $T_1w$  and then extracting the volume from the TQ-SILiCON volume before applying the segmentation process. In the future, the TQ-SILiCON approach could be improved by incorporating more than two contrasts to attain higher segmentation accuracy. An advantage of the TQ-SILiCON, particularly for its application in humans as opposed to the advanced deep learning based multi-contrast MRI image synthesis approach [Yu et al., 2020], is the simplicity of implementation, which does not require extensive computational resources. The linear combination of  $T_1w$  and QSM contrasts preserves the original data features, which are retained in the TQ-SILiCON image.

In conclusion, we believe that TQ-SILiCON can significantly improve the delineation of brain structures and the accuracy of morphometric studies.  $T_1w$  and QSM data sets could be obtained using clinically available 3T-MR-systems and in a reasonable short acquisition time. Importantly, the method works equally well for NHPs and humans facilitating translational studies. In the future, we will aim at studying the structural underpinnings of the MRI contrast observed in-vivo and hope to contribute to a more comprehensive understanding of the underlying pathophysiology behind neurodegenerative diseases.

*In the midst of where you're going don't forget to enjoy  
where you are*

unknown

# 5

## Multi-contrast MRI of the aging brain - A comparative study of cynomolgus macaques and common marmosets

### AUTHORS

**Rakshit Dadarwal<sup>1,2</sup>**, Judith Mylius<sup>1</sup> and Susann Boretius<sup>1,2</sup>

1. Functional Imaging Laboratory, German Primate Center – Leibniz Institute for Primate Research, Göttingen, Germany
2. Georg-August University of Göttingen, Göttingen, Germany

### ABSTRACT

Brain aging is a complex process in which the brain undergoes several structural and functional changes. Age-related brain changes are associated with tissue volume loss, white matter integrity loss, and iron accumulation in the basal ganglia. Non-human primate models are extremely useful in furthering our understanding of age-related brain changes and their relationship to neurodegenerative diseases. However, only a few non-human primate

studies have used MRI to investigate age-related alterations. Multiple MRI contrasts, including structural and quantitative parametric maps, are required to investigate age-related tissue restructuring in the brain. In this study, we looked at age-related morphological, tissue microstructural, and iron concentration changes in the brains of 14 macaques and 34 marmosets using several structural and parametric MRI contrasts. We found an age-related increase in magnetic susceptibility (QSM) and effective transverse relaxation rate ( $R_2^*$ ) in the iron-rich subcortical areas of macaque and marmoset brains. However, magnetization transfer (MT) saturation and diffusion MRI (dMRI) revealed increased MT saturation index (MTsat) and decreased mean and axial diffusivities in the corpus callosum of macaques and marmosets. The morphometric analyses displayed an age-related reduction in the gray-to-white matter ratio. We believe this study could help us better understand aging in non-human primates and how it relates to human brain aging.

The work described in this chapter resulted in the following output:

**Rakshit Dadarwal**, Judith Mylius, and Susann Boretius. "*Brain aging in cynomolgus macaques and common marmosets explored by mapping the magnetic susceptibility and  $R_2^*$* ", In: Proceedings of the 29th Annual Meeting of the International Society for Magnetic Resonance in Medicine (ISMRM), (Virtual) (2021).

**Rakshit Dadarwal**, Judith Mylius, and Susann Boretius. "*Multi-contrast MRI of the aging brain - A comparative study of cynomolgus macaques and common marmosets*" (manuscript in preparation).

## 5.1 INTRODUCTION

Brain aging has been considered a complex process in which the brain undergoes several structural and functional changes that eventually contribute to cognitive impairment and an increased risk of developing diseases [Peters, 2006, Sikora et al., 2021]. Age-related structural alterations are associated with a number of deleterious biological changes, including tissue volume loss, changes in white matter tissue integrity, iron accumulation in the brain, among others [Cox et al., 2016, Taubert et al., 2020, Ward et al., 2014]. Likewise, these changes have also been observed in human neurodegenerative diseases, indicating a close link between the underlying mechanisms.

Research on brain aging and neurodegenerative diseases depends on both valid animal models and diagnostic tools applicable to both animals and humans. Rodents have long been employed as an animal model in aging research, but findings do not necessarily translate well to humans [Nadon, 2006]. Non-human primates (NHPs), on the other hand, are

phylogenetically closer to humans and share many genetic, physiological, and behavioral features. Moreover, NHPs can help to bridge the gap between rodent animal models and humans [Colman, 2018, Mattison & Vaughan, 2017]. For example, macaques and marmosets share  $\approx 93\%$  sequence identity to the human genome [Gibbs et al., 2007, Worley et al., 2014, Zimin et al., 2014] and develop similar age-associated diseases and conditions. The short lifespan of macaques (25 - 30 years) and marmosets (maximum 16 years) makes them ideal models for studying aging [Colman, 2018, Choi et al., 2016, Tardif et al., 2011].

Multiple MRI contrasts are required for the in-depth *in vivo* characterization of age-related morphometric and microstructural tissue changes [MacDonald & Pike, 2021]. Because of their excellent cortical gray and white matter contrast,  $T_1$ -weighted ( $T_1w$ ) scans have been used to examine morphological changes (tissue volumes, cortical thickness, and surface area) in the brain with healthy aging [Lemaitre et al., 2012, Salat et al., 2004, Shaw et al., 2016, Tullo et al., 2019].  $T_2^*$  and magnetic susceptibility have been used to measure age-related changes in iron burden, primarily in the subcortical nuclei [Acosta-Cabronero et al., 2016, Betts et al., 2016, Bilgic et al., 2012, Dadarwal et al., 2021, Wen et al., 2020]. Age-related microstructural changes in the brain have also been evaluated using dMRI and magnetization transfer imaging [Bowley et al., 2010, Cox et al., 2016, Schiavone et al., 2009]. However, only a few studies combine multiple MRI contrasts to target both morphometric and tissue microstructural changes. Multiple MRI contrasts acquired simultaneously using identical parameters are necessary to get an overall perspective of dynamic neurodevelopment and tissue remodeling in healthy aging.

In this study, we used multiple anatomical contrasts ( $T_1w$ , and  $MTw$ ) and parametric maps (QSM,  $R_2^*$ ,  $MTsat$ ,  $T_{1app}$ , FA, MD, AD, and RD) to capture age-related changes in brain morphometry, tissue microstructure, and iron level in macaque and marmoset brains. Furthermore, We examine the structural properties of macaque and marmoset brains *in vivo* as they age, from young adulthood to geriatric, and how they differ across brain regions and species.

## 5.2 MATERIALS AND METHODS

### ANIMALS

This study included 14 healthy female cynomolgus macaques (*Macaca fascicularis*) between the ages of 7 - 20 years old and 34 healthy marmosets (*Callithrix jacchus*) between the ages of 2 - 15 years old (17 males and 17 females). The macaques were from two age groups, while the marmosets were from four, as shown in Figure 5.1.

Macaque ( <i>Macaca fascicularis</i> )				Marmoset ( <i>Callithrix jacchus</i> )				
Age (yr.)		7 - 8	15 - 20	Age (yr.)	2	4 - 6	7 - 10	12 - 15
Animals		4	9	Animals	8	7	10	9

Figure 5.1: The number of macaques and marmosets included in this study, together with their age groups.

### 5.2.1 ANIMAL EXPERIMENTS

All monkeys were purpose-bred, raised, and housed according to the standards for macaques of the German Primate Center (Göttingen, Germany). All aspects of the study were conducted in accordance with national and international guidelines of the German Animal Protection Law and the European Union Directive 2010/63/EU for the Protection of Animals used for Scientific Purposes. The macaque and marmoset studies were approved by the local authorities, the Animal Welfare Service, Lower Saxony State Office for Consumer Protection and Food Safety (macaque study license-number - 33.19-42502-04-16/2278; marmoset study license-number - 33.19-42502-04-17/2496).

#### MACAQUE

In preparation for anesthesia, the macaques were deprived of food overnight. Anesthesia was induced by a mixture of ketamine ( $8.05 \pm 2.65$  mg per kg body weight) and medetomidine ( $0.02 \pm 0.01$  mg per kg) and maintained by isoflurane (0.8 - 1.7 % in oxygen and ambient air) via endotracheal tube and pressure-controlled active ventilation. The monkeys were placed in a prone position, and their heads were fixed in an MR-compatible stereotactic apparatus (Kopf 1430 M, [kopfinstruments.com](http://kopfinstruments.com)).

#### MARMOSET

Marmosets were initially anesthetized with a mixture of alfaxalone (12 mg/kg, Alfaxan, Jurox) and diazepam (3 mg/Kg, Ratiopharm). Anesthesia was maintained with  $0.9 \pm 0.3$  % isoflurane in a mixture of oxygen and ambient air as required. Marmosets were mechanically ventilated via an endotracheal tube for the duration of the measurement (respiration rate = 35 bpm). The body temperature was kept constant by blankets filled with warm water.

During MRI, anesthetized marmosets were positioned in the sphinx position in a custom-made MRI-compatible stereotaxic frame to minimize movement artifacts. The ear bars served additionally as hearing protection and were dabbed with a lidocain containing ointment (Emla 5 %, AstraZeneca) for local anesthesia. Application of eye ointment (Bepanthen AS, Bayer) prevented the eyes from drying out during anesthesia.

## MRI DATA ACQUISITION

### MACAQUE

We collected macaque data on a 3 T Siemens MAGNETOM Prisma MR system (Siemens Healthineers, Erlangen, Germany). A 7 cm circular single loop coil was used for signal detection. The macaque brain imaging protocol consisted of anatomical T<sub>1</sub>w, multi-echo gradient-recalled echo (ME-GRE), dMRI (dMRI), magnetization transfer-weighted (MTw), proton density-weighted (PDw), and T<sub>1</sub>w sequences. The detailed data acquisition parameters have been previously listed in Table 3.1 (T<sub>1</sub>w, and ME-GRE), Table 2.1 (dMRI), and Table 3.2 (MTw, PDw, and T<sub>1</sub>w).

### MARMOSET

We collected marmoset data on a 9.4 T Bruker BioSpec MR system (Bruker BioSpin MRI GmbH, Ettlingen, Germany), equipped with the BGA 20S gradient. A 40 mm single loop coil was used for signal detection (Rapid Biomedical GmbH, Rimpar, Germany). The marmoset brain imaging protocol consisted of ME-GRE, dMRI, MTw, PDw, and T<sub>1</sub>w sequences. The detailed data acquisition parameters are listed in Table 5.1 (ME-GRE, and dMRI) and Table 5.2 (MTw, PDw, and T<sub>1</sub>w).

Parameters	ME-GRE	dMRI
Pulse sequence	3D ME-GRE	2D PGSE
Native resolution (mm <sup>3</sup> )	0.21 × 0.21 × 0.21	0.45 × 0.45 × 0.45
Field of view (mm <sup>2</sup> )	33.6 × 33.6	57.6 × 36
Acquisition matrix	160 × 160	128 × 80
Number of slices	80	38
Total acquisition time (min)	17.5	18.4
TR/TE (ms)	42/3:3:30	4000/24.5
b-value (s/mm <sup>2</sup> )	–	0, 1000
Diffusion gradient directions	–	30
Number of averages	2	2

Table 5.1: ME-GRE and dMRI scan parameters for the marmoset brain..

## MRI DATA ANALYSES

The data analysis pipelines for macaques and marmosets were nearly identical.

Parameters	MT	PD	T <sub>1</sub>
Pulse sequence	3D FLASH	3D FLASH	3D FLASH
Native resolution (mm <sup>3</sup> )	0.21 × 0.21 × 0.21	0.21 × 0.21 × 0.21	0.21 × 0.21 × 0.21
Field of view (mm <sup>2</sup> )	37.8 × 37.8	37.8 × 37.8	37.8 × 37.8
Acquisition matrix	180 × 180	180 × 180	180 × 180
Number of slices	180	180	180
Total acquisition time (min)	17.3	17.3	16.1
TR/TE (ms)	16.1/3.8	16.1/3.8	15/3.8
Flip angle (degree)	5	5	25
Number of averages	2	2	2

**Table 5.2:** MRI acquisition parameters for MTw, PDw, and T<sub>1</sub>w brain scans in marmosets.

## PREPROCESSING

Macaque T<sub>1</sub>w, ME-GRE, MTw, and dMRI dicom images were first converted into Nifti format using *Dcm2nii* [Li et al., 2016]. T<sub>1</sub>w, mean of ME-GRE across echo times (mGRE), and MTw Nifti images were denoised using ANTs *DenoiseImage* [Manjón et al., 2010]. The segmentation of the brain mask for each MRI contrast was carried out manually using the ITK-SNAP segmentation tool [Yushkevich et al., 2006], due to the unavailability of automatic skull-stripping tools for macaque brains. We used these segmented brain masks to correct T<sub>1</sub>w, mGRE, and MTw images for bias fields using ANTs *N4BiasFieldCorrection* [Tustison et al., 2010]. The skull-stripped mGRE and MTw images were affinely registered to the subject T<sub>1</sub>w brain volume using ANTs registration algorithm [Avants et al., 2008, Avants et al., 2011].

Marmoset MTw, ME-GRE, and dMRI Bruker files were converted into Nifti format using *Bru2*. MTw and mGRE images were denoised using ANTs *DenoiseImage* [Manjón et al., 2010]. The segmentation of the brain mask for each MRI contrast was carried out manually using the ITK-SNAP segmentation tool [Yushkevich et al., 2006]. These segmented brain masks were used to correct MTw, and mGRE images for bias fields using ANTs *N4BiasFieldCorrection* [Tustison et al., 2010]. The skull-stripped mGRE image was affinely registered to the subject T<sub>1</sub>w brain volume using the ANTs registration algorithm [Avants et al., 2008, Avants et al., 2011].

## POPULATION-AVERAGED BRAIN TEMPLATES

The preprocessed macaque T<sub>1</sub>w scans were rigidly registered to the symmetric DPZCYNO template (0.5 mm) (template developed is described in chapter 3) before being nonlinearly aligned to produce a population-averaged macaque template. Similarly, the preprocessed

macaque MTw scans were rigidly registered to the down-sampled (0.21 mm) version of the MBM v2 atlas (80  $\mu\text{m}$ ) [Liu et al., 2020a] before being nonlinearly aligned to construct a population-averaged marmoset template.

### QSM AND $R_2^*$

Macaque and marmoset ME-GRE magnitude images were utilized to calculate  $R_2^*$  maps by fitting the ME-GRE magnitude signal decay across all echo times with a mono-exponential model [Pei et al., 2015]. The QSM maps were reconstructed using the coil-combined ME-GRE phase images. This QSM reconstruction included phase unwrapping using the best-path algorithm, background field removal using Laplacian boundary value and variable spherical mean value filtering algorithms, and solving the inversion problem using the multiscale dipole inversion approach [Abdul-Rahman et al., 2007, Acosta-Cabronero et al., 2018, Zhou et al., 2014]. Finally,  $R_2^*$  and QSM average atlases were created using the previously calculated warps from subject magnitude to the population-averaged template (Figures 5.3 and 5.4).

The resulting macaque and marmoset QSM maps were not normalized using any reference tissue magnetic susceptibility values, as we previously demonstrated in the chapter 2 that whole-brain referenced magnetic susceptibility results do not differ from unnormalized magnetic susceptibility results.

### QSM ECHO TIME DEPENDENCE

Macaque and marmoset QSM maps were calculated for each echo using coil-combined single echo phase data. The temporal responses of magnetic susceptibility in macaque and marmoset brain ROIs are displayed in Figure 5.10.

### MT SATURATION

MTsat and apparent longitudinal relaxation time ( $T_{1\text{app}}$ ) maps were estimated using the method described by Helms et al. [Helms et al., 2008]. The steps of the method were implemented in MATLAB R2018a (The Mathworks Inc., Natick, MA) and are available at [github.com/RDadarwal/MTsat-MRI](https://github.com/RDadarwal/MTsat-MRI). Finally, macaque brain and marmoset brain MTsat and  $T_{1\text{app}}$  average atlases were created using the warps from subject native space to the population-averaged template (Figure 5.3 and 5.4).

### dMRI

The pipelines provided at [github.com/RDadarwal/Diffusion-MRI](https://github.com/RDadarwal/Diffusion-MRI) were used to analyze macaque and marmoset dMRI data. Macaque brain diffusion-weighted images were denoised [Veraart



et al., 2016], and corrected for susceptibility distortions, eddy current distortions, and subject movement artifacts [Andersson et al., 2003, Andersson & Sotiropoulos, 2016]. Marmoset brain diffusion-weighted images were denoised [Veraart et al., 2016] and corrected for eddy current distortions [Andersson et al., 2003] and subject movement artifacts using the ANTs motion correction algorithm. The correction of susceptibility distortions requires non-diffusion-weighted ( $b_0$ ) scans in both anterior-posterior and posterior-anterior phase encoding directions, which were unavailable for the marmoset measurements. Other pre-and post-processing steps in the dMRI data analysis pipelines of macaques and marmosets were similar. We then fit a diffusion tensor model (DTI) model to the preprocessed macaque and marmoset images and calculated fractional anisotropy (FA), and axial (AD), radial (RD), and mean (MD) diffusivity maps [Basser et al., 1994, Garyfallidis et al., 2014].

## REGIONS OF INTEREST

The macaque brain population-averaged  $T_1w$  template was nonlinearly registered to the DPZ-CYNO template to generate warp fields to and from the symmetric DPZCYNO  $T_1w$  template. These warp fields were applied to the DPZCYNO cortical, subcortical, and white matter label maps to propagate them into the group average  $T_1w$  image space and finally into the individual macaque native space (Figure 5.2).

Marmoset brain group average MTw image was nonlinearly registered to the MBM  $v_2, v_3$  templates [Liu et al., 2021, Liu et al., 2020a] to extract the cortical, subcortical and white matter ROIs (Figure 5.2).

All the macaque and marmoset ROIs were transferred into the subject native space, manually assessed, and refined wherever required. Finally, two cortical gray matter (frontal and occipital), five white matter (frontal, occipital, and callosal regions), and four subcortical gray matter ROIs were considered for the statistical analyses. The ROIs comprises the prefrontal cortex (PFC), visual cortical areas  $V_2 - V_4$  ( $V_2-V_4$ ), frontal white matter (Fw), occipital white matter (Ow), genu (CCg), corpus callosum body (CC-B), splenium (CC-Sp), putamen (Pu), thalamus (Thal), globus pallidus (GP), and substantia nigra (SN). The visual cortical areas  $V_2, V_3$ , and  $V_4$  of the marmoset brain were merged to produce the  $V_2-V_4$  ROI, while the sagittal stratum and occipital vertical fasciculus were combined to form the PFC ROI.

## MORPHOMETRY

We used nonlinear warp fields generated during registration from the native subject space to the species-specific average image space to create macaque and marmoset group averages MTsat,  $T_1app$ , QSM, and  $R_2^*$  maps for the respective age groups.

Age-related local volumetric changes in each voxel were determined by the Jacobian of the deformation from the native macaque or marmoset space to the population-averaged

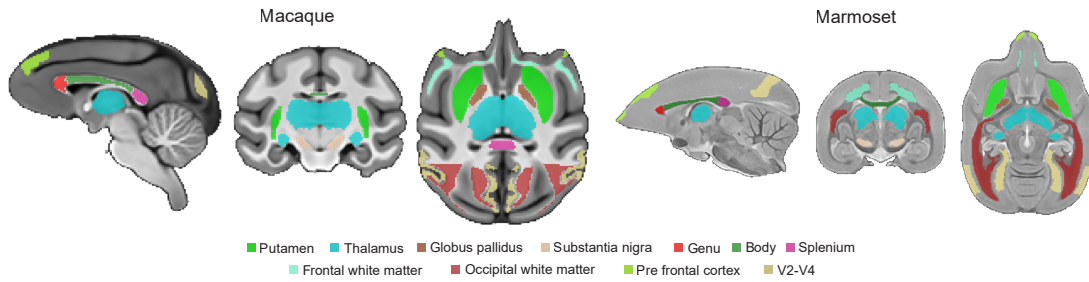


**Figure 5.2:** Selected regions-of-interest (ROIs) in the gray matter and white matter structures of the macaque and marmoset brains: putamen, thalamus, globus pallidus, substantia nigra, genu, body, splenium, frontal white matter, occipital white matter, prefrontal cortex, and V2-V4.

template space. For the macaque and marmoset brains, Jacobian determinant maps were computed using subject-to-template deformation warp files and smoothed using a 3D Gaussian kernel (FWHM 0.42 mm). The used relative Jacobian determinants were only based on nonlinear deformations after eliminating global linear deformations.

## STATISTICS

Macaque age group differences in QSM,  $R_2^*$ , MTsat,  $T_{1app}$ , FA, MD, AD, and RD were probed using paired t-test statistics. We used Bonferroni correction to remove the effects of multiple comparisons in macaque data analyses. Marmoset age group differences in QSM,  $R_2^*$ , MTsat,  $T_{1app}$ , FA, MD, AD, and RD were statistically tested using one-way ANOVA tests. Statistical tests on macaques and marmosets were conducted with a p-value of 0.05.

Student's t-test was performed on the Jacobian determinant maps for voxel-wise comparison of young adult and geriatric groups. Q-values (false discovery rate (FDR) adjusted p-values) and the respective z-scores were calculated using the 3dFDR function of AFNI [Cox & Hyde, 1997].

## 5.3 RESULTS

Macaque and marmoset age-group specific average brain templates are shown in Figure 5.3 and Figure 5.4. The significant increase in subcortical contrast in QSM and  $R_2^*$  templates is evident with increasing age in both macaque (Figure 5.3) and marmoset (Figure 5.4) brains. Specifically, the basal ganglia appear hyper-intense with an increase in age. Independent of age, the basal ganglia had higher QSM and  $R_2^*$  contrast than the thalamus, cortex, white matter, and hippocampus. However, no substantial brain tissue contrast differences with age were observed in MTsat and  $T_{1app}$ .

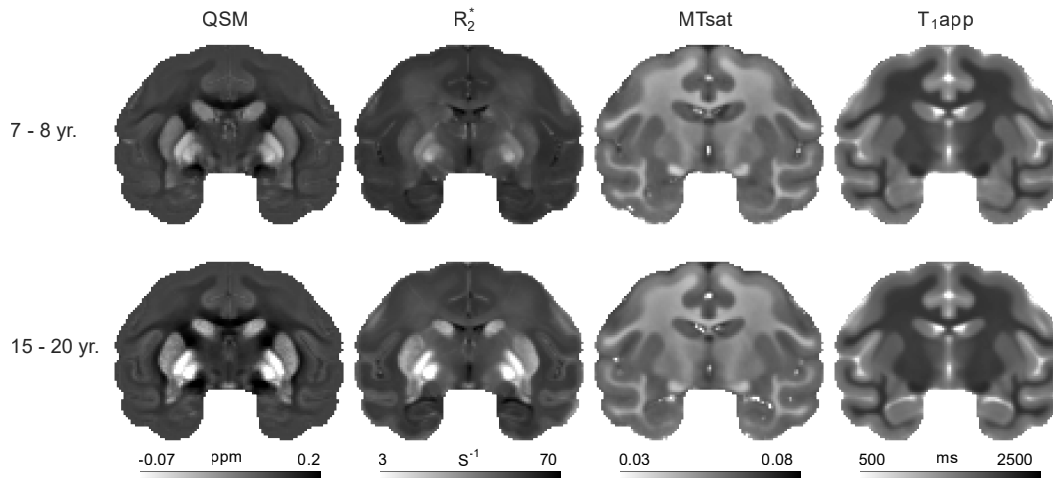


**Figure 5.3:** QSM,  $R_2^*$ , MTsat, and  $T_{1app}$  group averages of macaque brain across two age groups. QSM and  $R_2^*$  contrasts in macaque basal ganglia structures enhanced with an increase in age.

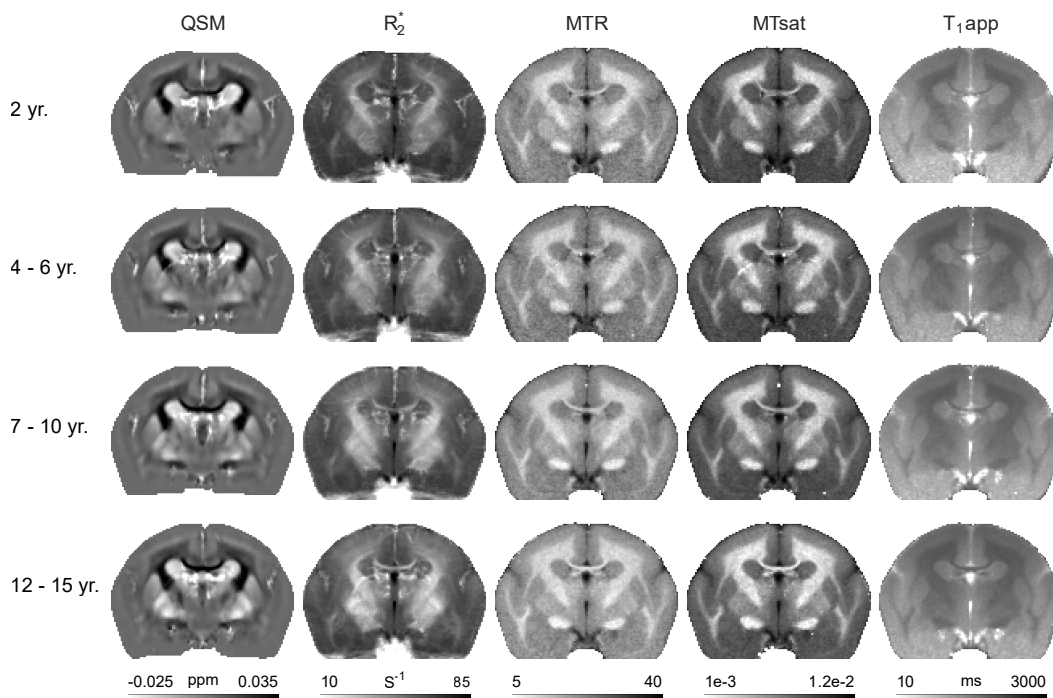


**Figure 5.4:** Marmoset brain QSM,  $R_2^*$ , MTR, MTsat, and  $T_{1app}$  average maps for four age groups. QSM and  $R_2^*$  contrasts in the basal ganglia of marmosets were increased with an increase in age.

### 5.3.1 QSM AND $R_2^*$

The cortical and subcortical gray matter ROI analyses revealed an age-related increase in magnetic susceptibility and  $R_2^*$ , which was more pronounced in the macaque brain than the marmoset brain (Figure 5.5A and B). The V2-V4 area of the macaque cerebral cortex had higher magnetic susceptibility and  $R_2^*$  values than the PFC area. In comparison to Pu, Thal, and SN, the GP had the highest magnetic susceptibility and  $R_2^*$  values. In macaque white matter ROIs, the observed magnetic susceptibility values in the macaque became relatively more diamagnetic with age. The Ow area of the macaque brain had higher diamagnetic susceptibility values than the Fw area. However, there were essentially no age-related changes in magnetic susceptibility in marmoset white matter ROIs. The  $R_2^*$  values in the white matter of the macaque and marmoset brains increased with age. In the hippocampus of macaques and marmosets, a significant age-related decrease in magnetic susceptibility and increase in  $R_2^*$  were found (Supplementary Figure A.9).

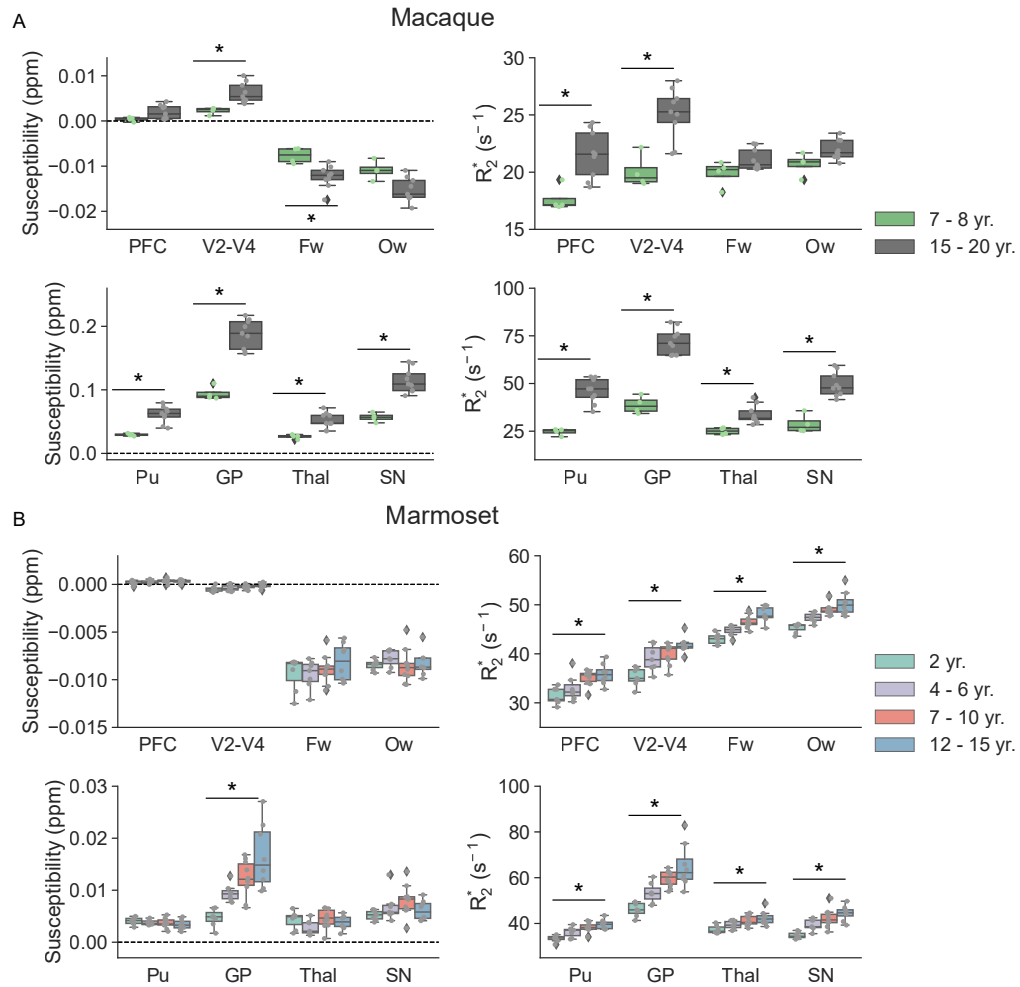


**Figure 5.5:** Macaque and marmoset magnetic susceptibility and  $R_2^*$  regional summary statistics for gray and white matter ROIs. **A.** Magnetic susceptibility values significantly increase with age in macaques in the V2-V4, Pu, GP, Thal, and SN. The  $R_2^*$  results were identical to the magnetic susceptibility results, with increasing  $R_2^*$  values in the PFC, V2-V4, Pu, GP, Thal, and SN. **B.** Marmoset brain showed significant age-related differences in magnetic susceptibility in the GP, and  $R_2^*$  in the all analyzed cortical, subcortical, and white matter ROIs. Abbreviations: PFC: the prefrontal cortex, V2-V4: visual cortical area V2, V3, and V4, Fw: frontal white matter, Ow: occipital white matter, Pu: putamen, GP: globus pallidus, Thal: thalamus, and SN: substantia nigra.

### 5.3.2 MT SATURATION

As shown in Figure 5.6, the cortical gray matter and white matter ROI analyses revealed no significant age-related differences in  $MT_{sat}$ , and  $T_{1app}$  in the macaque and marmoset brains. The white matter ROIs in the macaque and marmoset brains had greater  $MT_{sat}$  values than the cortical gray matter ROIs. In the macaque and marmoset brains, both frontal and occipital white matter ROIs (Fw and Ow) showed almost identical  $MT_{sat}$  values. The  $T_{1app}$  values in the cerebral gray matter were higher than in the white matter. The hippocampus of macaques and marmosets revealed no significant age-related differences in the  $MT_{sat}$  and  $T_{1app}$  (Supplementary Figure A.9).

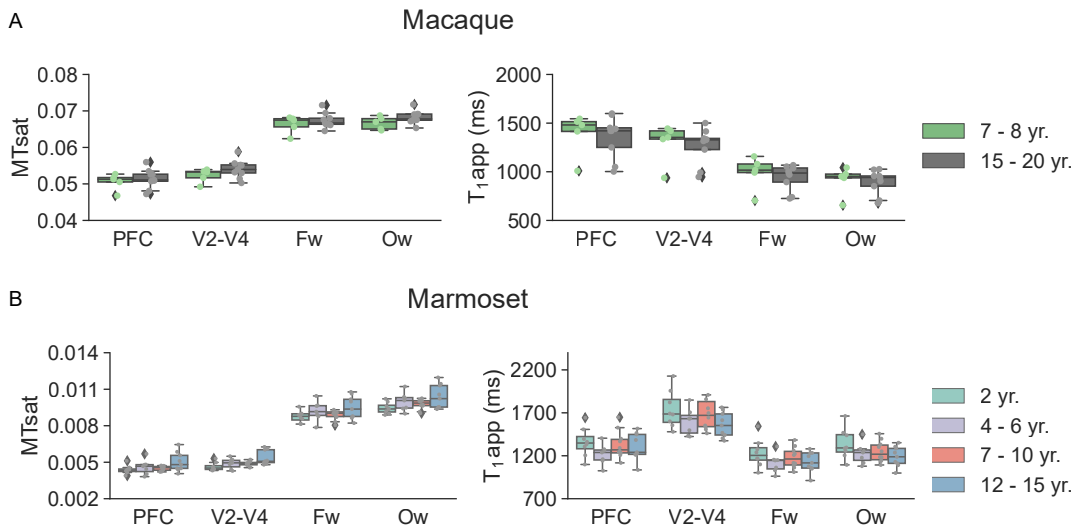


**Figure 5.6:** Macaque and marmoset  $MT_{sat}$ , and  $T_{1app}$  regional summary statistics for the gray and white matter ROIs. **A.** The  $MT_{sat}$  and  $T_{1app}$  in the macaque PFC, V2-V4, Fw, and Ow showed no significant age-related changes. **B.** Marmosets showed similar results, with  $MT_{sat}$ , and  $T_{1app}$  remaining unaltered across age groups.

### 5.3.3 dMRI

FA revealed no statistically significant age-related changes in the macaque and marmoset brain corpus callosum ROIs, as shown in Figure 5.7A. The observed FA values in the marmoset CC-B were lower than CCg and CC-Sp. In addition, all three corpus callosum ROIs revealed an age-related reduction in macaque and marmoset MD and AD, which was more evident in marmosets than in macaques. In both macaques and marmosets, no age-related changes in RD were found. Moreover, the CC-B had higher RD values than the CCg and CC-Sp.

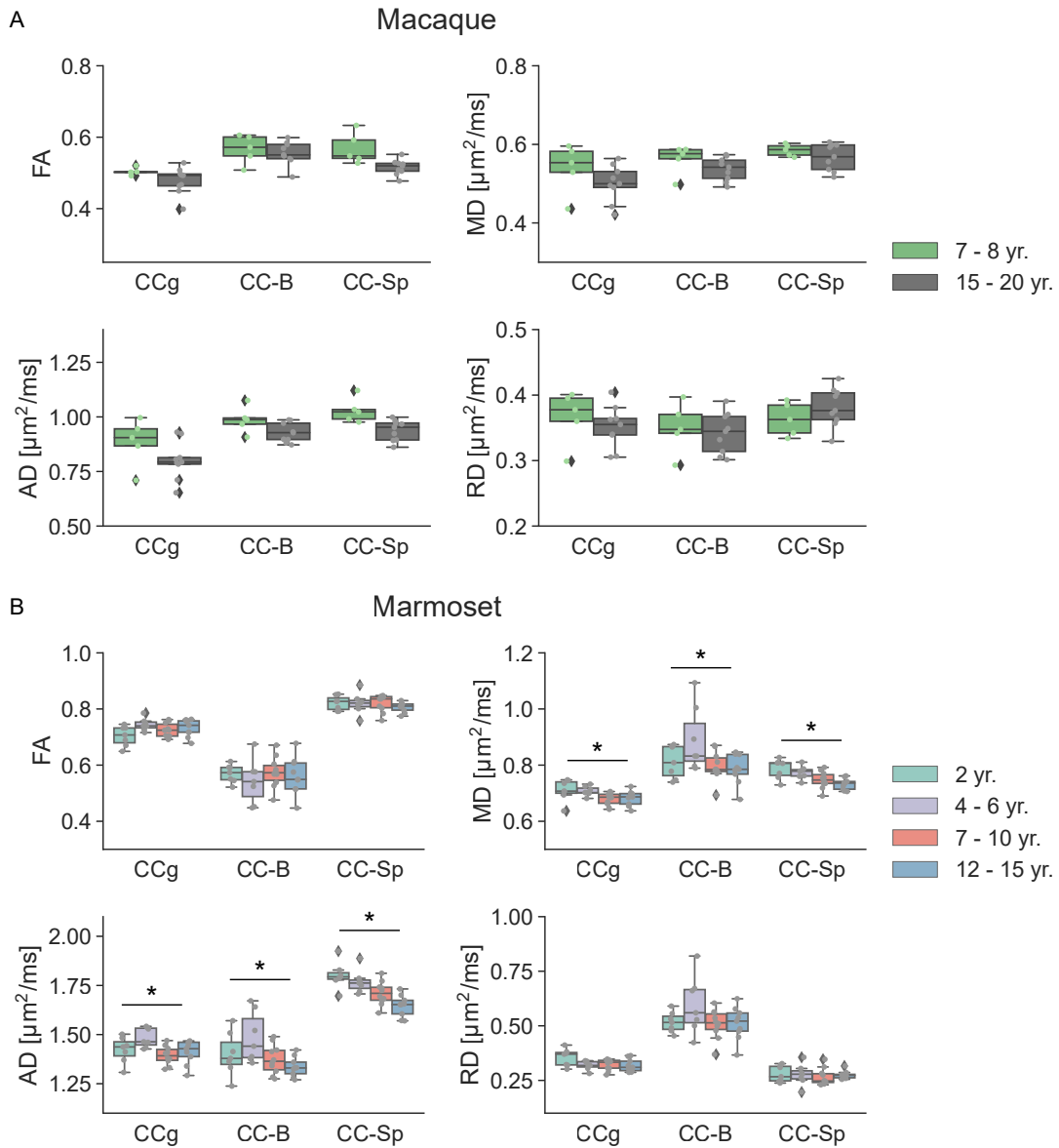


**Figure 5.7:** Age associations with the microstructural characteristics of callosal regions. Macaque and marmoset brains FA, MD, AD, and RD regional summary statistics for the three different parts of the corpus callosum. **A.** There were no significant differences in FA, MD, AD, and RD for the corpus callosum regions (CCg, CC-B, and CC-Sp) in the macaque brain. **B.** MD and AD decreased significantly with age in the marmoset brain, while FA and RD remained almost unaltered.

#### 5.3.4 MORPHOMETRY

Macaque and marmoset brain morphometry analyses showed a reduced gray-white matter volume ratio with age (Figure 5.8). The regression line fitted to the relationship between

gray-white matter volume ratio and age showed a decline in gray-white matter volume ratio with an increase in age.

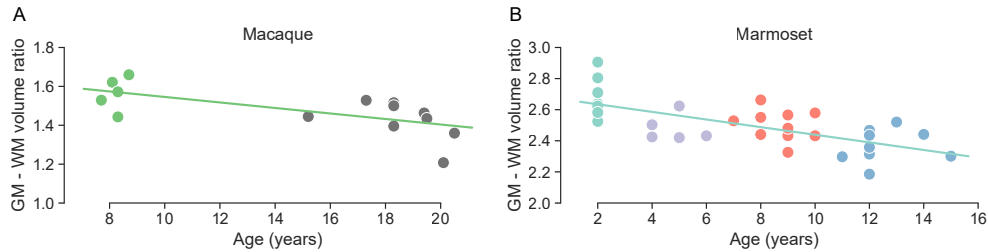


**Figure 5.8:** Macaque and marmoset brain morphometry results. **A.** The GM-WM volume ratio in macaque brains declined with age. **B.** The GM-WM volume ratio in marmoset brains also dropped as they became aged. Abbreviations: GM - gray matter, and WM - white matter.

#### CORPUS CALLOSUM MORPHOLOGY

The macaque brain Jacobian determinant analysis showed significant age-related expansion in a small portion (rostral body and anterior midbody) of the corpus callosum body (CC-B), as shown by the dotted black line on the relative Jacobian calculated z-score map in Figure 5.9A. The rest of the macaque brain corpus callosum showed no significant age-related effects. Tissue expansion with an increase in age is shown by positive z-score values, and tissue shrinkage is indicated by negative z-score values. The ROI analyses showed an increase in  $R_2^*$  values, particularly in the CCg area. However, no substantial age-related changes in magnetic susceptibility,  $MT_{sat}$ , and  $T_{1app}$  values were seen. The  $R_2^*$  values in the corpus callosum were highest in the CC-Sp region. Furthermore, In comparison to the CCg and CC-Sp, the CC-B region had the most increased diamagnetic susceptibility in the macaque brain.

The genu (CCg) and splenium (CC-Sp) parts of the marmoset brain showed a significant age-related expansion in the Jacobian determinant analysis, as shown by the dotted black line on the Jacobian analyzed z-score map in Figure 5.9B. The  $R_2^*$  and  $MT_{sat}$  values in the marmoset brain corpus callosum areas (CCg, CC-B, and CC-Sp) increased with age. Magnetic susceptibility, and  $T_{1app}$  values, on the other hand, showed no significant age-related variations.  $R_2^*$  values in the corpus callosum were highest in the CC-Sp region, similar to the marmoset results. In the corpus callosum, the CC-B region had the highest diamagnetic susceptibility.



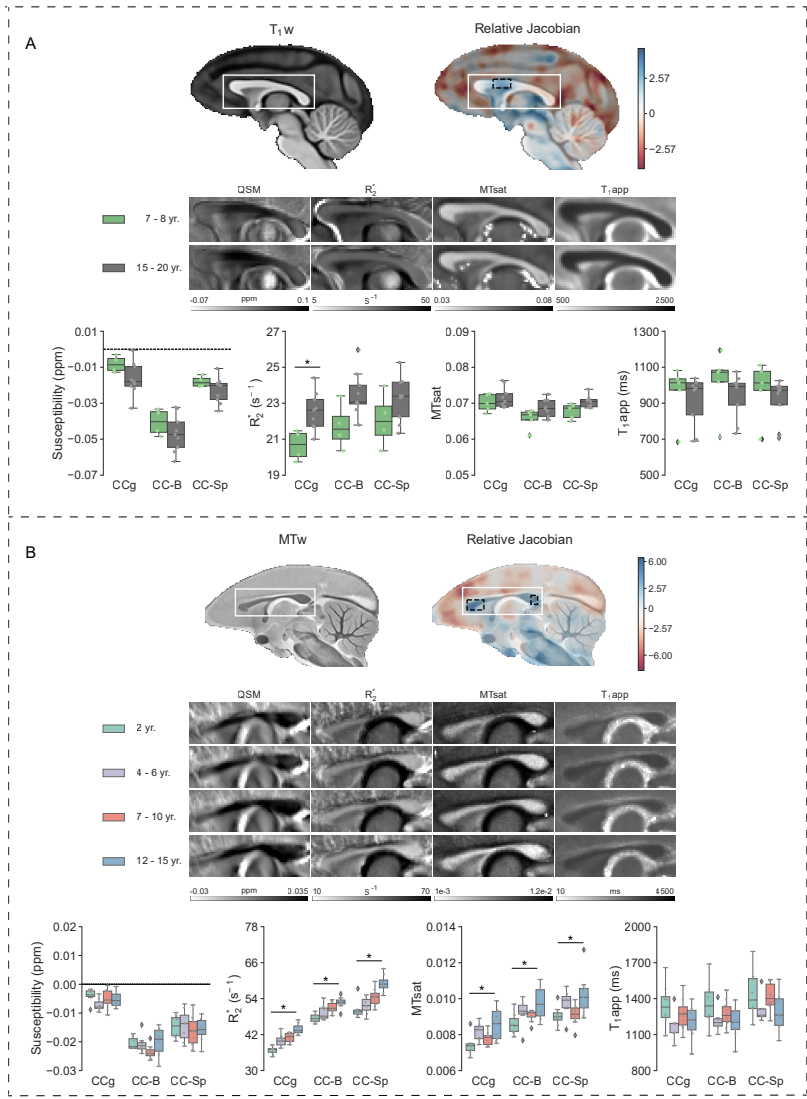


**Figure 5.9:** Age associations with the morphometric and microstructural characteristics of the corpus callosum. **A.** Macaque brain population-averaged  $T_1w$  template image, with overlaid Jacobian analyzed z-score map. The relative Jacobian determinant maps were calculated using warps from the subject  $T_1w$  scan to the final population-averaged template. Negative z-score values indicate tissue shrinkage, while positive z-score values indicate tissue expansion as monkeys get older. The dotted black box on the z-score map for the macaque brain shows significant age-related enlargement in one small area of the corpus callosum body. The macaque brain corpus callosum is highlighted in the QSM,  $R_2^*$ , MTsat, and  $T_{1app}$  average templates. The QSM,  $R_2^*$ , MTsat, and  $T_{1app}$  based regional differences across age groups are depicted in the box plots. **B.** Marmoset brain population-averaged MTw template image, with overlaid Jacobian determinant analysis calculated z-score map. The dotted black boxes on the z-score map for the marmoset brain show age-related significant expansion in genu and splenium of the corpus callosum. The relative Jacobian determinant maps were calculated using warps from the subject MTw scan to the final population-averaged template. Abbreviations: CCg - genu, CC-B - body, and CC-Sp - splenium.

### 5.3.5 QSM ECHO TIME DEPENDENCE

In both marmoset and macaque brains, the subcortical gray matter nuclei (Pu, GP, Thal, and SN) displayed susceptibility echo time (TE) dependence to varying degrees. All aging groups had different temporal curves of susceptibility (tQSM) for subcortical structures across ROIs. The macaque brain showed a more prominent age-related positive shift in tQSM profiles than the marmoset brain (Figure 5.10A and B). The nonlinearity of tQSM profiles in Pu, GP, and SN in the macaque brain increased with age (Figure 5.10A). In comparison to the other examined subcortical areas, the thalamus showed the least TE dependency. For small echo times, the tQSM profile differences in the GP were substantial, and the tQSM profile gradually deteriorated faster in elderly macaques than in young adults (Figure 5.10A).

In marmosets, only the GP showed age-related variations in tQSM profiles (Figure 5.10B). Specifically, tQSM profiles of the marmoset GP showed a positive shift with increasing age. The tQSM profiles of the remaining subcortical regions (Pu, Thal, and SN) showed no apparent age-related changes. Furthermore, the overall trend of tQSM profiles in macaque and marmoset brains was similar.

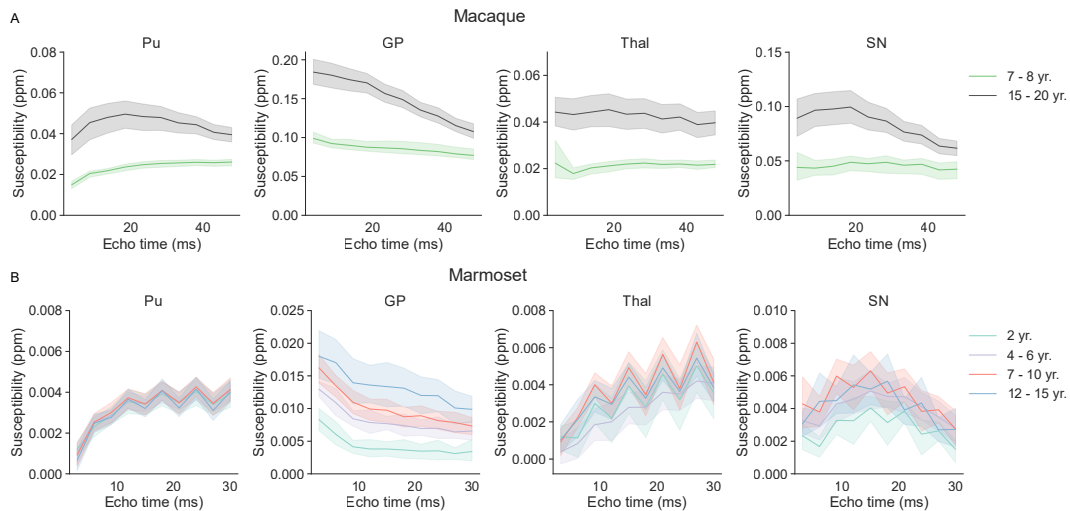


**Figure 5.10:** Magnetic susceptibility echo time dependence in macaque and marmoset brains. **A.** In the macaque brain, subcortical regions (Pu, GP, Thal, and SN) revealed a positive age-related shift in susceptibility temporal (tQSM) profiles over echo-times. A positive shift in the tQSM profiles in the macaque Pu, GP, and SN was associated with an increased nonlinearity in the curve. **B.** The tQSM profiles in the marmoset Pu, GP, Thal, and SN. In comparison to the macaque brain, the positive age-related shift in tQSM profiles was only found in the marmoset brain GP. In the marmoset brains Pu, Thal, and SN, no significant age-related changes in tQSM profiles were identified.

## 5.4 DISCUSSION

In this *in vivo* study, we demonstrated the capacity of multiple MRI contrasts to characterize age-related alterations in the macaque and marmoset brains. Brain morphometry, QSM,  $R_2^*$ , MTsat,  $T_{1app}$ , FA, MD, AD, and RD were assessed and reported across age groups in 14 healthy macaques and 34 healthy marmosets. Age-related morphological, white matter tissue integrity and tissue iron concentration changes in the brain are captured using a multi-contrast MRI approach. Macaques and marmosets' age-related alterations will help us figure out how effectively they mimic human aging. We believe this study contributes to a better understanding of macaques and marmosets' translational capacities as animal models for studying healthy human aging.

QSM and  $R_2^*$  are the most effective *in vivo* methods for determining iron content in the brain (Haacke et al., 2015; Hametner et al., 2018). Both macaques and marmosets showed a significant age-related increase in magnetic susceptibility and  $R_2^*$  in subcortical gray matter areas (Pu, GP, Thal, and SN), which is consistent with human aging studies [Betts et al., 2016, Bilgic et al., 2012, Li et al., 2021, Hallgren & Sourander, 1958, Daugherty & Raz, 2013]. The magnetic susceptibility and  $R_2^*$  values of Pu, GP, Thal, and SN were much higher than those of PFC, V2-V4, and white matter, regardless of age. This is because subcortical gray matter has a higher iron concentration than cortical gray and white matter. In macaque and marmoset brains, the globus pallidus (GP) showed the highest magnetic susceptibility and  $R_2^*$  values compared to other brain areas, as is also the case in the human brain [Bilgic et al., 2012]. However, several human studies have found that the putamen has the highest iron levels, followed by the globus pallidus [Ramos et al., 2014, Hallgren & Sourander, 1958, Acosta-Cabrero et al., 2016]. The hippocampus of macaques and marmosets showed a considerable increase in  $R_2^*$  with age, which was consistent with the human hippocampus [Betts et al., 2016, Rodrigue et al., 2013]. However, magnetic susceptibility of the macaque and marmoset hippocampus was found to decrease with age (Figure A.9). An increase in iron in the hippocampus has previously been related to memory loss and a reduction in hippocampal volume in humans [Rodrigue et al., 2013, Bartzokis et al., 2011].

There were no age-related white matter changes in macaque and marmoset MTsat, with the exception of the corpus callosum in marmosets. MTsat has been shown to be a marker of white matter integrity. The age-related increase in MTsat in the genu, body, and splenium areas of the marmoset corpus callosum was in contrast to previous human studies, which showed an age-related decline in MTsat [Callaghan et al., 2014, Gunning-Dixon et al., 2009, Seiler et al., 2014]. In humans, age-related reductions in white matter integrity, especially in the prefrontal cortex, are linked to deteriorated cognitive functions [Gunning-Dixon et al., 2009].

In macaques and marmosets, whole-brain morphometry analyses showed an age-related

decline in gray-white matter volume ratio, which has also been shown in human aging studies [Farokhian et al., 2017]. The corpus callosum morphometric analysis revealed an age-related expansion in specific sections. According to a recent study, a decrease in corpus callosum volume is a distinctive aspect of human brain aging [Westerhausen et al., 2021]. In baboons and capuchin monkeys, there was no evidence of an age-related reduction in corpus callosum volume, which is different from humans and Chimpanzees [Westerhausen & Meguerditchian, 2021, Westerhausen et al., 2021, Phillips & Sherwood, 2012]. A continuous linear increase in corpus callosum volume from young to old age is reported in baboons, which could explain some of the observed age-related changes in the macaque and marmoset corpus callosum. Furthermore, previous studies on the effects of aging on the corpus callosum morphology and density of myelinated nerve fibers in the rhesus macaque has also reported an age-related reduction in myelinated nerve fiber density (20% per unit area), degeneration of myelin sheath, and impaired remyelination [Bowley et al., 2010, Peters, 2002].

Independent of age, all studied subcortical areas in macaque and marmoset brains showed magnetic susceptibility echo time (TE) dependence. Overall, the tQSM profiles in the macaque and marmoset brains appeared to be similar. In the macaque brain subcortical areas, the positive age-related shift in tQSM profiles was stronger than in the marmoset brain. The shift in tQSM profiles was also accompanied by increased nonlinearity levels in the macaque brain Pu, GP, Thal, and SN. However, in marmosets, only GP showed an age-related positive shift in tQSM profiles, while Pu, Thal, and SN did not. The tQSM profiles in the GP, Thal, and SN of young macaques followed a similar pattern to the human profiles [Sood et al., 2017]. Furthermore, tQSM profiles in macaques and marmosets Pu followed a higher upward trend than tQSM profiles in humans, which showed a decline in tQSM profiles across TEs [Sood et al., 2017]. To our knowledge, this is the first study that focuses on QSM TE dependence across healthy aging. To establish a relationship between magnetic susceptibility, TE dependence, and tissue microstructure, more research is required.

The cross-sectional design of this study was one of its limitations. In order to measure changes in the brain, longitudinal studies are more robust and reliable in aging research.

In summary, we found age-related changes in iron and myelin content in cortical, subcortical, and white matter areas. In both macaques and marmosets, the effect of increased iron in subcortical nuclei was found to be the strongest age-related effect. MT saturation and dMRI results showed varying degrees of sensitivity to age-related white matter microstructural changes. Furthermore, the gray-white matter ratio in the brains of macaques and marmosets declined with age. Different MRI contrasts showed varying age-related changes, which prompts the validation of those contrasts against histology.

## MRI - HISTOLOGY COMPARISON

This study looks at how the brains of macaques and marmosets change with age *in vivo*. However, the empirical findings must be confirmed using histology as the ground truth. In a preliminary study, we have used one young adult and one geriatric marmoset brain. The brains were divided into two hemispheric portions (left and right). The right hemisphere was used to make a 3D brain holder that allowed for exact brain orientation during MRI scanning and histology sectioning. Young and elderly brain hemispheres were initially placed in 4 % paraformaldehyde (PFA), which is MRI sensitive. To scan the brains in an MRI insensitive solution, the brains were first placed in PBS for 24 hours before being placed in Fomblin, an MRI-invisible lubricant. Both hemispheres were scanned on a 9.4 T Bruker BioSpec MR system, equipped with the BGA 12S gradient. A 40 mm quadrature transmit/receive coil was used for signal transmission and detection.

Parameters	ME-GRE	MT	PD	T <sub>1</sub>
Pulse sequence	3D ME-GRE	3D FLASH	3D FLASH	3D FLASH
Native resolution (isotropic) ( $\mu\text{m}^3$ )	100	100	100	100
Field of view ( $\text{mm}^2$ )	$36 \times 25.6$	$36 \times 25.6$	$36 \times 25.6$	$36 \times 25.6$
Acquisition matrix	$360 \times 256$	$360 \times 256$	$360 \times 256$	$360 \times 256$
Total acquisition time (hrs)	5:37	4:06	4:18	4:18
TR/TE (ms)	43.8/[3.2/3.8/38]	16.8/4.2	16.8/4.2	16/4.2
Flip angle (degree)	25	5	5	25
Number of averages	5	10	10	10

**Table 5.3:** For postmortem marmoset brains, MRI acquisition parameters for ME-GRE, MTw, PDw, and T<sub>1</sub>w scans.

We used high-resolution (100  $\mu\text{m}$  isotropic) MRI data to compute QSM,  $R_2^*$ , MTsat, and T<sub>1</sub>app maps as demonstrated in Supplementary Figures A.10 and A.11. High-resolution QSM and  $R_2^*$  revealed increased contrast with age in subcortical structures (Supplementary Figure A.10). Furthermore, QSM,  $R_2^*$ , MTsat, and T<sub>1</sub>app also demonstrated higher sensitivity to cortical myelination, which is important for studying cortical myeloarchitecture. Multi-layer white matter structure can be clearly seen in the marmoset brain QSM,  $R_2^*$ , MTsat and T<sub>1</sub>app maps (Supplementary Figure A.11).

In preliminary findings, ferritin immunohistochemistry showed age-related iron accumulation in the basal ganglia, which mirrored the *in vivo* results. In future, MRI and histological results from all 34 marmosets will be compared. Furthermore, quantitative values from cortical, subcortical, and white matter areas will be compared between young and old marmoset brains (Supplementary Figure A.12).

In conclusion, we believe that comparing multi-contrast MRI with histology will aid in the translation of aging research from non-human primates to clinical populations.

*The end of one thing is just the beginning of another.*

Simone Elkeles

# 6

## General Discussion and Conclusions

MRI has been successfully used in basic neuroscience, clinical research, and daily diagnostics of human neurologic disease. Besides its undoubted benefits, MRI provides only an indirect measure of tissue microstructure. However, MRI comes with a variety of different contrast mechanisms. Suitable combinations of those may allow for a more precise *in vivo* tissue characterization. In humans, a direct comparison of MRI findings and postmortem analysis of brain tissue is limited. Animal models can help bridge this gap by correlating microstructural changes, such as alterations of myelin and axons, with the observed MRI signal. In this thesis, I took advantage of both, genetically modified mice, which often result in very specific, targeted changes in the brain, and NHPs, which provide a very close similarity to the human situation.

I focused on imaging the myelin and iron content in the brain by utilizing multiple MRI contrasts and advanced combinations of those contrasts. Myelin and iron are essential for normal brain functions. Altered myelin and iron are significant indicators of the development and progression of demyelinating and neurodegenerative diseases and may play a key role in the pathophysiology of these diseases. Changes in myelin and iron content have been observed in healthy aging and age-related disease.

The work described here investigated the sensitivity and specificity of currently available myelin and iron-related MR imaging techniques. Neuroimaging researchers have been seeking to image myelin and iron *in vivo* in the brain for decades. Recent meta-analytic studies show that myelin is sensitive to several quantitative MR biomarkers; however, no biomarker

seems to be more sensitive than another [Lazari & Lipp, 2021]. The findings of this thesis also support these conclusions. In mouse mutants with altered myelin, I discovered that current diffusion MRI techniques (DTI, DKI, WMTI, and NODDI) are sensitive and partially specific to myelin and axon-related alterations. However, none of the utilized diffusion model was superior to the other ones.

In addition, I looked into MR methods such as magnetization transfer saturation, magnetic susceptibility, and relaxometry. These techniques provide a number of quantitative MR markers that are sensitive to changes in myelin and iron but not necessarily specific to them [Hametner et al., 2018, Hagiwara et al., 2018]. As these quantitative markers reflect different biophysical mechanisms in a complex tissue environment [Edwards et al., 2018, Does, 2018, Möller et al., 2019], their combination may be advantageous here. And indeed, by appropriate linear combinations, I could significantly improve the segmentation of myelinated tissue.

These combinations of differently weighted images and parameter maps require MR templates in a common space [Jung et al., 2021, Bazin et al., 2020, Dadar et al., 2021]. Likewise, region-of-interest or tissue segmentation-based quantitative analysis strongly relies on such templates. To improve the neuroimaging data analysis in cynomolgus macaques, I developed a multi-contrast high-resolution MRI template. The created templates in stereotaxic orientation will serve as a common space for the single-subject MRI scan standardization and anatomical structural localization. Furthermore, the availability of multiple structural ( $T_1$ -weighted,  $T_2$ -weighted, Magnetization Transfer weighted, and Multi-echo gradient recalled echo) and parametric (QSM,  $R_2^*$ , MTsat, and  $T_{1app}$ ) contrasts in the same template space will aid in developing new brain parcellations and improving already existing parcellations. All the developed MRI templates, anatomical parcellations (including cortical, subcortical, and white matter), and brain surfaces will be openly made available to the scientific community.

Utilizing the imaging methods established here and the corresponding analysis pipelines, I compared the MRI finding in healthy adult humans and cynomolgus monkeys and did a comparative study on brain aging of cynomolgus monkeys and marmosets. Both studies will be briefly discussed in the following. The study of human brain neuroanatomy, brain circuitry, and functions of the healthy and sick brain has benefited greatly from NHPs [Vitek & Johnson, 2019]. However, the similarities and the differences in QSM and  $R_2^*$  measured iron and myelin content between human and NHP brains are neither well known nor well understood yet. In this thesis, I examined both humans and NHPs, using nearly identical MRI parameters to provide a thorough comparison. I found similar magnetic susceptibility and  $R_2^*$  values in the human and NHP brain, with the exception of a few areas such as the red nucleus and cerebrospinal fluid. Furthermore, I found that the human and NHP brains have similar QSM echo time dependence, except for a few areas further supporting the great



value of NHPs for biomedical research [Colman, 2018, Mattison & Vaughan, 2017].

In humans, brain aging has been associated with changes in gray and white matter volume [Hedman et al., 2012, Farokhian et al., 2017, Smith et al., 2007]. The morphometric analyses required for such studies strongly rely on the quality of the (mostly automatically performed) brain segmentation, commonly done on conventional  $T_1$ -weighted and  $T_2$ -weighted images [Tullo et al., 2019, Callaert et al., 2014, Smith et al., 2007]. However, in particular, the contrast between the subcortical structures and the adjacent white matter is very limited on those  $T_1$ - and  $T_2$ -weighted images.

In this thesis, I propose a method (SILiCON and TQ-SILiCON) to overcome these limitations. The weighted linear combination of images utilizing different contrast mechanisms (e.g.,  $T_1$ , MT, QSM) provides excellent visualization of cortical, subcortical, and white matter. By adopting a clinically appropriate MRI data acquisition and limiting the number of contrasts to the two most contributing, that is,  $T_1$  and QSM, the required measurement time becomes suitable for clinical use in humans.

Moreover, I have applied the multi-contrast MRI approach to detect age-related alterations in the macaque and marmoset brain. I compared monkeys of various ages, ranging from young adults to the elderly. In contrast to reports about older humans, I observed almost no changes in dMRI and magnetization transfer in the monkeys with increasing age [Callaghan et al., 2014, Gunning-Dixon et al., 2009]. However, similar to humans, macaques and marmosets showed a decreased gray-to-white matter ratio with age and age-related iron accumulation in subcortical areas.

This raises the possibility that the brain of NHPs is less affected by aging, or that the monkeys in our studies, who were old relative to their current life expectancy in captivity, are not comparable old to those humans whose life expectancy has been extended due to changing lifestyles and advanced therapeutic interventions in recent decades.

Future work will include histological validation of the proposed multi-contrast MRI method, as well as further investigation of the NHP brain's age-related alterations.

# A

## Supplementary Material

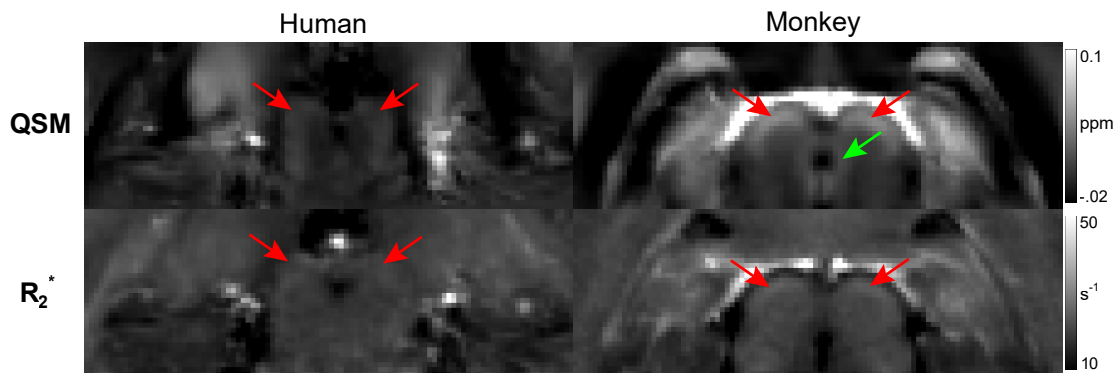


**Figure A.1:** In the axial view of the human and monkey brain Quantitative Susceptibility Mapping (QSM) and effective transverse relaxation rate ( $R_2^*$ ) templates, the superior colliculus is highlighted by the red arrows. In both human and monkey brains, the QSM template has stronger superior colliculus contrast than the  $R_2^*$  template. In comparison to the human brain QSM template, the periaqueductal gray is more evident on the monkey brain QSM template (highlighted by the green arrow).

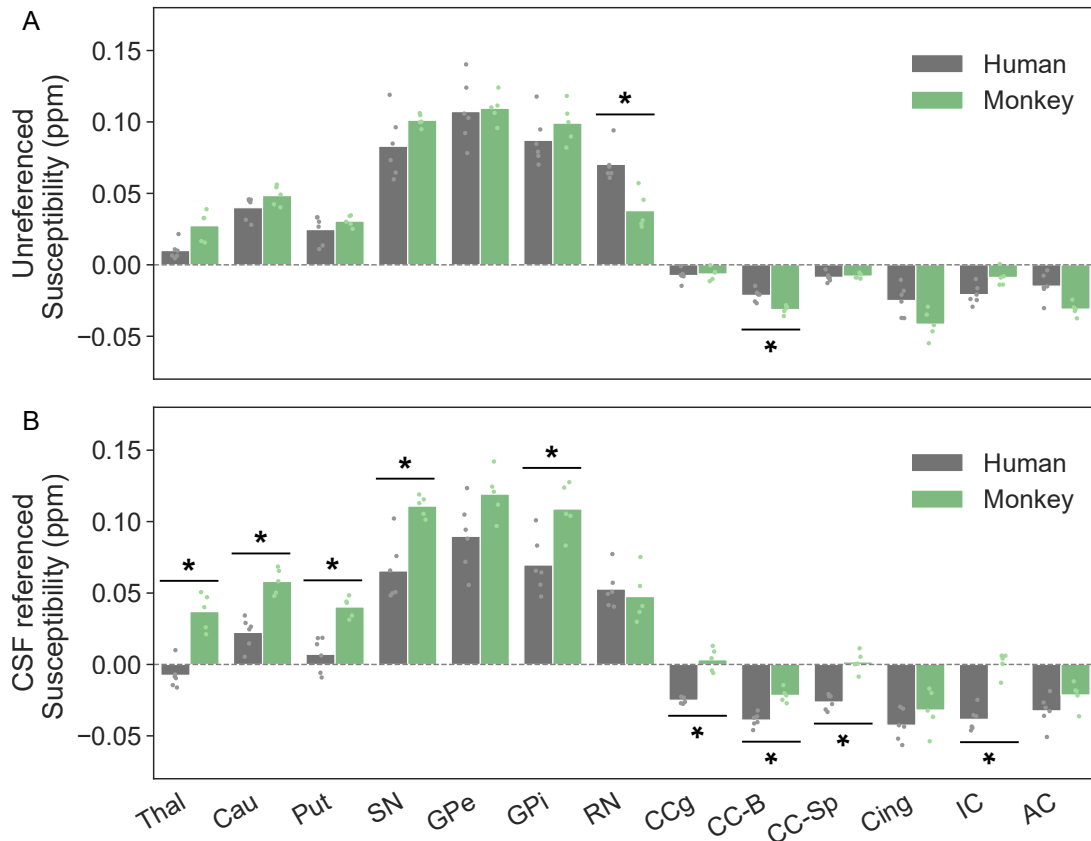


**Figure A.2:** Unreferenced (A) and cerebrospinal fluid (CSF) normalized (B) magnetic susceptibility values for seven gray and six white matter regions-of-interest (ROIs) in the human and monkey brains. Mean magnetic susceptibility with the distribution of individual observations for unreferenced (non-normalized) and CSF normalized maps (in parts per million). (A) In both the RN and the CC-B, unreferenced QSM data reveal significant differences between human and monkey brains. In comparison to the monkey red nucleus, the human red nucleus had higher magnetic susceptibility values. In addition, the monkey brain had relatively higher diamagnetic values than the human brain. (B) The Thal, Cau, Put, SN and GPi ROIs in the CSF normalized gray matter analysis revealed significantly higher QSM values in the monkey brain than in the human brain. In the white matter ROIs, the human brain displayed relatively higher diamagnetic susceptibility values than the monkey brain. Abbreviations: middle thalamus (Thal), caudate (Cau), putamen (Put), substantia nigra (SN), external globus pallidus (GPe), internal globus pallidus (GPi), red nucleus (RN), corpus callosum genu (CCg), corpus callosum body (CC-B), corpus callosum splenium (CC-Sp), cingulum (Cing), internal capsule (IC), anterior commissure (AC).

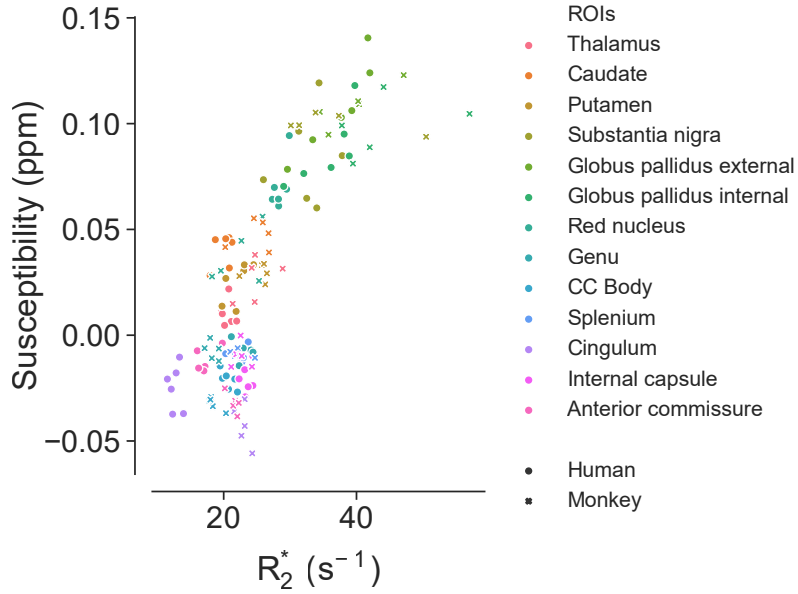


Figure A.3: Magnetic susceptibility versus  $R_2^*$  scatterplot for human and monkey brain regions-of-interest.

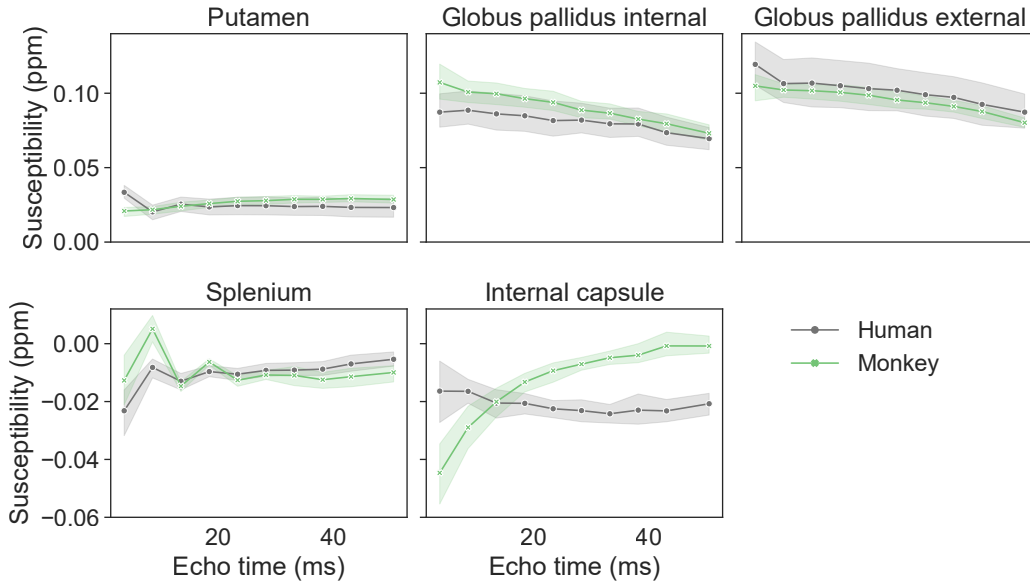
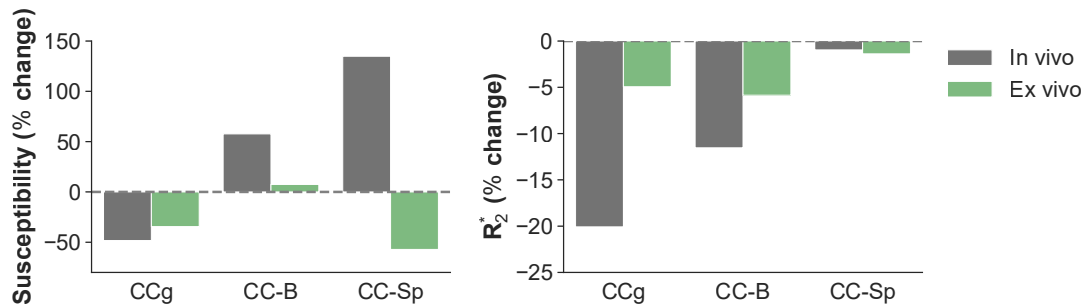
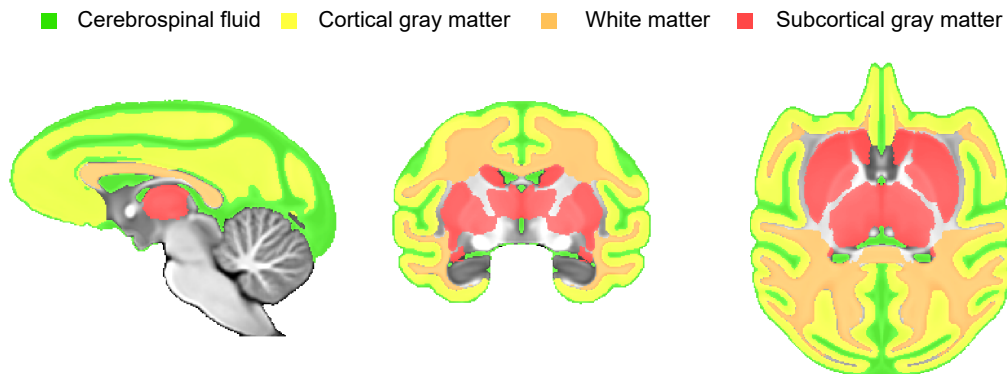


Figure A.4: Magnetic susceptibility echo time dependence for gray and white matter regions-of-interest in human and monkey brains. Magnetic susceptibility temporal profile results are displayed for putamen, internal globus pallidus, external globus pallidus, splenium, and internal capsule. The individual plot shows the susceptibility temporal response for the group mean (thin dotted line) and confidence interval (Shaded area). Except for the internal capsule, the tQSM profiles of human and monkey brains were very comparable.



**Figure A.5:** The effects of human and monkey head orientations in the magnetic field on magnetic susceptibility and  $R_2^*$ . *In vivo* measurements of the human and monkey brains were performed in the supine and prone positions, respectively (gray bars). To study the QSM and  $R_2^*$  changes produced by the subject's head orientation inside the magnetic field, one *ex vivo* macaque head was measured in supine and prone positions (green bars). In all of the brain areas examined, *in vivo* supine-prone differences are far greater than *ex vivo* supine-prone differences. Abbreviations: CCg - corpus callosum genu, CC-B - corpus callosum body, and CC-Sp - corpus callosum splenium.



**Figure A.6:** The contrast-to-noise ratio estimation was performed using segmented macaque brain regions-of-interest. The whole-brain tissue was segmented into four tissue types: cerebrospinal fluid, cortical gray matter, white matter, and subcortical gray matter.

# dpzCyno

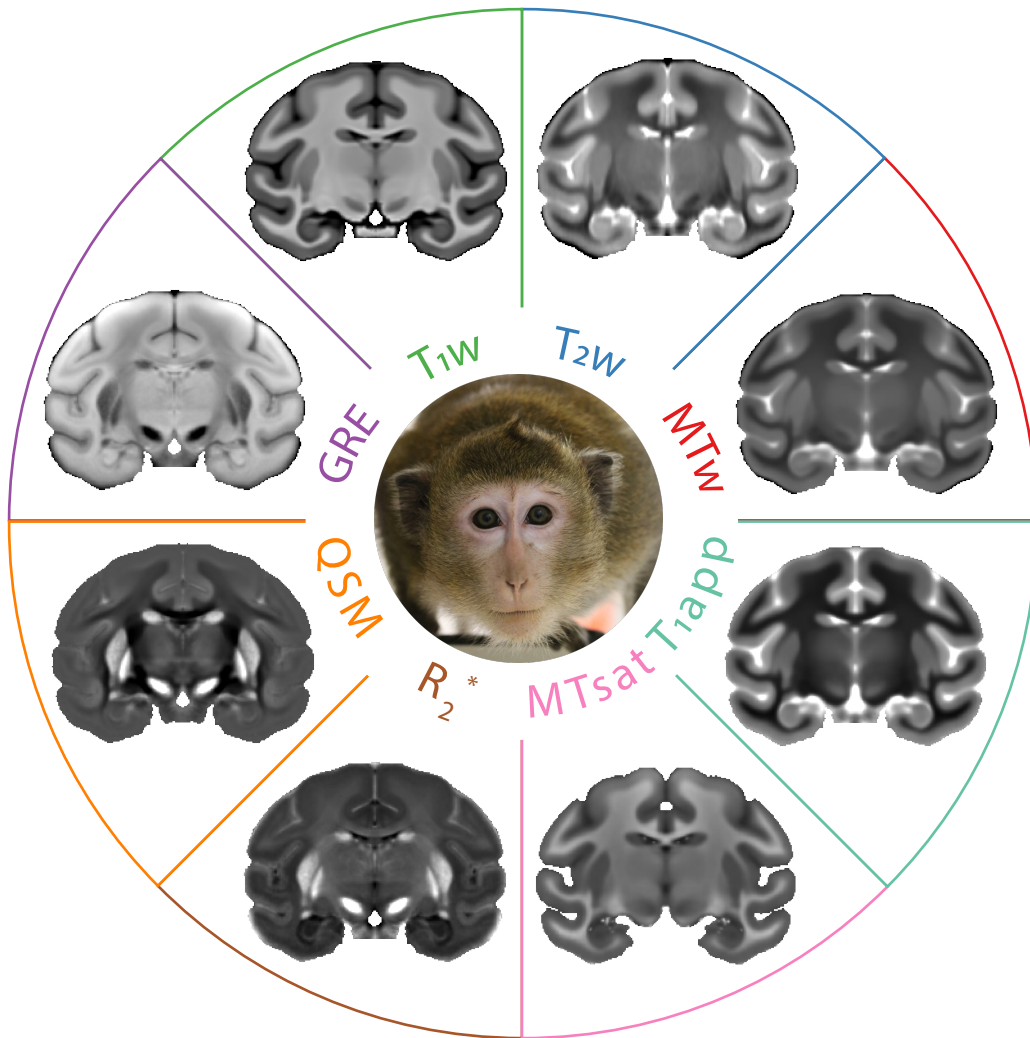


Figure A.7: Multi-contrast Deutsches Primatenzentrum cynomolgus macaque (DPZCYN0) standard templates.

Symmetric DPZCYNO templates

Contrasts	Cort GM - WM	Cort GM - Subcort GM	Subcort GM - WM
T <sub>1</sub> w	3.1	1.3	1.8
MTw	0.7	0.04	0.6
mGRE	0.05	1	1
T <sub>2</sub> w	0.6	0.2	0.4
QSM	0.7	3.4	2.8
R <sub>2</sub> <sup>*</sup>	0.1	1.6	1.7
MTsat	1	0.1	1.1
T <sub>1</sub> app	1.2	0.4	0.8

**Table A.1:** The contrast-to-noise ratio (CNR) in the symmetric DPZCYNO templates. The CNR between cortical gray and white matter (CNR = 3.1) was highest in the T<sub>1</sub>w template. Furthermore, the CNR between cortical and subcortical gray matter (CNR = 3.4) and subcortical gray and white matter (CNR = 2.8) was highest in the QSM template. Abbreviations: Cort GM - cortical gray matter, Subcort GM - subcortical gray matter, and WM - white matter.

Asymmetric DPZCYNO templates

Contrasts	Cort GM - WM	Cort GM - Subcort GM	Subcort GM - WM
T <sub>1</sub> w	2.7	1.1	1.5
MTw	0.4	0.1	0.4
mGRE	0.1	0.6	0.7
T <sub>2</sub> w	0.4	0.1	0.3
QSM	0.7	3.3	2.7
R <sub>2</sub> <sup>*</sup>	0.05	1.3	1.4
MTsat	0.7	0.1	0.6
T <sub>1</sub> app	0.7	0.3	0.5

**Table A.2:** The contrast-to-noise ratio (CNR) in the asymmetric DPZCYNO templates. The CNR between cortical gray and white matter (CNR = 2.7) was highest in the T<sub>1</sub>w template, just like in the symmetric templates. Cortical and subcortical gray matter (CNR = 3.3) and subcortical gray and white matter (CNR = 2.7) had the highest CNR in the QSM template. Abbreviations: Cort GM - cortical gray matter, Subcort GM - subcortical gray matter, and WM - white matter.

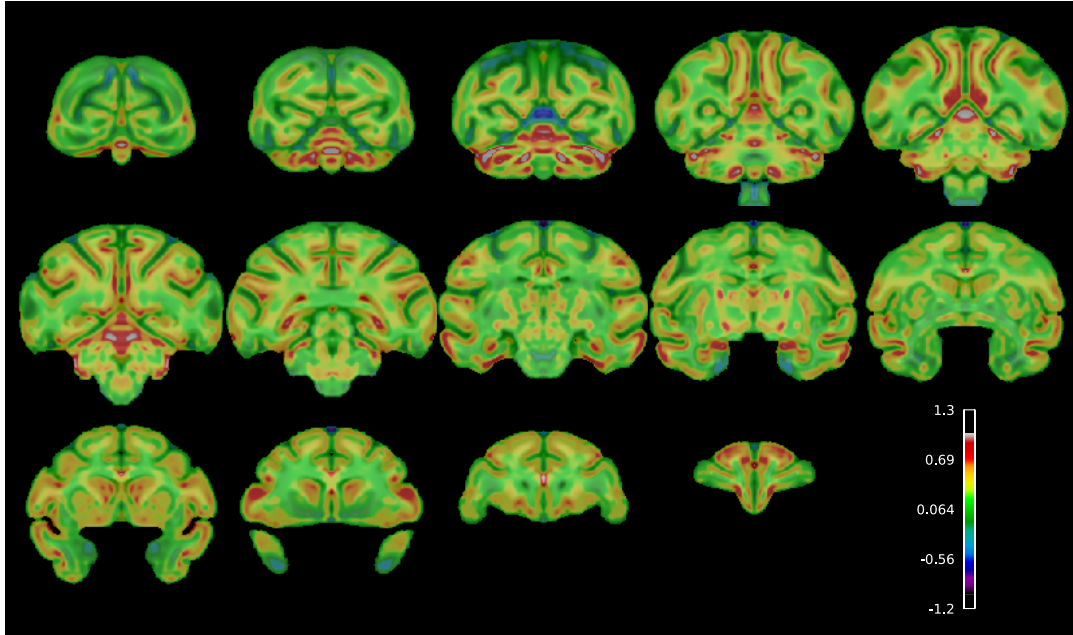


**Figure A.8:** We have used the Jacobian determinant analysis to estimate the morphological differences between the cynomolgus and rhesus macaque brains. First, we used only five young adults between the ages of 7 and 8 years old to create a rhesus macaque template age comparable symmetric template from cynomolgus macaques. We then nonlinearly registered the newly created symmetric  $T_1w$  template from cynomolgus macaques to asymmetric  $T_1w$  template from rhesus macaques (NMT v2) [Jung et al., 2021]. The rhesus macaques employed in the creation of the NMT v2 symmetric template were between the ages of 3.2 and 13.2 years. The log Jacobian determinant was calculated using the deformation fields generated by the nonlinear alignment of the symmetric cynomolgus macaque template to the rhesus macaque template. The positive log Jacobian values exhibit tissue expansion, and negative log Jacobian values exhibit tissue shrinkage from the cynomolgus macaque template to the rhesus macaque template. Cortical gray matter areas showed more tissue expansion than white matter areas. The symmetric  $T_1w$  template-based three-tissue segmentation results indicated that rhesus macaques had a higher gray-white matter volume ratio (1.74) than cynomolgus macaques (1.43). Some of the limitations of this method are: (1) The cynomolgus and rhesus macaques used in the template construction were of different ages. (2) The rhesus macaque template was made up of scans from 25 males and 6 females, whereas the cynomolgus macaque template was made up of scans from 5 females.



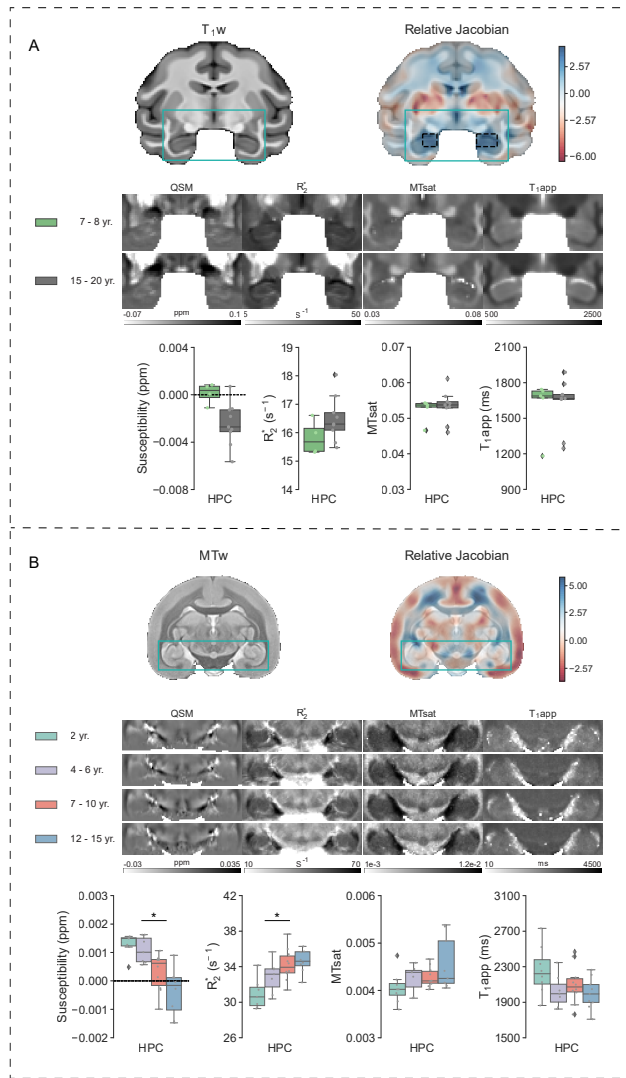


**Figure A.9:** Age associations with the morphometric and microstructural characteristics of the hippocampus. **A.** Macaque brain population-averaged  $T_{1w}$  template image, with overlaid Jacobian determinant analysis calculated z-score map. The relative Jacobian determinant maps were calculated using warps from the subject  $T_{1w}$  scan to the final population-averaged  $T_{1w}$  template. Positive z-score values indicate tissue enlargement, while negative z-score values indicate tissue shrinkage as monkeys get older. The dotted black box on the z-score map for the macaque brain shows substantial age-related enlargement in one small area of the hippocampus. The macaque brain hippocampus area is highlighted in the QSM,  $R_2^*$ , MTsat, and  $T_{1app}$  average templates. The QSM,  $R_2^*$ , MTsat, and  $T_{1app}$  based regional differences across two aging groups are depicted in the box plots. **B.** Marmoset brain population-averaged MTw template image, with overlaid Jacobian determinant analysis calculated z-score map. The relative Jacobian determinant maps were calculated using warps from the subject MTw scan to the final population-averaged MTw template. The marmoset brain hippocampus area is highlighted in the QSM,  $R_2^*$ , MTsat, and  $T_{1app}$  average templates. The QSM,  $R_2^*$ , MTsat, and  $T_{1app}$  based regional differences across four aging groups are depicted in the box plots. Abbreviations: HPC - the hippocampus.

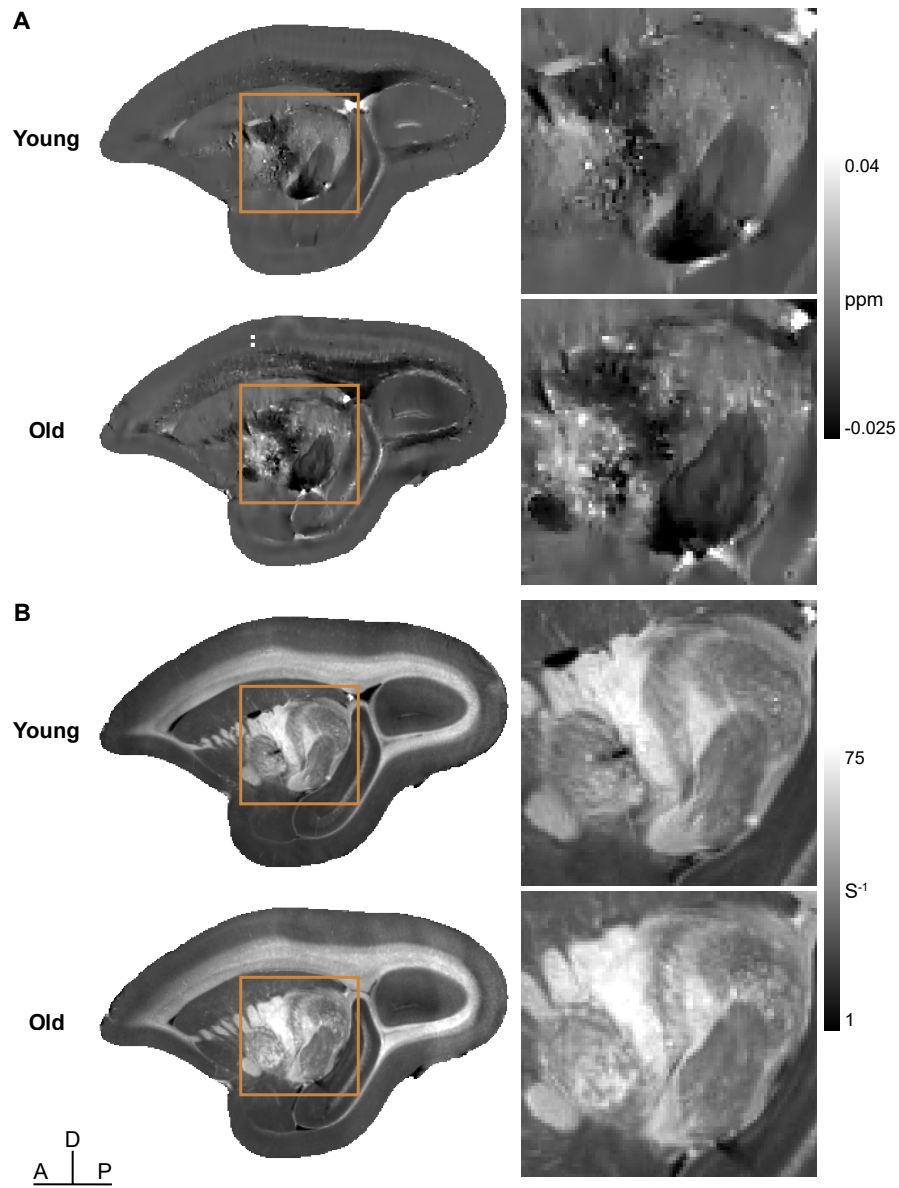


**Figure A.10:** QSM (A) and  $R_2^*$  (B) maps in the young and old marmoset brains. QSM and  $R_2^*$  maps were calculated from multi-echo gradient-recalled echo (ME-GRE) data acquired at 9.4 Tesla with  $100\ \mu\text{m}$  isotropic resolution. The locations of iron-rich subcortical structures in sagittal view are indicated on the magnified visualization of QSM (A) and  $R_2^*$  (B) maps. Abbreviations: A - anterior, P - posterior, and D - dorsal.

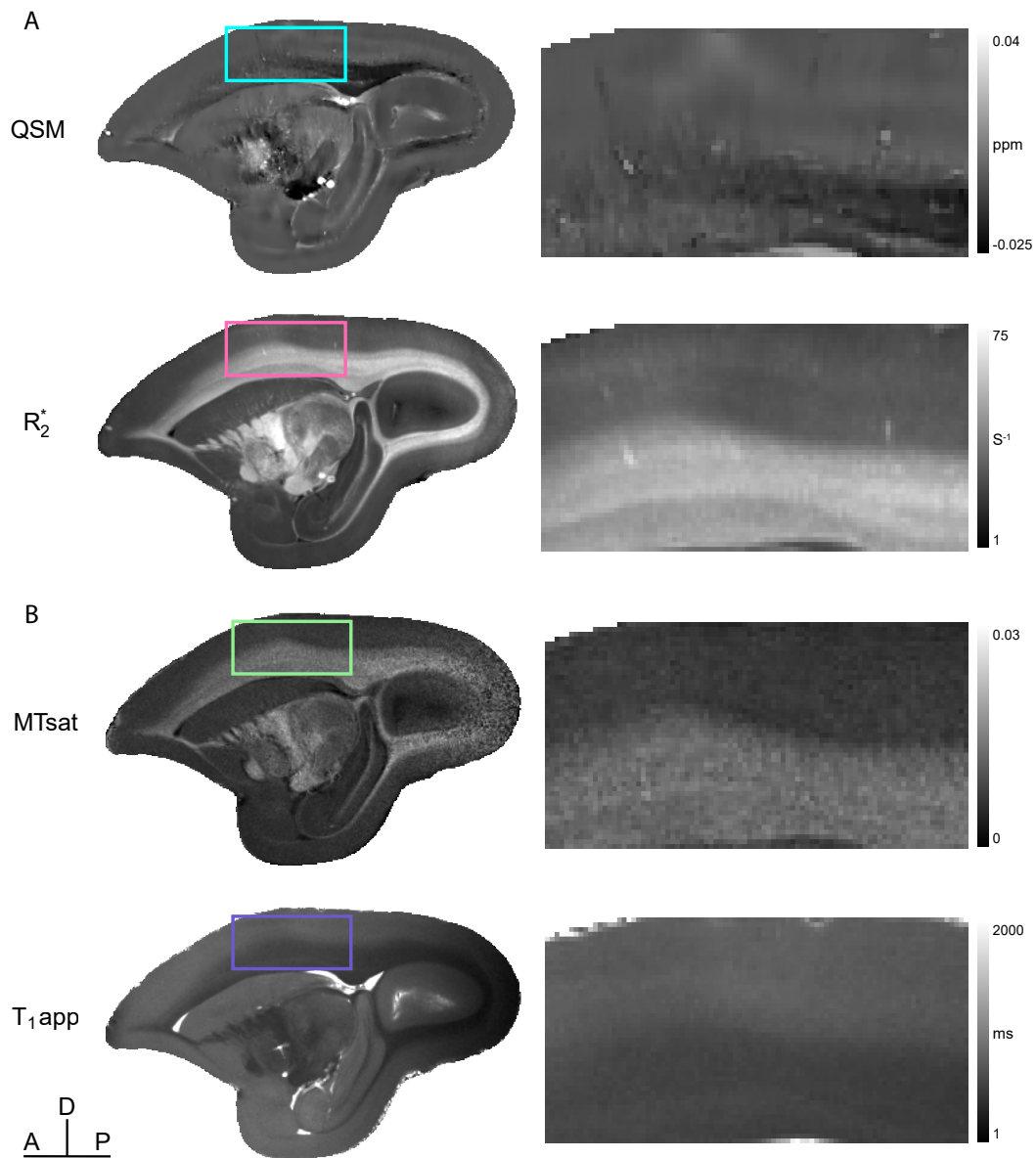


**Figure A.11:** A. QSM and  $R_2^*$  maps of the marmoset brain in sagittal view. The locations of iron and myelin-rich cortical and white matter structures are indicated on the magnified visualization of QSM and  $R_2^*$  maps.  $R_2^*$  is more reliable and sensitive to cortical iron and myelin than QSM [Hametner et al., 2018]. Myelin is diamagnetic within the white matter. B. MTsat and  $T_{1app}$  maps of the marmoset brain in sagittal view. The locations of cortical and white matter structures are indicated on the magnified visualization of MTsat and  $T_{1app}$  maps. Abbreviations: A - anterior, P - posterior, and D - dorsal.

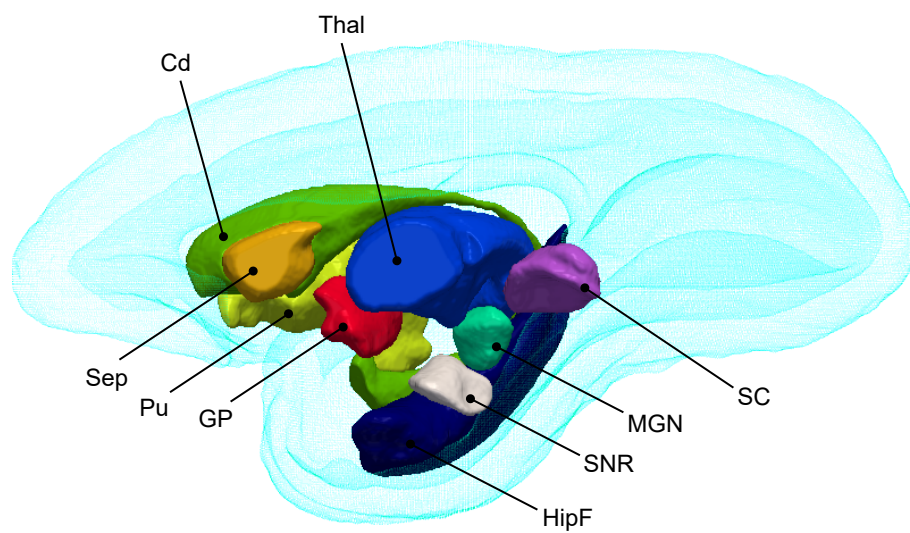


**Figure A.12:** The marmoset brain's subcortical regions-of-interest in sagittal view. Abbreviations: Cd - caudate, Thal - thalamus, Sep - septum, Pu - putamen, GP - globus pallidus, HipF - hippocampal formation, SNR - substantia nigra, MGN - medial geniculate nucleus, and SC - superior colliculus.

# B

## Research Outputs

### PEER-REVIEWED JOURNAL PUBLICATIONS

#### PREPRINT PUBLICATIONS

**Dadarwal, R.**, Ortiz-Rios, M., Boretius, S., 2021. *"Fusion of quantitative susceptibility maps and T<sub>1</sub>-weighted images improve brain tissue contrast in primates"*.  
<https://doi.org/10.1101/2021.10.05.462876> (link to the article)

#### MANUSCRIPTS IN PREPARATION

**Rakshit Dadarwal**, Amir Moussavi, and Susann Boretius. *"QSM and R<sub>2</sub><sup>\*</sup> mapping in human and non-human primate brains"*

**Rakshit Dadarwal**, and Susann Boretius. *"A multi-contrast MRI template of the cynomolgus macaque brain"*

**Rakshit Dadarwal**, Judith Mylius, and Susann Boretius. *"Multi-contrast MRI of the aging brain - A comparative study of cynomolgus macaques and common marmosets"*

## THE APPROACHES DESCRIBED IN THIS THESIS HAVE BEEN APPLIED IN THE PEER-REVIEWED PUBLICATIONS BELOW

Hafner, G., Guy, J., Witte, M., Truschow, P., Ruppel, A., Sirmipilatz, N., **Dadarwal, R.**, Boretius, S., Staiger, J.F., 2021. *Increased Callosal Connectivity in Reeler Mice Revealed by Brain-Wide Input Mapping of VIP Neurons in Barrel Cortex*. *Cereb. Cortex* 31, 1427–1443. <https://doi.org/10.1093/cercor/bhaa280> ([link to the article](#))

Lohrberg, M., Winkler, A., Franz, J., Meer, F. van der, Ruhwedel, T., Sirmipilatz, N., **Dadarwal, R.**, Handwerker, R., Esser, D., Wiegand, K., Hagel, C., Gocht, A., König, F.B., Boretius, S., Möbius, W., Stadelmann, C., Barrantes-Freer, A., 2020a. *Lack of astrocytes hinders parenchymal oligodendrocyte precursor cells from reaching a myelinating state in osmolyte-induced demyelination*. *Acta Neuropathol. Commun.* 8. <https://doi.org/10.1186/s40478-020-01105-2> ([link to the article](#))

Messinger, A., Sirmipilatz, N., Heuer, K., Loh, K.K., Mars, R.B., Sein, J., Xu, T., Glen, D., Jung, B., Seidlitz, J., Taylor, P., Toro, R., Garza-Villarreal, E.A., Sponheim, C., Wang, X., Benn, R.A., Cagna, B., **Dadarwal, R.**, Evrard, H.C., Garcia-Saldivar, P., Giavasis, S., Hartig, R., Lepage, C., Liu, C., Majka, P., Merchant, H., Milham, M.P., Rosa, M.G.P., Tasserie, J., Uhrig, L., Margulies, D.S., Klink, P.C., 2021. *A collaborative resource platform for non-human primate neuroimaging*. *NeuroImage* 226, 117519. <https://doi.org/10.1016/j.neuroimage.2020.117519> ([link to the article](#))

Wilke, J.B.H., Hindermann, M., Moussavi, A., Butt, U.J., **Dadarwal, R.**, Berghoff, S.A., Sarcheshmeh, A.K., Ronnenberg, A., Zihler, S., Arinrad, S., Hardeland, R., Seidel, J., Lühder, F., Nave, K.-A., Boretius, S., Ehrenreich, H., 2021. *Inducing sterile pyramidal neuronal death in mice to model distinct aspects of gray matter encephalitis*. *Acta Neuropathol. Commun.* 9, 121. <https://doi.org/10.1186/s40478-021-01214-6> ([link to the article](#))

## SELECTED CONFERENCE ABSTRACTS (PEER-REVIEWED)

**Rakshit Dadarwal**, and Susann Boretius. *”Multi-contrast MRI Atlas of the Cynomolgus Macaque Brain”*, In Proceedings of the 29th Annual Meeting of the International Society for Magnetic Resonance in Medicine (ISMRM), Vancouver, BC, Canada 2021; Abstract 2641.

**Rakshit Dadarwal**, and Susann Boretius. *”Merging  $T_1$  weighted images with QSM provides a unique contrast for brain tissue segmentation in humans and nonhuman primates”*, In Pro-

ceedings of the 29th Annual Meeting of the International Society for Magnetic Resonance in Medicine (ISMRM), (Virtual) 2021; Abstract 2671.

**Rakshit Dadarwal**, Judith Mylius, and Susann Boretius. *"Brain aging in cynomolgus macaques and common marmosets explored by mapping the magnetic susceptibility and  $R_2^*$ "*, In Proceedings of the 29th Annual Meeting of the International Society for Magnetic Resonance in Medicine (ISMRM), (Virtual) 2021; Abstract 3158.

**Rakshit Dadarwal**, Fabien Balezeau, Marcus Haag, Michael C. Schmid, Susann Boretius, and Michael Ortiz-Rios. *"Mapping white matter bundle tracts and cortical myelin from multi-contrast imaging in the awake macaque monkey"*, In Proceedings of the 29th Annual Meeting of the International Society for Magnetic Resonance in Medicine (ISMRM), (Virtual) 2021; Abstract 3108.

**Rakshit Dadarwal**, Amir Moussavi, and Susann Boretius. *"Quantitative Susceptibility Mapping (QSM): Echo time dependence in the human and nonhuman primate brain"*, In Proceedings of the 36th Annual Scientific Meeting of the European Society for Magnetic Resonance in Medicine and Biology (ESMRMB), Rotterdam, Netherlands 2019; Abstract S20.05.

**Rakshit Dadarwal**, Luzia Hintz, Amir Moussavi, and Susann Boretius. *"Quantitative Susceptibility Mapping of the Brain – A Comparative In vivo Study of Humans and Nonhuman Primates"*, In Proceedings of the 27th Annual Meeting of the International Society for Magnetic Resonance in Medicine (ISMRM), Montreal, QC, Canada 2019; Abstract 4921.

**Rakshit Dadarwal**, Amir Moussavi, Wiebke Möbius and Susann Boretius. *"How do current diffusion-based MR methods reflect hypomyelination – comparison of diffusion tensor, neurite orientation dispersion and density, and diffusion kurtosis imaging"*, In Proceedings of the Joint Annual Meeting of the International Society for Magnetic Resonance in Medicine (ISMRM) – European Society for Magnetic Resonance in Medicine and Biology (ESMRMB), Paris, France 2018; Abstract 3219.

**Rakshit Dadarwal**, Amir Moussavi, and Susann Boretius. *"The effects of b-shell selection on estimation of multi-compartment microscopic diffusion parameters"*, In: Proceedings of the 34th Annual Meeting of the European Society for Magnetic Resonance in Medicine and Biology (ESMRMB), Barcelona, Spain 2017; Abstract 206.

## References

- [Abdul-Rahman et al., 2007] Abdul-Rahman, H. S., Gdeisat, M. A., Burton, D. R., Lalor, M. J., Lilley, F., & Moore, C. J. (2007). Fast and robust three-dimensional best path phase unwrapping algorithm. *Applied Optics*, 46(26), 6623–6635. Publisher: Optical Society of America.
- [Abel et al., 2020] Abel, S., Vavasour, I., Lee, L. E., Johnson, P., Ackermans, N., Chan, J., Dvorak, A., Schabas, A., Wiggermann, V., Tam, R., Kuan, A. J., Morrow, S. A., Wilken, J., Laule, C., Rauscher, A., Bhan, V., Sayao, A.-L., Devonshire, V., Li, D. K., Carruthers, R., Traboulsee, A., & Kolind, S. H. (2020). Myelin Damage in Normal Appearing White Matter Contributes to Impaired Cognitive Processing Speed in Multiple Sclerosis. *Journal of Neuroimaging*, 30(2), 205–211. \_eprint: <https://onlinelibrary.wiley.com/doi/pdf/10.1111/jon.12679>.
- [Acosta-Cabronero et al., 2016] Acosta-Cabronero, J., Betts, M. J., Cardenas-Blanco, A., Yang, S., & Nestor, P. J. (2016). In Vivo MRI Mapping of Brain Iron Deposition across the Adult Lifespan. *The Journal of Neuroscience: The Official Journal of the Society for Neuroscience*, 36(2), 364–374.
- [Acosta-Cabronero et al., 2017] Acosta-Cabronero, J., Cardenas-Blanco, A., Betts, M. J., Butryn, M., Valdes-Herrera, J. P., Galazky, I., & Nestor, P. J. (2017). The whole-brain pattern of magnetic susceptibility perturbations in Parkinson’s disease. *Brain*, 140(1), 118–131.
- [Acosta-Cabronero et al., 2018] Acosta-Cabronero, J., Milovic, C., Mattern, H., Tejos, C., Speck, O., & Callaghan, M. F. (2018). A robust multi-scale approach to quantitative susceptibility mapping. *NeuroImage*, 183, 7–24.
- [Acosta-Cabronero et al., 2013] Acosta-Cabronero, J., Williams, G. B., Cardenas-Blanco, A., Arnold, R. J., Lupson, V., & Nestor, P. J. (2013). In Vivo Quantitative Susceptibility Mapping (QSM) in Alzheimer’s Disease. *PLOS ONE*, 8(11), e81093.



- [Alexander et al., 2007] Alexander, A. L., Lee, J. E., Lazar, M., & Field, A. S. (2007). Diffusion Tensor Imaging of the Brain. *Neurotherapeutics*, 4(3), 316–329.
- [Alexander et al., 2019] Alexander, D. C., Dyrby, T. B., Nilsson, M., & Zhang, H. (2019). Imaging brain microstructure with diffusion MRI: practicality and applications. *NMR in Biomedicine*, 32(4), e3841. \_eprint: <https://analyticalsciencejournals.onlinelibrary.wiley.com/doi/pdf/10.1002/nbm.3841>.
- [Alkemade et al., 2017] Alkemade, A., Hollander, G. d., Keuken, M. C., Schäfer, A., Ott, D. V. M., Schwarz, J., Weise, D., Kotz, S. A., & Forstmann, B. U. (2017). Comparison of T2\*-weighted and QSM contrasts in Parkinson’s disease to visualize the STN with MRI. *PLOS ONE*, 12(4), e0176130. Publisher: Public Library of Science.
- [Altman & Dittmer, 1974] Altman, P. & Dittmer, D. (1974). *Biology Data Book, Volume 3. 2nd edition*. Bethesda: Federation of American Societies for Experimental Biology, 2nd edition edition.
- [Andersson et al., 2003] Andersson, J. L. R., Skare, S., & Ashburner, J. (2003). How to correct susceptibility distortions in spin-echo echo-planar images: application to diffusion tensor imaging. *NeuroImage*, 20(2), 870–888.
- [Andersson & Sotiropoulos, 2016] Andersson, J. L. R. & Sotiropoulos, S. N. (2016). An integrated approach to correction for off-resonance effects and subject movement in diffusion MR imaging. *NeuroImage*, 125, 1063–1078.
- [Aung et al., 2013] Aung, W. Y., Mar, S., & Benzinger, T. L. (2013). Diffusion tensor MRI as a biomarker in axonal and myelin damage. *Imaging in medicine*, 5(5), 427–440.
- [Avants et al., 2008] Avants, B. B., Epstein, C. L., Grossman, M., & Gee, J. C. (2008). Symmetric diffeomorphic image registration with cross-correlation: evaluating automated labeling of elderly and neurodegenerative brain. *Medical Image Analysis*, 12(1), 26–41.
- [Avants et al., 2011] Avants, B. B., Tustison, N. J., Song, G., Cook, P. A., Klein, A., & Gee, J. C. (2011). A reproducible evaluation of ANTs similarity metric performance in brain image registration. *NeuroImage*, 54(3), 2033–2044.
- [Ballanger et al., 2013] Ballanger, B., Tremblay, L., Sgambato-Faure, V., Beaudoin-Gobert, M., Lavenne, F., Le Bars, D., & Costes, N. (2013). A multi-atlas based method for automated anatomical Macaca fascicularis brain MRI segmentation and PET kinetic extraction. *NeuroImage*, 77, 26–43.

- [Barkovich, 2005] Barkovich, A. J. (2005). Magnetic resonance techniques in the assessment of myelin and myelination. *Journal of Inherited Metabolic Disease*, 28(3), 311–343.
- [Baron et al., 2002] Baron, M. S., Wichmann, T., Ma, D., & DeLong, M. R. (2002). Effects of Transient Focal Inactivation of the Basal Ganglia in Parkinsonian Primates. *Journal of Neuroscience*, 22(2), 592–599. Publisher: Society for Neuroscience Section: ARTICLE.
- [Bartzokis et al., 2011] Bartzokis, G., Lu, P. H., Tingus, K., Peters, D. G., Amar, C. P., Tishler, T. A., Finn, J. P., Villablanca, P., Altshuler, L. L., Mintz, J., Neely, E., & Connor, J. R. (2011). Gender and Iron Genes May Modify Associations Between Brain Iron and Memory in Healthy Aging. *Neuropsychopharmacology*, 36(7), 1375–1384. Bandiera\_abtest: a Cg\_type: Nature Research Journals Number: 7 Primary\_atype: Research Publisher: Nature Publishing Group Subject\_term: Ageing;Genetic variation;Learning and memory;Metabolism Subject\_term\_id: ageing;genetic-variation;learning-and-memory;metabolism.
- [Basile et al., 2021] Basile, G. A., Quartu, M., Bertino, S., Serra, M. P., Boi, M., Bramanti, A., Anastasi, G. P., Milardi, D., & Cacciola, A. (2021). Red nucleus structure and function: from anatomy to clinical neurosciences. *Brain Structure and Function*, 226(1), 69–91.
- [Basser et al., 1994] Basser, P. J., Mattiello, J., & LeBihan, D. (1994). MR diffusion tensor spectroscopy and imaging. *Biophysical Journal*, 66(1), 259–267.
- [Bazin et al., 2020] Bazin, P.-L., Alkemade, A., Mulder, M. J., Henry, A. G., & Forstmann, B. U. (2020). Multi-contrast anatomical subcortical structures parcellation. *eLife*, 9, e59430. Publisher: eLife Sciences Publications, Ltd.
- [Benitez et al., 2014] Benitez, A., Fieremans, E., Jensen, J. H., Falangola, M. F., Tabesh, A., Ferris, S. H., & Helpert, J. A. (2014). White matter tract integrity metrics reflect the vulnerability of late-myelinating tracts in Alzheimer’s disease. *NeuroImage: Clinical*, 4, 64–71.
- [Bergen et al., 2016] Bergen, J. M. G. v., Hua, J., Unschuld, P. G., Lim, I. a. L., Jones, C. K., Margolis, R. L., Ross, C. A., Zijl, P. C. M. v., & Li, X. (2016). Quantitative Susceptibility Mapping Suggests Altered Brain Iron in Premanifest Huntington Disease. *American Journal of Neuroradiology*, 37(5), 789–796.

- [Betts et al., 2016] Betts, M. J., Acosta-Cabronero, J., Cardenas-Blanco, A., Nestor, P. J., & Düzel, E. (2016). High-resolution characterisation of the aging brain using simultaneous quantitative susceptibility mapping (QSM) and  $R_2^*$  measurements at 7T. *NeuroImage*, 138, 43–63.
- [Bian et al., 2016] Bian, W., Tranvinh, E., Tourdias, T., Han, M., Liu, T., Wang, Y., Rutt, B., & Zeineh, M. M. (2016). In vivo 7T MR Quantitative Susceptibility Mapping Reveals Opposite Susceptibility Contrast Between Cortical and White Matter Lesions in Multiple Sclerosis. *AJNR. American journal of neuroradiology*, 37(10), 1808–1815.
- [Bihan, 1995] Bihan, D. L. (1995). Molecular diffusion, tissue microdynamics and microstructure. *NMR in Biomedicine*, 8(7), 375–386. \_eprint: <https://analyticalsciencejournals.onlinelibrary.wiley.com/doi/pdf/10.1002/nbm.1940080711>.
- [Bilgic et al., 2012] Bilgic, B., Pfefferbaum, A., Rohlfing, T., Sullivan, E. V., & Adalsteinson, E. (2012). MRI estimates of brain iron concentration in normal aging using quantitative susceptibility mapping. *NeuroImage*, 59(3), 2625–2635.
- [Biondetti et al., 2020] Biondetti, E., Karsa, A., Thomas, D. L., & Shmueli, K. (2020). Investigating the accuracy and precision of TE-dependent versus multi-echo QSM using Laplacian-based methods at 3 T. *Magnetic Resonance in Medicine*, 84(6), 3040–3053. \_eprint: <https://onlinelibrary.wiley.com/doi/pdf/10.1002/mrm.28331>.
- [Blezer et al., 2007] Blezer, E. L. A., Bauer, J., Brok, H. P. M., Nicolay, K., & Hart, B. A. t. (2007). Quantitative MRI-pathology correlations of brain white matter lesions developing in a non-human primate model of multiple sclerosis. *NMR in Biomedicine*, 20(2), 90–103. \_eprint: <https://onlinelibrary.wiley.com/doi/pdf/10.1002/nbm.1085>.
- [Boer, 1995a] Boer, R. W. (1995a). Magnetization transfer contrast Part 1 : MR physics.
- [Boer, 1995b] Boer, R. W. (1995b). Magnetization transfer contrast Part 2 : Clinical applications.
- [Bonfanti et al., 2009] Bonfanti, U., Lamparelli, D., Colombo, P., & Bernardi, C. (2009). Hematology and serum chemistry parameters in juvenile cynomolgus monkeys (*Macaca fascicularis*) of Mauritius origin: comparison between purpose-bred and captured animals. *Journal of Medical Primatology*, 38(4), 228–235.
- [Borich et al., 2013] Borich, M. R., MacKay, A. L., Vavasour, I. M., Rauscher, A., & Boyd, L. A. (2013). Evaluation of white matter myelin water fraction in chronic stroke. *NeuroImage: Clinical*, 2, 569–580.

- [Bouhrara et al., 2020] Bouhrara, M., Cortina, L. E., Rejimon, A. C., Khattar, N., Bergeron, C., Bergeron, J., Melvin, D., Zukley, L., & Spencer, R. G. (2020). Quantitative age-dependent differences in human brainstem myelination assessed using high-resolution magnetic resonance mapping. *NeuroImage*, 206, 116307.
- [Bowley et al., 2010] Bowley, M. P., Cabral, H., Rosene, D. L., & Peters, A. (2010). Age changes in myelinated nerve fibers of the cingulate bundle and corpus callosum in the rhesus monkey. *Journal of Comparative Neurology*, 518(15), 3046–3064. \_eprint: <https://onlinelibrary.wiley.com/doi/pdf/10.1002/cne.22379>.
- [Brennan et al., 2017] Brennan, F. R., Cavagnaro, J., McKeever, K., Ryan, P. C., Schutten, M. M., Vahle, J., Weinbauer, G. F., Marrer-Berger, E., & Black, L. E. (2017). Safety testing of monoclonal antibodies in non-human primates: Case studies highlighting their impact on human risk assessment. *mAbs*, 10(1), 1–17.
- [Burt et al., 2018] Burt, J. B., Demirtaş, M., Eckner, W. J., Navejar, N. M., Ji, J. L., Martin, W. J., Bernacchia, A., Anticevic, A., & Murray, J. D. (2018). Hierarchy of transcriptomic specialization across human cortex captured by structural neuroimaging topography. *Nature Neuroscience*, 21(9), 1251–1259. Bandiera\_abtest: a Cg\_type: Nature Research Journals Number: 9 Primary\_atype: Research Publisher: Nature Publishing Group Subject\_term: Epigenetics in the nervous system;Neural circuits Subject\_term\_id: epigenetics-in-the-nervous-system;neural-circuit.
- [Calabrese et al., 2015] Calabrese, E., Badea, A., Coe, C. L., Lubach, G. R., Shi, Y., Styner, M. A., & Johnson, G. A. (2015). A diffusion tensor MRI atlas of the postmortem rhesus macaque brain. *NeuroImage*, 117, 408–416.
- [Callaert et al., 2014] Callaert, D. V., Ribbens, A., Maes, F., Swinnen, S. P., & Wenderoth, N. (2014). Assessing age-related gray matter decline with voxel-based morphometry depends significantly on segmentation and normalization procedures. *Frontiers in Aging Neuroscience*, 6, 124.
- [Callaghan et al., 2014] Callaghan, M. F., Freund, P., Draganski, B., Anderson, E., Cappelletti, M., Chowdhury, R., Diedrichsen, J., FitzGerald, T. H. B., Smittenaar, P., Helms, G., Lutti, A., & Weiskopf, N. (2014). Widespread age-related differences in the human brain microstructure revealed by quantitative magnetic resonance imaging. *Neurobiology of Aging*, 35(8), 1862–1872.
- [Caminiti et al., 2013] Caminiti, R., Carducci, F., Piervincenzi, C., Battaglia-Mayer, A., Confalone, G., Visco-Comandini, F., Pantano, P., & Innocenti, G. M. (2013). Diameter, Length, Speed, and Conduction Delay of Callosal Axons in Macaque Monkeys

- and Humans: Comparing Data from Histology and Magnetic Resonance Imaging Diffusion Tractography. *Journal of Neuroscience*, 33(36), 14501–14511.
- [Campbell et al., 2018] Campbell, J. S. W., Leppert, I. R., Narayanan, S., Boudreau, M., Duval, T., Cohen-Adad, J., Pike, G. B., & Stikov, N. (2018). Promise and pitfalls of g-ratio estimation with MRI. *NeuroImage*, 182, 80–96.
- [Caspers et al., 2011] Caspers, S., Eickhoff, S. B., Rick, T., von Kapri, A., Kuhlen, T., Huang, R., Shah, N. J., & Zilles, K. (2011). Probabilistic fibre tract analysis of cytoarchitectonically defined human inferior parietal lobule areas reveals similarities to macaques. *NeuroImage*, 58(2), 362–380.
- [Cercignani & Bouyagoub, 2018] Cercignani, M. & Bouyagoub, S. (2018). Brain microstructure by multi-modal MRI: Is the whole greater than the sum of its parts? *NeuroImage*, 182, 117–127.
- [Chai et al., 2017] Chai, C., Guo, R., Zuo, C., Fan, L., Liu, S., Qian, T., Mark Haacke, E., Xia, S., & Shen, W. (2017). Decreased susceptibility of major veins in mild traumatic brain injury is correlated with post-concussive symptoms: A quantitative susceptibility mapping study. *NeuroImage: Clinical*, 15, 625–632.
- [Chawla et al., 2018] Chawla, S., Kister, I., Sinnecker, T., Wuerfel, J., Brisset, J.-C., Paul, F., & Ge, Y. (2018). Longitudinal study of multiple sclerosis lesions using ultra-high field (7T) multiparametric MR imaging. *PLoS ONE*, 13(9).
- [Chen et al., 2013] Chen, W., Zhu, W., Kovanlikaya, I., Kovanlikaya, A., Liu, T., Wang, S., Salustri, C., & Wang, Y. (2013). Intracranial Calcifications and Hemorrhages: Characterization with Quantitative Susceptibility Mapping. *Radiology*, 270(2), 496–505. Publisher: Radiological Society of North America.
- [Choi et al., 2016] Choi, K., Chang, J., Lee, M.-J., Wang, S., In, K., Galano-tan, W. C., Jun, S., Cho, K., Hwang, Y.-H., Kim, S.-J., & Park, W. (2016). Reference values of hematology, biochemistry, and blood type in cynomolgus monkeys from cambodia origin. *Laboratory Animal Research*, 32(1), 46–55.
- [Churchill et al., 2017] Churchill, N. W., Caverzasi, E., Graham, S. J., Hutchison, M. G., & Schweizer, T. A. (2017). White matter microstructure in athletes with a history of concussion: Comparing diffusion tensor imaging (DTI) and neurite orientation dispersion and density imaging (NODDI). *Human Brain Mapping*, 38(8), 4201–4211. \_eprint: <https://onlinelibrary.wiley.com/doi/pdf/10.1002/hbm.23658>.

- [Ciccarelli et al., 2008] Ciccarelli, O., Catani, M., Johansen-Berg, H., Clark, C., & Thompson, A. (2008). Diffusion-based tractography in neurological disorders: concepts, applications, and future developments. *The Lancet Neurology*, 7(8), 715–727.
- [Collantes et al., 2009] Collantes, M., Prieto, E., Peñuelas, I., Blesa, J., Juri, C., Martí-Climent, J. M., Quincoces, G., Arbizu, J., Riverol, M., Zubieta, J. L., Rodríguez-Oroz, M. C., Luquin, M. R., Richter, J. A., & Obeso, J. A. (2009). New MRI, 18F-DOPA and 11C-(+)-alpha-dihydrotrabenazine templates for *Macaca fascicularis* neuroimaging: advantages to improve PET quantification. *NeuroImage*, 47(2), 533–539.
- [Colman, 2018] Colman, R. J. (2018). Non-human primates as a model for aging. *Biochimica et Biophysica Acta (BBA) - Molecular Basis of Disease*, 1864(9, Part A), 2733–2741.
- [Cox & Hyde, 1997] Cox, R. W. & Hyde, J. S. (1997). Software tools for analysis and visualization of fMRI data. *NMR in Biomedicine*, 10(4-5), 171–178. \_eprint: <https://analyticalsciencejournals.onlinelibrary.wiley.com/doi/pdf/10.1002/%28SICI%291099-1492%28199706/08%2910%3A4/5%3C171%3A%3AAID-NBM453%3E3.o.CO%3B2-L>.
- [Cox et al., 2016] Cox, S. R., Ritchie, S. J., Tucker-Drob, E. M., Liewald, D. C., Hagenaars, S. P., Davies, G., Wardlaw, J. M., Gale, C. R., Bastin, M. E., & Deary, I. J. (2016). Ageing and brain white matter structure in 3,513 UK Biobank participants. *Nature Communications*, 7(1), 13629. Number: 1 Publisher: Nature Publishing Group.
- [Cronin et al., 2017] Cronin, M. J., Wang, N., Decker, K. S., Wei, H., Zhu, W.-Z., & Liu, C. (2017). Exploring the origins of echo-time-dependent quantitative susceptibility mapping (QSM) measurements in healthy tissue and cerebral microbleeds. *NeuroImage*, 149, 98–113.
- [D et al., 2016] D, J. F. D., Ng, A. C. L., Poudel, G., Stout, J. C., Churchyard, A., Chua, P., Egan, G. F., & Georgiou-Karistianis, N. (2016). Iron accumulation in the basal ganglia in Huntington's disease: cross-sectional data from the IMAGE-HD study. *Journal of Neurology, Neurosurgery & Psychiatry*, 87(5), 545–549. Publisher: BMJ Publishing Group Ltd Section: Movement disorders.
- [Dadar et al., 2021] Dadar, M., Camicioli, R., Duchesne, S., & Group, F. t. C. (2021). *Multi-Sequence Average Templates for Aging and Neurodegenerative Disease Populations*. Technical report. Company: Cold Spring Harbor Laboratory Press Distributor: Cold Spring Harbor Laboratory Press Label: Cold Spring Harbor Laboratory Press Type: article.

- [Dadarwal & Boretius, 2021a] Dadarwal, R. & Boretius, S. (2021a). Merging T<sub>1</sub> weighted images with QSM provides a unique contrast for brain tissue segmentation in humans and non-human primates.
- [Dadarwal & Boretius, 2021b] Dadarwal, R. & Boretius, S. (2021b). Multi-contrast MRI Atlas of the Cynomolgus Macaque Brain.
- [Dadarwal et al., 2019] Dadarwal, R., Hintz, L., Moussavi, A., & Boretius, S. (2019). Quantitative Susceptibility Mapping of the Brain – A Comparative In vivo Study of Humans and Nonhuman Primates.
- [Dadarwal et al., 2021] Dadarwal, R., Mylius, J., & Boretius, S. (2021). Brain aging in cynomolgus macaques and common marmosets explored by mapping the magnetic susceptibility and R<sub>2</sub>\*.
- [Daducci et al., 2015] Daducci, A., Canales-Rodríguez, E. J., Zhang, H., Dyrby, T. B., Alexander, D. C., & Thiran, J.-P. (2015). Accelerated Microstructure Imaging via Convex Optimization (AMICO) from diffusion MRI data. *NeuroImage*, 105, 32–44.
- [Das et al., 2009] Das, S. R., Avants, B. B., Grossman, M., & Gee, J. C. (2009). Registration based cortical thickness measurement. *NeuroImage*, 45(3), 867–879.
- [Daugherty & Raz, 2013] Daugherty, A. & Raz, N. (2013). Age-related differences in iron content of subcortical nuclei observed in vivo: A meta-analysis. *NeuroImage*, 70, 113–121.
- [Deistung et al., 2013] Deistung, A., Schäfer, A., Schweser, F., Biedermann, U., Turner, R., & Reichenbach, J. R. (2013). Toward in vivo histology: A comparison of quantitative susceptibility mapping (QSM) with magnitude-, phase-, and R<sub>2</sub>\*-imaging at ultra-high magnetic field strength. *NeuroImage*, 65, 299–314.
- [Does, 2018] Does, M. D. (2018). Inferring brain tissue composition and microstructure via MR relaxometry. *NeuroImage*, 182, 136–148.
- [Dousset et al., 1992] Dousset, V., Grossman, R. I., Ramer, K. N., Schnall, M. D., Young, L. H., Gonzalez-Scarano, F., Lavi, E., & Cohen, J. A. (1992). Experimental allergic encephalomyelitis and multiple sclerosis: lesion characterization with magnetization transfer imaging. *Radiology*, 182(2), 483–491. Publisher: Radiological Society of North America.

- [Dula et al., 2010] Dula, A. N., Gochberg, D. F., Valentine, H. L., Valentine, W. M., & Does, M. D. (2010). Multiexponential T<sub>2</sub>, magnetization transfer, and quantitative histology in white matter tracts of rat spinal cord. *Magnetic Resonance in Medicine*, 63(4), 902–909. \_eprint: <https://onlinelibrary.wiley.com/doi/pdf/10.1002/mrm.22267>.
- [Duyn & Schenck, 2017] Duyn, J. H. & Schenck, J. (2017). Contributions to magnetic susceptibility of brain tissue. *NMR in biomedicine*, 30(4).
- [Edwards et al., 2018] Edwards, L. J., Kirilina, E., Mohammadi, S., & Weiskopf, N. (2018). Microstructural imaging of human neocortex in vivo. *NeuroImage*, 182, 184–206.
- [Edzes & Samulski, 1978] Edzes, H. T. & Samulski, E. T. (1978). The measurement of cross-relaxation effects in the proton NMR spin-lattice relaxation of water in biological systems: Hydrated collagen and muscle. *Journal of Magnetic Resonance (1969)*, 31(2), 207–229.
- [Ellerbrock & Mohammadi, 2018] Ellerbrock, I. & Mohammadi, S. (2018). Four in vivo g-ratio-weighted imaging methods: Comparability and repeatability at the group level. *Human Brain Mapping*, 39(1), 24–41.
- [Engel et al., 2013] Engel, J., Thompson, P. M., Stern, J. M., Staba, R. J., Bragin, A., & Mody, I. (2013). Connectomics and epilepsy. *Current opinion in neurology*, 26(2), 186–194.
- [Eskreis-Winkler et al., 2017] Eskreis-Winkler, S., Zhang, Y., Zhang, J., Liu, Z., Dimov, A., Gupta, A., & Wang, Y. (2017). The clinical utility of QSM: disease diagnosis, medical management, and surgical planning. *NMR in Biomedicine*, 30(4), e3668. \_eprint: <https://analyticalsciencejournals.onlinelibrary.wiley.com/doi/pdf/10.1002/nbm.3668>.
- [Essen & Dierker, 2007] Essen, D. C. V. & Dierker, D. L. (2007). Surface-Based and Probabilistic Atlases of Primate Cerebral Cortex. *Neuron*, 56(2), 209–225. Publisher: Elsevier.
- [Faizy et al., 2020] Faizy, T. D., Thaler, C., Broocks, G., Flottmann, F., Leischner, H., Kniep, H., Nawabi, J., Schön, G., Stellmann, J.-P., Kemmling, A., Reddy, R., Heit, J. J., Fiehler, J., Kumar, D., & Hanning, U. (2020). The Myelin Water Fraction Serves as a Marker for Age-Related Myelin Alterations in the Cerebral White Matter – A Multiparametric MRI Aging Study. *Frontiers in Neuroscience*, 14. Publisher: Frontiers.



- [Falangola et al., 2014] Falangola, M. F., Guilfoyle, D. N., Tabesh, A., Hui, E. S., Nie, X., Jensen, J. H., Gerum, S. V., Hu, C., LaFrancois, J., Collins, H. R., & Helpert, J. A. (2014). Histological correlation of diffusional kurtosis and white matter modeling metrics in cuprizone-induced corpus callosum demyelination. *NMR in Biomedicine*, 27(8), 948–957. [\\_eprint: https://analyticalsciencejournals.onlinelibrary.wiley.com/doi/pdf/10.1002/nbm.3140](https://analyticalsciencejournals.onlinelibrary.wiley.com/doi/pdf/10.1002/nbm.3140).
- [Farokhian et al., 2017] Farokhian, F., Yang, C., Beheshti, I., Matsuda, H., & Wu, S. (2017). Age-Related Gray and White Matter Changes in Normal Adult Brains. *Aging and Disease*, 8(6), 899–909.
- [Feng et al., 2018] Feng, X., Deistung, A., & Reichenbach, J. R. (2018). Quantitative susceptibility mapping (QSM) and  $R_2^*$  in the human brain at 3T: Evaluation of intra-scanner repeatability. *Zeitschrift für Medizinische Physik*, 28(1), 36–48.
- [Fields, 2015] Fields, R. D. (2015). A new mechanism of nervous system plasticity: activity-dependent myelination. *Nature Reviews Neuroscience*, 16(12), 756–767. Bandiera\_abtest: a Cg\_type: Nature Research Journals Number: 12 Primary\_atype: Reviews Publisher: Nature Publishing Group Subject\_term: Demyelinating diseases; Myelin biology and repair; Oligodendrocyte; Schwann cell Subject\_term\_id: demyelinating-diseases; myelin-biology-and-repair; oligodendrocyte; schwann-cell.
- [Fieremans et al., 2011] Fieremans, E., Jensen, J. H., & Helpert, J. A. (2011). White matter characterization with diffusional kurtosis imaging. *NeuroImage*, 58(1), 177–188.
- [Fischl, 2012] Fischl, B. (2012). FreeSurfer. *NeuroImage*, 62(2), 774–781.
- [Fox et al., 2011] Fox, R. J., Cronin, T., Lin, J., Wang, X., Sakaie, K., Ontaneda, D., Mahmoud, S. Y., Lowe, M. J., & Phillips, M. D. (2011). Measuring Myelin Repair and Axonal Loss with Diffusion Tensor Imaging. *American Journal of Neuroradiology*, 32(1), 85–91. Publisher: American Journal of Neuroradiology Section: Brain.
- [Franklin et al., 2000] Franklin, M. S., Kraemer, G. W., Shelton, S. E., Baker, E., Kalin, N. H., & Uno, H. (2000). Gender differences in brain volume and size of corpus callosum and amygdala of rhesus monkey measured from MRI images. *Brain Research*, 852(2), 263–267.
- [Frey et al., 2011] Frey, S., Pandya, D. N., Chakravarty, M. M., Bailey, L., Petrides, M., & Collins, D. L. (2011). An MRI based average macaque monkey stereotaxic atlas and space (MNI monkey space). *NeuroImage*, 55(4), 1435–1442.

- [Fu et al., 2020] Fu, X., Shrestha, S., Sun, M., Wu, Q., Luo, Y., Zhang, X., Yin, J., & Ni, H. (2020). Microstructural White Matter Alterations in Mild Cognitive Impairment and Alzheimer's Disease. *Clinical Neuroradiology*, 30(3), 569–579.
- [Galvan et al., 2017] Galvan, A., Stauffer, W. R., Acker, L., El-Shamayleh, Y., Inoue, K.-i., Ohayon, S., & Schmid, M. C. (2017). Nonhuman Primate Optogenetics: Recent Advances and Future Directions. *Journal of Neuroscience*, 37(45), 10894–10903. Publisher: Society for Neuroscience Section: Symposium and Mini-Symposium.
- [Garyfallidis et al., 2014] Garyfallidis, E., Brett, M., Amirbekian, B., Rokem, A., van der Walt, S., Descoteaux, M., & Nimmo-Smith, I. (2014). Dipy, a library for the analysis of diffusion MRI data. *Frontiers in Neuroinformatics*, 8.
- [Gibbs et al., 2007] Gibbs, R. A., Rogers, J., Katze, M. G., Bumgarner, R., Weinstock, G. M., Mardis, E. R., Remington, K. A., Strausberg, R. L., Venter, J. C., Wilson, R. K., Batzer, M. A., Bustamante, C. D., Eichler, E. E., Hahn, M. W., Hardison, R. C., Makova, K. D., Miller, W., Milosavljevic, A., Palermo, R. E., Siepel, A., Sikela, J. M., Attaway, T., Bell, S., Bernard, K. E., Buhay, C. J., Chandrabose, M. N., Dao, M., Davis, C., Delehaunty, K. D., Ding, Y., Dinh, H. H., Dugan-Rocha, S., Fulton, L. A., Gabisi, R. A., Garner, T. T., Godfrey, J., Hawes, A. C., Hernandez, J., Hines, S., Holder, M., Hume, J., Jhangiani, S. N., Joshi, V., Khan, Z. M., Kirkness, E. F., Cree, A., Fowler, R. G., Lee, S., Lewis, L. R., Li, Z., Liu, Y.-s., Moore, S. M., Muzny, D., Nazareth, L. V., Ngo, D. N., Okwuonu, G. O., Pai, G., Parker, D., Paul, H. A., Pfannkoch, C., Pohl, C. S., Rogers, Y.-H., Ruiz, S. J., Sabo, A., Santibanez, J., Schneider, B. W., Smith, S. M., Sodergren, E., Svatek, A. F., Utterback, T. R., Vattathil, S., Warren, W., White, C. S., Chinwalla, A. T., Feng, Y., Halpern, A. L., Hillier, L. W., Huang, X., Minx, P., Nelson, J. O., Pepin, K. H., Qin, X., Sutton, G. G., Venter, E., Walenz, B. P., Wallis, J. W., Worley, K. C., Yang, S.-P., Jones, S. M., Marra, M. A., Rocchi, M., Schein, J. E., Baertsch, R., Clarke, L., Csürös, M., Glasscock, J., Harris, R. A., Havlak, P., Jackson, A. R., Jiang, H., Liu, Y., Messina, D. N., Shen, Y., Song, H. X.-Z., Wylie, T., Zhang, L., Birney, E., Han, K., Konkel, M. K., Lee, J., Smit, A. F. A., Ullmer, B., Wang, H., Xing, J., Burhans, R., Cheng, Z., Karro, J. E., Ma, J., Raney, B., She, X., Cox, M. J., Demuth, J. P., Dumas, L. J., Han, S.-G., Hopkins, J., Karimpour-Fard, A., Kim, Y. H., Pollack, J. R., Vinar, T., Addo-Quaye, C., Degenhardt, J., Denby, A., Hubisz, M. J., Indap, A., Kosiol, C., Lahn, B. T., Lawson, H. A., Marklein, A., Nielsen, R., Vallender, E. J., Clark, A. G., Ferguson, B., Hernandez, R. D., Hirani, K., Kehrer-Sawatzki, H., Kolb, J., Patil, S., Pu, L.-L., Ren, Y., Smith, D. G., Wheeler, D. A., Schenck, I., Ball, E. V., Chen, R., Cooper, D. N., Giardine, B., Hsu, F., Kent, W. J., Lesk, A., Nelson, D. L., O'Brien, W. E., Prüfer, K., Stenson,

- P. D., Wallace, J. C., Ke, H., Liu, X.-M., Wang, P., Xiang, A. P., Yang, F., Barber, G. P., Haussler, D., Karolchik, D., Kern, A. D., Kuhn, R. M., Smith, K. E., & Zwing, A. S. (2007). Evolutionary and Biomedical Insights from the Rhesus Macaque Genome. *Science*, 316(5822), 222–234. Publisher: American Association for the Advancement of Science.
- [Glasser & Essen, 2011] Glasser, M. F. & Essen, D. C. V. (2011). Mapping Human Cortical Areas In Vivo Based on Myelin Content as Revealed by T1- and T2-Weighted MRI. *Journal of Neuroscience*, 31(32), 11597–11616. Publisher: Society for Neuroscience Section: Articles.
- [Golby et al., 2011] Golby, A. J., Kindlmann, G., Norton, I., Yarmarkovich, A., Pieper, S., & Kikinis, R. (2011). Interactive Diffusion Tensor Tractography Visualization for Neurosurgical Planning. *Neurosurgery*, 68(2), 496–505.
- [Gong et al., 2020] Gong, N.-J., Dibb, R., Pletnikov, M., Benner, E., & Liu, C. (2020). Imaging microstructure with diffusion and susceptibility MR: neuronal density correlation in Disrupted-in-Schizophrenia-1 mutant mice. *NMR in Biomedicine*, 33(10), e4365. \_eprint: <https://analyticalsciencejournals.onlinelibrary.wiley.com/doi/pdf/10.1002/nbm.4365>.
- [Gong et al., 2014] Gong, N.-J., Wong, C.-S., Chan, C.-C., Leung, L.-M., & Chu, Y.-C. (2014). Aging in deep gray matter and white matter revealed by diffusional kurtosis imaging. *Neurobiology of Aging*, 35(10), 2203–2216.
- [Gorgolewski et al., 2011] Gorgolewski, K., Burns, C. D., Madison, C., Clark, D., Halchenko, Y. O., Waskom, M. L., & Ghosh, S. S. (2011). Nipype: A Flexible, Lightweight and Extensible Neuroimaging Data Processing Framework in Python. *Frontiers in Neuroinformatics*, 5.
- [Guan et al., 2019] Guan, X., Huang, P., Zeng, Q., Liu, C., Wei, H., Xuan, M., Gu, Q., Xu, X., Wang, N., Yu, X., Luo, X., & Zhang, M. (2019). Quantitative susceptibility mapping as a biomarker for evaluating white matter alterations in Parkinson's disease. *Brain Imaging and Behavior*, 13(1), 220–231.
- [Guan et al., 2017] Guan, X., Xuan, M., Gu, Q., Huang, P., Liu, C., Wang, N., Xu, X., Luo, W., & Zhang, M. (2017). Regionally progressive accumulation of iron in Parkinson's disease as measured by quantitative susceptibility mapping. *NMR in Biomedicine*, 30(4), e3489.

- [Gucht et al., 2006] Gucht, E. V. D., Youakim, M., Arckens, L., Hof, P. R., & Baizer, J. S. (2006). Variations in the structure of the prelunate gyrus in Old World monkeys. *The Anatomical Record Part A: Discoveries in Molecular, Cellular, and Evolutionary Biology*, 288A(7), 753–775. \_eprint: <https://anatomypubs.onlinelibrary.wiley.com/doi/pdf/10.1002/ar.a.20350>.
- [Guglielmetti et al., 2016] Guglielmetti, C., Veraart, J., Roelant, E., Mai, Z., Daans, J., Van Audekerke, J., Naeyaert, M., Vanhoutte, G., Delgado y Palacios, R., Praet, J., Fieremans, E., Ponsaerts, P., Sijbers, J., Van der Linden, A., & Verhoye, M. (2016). Diffusion kurtosis imaging probes cortical alterations and white matter pathology following cuprizone induced demyelination and spontaneous remyelination. *NeuroImage*, 125, 363–377.
- [Gunning-Dixon et al., 2009] Gunning-Dixon, F. M., Brickman, A. M., Cheng, J. C., & Alexopoulos, G. S. (2009). Aging of cerebral white matter: a review of MRI findings. *International Journal of Geriatric Psychiatry*, 24(2), 109–117. \_eprint: <https://onlinelibrary.wiley.com/doi/pdf/10.1002/gps.2087>.
- [Haacke et al., 2009a] Haacke, E., Mittal, S., Wu, Z., Neelavalli, J., & Cheng, Y.-C. (2009a). Susceptibility-Weighted Imaging: Technical Aspects and Clinical Applications, Part 1. *AJNR: American Journal of Neuroradiology*, 30(1), 19–30.
- [Haacke et al., 2005] Haacke, E. M., Cheng, N. Y. C., House, M. J., Liu, Q., Neelavalli, J., Ogg, R. J., Khan, A., Ayaz, M., Kirsch, W., & Obenaus, A. (2005). Imaging iron stores in the brain using magnetic resonance imaging. *Magnetic Resonance Imaging*, 23(1), 1–25.
- [Haacke et al., 2009b] Haacke, E. M., Makki, M., Ge, Y., Maheshwari, M., Sehgal, V., Hu, J., Selvan, M., Wu, Z., Latif, Z., Xuan, Y., Khan, O., Garbern, J., & Grossman, R. I. (2009b). Characterizing iron deposition in multiple sclerosis lesions using susceptibility weighted imaging. *Journal of magnetic resonance imaging: JMIR*, 29(3), 537–544.
- [Haacke et al., 2004] Haacke, E. M., Xu, Y., Cheng, Y.-C. N., & Reichenbach, J. R. (2004). Susceptibility weighted imaging (SWI). *Magnetic Resonance in Medicine*, 52(3), 612–618.
- [Hadaczek et al., 2016] Hadaczek, P., Stanek, L., Ciesielska, A., Sudhakar, V., Samaranch, L., Pivrotto, P., Bringas, J., O’Riordan, C., Mastis, B., San Sebastian, W., Forsayeth, J., Cheng, S. H., Bankiewicz, K. S., & Shihabuddin, L. S. (2016). Widespread AAV1- and AAV2-mediated transgene expression in the nonhuman primate brain: implications

- for Huntington's disease. *Molecular Therapy. Methods & Clinical Development*, 3, 16037.
- [Hagiwara et al., 2018] Hagiwara, A., Hori, M., Kamagata, K., Warntjes, M., Matsuyoshi, D., Nakazawa, M., Ueda, R., Andica, C., Koshino, S., Maekawa, T., Irie, R., Takamura, T., Kumamaru, K. K., Abe, O., & Aoki, S. (2018). Myelin Measurement: Comparison Between Simultaneous Tissue Relaxometry, Magnetization Transfer Saturation Index, and T<sub>1w</sub>/T<sub>2w</sub> Ratio Methods. *Scientific Reports*, 8.
- [Hallgren & Sourander, 1958] Hallgren, B. & Sourander, P. (1958). The Effect of Age on the Non-Haemin Iron in the Human Brain. *Journal of Neurochemistry*, 3(1), 41–51.
- [Hambleton et al., 1981] Hambleton, P., BASKERVILLE, A., WADE, J. J., & BAILEY, N. E. (1981). Some normal clinical chemistry values for cerebrospinal fluid of the rhesus monkey (*Macaca mulatta*). *Laboratory Animals*, 15(2), 181–186.
- [Hametner et al., 2018] Hametner, S., Endmayr, V., Deistung, A., Palmrich, P., Prihoda, M., Haimburger, E., Menard, C., Feng, X., Haider, T., Leisser, M., Köck, U., Kaider, A., Höftberger, R., Robinson, S., Reichenbach, J. R., Lassmann, H., Traxler, H., Trattnig, S., & Grabner, G. (2018). The influence of brain iron and myelin on magnetic susceptibility and effective transverse relaxation - A biochemical and histological validation study. *NeuroImage*, 179, 117–133.
- [Hara et al., 2019] Hara, S., Hori, M., Ueda, R., Hayashi, S., Inaji, M., Tanaka, Y., Maehara, T., Ishii, K., Aoki, S., & Nariai, T. (2019). Unraveling Specific Brain Microstructural Damage in Moyamoya Disease Using Diffusion Magnetic Resonance Imaging and Positron Emission Tomography. *Journal of Stroke and Cerebrovascular Diseases*, 28(4), 1113–1125. Publisher: Elsevier.
- [Hartig et al., 2021] Hartig, R., Glen, D., Jung, B., Logothetis, N. K., Paxinos, G., Garza-Villarreal, E. A., Messinger, A., & Evrard, H. C. (2021). The Subcortical Atlas of the Rhesus Macaque (SARM) for neuroimaging. *NeuroImage*, 235, 117996.
- [Hedman et al., 2012] Hedman, A. M., van Haren, N. E., Schnack, H. G., Kahn, R. S., & Hulshoff Pol, H. E. (2012). Human brain changes across the life span: A review of 56 longitudinal magnetic resonance imaging studies. *Human Brain Mapping*, 33(8), 1987–2002. \_eprint: <https://onlinelibrary.wiley.com/doi/pdf/10.1002/hbm.21334>.
- [Helms et al., 2008] Helms, G., Dathe, H., Kallenberg, K., & Dechent, P. (2008). High-resolution maps of magnetization transfer with inherent correction for RF inhomogeneity and T<sub>1</sub> relaxation obtained from 3D FLASH MRI. *Magnetic Resonance in Medicine*, 60(6), 1396–1407.

- [Henkelman et al., 2001] Henkelman, R. M., Stanisz, G. J., & Graham, S. J. (2001). Magnetization transfer in MRI: a review. *NMR in Biomedicine*, 14(2), 57–64. \_eprint: <https://analyticalsciencejournals.onlinelibrary.wiley.com/doi/pdf/10.1002/nbm.683>.
- [Hicks & Onodera, 2012] Hicks, T. P. & Onodera, S. (2012). The mammalian red nucleus and its role in motor systems, including the emergence of bipedalism and language. *Progress in Neurobiology*, 96(2), 165–175.
- [Hofer et al., 2008] Hofer, S., Merboldt, K.-D., Tammer, R., & Frahm, J. (2008). Rhesus Monkey and Human Share a Similar Topography of the Corpus Callosum as Revealed by Diffusion Tensor MRI In Vivo. *Cerebral Cortex*, 18(5), 1079–1084.
- [Hui et al., 2012] Hui, E. S., Fieremans, E., Jensen, J. H., Tabesh, A., Feng, W., Bonilha, L., Spampinato, M. V., Adams, R., & Helpert, J. A. (2012). Stroke Assessment With Diffusional Kurtosis Imaging. *Stroke*, 43(11), 2968–2973. Publisher: American Heart Association.
- [Inoue et al., 2015] Inoue, K.-i., Takada, M., & Matsumoto, M. (2015). Neuronal and behavioural modulations by pathway-selective optogenetic stimulation of the primate oculomotor system. *Nature Communications*, 6(1), 8378. Bandiera\_abtest: a Cc\_license\_type: cc\_by Cg\_type: Nature Research Journals Number: 1 Primary\_atype: Research Publisher: Nature Publishing Group Subject\_term: Oculomotor system;Optogenetics Subject\_term\_id: oculomotor-system;optogenetics.
- [Iwama et al., 2020] Iwama, T., Ohba, T., Okita, G., Ebata, S., Ueda, R., Motosugi, U., Onishi, H., Haro, H., & Hori, M. (2020). Utility and validity of neurite orientation dispersion and density imaging with diffusion tensor imaging to quantify the severity of cervical spondylotic myelopathy and assess postoperative neurological recovery. *The Spine Journal*, 20(3), 417–425. Publisher: Elsevier.
- [Jelescu et al., 2020] Jelescu, I. O., Palombo, M., Bagnato, F., & Schilling, K. G. (2020). Challenges for biophysical modeling of microstructure. *Journal of Neuroscience Methods*, 344, 108861.
- [Jelescu et al., 2016] Jelescu, I. O., Zurek, M., Winters, K. V., Veraart, J., Rajaratnam, A., Kim, N. S., Babb, J. S., Shepherd, T. M., Novikov, D. S., Kim, S. G., & Fieremans, E. (2016). In vivo quantification of demyelination and recovery using compartment-specific diffusion MRI metrics validated by electron microscopy. *NeuroImage*, 132, 104–114.

- [Jensen et al., 2005] Jensen, J. H., Helpers, J. A., Ramani, A., Lu, H., & Kaczynski, K. (2005). Diffusional kurtosis imaging: the quantification of non-gaussian water diffusion by means of magnetic resonance imaging. *Magnetic Resonance in Medicine*, 53(6), 1432–1440.
- [Jespersen et al., 2010] Jespersen, S. N., Bjarkam, C. R., Nyengaard, J. R., Chakravarty, M. M., Hansen, B., Vosegaard, T., Østergaard, L., Yablonskiy, D., Nielsen, N. C., & Vestergaard-Poulsen, P. (2010). Neurite density from magnetic resonance diffusion measurements at ultrahigh field: comparison with light microscopy and electron microscopy. *NeuroImage*, 49(1), 205–216.
- [Jeurissen et al., 2019] Jeurissen, B., Descoteaux, M., Mori, S., & Leemans, A. (2019). Diffusion MRI fiber tractography of the brain. *NMR in Biomedicine*, 32(4), e3785. [\\_eprint: https://onlinelibrary.wiley.com/doi/pdf/10.1002/nbm.3785](https://onlinelibrary.wiley.com/doi/pdf/10.1002/nbm.3785).
- [Jung et al., 2021] Jung, B., Taylor, P. A., Seidlitz, J., Sponheim, C., Perkins, P., Ungerleider, L. G., Glen, D., & Messinger, A. (2021). A comprehensive macaque fMRI pipeline and hierarchical atlas. *NeuroImage*, 235, 117997.
- [Kaden et al., 2016] Kaden, E., Kelm, N. D., Carson, R. P., Does, M. D., & Alexander, D. C. (2016). Multi-compartment microscopic diffusion imaging. *NeuroImage*, 139, 346–359.
- [Kelm et al., 2016] Kelm, N. D., West, K. L., Carson, R. P., Gochberg, D. F., Ess, K. C., & Does, M. D. (2016). Evaluation of diffusion kurtosis imaging in ex vivo hypomyelinated mouse brains. *NeuroImage*, 124, 612–626.
- [Keuken et al., 2017] Keuken, M. C., Bazin, P.-L., Backhouse, K., Beekhuizen, S., Himmer, L., Kandola, A., Lafeber, J. J., Prochazkova, L., Trutti, A., Schäfer, A., Turner, R., & Forstmann, B. U. (2017). Effects of aging on  $T_1$ ,  $T_2^*$ , and QSM MRI values in the subcortex. *Brain Structure and Function*, 222(6), 2487–2505.
- [Kirk, 2006] Kirk, E. C. (2006). Visual influences on primate encephalization. *Journal of Human Evolution*, 51(1), 76–90.
- [Klink et al., 2021] Klink, P. C., Aubry, J.-F., Ferrera, V. P., Fox, A. S., Froud-Walsh, S., Jarraya, B., Konofagou, E. E., Krauzlis, R. J., Messinger, A., Mitchell, A. S., Ortiz-Rios, M., Oya, H., Roberts, A. C., Roe, A. W., Rushworth, M. F. S., Sallet, J., Schmid, M. C., Schroeder, C. E., Tasserie, J., Tsao, D. Y., Uhrig, L., Vanduffel, W., Wilke, M., Kagan, I., & Petkov, C. I. (2021). Combining brain perturbation and neuroimaging in non-human primates. *NeuroImage*, 235, 118017.

- [Kraguljac et al., 2019] Kraguljac, N. V., Anthony, T., Monroe, W. S., Skidmore, F. M., Morgan, C. J., White, D. M., Patel, N., & Lahti, A. C. (2019). A longitudinal neurite and free water imaging study in patients with a schizophrenia spectrum disorder. *Neuropsychopharmacology*, 44(11), 1932–1939. Number: 11 Publisher: Nature Publishing Group.
- [Kunimatsu et al., 2015] Kunimatsu, J., Miyamoto, N., Ishikawa, M., Shirato, H., & Tanaka, M. (2015). Application of radiosurgical techniques to produce a primate model of brain lesions. *Frontiers in Systems Neuroscience*, 9.
- [Lampinen et al., 2017] Lampinen, B., Szczepankiewicz, F., Mårtensson, J., van Westen, D., Sundgren, P. C., & Nilsson, M. (2017). Neurite density imaging versus imaging of microscopic anisotropy in diffusion MRI: A model comparison using spherical tensor encoding. *NeuroImage*, 147, 517–531.
- [Lancione et al., 2019] Lancione, M., Donatelli, G., Cecchi, P., Cosottini, M., Tosetti, M., & Costagli, M. (2019). Echo-time dependency of quantitative susceptibility mapping reproducibility at different magnetic field strengths. *NeuroImage*, 197, 557–564.
- [Langkammer et al., 2013] Langkammer, C., Liu, T., Khalil, M., Enzinger, C., Jehna, M., Fuchs, S., Fazekas, F., Wang, Y., & Ropele, S. (2013). Quantitative Susceptibility Mapping in Multiple Sclerosis. *Radiology*, 267(2), 551–559. Publisher: Radiological Society of North America.
- [Langkammer et al., 2016] Langkammer, C., Pirpamer, L., Seiler, S., Deistung, A., Schweser, F., Franthal, S., Homayoon, N., Katschnig-Winter, P., Koegl-Wallner, M., Pendl, T., Stoegerer, E. M., Wenzel, K., Fazekas, F., Ropele, S., Reichenbach, J. R., Schmidt, R., & Schwingenschuh, P. (2016). Quantitative Susceptibility Mapping in Parkinson's Disease. *PLOS ONE*, 11(9), e0162460. Publisher: Public Library of Science.
- [Langkammer et al., 2012] Langkammer, C., Schweser, F., Krebs, N., Deistung, A., Goessler, W., Scheurer, E., Sommer, K., Reishofer, G., Yen, K., Fazekas, F., Ropele, S., & Reichenbach, J. R. (2012). Quantitative susceptibility mapping (QSM) as a means to measure brain iron? A post mortem validation study. *NeuroImage*, 62(3), 1593–1599.
- [Lappe-Siefke et al., 2003] Lappe-Siefke, C., Goebbels, S., Gravel, M., Nicksch, E., Lee, J., Braun, P. E., Griffiths, I. R., & Nave, K.-A. (2003). Disruption of Cnp1 uncouples oligodendroglial functions in axonal support and myelination. *Nature Genetics*, 33(3), 366–374. Number: 3 Publisher: Nature Publishing Group.



- [Lazari & Lipp, 2021] Lazari, A. & Lipp, I. (2021). Can MRI measure myelin? Systematic review, qualitative assessment, and meta-analysis of studies validating microstructural imaging with myelin histology. *NeuroImage*, 230, 117744.
- [Le Bihan et al., 2001] Le Bihan, D., Mangin, J.-F., Poupon, C., Clark, C. A., Pappata, S., Molko, N., & Chabriat, H. (2001). Diffusion tensor imaging: Concepts and applications. *Journal of Magnetic Resonance Imaging*, 13(4), 534–546. \_eprint: <https://onlinelibrary.wiley.com/doi/pdf/10.1002/jmri.1076>.
- [Le Bihan et al., 1992] Le Bihan, D., Turner, R., Douek, P., & Patronas, N. (1992). Diffusion MR imaging: clinical applications. *American Journal of Roentgenology*, 159(3), 591–599. Publisher: American Roentgen Ray Society.
- [Lee et al., 2021] Lee, J., Hyun, J.-W., Lee, J., Choi, E.-J., Shin, H.-G., Min, K., Nam, Y., Kim, H. J., & Oh, S.-H. (2021). So You Want to Image Myelin Using MRI: An Overview and Practical Guide for Myelin Water Imaging. *Journal of Magnetic Resonance Imaging*, 53(2), 360–373. \_eprint: <https://onlinelibrary.wiley.com/doi/pdf/10.1002/jmri.27059>.
- [Lema et al., 2017] Lema, A., Bishop, C., Malik, O., Mattoscio, M., Ali, R., Nicholas, R., Muraro, P. A., Matthews, P. M., Waldman, A. D., & Newbould, R. D. (2017). A Comparison of Magnetization Transfer Methods to Assess Brain and Cervical Cord Microstructure in Multiple Sclerosis. *Journal of Neuroimaging: Official Journal of the American Society of Neuroimaging*, 27(2), 221–226.
- [Lemaitre et al., 2012] Lemaitre, H., Goldman, A., Sambataro, F., Verchinski, B., Meyer-Lindenberg, A., Weinberger, D., & Mattay, V. (2012). Normal age-related brain morphometric changes: Nonuniformity across cortical thickness, surface area and grey matter volume? *Neurobiology of Aging*, 33(3), 617.e1–617.e9.
- [Lepage et al., 2021] Lepage, C., Wagstyl, K., Jung, B., Seidlitz, J., Sponheim, C., Ungerleider, L., Wang, X., Evans, A. C., & Messinger, A. (2021). CIVET-Macaque: An automated pipeline for MRI-based cortical surface generation and cortical thickness in macaques. *NeuroImage*, 227, 117622.
- [Li et al., 2013] Li, L., Hu, X., Preuss, T. M., Glasser, M. F., Damen, F. W., Qiu, Y., & Rilling, J. (2013). Mapping putative hubs in human, chimpanzee and rhesus macaque connectomes via diffusion tractography. *NeuroImage*, 80, 462–474.
- [Li & Leigh, 2001] Li, L. & Leigh, J. S. (2001). High-precision mapping of the magnetic field utilizing the harmonic function mean value property. *Journal of Magnetic Resonance (San Diego, Calif.: 1997)*, 148(2), 442–448.


- [Li et al., 2014] Li, W., Wu, B., Batrachenko, A., Bancroft-Wu, V., Morey, R. A., Shashi, V., Langkammer, C., De Bellis, M. D., Ropele, S., Song, A. W., & Liu, C. (2014). Differential developmental trajectories of magnetic susceptibility in human brain gray and white matter over the lifespan. *Human Brain Mapping*, 35(6), 2698–2713.
- [Li et al., 2011] Li, W., Wu, B., & Liu, C. (2011). Quantitative susceptibility mapping of human brain reflects spatial variation in tissue composition. *NeuroImage*, 55(4), 1645–1656.
- [Li et al., 2016] Li, X., Morgan, P. S., Ashburner, J., Smith, J., & Rorden, C. (2016). The first step for neuroimaging data analysis: DICOM to NIfTI conversion. *Journal of Neuroscience Methods*, 264, 47–56.
- [Li et al., 2021] Li, Y., Sethi, S. K., Zhang, C., Miao, Y., Yerramsetty, K. K., Palutla, V. K., Gharabaghi, S., Wang, C., He, N., Cheng, J., Yan, F., & Haacke, E. M. (2021). Iron Content in Deep Gray Matter as a Function of Age Using Quantitative Susceptibility Mapping: A Multicenter Study. *Frontiers in Neuroscience*, 14, 1389.
- [Liu et al., 2015] Liu, C., Wei, H., Gong, N.-J., Cronin, M., Dibb, R., & Decker, K. (2015). Quantitative Susceptibility Mapping: Contrast Mechanisms and Clinical Applications. *Tomography*, 1(1), 3–17.
- [Liu et al., 2020a] Liu, C., Ye, F. Q., Newman, J. D., Szczupak, D., Tian, X., Yen, C. C.-C., Majka, P., Glen, D., Rosa, M. G. P., Leopold, D. A., & Silva, A. C. (2020a). A resource for the detailed 3D mapping of white matter pathways in the marmoset brain. *Nature Neuroscience*, 23(2), 271–280. Number: 2 Publisher: Nature Publishing Group.
- [Liu et al., 2021] Liu, C., Yen, C. C.-C., Szczupak, D., Tian, X., Glen, D., & Silva, A. C. (2021). Marmoset Brain Mapping V3: Population multi-modal standard volumetric and surface-based templates. *NeuroImage*, 226, 117620.
- [Liu et al., 2017] Liu, H., MacMillan, E. L., Jutzeler, C. R., Ljungberg, E., MacKay, A. L., Kolind, S. H., Mädler, B., Li, D. K. B., Dvorak, M. F., Curt, A., Laule, C., & Kramer, J. L. K. (2017). Assessing structure and function of myelin in cervical spondylotic myelopathy: Evidence of demyelination. *Neurology*, 89(6), 602–610. Publisher: Wolters Kluwer Health, Inc. on behalf of the American Academy of Neurology Section: Article.
- [Liu et al., 2009] Liu, T., Spincemille, P., Rochefort, L. d., Kressler, B., & Wang, Y. (2009). Calculation of susceptibility through multiple orientation sampling (COSMOS): A method for conditioning the inverse problem from measured magnetic field map to

- susceptibility source image in MRI. *Magnetic Resonance in Medicine*, 61(1), 196–204. \_eprint: <https://onlinelibrary.wiley.com/doi/pdf/10.1002/mrm.21828>.
- [Liu et al., 2012] Liu, T., Surapaneni, K., Lou, M., Cheng, L., Spincemaille, P., & Wang, Y. (2012). Cerebral Microbleeds: Burden Assessment by Using Quantitative Susceptibility Mapping. *Radiology*, 262(1), 269–278. Publisher: Radiological Society of North America.
- [Liu et al., 2020b] Liu, Z., Wang, X., Newman, N., Grant, K. A., Studholme, C., & Kroenke, C. D. (2020b). Anatomical and diffusion MRI brain atlases of the fetal rhesus macaque brain at 85, 110 and 135 days gestation. *NeuroImage*, 206, 116310.
- [Logothetis, 2003] Logothetis, N. K. (2003). MR imaging in the non-human primate: studies of function and of dynamic connectivity. *Current Opinion in Neurobiology*, 13(5), 630–642.
- [Logothetis et al., 1999] Logothetis, N. K., Guggenberger, H., Peled, S., & Pauls, J. (1999). Functional imaging of the monkey brain. *Nature Neuroscience*, 2(6), 555–562. Bandiera\_abtest: a Cg\_type: Nature Research Journals Number: 6 Primary\_atype: Research Publisher: Nature Publishing Group.
- [Luo et al., 2019a] Luo, T., Oladosu, O., Rawji, K. S., Zhai, P., Pridham, G., Hossain, S., & Zhang, Y. (2019a). Characterizing Structural Changes With Evolving Remyelination Following Experimental Demyelination Using High Angular Resolution Diffusion MRI and Texture Analysis. *Journal of Magnetic Resonance Imaging*, 49(6), 1750–1759. \_eprint: <https://onlinelibrary.wiley.com/doi/pdf/10.1002/jmri.26328>.
- [Luo et al., 2019b] Luo, X., Li, K., Zeng, Q., Huang, P., Jiaerken, Y., Wang, S., Shen, Z., Xu, X., Xu, J., Wang, C., Kong, L., Zhou, J., & Zhang, M. (2019b). Application of T1-/T2-Weighted Ratio Mapping to Elucidate Intracortical Demyelination Process in the Alzheimer’s Disease Continuum. *Frontiers in Neuroscience*, 13, 904.
- [Lv et al., 2021] Lv, Q., Yan, M., Shen, X., Wu, J., Yu, W., Yan, S., Yang, F., Zeljic, K., Shi, Y., Zhou, Z., Lv, L., Hu, X., Menon, R., & Wang, Z. (2021). Normative Analysis of Individual Brain Differences Based on a Population MRI-Based Atlas of Cynomolgus Macaques. *Cerebral Cortex (New York, N.Y.: 1991)*, 31(1), 341–355.
- [MacDonald & Pike, 2021] MacDonald, M. E. & Pike, G. B. (2021). MRI of healthy brain aging: A review. *NMR in Biomedicine*, n/a(n/a), e4564. \_eprint: <https://analyticalsciencejournals.onlinelibrary.wiley.com/doi/pdf/10.1002/nbm.4564>.

- [MacKay et al., 1994] MacKay, A., Whittall, K., Adler, J., Li, D., Paty, D., & Graeb, D. (1994). In vivo visualization of myelin water in brain by magnetic resonance. *Magnetic Resonance in Medicine*, 31(6), 673–677.
- [MacKay & Laule, 2016] MacKay, A. L. & Laule, C. (2016). Magnetic Resonance of Myelin Water: An in vivo Marker for Myelin. *Brain Plasticity*, 2(1), 71–91. Publisher: IOS Press.
- [Majka et al., 2016] Majka, P., Chaplin, T. A., Yu, H.-H., Tolpygo, A., Mitra, P. P., Wójcik, D. K., & Rosa, M. G. P. (2016). Towards a comprehensive atlas of cortical connections in a primate brain: Mapping tracer injection studies of the common marmoset into a reference digital template. *Journal of Comparative Neurology*, 524(11), 2161–2181. \_eprint: <https://onlinelibrary.wiley.com/doi/pdf/10.1002/cne.24023>.
- [Mancini et al., 2020] Mancini, M., Karakuzu, A., Cohen-Adad, J., Cercignani, M., Nichols, T. E., & Stikov, N. (2020). An interactive meta-analysis of MRI biomarkers of myelin. *eLife*, 9, e61523. Publisher: eLife Sciences Publications, Ltd.
- [Manjón et al., 2010] Manjón, J. V., Coupé, P., Martí-Bonmatí, L., Collins, D. L., & Robles, M. (2010). Adaptive non-local means denoising of MR images with spatially varying noise levels. *Journal of Magnetic Resonance Imaging*, 31(1), 192–203. \_eprint: <https://onlinelibrary.wiley.com/doi/pdf/10.1002/jmri.22003>.
- [Manogaran et al., 2016] Manogaran, P., Vavasour, I. M., Lange, A. P., Zhao, Y., McMullen, K., Rauscher, A., Carruthers, R., Li, D. K. B., Traboulsee, A. L., & Kolind, S. H. (2016). Quantifying visual pathway axonal and myelin loss in multiple sclerosis and neuromyelitis optica. *NeuroImage: Clinical*, 11, 743–750.
- [Marcus et al., 2011] Marcus, D. S., Harwell, J., Olsen, T., Hodge, M., Glasser, M. F., Prior, F., Jenkinson, M., Laumann, T., Curtiss, S. W., & Van Essen, D. C. (2011). Informatics and data mining tools and strategies for the human connectome project. *Frontiers in Neuroinformatics*, 5, 4.
- [Martin et al., 2006] Martin, M., Hiltner, T. D., Wood, J. C., Fraser, S. E., Jacobs, R. E., & Readhead, C. (2006). Myelin deficiencies visualized in vivo: Visually evoked potentials and T2-weighted magnetic resonance images of shiverer mutant and wild-type mice. *Journal of Neuroscience Research*, 84(8), 1716–1726. \_eprint: <https://onlinelibrary.wiley.com/doi/pdf/10.1002/jnr.21086>.
- [Mattison & Vaughan, 2017] Mattison, J. A. & Vaughan, K. L. (2017). An overview of non-human primates in aging research. *Experimental Gerontology*, 94, 41–45.

- [McColgan et al., 2021] McColgan, P., Helbling, S., Vaculčíaková, L., Pine, K., Wagstyl, K., Attar, F. M., Edwards, L., Papoutsis, M., Wei, Y., Van den Heuvel, M. P., Tabrizi, S. J., Rees, G., & Weiskopf, N. (2021). Relating quantitative 7T MRI across cortical depths to cytoarchitectonics, gene expression and connectomics. *Human Brain Mapping*, 42(15), 4996–5009. \_eprint: <https://onlinelibrary.wiley.com/doi/pdf/10.1002/hbm.25595>.
- [McCreary et al., 2009] McCreary, C. R., Bjarnason, T. A., Skihar, V., Mitchell, J. R., Yong, V. W., & Dunn, J. F. (2009). Multiexponential T2 and magnetization transfer MRI of demyelination and remyelination in murine spinal cord. *NeuroImage*, 45(4), 1173–1182.
- [McLaren et al., 2009] McLaren, D. G., Kosmatka, K. J., Oakes, T. R., Kroenke, C. D., Kohama, S. G., Matochik, J. A., Ingram, D. K., & Johnson, S. C. (2009). A Population-Average MRI-Based Atlas Collection of the Rhesus Macaque. *NeuroImage*, 45(1), 52–59.
- [Mimura et al., 2021] Mimura, K., Nagai, Y., Inoue, K.-i., Matsumoto, J., Hori, Y., Sato, C., Kimura, K., Okauchi, T., Hirabayashi, T., Nishijo, H., Yahata, N., Takada, M., Suhara, T., Higuchi, M., & Minamimoto, T. (2021). Chemogenetic activation of nigrostriatal dopamine neurons in freely moving common marmosets. *iScience*, 24(9), 103066.
- [Mitchell et al., 2019] Mitchell, T., Archer, D. B., Chu, W. T., Coombes, S. A., Lai, S., Wilkes, B. J., McFarland, N. R., Okun, M. S., Black, M. L., Herschel, E., Simuni, T., Comella, C., Xie, T., Li, H., Parrish, T. B., Kurani, A. S., Corcos, D. M., & Vailancourt, D. E. (2019). Neurite orientation dispersion and density imaging (NODDI) and free-water imaging in Parkinsonism. *Human Brain Mapping*, 40(17), 5094–5107. \_eprint: <https://onlinelibrary.wiley.com/doi/pdf/10.1002/hbm.24760>.
- [Moon et al., 2016] Moon, Y., Han, S.-H., & Moon, W.-J. (2016). Patterns of Brain Iron Accumulation in Vascular Dementia and Alzheimer’s Dementia Using Quantitative Susceptibility Mapping Imaging. *Journal of Alzheimer’s Disease*, 51(3), 737–745.
- [Moore et al., 2020] Moore, S., Meschkat, M., Ruhwedel, T., Trevisiol, A., Tzvetanova, I. D., Battefeld, A., Kusch, K., Kole, M. H. P., Strenzke, N., Möbius, W., de Hoz, L., & Nave, K.-A. (2020). A role of oligodendrocytes in information processing. *Nature Communications*, 11(1), 5497. Number: 1 Publisher: Nature Publishing Group.

- [Morell & Quarles, 1999] Morell, P. & Quarles, R. H. (1999). Characteristic Composition of Myelin. *Basic Neurochemistry: Molecular, Cellular and Medical Aspects. 6th edition*. Publisher: Lippincott-Raven.
- [Mukherjee, 2005] Mukherjee, P. (2005). Diffusion Tensor Imaging and Fiber Tractography in Acute Stroke. *Neuroimaging Clinics*, 15(3), 655–665. Publisher: Elsevier.
- [Murayama et al., 2006] Murayama, Y., Weber, B., Saleem, K. S., Augath, M., & Logothetis, N. K. (2006). Tracing neural circuits in vivo with Mn-enhanced MRI. *Magnetic Resonance Imaging*, 24(4), 349–358.
- [Möller et al., 2019] Möller, H. E., Bossoni, L., Connor, J. R., Crichton, R. R., Does, M. D., Ward, R. J., Zecca, L., Zucca, F. A., & Ronen, I. (2019). Iron, Myelin, and the Brain: Neuroimaging Meets Neurobiology. *Trends in Neurosciences*, 42(6), 384–401. Publisher: Elsevier.
- [Müller & Kassubek, 2013] Müller, H.-P. & Kassubek, J. (2013). Diffusion Tensor Magnetic Resonance Imaging in the Analysis of Neurodegenerative Diseases. *Journal of Visualized Experiments: JoVE*, (77), 50427.
- [Nadon, 2006] Nadon, N. L. (2006). Of Mice and Monkeys: National Institute on Aging Resources Supporting the Use of Animal Models in Biogerontology Research. *The Journals of Gerontology: Series A*, 61(8), 813–815.
- [Nakamura et al., 2017] Nakamura, K., Chen, J. T., Ontaneda, D., Fox, R. J., & Trapp, B. D. (2017). T<sub>1</sub>-/T<sub>2</sub>-weighted ratio differs in demyelinated cortex in multiple sclerosis. *Annals of Neurology*, 82(4), 635–639. \_eprint: <https://onlinelibrary.wiley.com/doi/pdf/10.1002/ana.25019>.
- [Nambu et al., 2015] Nambu, A., Tachibana, Y., & Chiken, S. (2015). Cause of parkinsonian symptoms: Firing rate, firing pattern or dynamic activity changes? *Basal Ganglia*, 5(1), 1–6.
- [Nave & Werner, 2014] Nave, K.-A. & Werner, H. B. (2014). Myelination of the nervous system: mechanisms and functions. *Annual Review of Cell and Developmental Biology*, 30, 503–533.
- [Nave & Werner, 2021] Nave, K.-A. & Werner, H. B. (2021). Ensheathment and Myelination of Axons: Evolution of Glial Functions. *Annual Review of Neuroscience*, 44(1), null. \_eprint: <https://doi.org/10.1146/annurev-neuro-100120-122621>.

- [Norbom et al., 2020] Norbom, L. B., Rokicki, J., Alnæs, D., Kaufmann, T., Doan, N. T., Andreassen, O. A., Westlye, L. T., & Tamnes, C. K. (2020). Maturation of cortical microstructure and cognitive development in childhood and adolescence: A T1w/T2w ratio MRI study. *Human Brain Mapping*, 41(16), 4676–4690. [\\_eprint: https://onlinelibrary.wiley.com/doi/pdf/10.1002/hbm.25149](https://onlinelibrary.wiley.com/doi/pdf/10.1002/hbm.25149).
- [Onodera & Hicks, 2009] Onodera, S. & Hicks, T. P. (2009). A Comparative Neuroanatomical Study of the Red Nucleus of the Cat, Macaque and Human. *PLOS ONE*, 4(8), e6623.
- [Park et al., 2009] Park, J.-H., Park, S.-W., Kang, S.-H., Nam, T.-K., Min, B.-K., & Hwang, S.-N. (2009). Detection of Traumatic Cerebral Microbleeds by Susceptibility-Weighted Image of MRI. *Journal of Korean Neurosurgical Society*, 46(4), 365–369.
- [Pedregosa et al., 2011] Pedregosa, F., Varoquaux, G., Gramfort, A., Michel, V., Thirion, B., Grisel, O., Blondel, M., Prettenhofer, P., Weiss, R., Dubourg, V., Vanderplas, J., Passos, A., Cournapeau, D., Brucher, M., Perrot, M., & Duchesnay, . (2011). Scikit-learn: Machine Learning in Python. *Journal of Machine Learning Research*, 12(85), 2825–2830.
- [Pei et al., 2015] Pei, M., Nguyen, T. D., Thimmappa, N. D., Salustri, C., Dong, F., Cooper, M. A., Li, J., Prince, M. R., & Wang, Y. (2015). An Algorithm for Fast Mono-exponential Fitting Based on Auto-Regression on Linear Operations (ARLO) of Data. *Magnetic resonance in medicine : official journal of the Society of Magnetic Resonance in Medicine / Society of Magnetic Resonance in Medicine*, 73(2), 843–850.
- [Peters, 2002] Peters, A. (2002). The effects of normal aging on myelin and nerve fibers: a review. *Journal of Neurocytology*, 31(8-9), 581–593.
- [Peters, 2006] Peters, R. (2006). Ageing and the brain. *Postgraduate Medical Journal*, 82(964), 84–88.
- [Phillips & Sherwood, 2012] Phillips, K. A. & Sherwood, C. C. (2012). Age-related differences in corpus callosum area of capuchin monkeys. *Neuroscience*, 202, 202–208.
- [Postelnicu et al., 2009] Postelnicu, G., Zöllei, L., & Fischl, B. (2009). Combined Volumetric and Surface Registration. *IEEE transactions on medical imaging*, 28(4), 508–522.
- [Raasakka et al., 2017] Raasakka, A., Ruskamo, S., Kowal, J., Barker, R., Baumann, A., Martel, A., Tuusa, J., Myllykoski, M., Bürck, J., Ulrich, A. S., Stahlberg, H., & Kurula, P. (2017). Membrane Association Landscape of Myelin Basic Protein Portrays

- Formation of the Myelin Major Dense Line. *Scientific Reports*, 7(1), 4974. Number: 1 Publisher: Nature Publishing Group.
- [Ramos et al., 2014] Ramos, P., Santos, A., Pinto, N. R., Mendes, R., Magalhães, T., & Almeida, A. (2014). Iron levels in the human brain: A post-mortem study of anatomical region differences and age-related changes. *Journal of Trace Elements in Medicine and Biology*, 28(1), 13–17.
- [Ravanfar et al., 2021] Ravanfar, P., Loi, S. M., Syeda, W. T., Van Rheenen, T. E., Bush, A. I., Desmond, P., Cropley, V. L., Lane, D. J. R., Opazo, C. M., Moffat, B. A., Velakoulis, D., & Pantelis, C. (2021). Systematic Review: Quantitative Susceptibility Mapping (QSM) of Brain Iron Profile in Neurodegenerative Diseases. *Frontiers in Neuroscience*, 15, 618435.
- [Readhead & Hood, 1990] Readhead, C. & Hood, L. (1990). The dysmyelinating mouse mutations shiverer (shi) and myelin deficient (shimld). *Behavior Genetics*, 20(2), 213–234.
- [Reveley et al., 2017] Reveley, C., Gruslys, A., Ye, F. Q., Glen, D., Samaha, J., E. Russ, B., Saad, Z., K. Seth, A., Leopold, D. A., & Saleem, K. S. (2017). Three-Dimensional Digital Template Atlas of the Macaque Brain. *Cerebral Cortex (New York, NY)*, 27(9), 4463–4477.
- [Rilling, 2006] Rilling, J. K. (2006). Human and nonhuman primate brains: Are they allometrically scaled versions of the same design? *Evolutionary Anthropology: Issues, News, and Reviews*, 15(2), 65–77.
- [Robinson & Bhuta, 2011] Robinson, R. J. & Bhuta, S. (2011). Susceptibility-Weighted Imaging of the Brain: Current Utility and Potential Applications. *Journal of Neuroimaging*, 21(4), e189–e204. \_eprint: <https://onlinelibrary.wiley.com/doi/pdf/10.1111/j.1552-6569.2010.00516.x>.
- [Robinson et al., 2017] Robinson, S. D., Bredies, K., Khabipova, D., Dymerska, B., Marques, J. P., & Schweser, F. (2017). An illustrated comparison of processing methods for MR phase imaging and QSM: combining array coil signals and phase unwrapping. *NMR in Biomedicine*, 30(4), e3601. \_eprint: <https://analyticalsciencejournals.onlinelibrary.wiley.com/doi/pdf/10.1002/nbm.3601>.
- [Rodrigue et al., 2013] Rodrigue, K. M., Daugherty, A. M., Haacke, E. M., & Raz, N. (2013). The Role of Hippocampal Iron Concentration and Hippocampal Volume in Age-Related Differences in Memory. *Cerebral Cortex*, 23(7), 1533–1541.



- [Rohlfing et al., 2012] Rohlfing, T., Kroenke, C. D., Sullivan, E. V., Dubach, M. F., Bowden, D. M., Grant, K., & Pfefferbaum, A. (2012). The INIA19 Template and NeuroMaps Atlas for Primate Brain Image Parcellation and Spatial Normalization. *Frontiers in Neuroinformatics*, 6. Publisher: Frontiers.
- [Rushmore et al., 2020] Rushmore, R. J., Bouix, S., Kubicki, M., Rathi, Y., Rosene, D. L., Yeterian, E. H., & Makris, N. (2020). MRI-based Parcellation and Morphometry of the Individual Rhesus Monkey Brain: the macaque Harvard-Oxford Atlas (mHOA), a translational system referencing a standardized ontology. *Brain Imaging and Behavior*.
- [Salat et al., 2004] Salat, D. H., Buckner, R. L., Snyder, A. Z., Greve, D. N., Desikan, R. S., Busa, E., Morris, J. C., Dale, A. M., & Fischl, B. (2004). Thinning of the Cerebral Cortex in Aging. *Cerebral Cortex*, 14(7), 721–730.
- [Saleem & Logothetis, 2012] Saleem, K. S. & Logothetis, N. K. (2012). *A Combined MRI and Histology Atlas of the Rhesus Monkey Brain in Stereotaxic Coordinates*. Academic Press.
- [Schenck & Zimmerman, 2004] Schenck, J. F. & Zimmerman, E. A. (2004). High-field magnetic resonance imaging of brain iron: birth of a biomarker? *NMR in biomedicine*, 17(7), 433–445.
- [Schiavone et al., 2009] Schiavone, F., Charlton, R. A., Barrick, T. R., Morris, R. G., & Markus, H. S. (2009). Imaging age-related cognitive decline: A comparison of diffusion tensor and magnetization transfer MRI. *Journal of Magnetic Resonance Imaging*, 29(1), 23–30. \_eprint: <https://onlinelibrary.wiley.com/doi/pdf/10.1002/jmri.21572>.
- [Schmierer et al., 2008] Schmierer, K., Wheeler-Kingshott, C. A. M., Tozer, D. J., Boulby, P. A., Parkes, H. G., Yousry, T. A., Scaravilli, F., Barker, G. J., Tofts, P. S., & Miller, D. H. (2008). Quantitative magnetic resonance of postmortem multiple sclerosis brain before and after fixation. *Magnetic Resonance in Medicine*, 59(2), 268–277. \_eprint: <https://onlinelibrary.wiley.com/doi/pdf/10.1002/mrm.21487>.
- [Schneider, 2020] Schneider, S. A. (2020). Chapter 46 - Neurodegeneration with brain iron accumulation. In R. N. Rosenberg & J. M. Pascual (Eds.), *Rosenberg's Molecular and Genetic Basis of Neurological and Psychiatric Disease (Sixth Edition)* (pp. 621–631). Academic Press.
- [Schweser et al., 2010] Schweser, F., Deistung, A., Lehr, B. W., & Reichenbach, J. R. (2010). Differentiation between diamagnetic and paramagnetic cerebral lesions based on

- magnetic susceptibility mapping. *Medical Physics*, 37(10), 5165–5178. \_eprint: <https://aapm.onlinelibrary.wiley.com/doi/pdf/10.1118/1.3481505>.
- [Seidlitz et al., 2018] Seidlitz, J., Sponheim, C., Glen, D., Ye, F. Q., Saleem, K. S., Leopold, D. A., Ungerleider, L., & Messinger, A. (2018). A population MRI brain template and analysis tools for the macaque. *NeuroImage*, 170, 121–131.
- [Seiler et al., 2014] Seiler, S., Ropele, S., & Schmidt, R. (2014). Magnetization Transfer Imaging for in vivo Detection of Microstructural Tissue Changes in Aging and Dementia: A Short Literature Review. *Journal of Alzheimer's Disease*, 42(s3), S229–S237. Publisher: IOS Press.
- [Shahmaei et al., 2019] Shahmaei, V., Faeghi, F., Mohammadbeigi, A., Hashemi, H., & Ashrafi, F. (2019). Evaluation of iron deposition in brain basal ganglia of patients with Parkinson's disease using quantitative susceptibility mapping. *European Journal of Radiology Open*, 6, 169–174.
- [Shams et al., 2019] Shams, Z., Norris, D. G., & Marques, J. P. (2019). A comparison of in vivo MRI based cortical myelin mapping using T1w/T2w and R1 mapping at 3T. *PLoS ONE*, 14(7).
- [Shaw et al., 2016] Shaw, M. E., Sachdev, P. S., Anstey, K. J., & Cherbuin, N. (2016). Age-related cortical thinning in cognitively healthy individuals in their 60s: the PATH Through Life study. *Neurobiology of Aging*, 39, 202–209.
- [Shi et al., 2017] Shi, Y., Budin, F., Yapuncich, E., Rumble, A., Young, J. T., Payne, C., Zhang, X., Hu, X., Godfrey, J., Howell, B., Sanchez, M. M., & Styner, M. A. (2017). UNC-Emory Infant Atlases for Macaque Brain Image Analysis: Postnatal Brain Development through 12 Months. *Frontiers in Neuroscience*, 10. Publisher: Frontiers.
- [Shmueli et al., 2009] Shmueli, K., Zwart, J. A. d., Gelderen, P. v., Li, T.-Q., Dodd, S. J., & Duyn, J. H. (2009). Magnetic susceptibility mapping of brain tissue in vivo using MRI phase data. *Magnetic Resonance in Medicine*, 62(6), 1510–1522.
- [Shu et al., 2011] Shu, N., Liu, Y., Li, K., Duan, Y., Wang, J., Yu, C., Dong, H., Ye, J., & He, Y. (2011). Diffusion Tensor Tractography Reveals Disrupted Topological Efficiency in White Matter Structural Networks in Multiple Sclerosis. *Cerebral Cortex*, 21(11), 2565–2577.
- [Sikora et al., 2021] Sikora, E., Bielak-Zmijewska, A., Dudkowska, M., Krzystyniak, A., Mosieniak, G., Wesierska, M., & Wlodarczyk, J. (2021). Cellular Senescence in Brain Aging. *Frontiers in Aging Neuroscience*, 13, 71.

- [Smith et al., 2007] Smith, C. D., Chebrolu, H., Wekstein, D. R., Schmitt, F. A., & Markesbery, W. R. (2007). Age and gender effects on human brain anatomy: a voxel-based morphometric study in healthy elderly. *Neurobiology of Aging*, 28(7), 1075–1087.
- [Song et al., 2003] Song, S.-K., Sun, S.-W., Ju, W.-K., Lin, S.-J., Cross, A. H., & Neufeld, A. H. (2003). Diffusion tensor imaging detects and differentiates axon and myelin degeneration in mouse optic nerve after retinal ischemia. *NeuroImage*, 20(3), 1714–1722.
- [Sood et al., 2017] Sood, S., Urriola, J., Reutens, D., O'Brien, K., Bollmann, S., Barth, M., & Vegh, V. (2017). Echo time-dependent quantitative susceptibility mapping contains information on tissue properties. *Magnetic Resonance in Medicine*, 77(5), 1946–1958.
- [Stadelmann et al., 2011] Stadelmann, C., Wegner, C., & Brück, W. (2011). Inflammation, demyelination, and degeneration — Recent insights from MS pathology. *Biochimica et Biophysica Acta (BBA) - Molecular Basis of Disease*, 1812(2), 275–282.
- [Steven et al., 2014] Steven, A. J., Zhuo, J., & Melhem, E. R. (2014). Diffusion Kurtosis Imaging: An Emerging Technique for Evaluating the Microstructural Environment of the Brain. *American Journal of Roentgenology*, 202(1), W26–W33. Publisher: American Roentgen Ray Society.
- [Stikov et al., 2015] Stikov, N., Campbell, J. S. W., Stroh, T., Lavelée, M., Frey, S., Novek, J., Nuara, S., Ho, M.-K., Bedell, B. J., Dougherty, R. F., Leppert, I. R., Boudreau, M., Narayanan, S., Duval, T., Cohen-Adad, J., Picard, P.-A., Gasecka, A., Côté, D., & Pike, G. B. (2015). In vivo histology of the myelin g-ratio with magnetic resonance imaging. *NeuroImage*, 118, 397–405.
- [Stokum et al., 2015] Stokum, J. A., Sours, C., Zhuo, J., Kane, R., Shanmuganathan, K., & Gullapalli, R. P. (2015). A longitudinal evaluation of diffusion kurtosis imaging in patients with mild traumatic brain injury. *Brain Injury*, 29(1), 47–57. Publisher: Taylor & Francis \_eprint: <https://doi.org/10.3109/02699052.2014.947628>.
- [Straub et al., 2017] Straub, S., Schneider, T. M., Emmerich, J., Freitag, M. T., Ziener, C. H., Schlemmer, H.-P., Ladd, M. E., & Laun, F. B. (2017). Suitable reference tissues for quantitative susceptibility mapping of the brain. *Magnetic Resonance in Medicine*, 78(1), 204–214.
- [Swash et al., 2020] Swash, M., Burke, D., Turner, M. R., Grosskreutz, J., Leigh, P. N., de-Carvalho, M., & Kiernan, M. C. (2020). Occasional essay: Upper motor neuron

- syndrome in amyotrophic lateral sclerosis. *Journal of Neurology, Neurosurgery & Psychiatry*, 91(3), 227–234. Publisher: BMJ Publishing Group Ltd Section: 2020 Hind-sight.
- [Tardif et al., 2011] Tardif, S. D., Mansfield, K. G., Ratnam, R., Ross, C. N., & Ziegler, T. E. (2011). The Marmoset as a Model of Aging and Age-Related Diseases. *ILAR journal / National Research Council, Institute of Laboratory Animal Resources*, 52(1), 54–65.
- [Taubert et al., 2020] Taubert, M., Roggenhofer, E., Melie-Garcia, L., Muller, S., Lehmann, N., Preisig, M., Vollenweider, P., Marques-Vidal, P., Lutti, A., Kherif, F., & Dragan-ski, B. (2020). Converging patterns of aging-associated brain volume loss and tissue microstructure differences. *Neurobiology of Aging*, 88, 108–118.
- [Tendler & Bowtell, 2019] Tendler, B. C. & Bowtell, R. (2019). Frequency difference map-ping applied to the corpus callosum at 7T. *Magnetic Resonance in Medicine*, 81(5), 3017–3031.
- [Timmler & Simons, 2019] Timmler, S. & Simons, M. (2019). Grey matter myelination. *Glia*, 67(11), 2063–2070. \_eprint: <https://onlinelibrary.wiley.com/doi/pdf/10.1002/glia.23614>.
- [Tullo et al., 2019] Tullo, S., Patel, R., Devenyi, G. A., Salaciak, A., Bedford, S. A., Farzin, S., Wlodarski, N., Tardif, C. L., Breitner, J. C. S., & Chakravarty, M. M. (2019). MR-based age-related effects on the striatum, globus pallidus, and thalamus in healthy in-dividuals across the adult lifespan. *Human Brain Mapping*, 40(18), 5269–5288.
- [Tustison et al., 2010] Tustison, N. J., Avants, B. B., Cook, P. A., Zheng, Y., Egan, A., Yushkevich, P. A., & Gee, J. C. (2010). N4ITK: improved N3 bias correction. *IEEE transactions on medical imaging*, 29(6), 1310–1320.
- [Utter & Basso, 2008] Utter, A. A. & Basso, M. A. (2008). The basal ganglia: An overview of circuits and function. *Neuroscience & Biobehavioral Reviews*, 32(3), 333–342.
- [Vaidya et al., 2019] Vaidya, A. R., Pujara, M. S., Petrides, M., Murray, E. A., & Fellows, L. K. (2019). Lesion studies in contemporary neuroscience. *Trends in cognitive sci-ences*, 23(8), 653–671.
- [Vargas et al., 2015] Vargas, W. S., Monohan, E., Pandya, S., Raj, A., Vartanian, T., Nguyen, T. D., Hurtado Rúa, S. M., & Gauthier, S. A. (2015). Measuring longitudinal myelin water fraction in new multiple sclerosis lesions. *NeuroImage: Clinical*, 9, 369–375.

- [Veraart et al., 2016] Veraart, J., Novikov, D. S., Christiaens, D., Ades-Aron, B., Sijbers, J., & Fieremans, E. (2016). Denoising of diffusion MRI using random matrix theory. *NeuroImage*, 142, 394–406.
- [Vitek & Johnson, 2019] Vitek, J. L. & Johnson, L. A. (2019). Understanding Parkinson's disease and deep brain stimulation: Role of monkey models. *Proceedings of the National Academy of Sciences*, 116(52), 26259–26265. Publisher: National Academy of Sciences Section: Colloquium Paper.
- [Wagstyl et al., 2015] Wagstyl, K., Ronan, L., Goodyer, I. M., & Fletcher, P. C. (2015). Cortical thickness gradients in structural hierarchies. *NeuroImage*, 111, 241–250.
- [Wang et al., 2019] Wang, N., Zhang, J., Cofer, G., Qi, Y., Anderson, R. J., White, L. E., & Allan Johnson, G. (2019). Neurite orientation dispersion and density imaging of mouse brain microstructure. *Brain Structure and Function*, 224(5), 1797–1813.
- [Wang & Liu, 2015] Wang, Y. & Liu, T. (2015). Quantitative susceptibility mapping (QSM): Decoding MRI data for a tissue magnetic biomarker. *Magnetic Resonance in Medicine*, 73(1), 82–101.
- [Ward et al., 2014] Ward, R. J., Zucca, F. A., Duyn, J. H., Crichton, R. R., & Zecca, L. (2014). The role of iron in brain ageing and neurodegenerative disorders. *The Lancet Neurology*, 13(10), 1045–1060.
- [Weber et al., 2020] Weber, K., Häcker, R., Hardisty, J. F., Harris, S. B., & Hayes, A. W. (2020). Oral repeated-dose toxicity studies of BIA 10–2474 in cynomolgus monkeys. *Regulatory Toxicology and Pharmacology*, 111, 104547.
- [Weiss et al., 2020] Weiss, A. R., Liu, Z., Wang, X., Liguore, W. A., Kroenke, C. D., & McBride, J. L. (2020). The macaque brain ONPRC18 template with combined gray and white matter labelmap for multimodal neuroimaging studies of nonhuman primates. *NeuroImage*, (pp. 117517).
- [Wen et al., 2020] Wen, Q., Yang, H., Li, J., Zhang, J., Tong, H., Ye, Q., & Zhong, K. (2020). Ultra-High-Resolution in vitro MRI Study of Age-Related Brain Subcortical Susceptibility Alteration in Rhesus Monkeys at 9.4 T. *Frontiers in Aging Neuroscience*, 12, 259.
- [Westerhausen et al., 2021] Westerhausen, R., Fjell, A. M., Kompus, K., Schapiro, S. J., Sherwood, C. C., Walhovd, K. B., & Hopkins, W. D. (2021). Comparative morphology of the corpus callosum across the adult lifespan in chimpanzees (*Pan troglodytes*)

- and humans. *Journal of Comparative Neurology*, 529(7), 1584–1596. \_eprint: <https://onlinelibrary.wiley.com/doi/pdf/10.1002/cne.25039>.
- [Westerhausen & Meguerditchian, 2021] Westerhausen, R. & Meguerditchian, A. (2021). Corpus callosum morphology across the lifespan in baboons (*Papio anubis*): A cross-sectional study of relative mid-sagittal surface area and thickness. *Neuroscience Research*.
- [Wey et al., 2014] Wey, H.-Y., Phillips, K. A., McKay, D. R., Laird, A. R., Kochunov, P., Davis, M. D., Glahn, D. C., Blangero, J., Duong, T. Q., & Fox, P. T. (2014). Multi-region hemispheric specialization differentiates human from nonhuman primate brain function. *Brain Structure & Function*, 219(6), 2187–2194.
- [Wharton & Bowtell, 2012] Wharton, S. & Bowtell, R. (2012). Fiber orientation-dependent white matter contrast in gradient echo MRI. *Proceedings of the National Academy of Sciences*, 109(45), 18559–18564. ISBN: 9781211075100 Publisher: National Academy of Sciences Section: Biological Sciences.
- [Wharton & Bowtell, 2015] Wharton, S. & Bowtell, R. (2015). Effects of white matter microstructure on phase and susceptibility maps. *Magnetic Resonance in Medicine*, 73(3), 1258–1269.
- [Winston et al., 2020] Winston, G. P., Vos, S. B., Caldairou, B., Hong, S.-J., Czech, M., Wood, T. C., Wastling, S. J., Barker, G. J., Bernhardt, B. C., Bernasconi, N., Duncan, J. S., & Bernasconi, A. (2020). Microstructural imaging in temporal lobe epilepsy: Diffusion imaging changes relate to reduced neurite density. *NeuroImage: Clinical*, 26, 102231.
- [Wolff & Balaban, 1989] Wolff, S. D. & Balaban, R. S. (1989). Magnetization transfer contrast (MTC) and tissue water proton relaxation in vivo. *Magnetic Resonance in Medicine*, 10(1), 135–144.
- [Worley et al., 2014] Worley, K. C., Warren, W. C., Rogers, J., Locke, D., Muzny, D. M., Mardis, E. R., Weinstock, G. M., Tardif, S. D., Aagaard, K. M., Archidiacono, N., Rayan, N. A., Batzer, M. A., Beal, K., Brejova, B., Capozzi, O., Capuano, S. B., Casola, C., Chandrabose, M. M., Cree, A., Dao, M. D., de Jong, P. J., del Rosario, R. C.-H., Delehaunty, K. D., Dinh, H. H., Eichler, E. E., Fitzgerald, S., Flicek, P., Fontenot, C. C., Fowler, R. G., Fronick, C., Fulton, L. A., Fulton, R. S., Gabisi, R. A., Gerlach, D., Graves, T. A., Gunaratne, P. H., Hahn, M. W., Haig, D., Han, Y., Harris, R. A., Herrero, J., Hillier, L. W., Hubley, R., Hughes, J. F., Hume, J., Jhangiani, S. N., Jorde, L. B., Joshi, V., Karakor, E., Konkol, M. K., Kosiol, C., Kovar,

C. L., Kriventseva, E. V., Lee, S. L., Lewis, L. R., Liu, Y.-s., Lopez, J., Lopez-Otin, C., Lorente-Galdos, B., Mansfield, K. G., Marques-Bonet, T., Minx, P., Misceo, D., Moncrieff, J. S., Morgan, M. B., Nazareth, L. V., Newsham, I., Nguyen, N. B., Okwuonu, G. O., Prabhakar, S., Perales, L., Pu, L.-L., Puente, X. S., Quesada, V., Ranck, M. C., Raney, B. J., Raveendran, M., Deiros, D. R., Rocchi, M., Rodriguez, D., Ross, C., Ruffier, M., Ruiz, S. J., Sajjadian, S., Santibanez, J., Schridder, D. R., Searle, S., Skaletsky, H., Soibam, B., Smit, A. F. A., Tennakoon, J. B., Tomaska, L., Ullmer, B., Vajnar, C. E., Ventura, M., Vilella, A. J., Vinar, T., Vogel, J.-H., Walker, J. A., Wang, Q., Warner, C. M., Wildman, D. E., Witherspoon, D. J., Wright, R. A., Wu, Y., Xiao, W., Xing, J., Zdobnov, E. M., Zhu, B., Gibbs, R. A., Wilson, R. K., & The Marmoset Genome Sequencing and Analysis Consortium (2014). The common marmoset genome provides insight into primate biology and evolution. *Nature Genetics*, 46(8), 850–857. Bandiera\_abtest: a Cc\_license\_type: cc\_y Cg\_type: Nature Research Journals Number: 8 Primary\_atype: Research Publisher: Nature Publishing Group Subject\_term: Animal physiology;Genomics;Sequencing Subject\_term\_id: animal-physiology;genomics;sequencing.

[Wright et al., 2016] Wright, A. D., Jarrett, M., Vavasour, I., Shahinfard, E., Kolind, S., Donkelaar, P. v., Taunton, J., Li, D., & Rauscher, A. (2016). Myelin Water Fraction Is Transiently Reduced after a Single Mild Traumatic Brain Injury – A Prospective Cohort Study in Collegiate Hockey Players. *PLOS ONE*, 11(2), e0150215. Publisher: Public Library of Science.

[Wu et al., 2010] Wu, Z., Li, S., Lei, J., An, D., & Haacke, E. M. (2010). Evaluation of Traumatic Subarachnoid Hemorrhage Using Susceptibility-Weighted Imaging. *American Journal of Neuroradiology*, 31(7), 1302–1310. Publisher: American Journal of Neuroradiology Section: Brain.

[Xiao et al., 2015] Xiao, Y., Fonov, V., Bériault, S., Subaie, F. A., Chakravarty, M. M., Sadikot, A. F., Pike, G. B., & Collins, D. L. (2015). Multi-contrast unbiased MRI atlas of a Parkinson’s disease population. *International Journal of Computer Assisted Radiology and Surgery*, 10(3), 329–341.

[Yoshida et al., 2021] Yoshida, A., Ye, F. Q., Yu, D. K., Leopold, D. A., & Hikosaka, O. (2021). Visualization of iron-rich subcortical structures in non-human primates in vivo by quantitative susceptibility mapping at 3T MRI. *NeuroImage*, 241, 118429.

[Yu et al., 2020] Yu, B., Wang, Y., Wang, L., Shen, D., & Zhou, L. (2020). Medical Image Synthesis via Deep Learning. *Advances in Experimental Medicine and Biology*, 1213, 23–44.

- [Yushkevich et al., 2006] Yushkevich, P. A., Piven, J., Hazlett, H. C., Smith, R. G., Ho, S., Gee, J. C., & Gerig, G. (2006). User-guided 3D active contour segmentation of anatomical structures: significantly improved efficiency and reliability. *NeuroImage*, 31(3), 1116–1128.
- [Zhang et al., 2012] Zhang, H., Schneider, T., Wheeler-Kingshott, C. A., & Alexander, D. C. (2012). NODDI: practical in vivo neurite orientation dispersion and density imaging of the human brain. *NeuroImage*, 61(4), 1000–1016.
- [Zhang et al., 2018] Zhang, J., Gregory, S., Scahill, R. I., Durr, A., Thomas, D. L., Lehericy, S., Rees, G., Tabrizi, S. J., & Zhang, H. (2018). In vivo characterization of white matter pathology in premanifest huntington’s disease. *Annals of Neurology*, 84(4), 497–504. \_eprint: <https://onlinelibrary.wiley.com/doi/pdf/10.1002/ana.25309>.
- [Zhang et al., 2016a] Zhang, Y., Gauthier, S. A., Gupta, A., Chen, W., Comunale, J., Chiang, G. C.-Y., Zhou, D., Askin, G., Zhu, W., Pitt, D., & Wang, Y. (2016a). QSM and  $R_2^*$  measured changes during white matter lesion development in multiple sclerosis: myelin breaking down, myelin debris degradation and removal, and iron accumulation. *AJNR. American journal of neuroradiology*, 37(9), 1629–1635.
- [Zhang et al., 2016b] Zhang, Y., Gauthier, S. A., Gupta, A., Chen, W., Comunale, J., Chiang, G. C.-Y., Zhou, D., Askin, G., Zhu, W., Pitt, D., & Wang, Y. (2016b). Quantitative Susceptibility Mapping and  $R_2^*$  Measured Changes during White Matter Lesion Development in Multiple Sclerosis: Myelin Breakdown, Myelin Debris Degradation and Removal, and Iron Accumulation. *American Journal of Neuroradiology*, 37(9), 1629–1635.
- [Zhou et al., 2014] Zhou, D., Liu, T., Spincemille, P., & Wang, Y. (2014). Background field removal by solving the Laplacian boundary value problem. *NMR in Biomedicine*, 27(3), 312–319. \_eprint: <https://analyticalsciencejournals.onlinelibrary.wiley.com/doi/pdf/10.1002/nbm.3064>.
- [Zhou et al., 2020] Zhou, Z., Tong, Q., Zhang, L., Ding, Q., Lu, H., Jonkman, L. E., Yao, J., He, H., Zhu, K., & Zhong, J. (2020). Evaluation of the diffusion MRI white matter tract integrity model using myelin histology and Monte-Carlo simulations. *NeuroImage*, 223, 117313.
- [Zimin et al., 2014] Zimin, A. V., Cornish, A. S., Maudhoo, M. D., Gibbs, R. M., Zhang, X., Pandey, S., Meehan, D. T., Wipfler, K., Bosinger, S. E., Johnson, Z. P., Tharp, G. K., Marçais, G., Roberts, M., Ferguson, B., Fox, H. S., Treangen, T., Salzberg, S. L., Yorke,



J. A., & Norgren, R. B. (2014). A new rhesus macaque assembly and annotation for next-generation sequencing analyses. *Biology Direct*, 9(1), 20.

# Declaration

I hereby confirm that the work presented in this thesis entitled "*Multi-contrast Magnetic Resonance Imaging of Myelin and Iron in the Brain*" is my own. Where information derived from other sources has been quoted rightly in the thesis.

*Göttingen, 31/10/2021*

---

Rakshit Dadarwal